

# Electroplating Dysprosium from Ionic Liquid-Based Solutions.

-

A Promising Electrochemical Step to Produce  
Stronger High Performance Nd(Dy)-Fe-B Sintered  
Magnets.



A Thesis presented for the Degree of Doctor of Natural Sciences  
(Dr. rer. nat.)

Institute of Physical and Theoretical Chemistry  
Faculty of Natural Sciences IV  
Chemistry and Pharmacy  
University of Regensburg

**Gottfried Suppan**

Regensburg  
2015



Official Registration:	13.05.2015
Defense:	10.06.2015
Ph.D. Supervisor	Prof. Dr. Heiner J. Gores
Chair:	Prof. Dr. Dominik Horinek
Adjudicators:	Prof. Dr. Heiner J. Gores
	Prof. Dr. Hubert Motschmann
	Prof. Dr. Arno Pfitzner

*For my family*



# Preface

The work described in this thesis was carried out under the supervision of Prof. Dr. Heiner Jakob Gores in the facilities of the Siemens AG, Research and Technology Center from March 2011 to September 2014. Within the framework of “PerEMot”- a project partially funded by the German Federal Ministry of Education and Research, the author was part of the group MAT-MSR-DE, which investigates strategical and sustainable application, substitution and recycling of critical materials.

The work presented continued until Mai 2015 at the University of Regensburg at the Institute of Physical and Theoretical Chemistry, Faculty of Natural Sciences IV, University of Regensburg.

## Acknowledgements

This work could not have been possible without the contribution of several people to whom I want to express my gratitude now.

First and foremost I express my deepest gratitude to Prof. Dr. Heiner Jakob Gores for his immeasurable support, dedication and guidance throughout the scope of this work.

Furthermore, I am very grateful to the Head of the Institute of Physical and Theoretical Chemistry and Chair of the Department of Physical Chemistry II, Prof. Dr. W. Kunz for his support.

In particular I thank Dr. Manfred Rühlig for his professional support during the progress of this work at the Siemens AG and Dr. Günter Schmid for providing the laboratory space and equipment.

My thanks to all the staff members, in particular Herbert Mai for the preparation of PVD-coatings, Dr. Andreas Rucki for sample analysis and Dr. Andreas Kanitz from Siemens AG, Erlangen for his help with in the chemistry laboratories.

In addition, I thank my fellow colleagues Anna-Maria Krestel, Renate Kellermann, Sebastián Pecqueur, Carina Ehrig, Dr. Dan Taroata, Dr. Ralf Krause and Dr. Florian Kessler for the nice atmosphere in the office and laboratories, respectively.

My thanks to my student colleagues and staff members from the Institute of Physical and Theoretical Chemistry and the Institute of Inorganic Chemistry for their warm reception after my return to the University of Regensburg.

Many thanks to the German Federal Ministry of Education and Research and the Siemens AG for their financial support.

Finally, I thank my family for their unconditional support.

# Contents

<b>1</b>	<b>Introduction</b>	<b>1</b>
<b>2</b>	<b>Theoretical Background</b>	<b>5</b>
2.1	Electrochemical Fundamentals . . . . .	5
2.1.1	Electrochemical Deposition Kinetics and Mechanism . . . . .	5
2.1.2	The Electrochemical Double Layer . . . . .	10
2.1.3	Nucleation and Growth Models . . . . .	14
2.1.4	Atomistic Aspect of Metal Electrodeposition . . . . .	16
2.1.5	Nucleation of Surface Nuclei . . . . .	22
2.1.6	Electrolytes for Electrodeposition . . . . .	25
2.2	Magnetism . . . . .	29
2.2.1	Quantum Origin of Magnetism . . . . .	29
2.2.2	Many-Electron Systems . . . . .	30
2.2.3	Magnetic Properties . . . . .	32
2.2.4	Rare Earth-3d Metal Alloys . . . . .	35
2.2.5	Nd-Fe-B-Type Magnetic Materials . . . . .	35
2.2.6	Production of sintered high performance Nd-Fe-B-magnets . . . . .	39
2.2.7	Grain Boundary Diffusion Process . . . . .	41
<b>3</b>	<b>Experimental Methods and Instrumentation</b>	<b>43</b>
3.1	Electrochemical Techniques . . . . .	43
3.1.1	Cyclic Voltammetry . . . . .	43
3.1.2	Chronoamperometry and Chronopotentiometry . . . . .	46
3.1.3	The Fast Impedance Scanning - Quartz Crystal Microbalance . . . . .	47
<b>4</b>	<b>Analytical Methods</b>	<b>52</b>
4.1	Determination of Water Contents . . . . .	52
4.2	Elemental Analysis . . . . .	54
4.3	Thermogravimetric Analysis . . . . .	54
4.4	Surface Analytical Methods . . . . .	54
4.4.1	X-Ray Photoelectron Spectroscopy . . . . .	54
4.4.2	Electron Probe Micro-Analysis . . . . .	55
4.5	Magnetic Characterization . . . . .	57
4.5.1	Hysteresis graph for Hard Magnetic Materials . . . . .	57
4.5.2	Pulse Field Magnetometer . . . . .	58
4.6	Materials and Purity . . . . .	60
4.6.1	Solvents . . . . .	60
4.6.2	Metal Salts . . . . .	60

<b>5</b>	<b>Metal Additions by Physical Vapor Deposition</b>	<b>61</b>
5.1	Addition of Aluminum . . . . .	62
5.1.1	Deposition of Aluminum . . . . .	63
5.1.2	Effects of Al-addition . . . . .	63
5.2	Addition of Copper . . . . .	66
5.3	Deposition of Copper . . . . .	66
5.3.1	Effects of Cu-addition . . . . .	66
5.4	Addition of Terbium . . . . .	69
5.4.1	Deposition of Terbium . . . . .	69
5.4.2	Effects of Tb-Addition . . . . .	69
5.4.3	Comparison of Dy and Tb Grain Boundary Treated Sintered Magnets	76
<b>6</b>	<b>Grain Boundary Diffusion of Metal Alloys by Physical Vapor Deposition</b>	<b>78</b>
6.1	Grain Boundary Diffusion of Aluminum-Dysprosium Alloys . . . . .	79
6.1.1	Magnetic Properties of Grain Boundary Diffusion-Processed Sintered Magnets coated with Al–Dy-Alloys . . . . .	81
<b>7</b>	<b>Material Synthesis</b>	<b>87</b>
7.1	Synthesis of Silver-(I)-Bis(trifluoromethylsulfonyl)imide . . . . .	87
7.2	Synthesis of Copper-(II)-Bis(trifluoromethylsulfonyl)imide . . . . .	87
7.3	Synthesis of Dysprosium-(III)-Bis(trifluoromethylsulfonyl)imide . . . . .	88
7.4	Synthesis of Terbium-(III)-Bis(trifluoromethylsulfonyl)imide . . . . .	88
7.5	Synthesis of Neodymium-(III)-Bis(trifluoromethylsulfonyl)imide . . . . .	88
7.6	Synthesis of Cobalt-(II)-Bis(trifluoromethylsulfonyl)imide . . . . .	89
7.7	Synthesis of Iron-(II)-Bis(trifluoromethylsulfonyl)imide . . . . .	89
<b>8</b>	<b>Metal Electrodeposition</b>	<b>90</b>
8.1	Electrodeposition of Copper . . . . .	90
8.1.1	Electroplating of Copper from Triflate-based Electrolytes . . . . .	92
8.1.2	Electrodeposition from a bis(trifluoromethylsulfonyl)imide-based electrolyte . . . . .	99
8.2	Electrodeposition of Dysprosium . . . . .	102
8.2.1	Electrodeposition from Solutions Based on Dysprosium-(III)-Halides	102
8.2.2	Electrodeposition from Solutions Based on Dysprosium-(III)-trifluoromethanesulfonate . . . . .	105
8.2.3	Electrodeposition from Solutions Based on Dysprosium-(III) Bis(trifluoromethylsulfonyl)imides . . . . .	109
8.3	Electrodeposition of Terbium . . . . .	119
8.3.1	Electrodeposition from Solutions Containing Terbium-(III)-Trifluoromethanesulfonate . . . . .	119
8.3.2	Electrodeposition from Solutions Containing Terbium-(III) Bis(trifluoromethylsulfonyl)imides . . . . .	121

8.4	Electrodeposition of Neodymium . . . . .	127
8.4.1	Electrochemical Deposition from $\text{Nd}[\text{NTf}_2]_3$ in 1-Butyl-1-methylpyrrolidinium Bis(trifluoromethylsulfonyl)imide . . . . .	127
8.5	Electrodeposition of Transition-Metals and Rare-Earth-Transition-Metal Alloys	130
8.6	Electrodeposition of Cobalt-Dysprosium Alloys . . . . .	131
8.7	Electrodeposition of Iron-Dysprosium Alloys . . . . .	138
<b>9</b>	<b>Summary and Conclusions</b>	<b>144</b>
9.1	Aim and Results of this Thesis . . . . .	144
9.2	Innovations presented in this Work . . . . .	148
9.3	Scientific Contributions . . . . .	150
9.3.1	Poster Presentations . . . . .	150
9.3.2	Oral Contributions . . . . .	150
9.3.3	Publications . . . . .	150
9.3.4	Patents . . . . .	151
<b>Appendix</b>		<b>xxii</b>



# 1 Introduction

The quick rise of environmentally friendly technologies based on fairly large motors and generators used in HEVs, EVs as well as wind power generation has raised the demand of permanent magnet materials. Due to the highest energy product of any known magnet, Nd–Fe–B magnets are widely used in high-performance electric machines where high efficiency, weight reduction, safe operation and comfort improvements are desired.

For instance, permanent magnet excited synchronous motors have a high efficiency as there is no need for electrical excitation, which eliminates electrical losses in the rotor and achieves motor efficiencies of up to 97 %<sup>[1,2]</sup>. In addition, a more compact design leading to higher power densities (power to space ratio) is possible and makes this type specially interesting for electrical drive applications.

Furthermore, permanent magnet excited generators can be produced in both, a slip-ring and a transmission free (direct drive) design, hence the number of wear susceptible and maintenance-intensive components in wind turbines can be considerably reduced and service intervals can be extended<sup>[1,3]</sup> which makes them predestinated for off-shore applications where long service intervals are pursued.

As a consequence, rare earth elements have increasingly been used for the production of permanent magnet materials for the last decade and this trend is expected to continue (Figure 1.1).

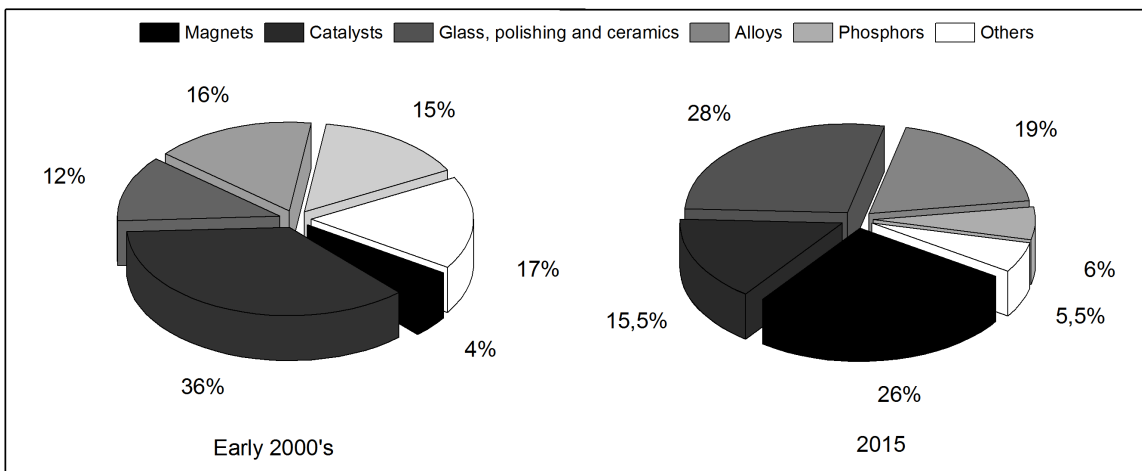


Figure 1.1: Projected development of REEs from the early 2000's to 2015. Data adopted from [ 4] and [ 5].

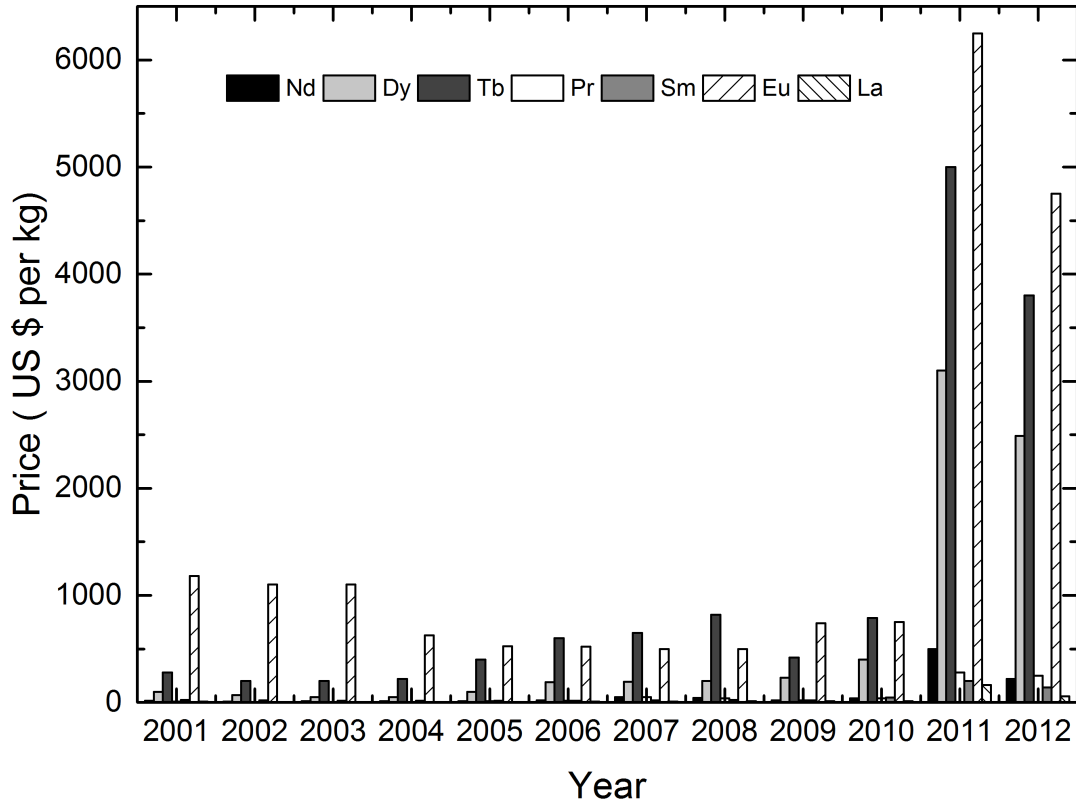


Figure 1.2: Price trends for selected rare earths<sup>[6]</sup>.

The steadily escalating demand has consequently risen concern about the availability and sustainability of supply of rare earth elements (REEs). A valid point for this is the limited geographical concentration abundance of adequate mining sites. While natural reserves of rare earth metals can be found in Russia, USA, Democratic Republic of Congo, Greenland and Brazil, China produces 97 % of the world's rare earth supply which was reflected in the price increase of rare earth oxides and metals in 2010 and 2011 due to a restriction on Chinese exports, as shown in Figure 1.2. After export quotas increase by the end of 2011, oxide and metal prices decreased as a result. However there is still concern that due to the above described applications and due to the increasing demand of emerging economies the demand will increase beyond supply in the near future<sup>[4]</sup>.

In the light of these facts, a special focus has been placed on the efficient use of REE's for permanent magnet applications. In this context, it is not necessarily the light rare earths such as praseodymium or neodymium but the heavy rare earths such as dysprosium and terbium which are the main concern since they are currently almost exclusively mined in Chinese deposits.



The reliability of permanent magnet excited electrical machines presupposes that the integrated permanent magnet cannot be demagnetized, thus the coercivity has to be high enough during regular and especially even during faulty operation (e.g. a short circuit in the stator). Electricity-driven/assisted vehicles require permanent magnets in the DC motors to operate at temperatures as high as 200 °C. Operating at high temperatures equals a substantial loss in coercive field strength  $H_{cJ}$  which in turn reduces the ability of the permanent magnet to withstand demagnetizing fields. To prevent this, a certain minimal value for  $H_{cJ}$  at room temperature is necessary.

A frequently used approach to solve this issue is the partial substitution of Nd by up to 10 wt. % heavy rare earth elements (HREEs) such as terbium or dysprosium to dramatically enhance the coercivity in Nd-Fe-B-type magnets for high temperature operations. In the first instance, this approach is disadvantageous from an economical standpoint. As previously discussed and because Tb is far more scarce and thus far more expensive for industrial application, Dy is used for substitution although it is inferior in regard of improvement to the initial material<sup>[9,11]</sup>.

A further drawback that has to be pointed out is the anti-parallel coupling of the magnetic moment of Dy with that of Fe in the  $RE_2Fe_{14}B$ -lattice caused by the partial substitution of Nd which leads to much lower levels of magnetization, which will be discussed in detail in chapter 2. Lower magnetization, in turn leads to a lower energy product  $(BH)_{max}$ . The loss in  $(BH)_{max}$ , an index for the maximal magnetic energy stored per unit volume, can be compensated by the use of more magnetic material which results in an increase of material costs as well as a significant weight increase, thus limiting the application of high performance Nd-Fe-B magnets.

This has called for increasing research in the development of HREE sparring or even HREE-free Nd-Fe-B-type magnetic materials.

It has been shown that the substitution of LREEs by HREEs by application of HREE-metal coatings on Nd-Fe-B-sintered magnets with subsequent annealing and low-temperature aging results in the allocation of the HREE along the grain boundaries and then into the outer shell of the grains resulting in an increased coercivity  $H_{cJ}$  with only negligible reduction in remanence  $B_r$ <sup>[12]</sup>, called “Grain Boundary Diffusion Process” (GBDP).

However, high-purity metallic coatings of rare earth elements have to be produced by PVD-techniques, which are not only very costly due to the required high vacuum conditions but also have relatively low deposition rates making it cost ineffective as a large-scale industrial process.

The overall aim of this study is to develop an alternate electrochemical process for the coating of permanent magnets with metallic heavy rare-earth elements as a source for the grain bound-

## *1 Introduction*

ary diffusion process, which combines up-scalability, low cost, versatility and fast deposition rates without corrosion promotion as well as being able to overcome geometric restrictions. This work was based on our previous experience with electrodeposition of dysprosium from solutions with organic solvents<sup>[13,14]</sup>. Due to a number of promising features of ionic liquids (ILs) replacement of organic solvents by ILs was tested as well.

## 2 Theoretical Background

### 2.1 Electrochemical Fundamentals

#### 2.1.1 Electrochemical Deposition Kinetics and Mechanism

##### Essentials of Electrode Reactions

For every electrochemical reaction one can state the corresponding equation:



where  $\text{Ox}$  represents the oxidized form of a species and  $\text{Red}$  its reduced form. In the case of equilibrium, the electrode potential  $E$  is linked to the bulk concentrations  $c_{\text{Ox}}$  and  $c_{\text{Red}}$  of the participants by the Nernst equation<sup>[29]</sup>:

$$E = E^0 + \frac{RT}{zF} \ln \frac{c_{\text{Ox}}}{c_{\text{Red}}} \quad (2.1)$$

here,  $E^0$  represents the so called formal potential. In contrast to standard electrode potential it is affected by omitting activity coefficients in Eq. (2.1).

For the case that mass transport is not a limiting factor, the current is often related exponentially to the overpotential  $\eta$ . A linear form has been given by Tafel in 1905<sup>[29]</sup>:

$$\eta = a + b \log(i) \quad (2.2)$$

A valid model of electrode kinetics must satisfy Eq. (2.1) and Eq. (2.2). Eq (2.2) is known as the Tafel equation.

Considering the reactions in equation [1], the reaction rates  $v$  are linked to the concentrations  $c(x, t)$  of the species by rate constants  $k$  for the reduction and oxidation, respectively:

$$v_{\text{Red}} = k_{\text{Red}} c_{\text{Ox}}(0, t) = \frac{i_{\text{Red}}}{zFA} \quad (2.3)$$

for the reduction reaction and

## 2 Theoretical Background

$$v_{Ox} = k_{Ox}c_{Red}(0,t) = \frac{i_{Ox}}{zFA} \quad (2.4)$$

for the oxidation reaction.  $R$  describes the gas constant,  $F$  is the Faraday constant,  $A$  is the area and  $z$  the number of transferred electrons. The net reaction rate is given by:

$$v_{net} = v_{Red} - v_{Ox} = k_{Red}c_{Ox}(0,t) - k_{Ox}c_{Red}(0,t) = \frac{i}{zFA} \quad (2.5)$$

and by resolving Eq. (2.5) into  $i$ , the current  $i$  in terms of the electrochemical rate is given by:

$$i = i_{Red} - i_{Ox} = zFA [k_{Red}c_{Ox}(0,t) - k_{Ox}c_{Red}(0,t)] \quad (2.6)$$

The rate constant in the general chemical reaction [1] can be written as:

$$k_{Red} = B_{Red} \exp \left[ -\frac{\Delta G_{Red}^{\#}}{RT} \right] \text{ and } k_{Ox} = B_{Ox} \exp \left[ -\frac{\Delta G_{Ox}^{\#}}{RT} \right] \quad (2.7)$$

for the reduction and oxidation reaction.  $R$  is the gas constant,  $T$  the absolute temperature and  $\Delta G^{\#}$  the activation energy for reduction or oxidation.

The rate constant  $k$  and the reaction rate  $v$  depend on the electrode potential in an electrochemical reaction, so one can state:

$$\Delta G^{\#} = f(E) \quad (2.8)$$

When the electrode potential is shifted by  $\Delta E$ , the free energy  $\Delta G^{\#}$  also changes by  $-zF\Delta E = -zF(E - E^0)$ . This is illustrated in Fig 2.1.

For  $\Delta E > 0$  the energy barrier for the oxidation reaction,  $\Delta G_{Ox}^{\#}$ , is reduced by  $(1 - \alpha)zF(E - E^0)$  while the reduction barrier  $\Delta G_{Red}^{\#}$  increases by  $\alpha zF(E - E^0)$ :

$$\Delta G_{Ox}^{\#} = \Delta G_{Ox}^{\#0} - (1 - \alpha)zF(E - E^0) \quad (2.9)$$

and

$$\Delta G_{Red}^{\#} = \Delta G_{Red}^{\#0} + \alpha zF(E - E^0) \quad (2.10)$$

where  $\alpha$  represents the transfer coefficient in the range of 0 to 1 and is often assumed to be 0.5 corresponding to a symmetric energy barrier.

After combination of Eq. (2.7) with Eq. (2.9) and Eq (2.10), one can see the dependence of the rate constant on the electrode potential:

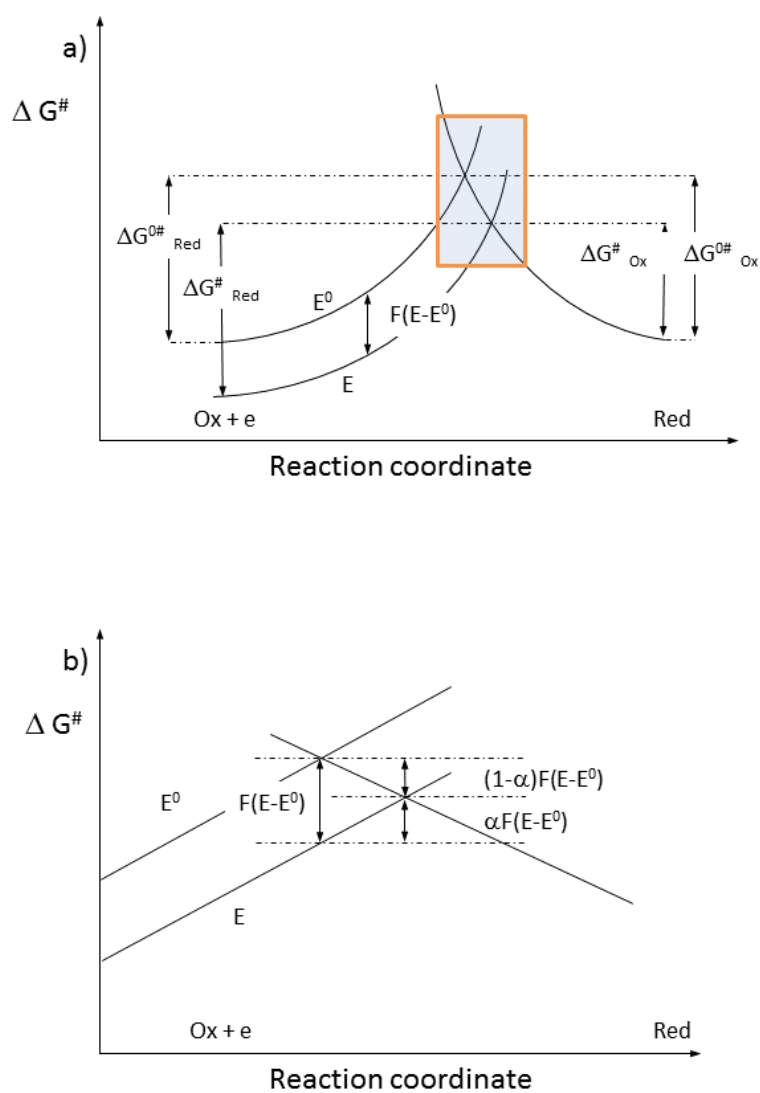


Figure 2.1: a) Dependence of the free energy  $\Delta G^\ddagger$  from the potential shift  $\Delta E$  b) Magnification of the highlighted area in a). Figures redrawn according to Ref. [29].

## 2 Theoretical Background

$$k_{Ox} = B_{Ox} \exp \left[ -\frac{\Delta G^0 \#_{Ox}}{RT} \right] \exp \left[ \frac{(1-\alpha)zF\Delta E}{RT} \right] \quad (2.11)$$

for the oxidation process and

$$k_{Red} = B_{Red} \exp \left[ -\frac{\Delta G^0 \#_{Red}}{RT} \right] \exp \left[ -\frac{\alpha zF\Delta E}{RT} \right] \quad (2.12)$$

for the reduction process. The first two factors in 2.11 and 2.12 are independent of potential and represent the rate constant at equilibrium ( $E = E_0$ ).

Finally, the combination of the current with  $k$  yields the current-potential relationship for partial reactions:

$$i_{Red} = zF A c_{Ox} B_{Red} \exp \left[ -\frac{\Delta G_{in} \#_{Red}}{RT} \right] \exp \left[ -\frac{\alpha zF\Delta E}{RT} \right] \quad (2.13)$$

for the cathodic partial current  $i_{Red}$  and

$$i_{Ox} = zF A c_{Red} B_{Ox} \exp \left[ -\frac{-\Delta G_{in} \#_{Ox}}{RT} \right] \exp \left[ \frac{(1-\alpha)zF\Delta E}{RT} \right] \quad (2.14)$$

for the anodic partial current.

In the case of equilibrium of an electrode immersed in an electrolyte (at equilibrium potential  $E = E_0$  and  $\Delta E = 0$ ), the partial current densities for reduction and oxidation,  $j_{Red}$  and  $j_{Ox}$  are equal:

$$\begin{aligned} j_{Red} &= zF c_{Ox} B_{Red} \exp \left[ -\frac{\Delta G_{in} \#_{Red}}{RT} \right] \exp \left[ -\frac{\alpha zF\Delta E}{RT} \right] = \\ j_{Ox} &= zF c_{Red} B_{Ox} \exp \left[ -\frac{-\Delta G_{in} \#_{Ox}}{RT} \right] \exp \left[ \frac{(1-\alpha)zF\Delta E}{RT} \right] = \\ &= i_0 \end{aligned} \quad (2.15)$$

thus, the net current density  $i(E_0)$  is zero and becomes the exchange current density  $j_0$ :

$$j_{ox} - j_{red} = 0 \quad (2.16)$$

For the general case where the applied potential departs from equilibrium by an amount, also known as the overpotential  $\eta$ , the applied potential  $E$  can be described as:

$$E = E_0 + \eta \quad (2.17)$$

therefore Eq. (2.13) and Eq. (2.14) can be expanded to:

$$j_{red} = zF c_{ox} B_{red} \exp \left[ -\frac{\Delta G_{in}^{\#_{Red}}}{RT} \right] \exp \left[ -\frac{\alpha z F E_0}{RT} \right] \exp \left[ -\frac{\alpha z F \eta}{RT} \right] \quad (2.18)$$

and

$$j_{ox} = zF c_{red} B_{ox} \exp \left[ -\frac{\Delta G_{in}^{\#_{Ox}}}{RT} \right] \exp \left[ \frac{(1-\alpha) z F E_0}{RT} \right] \exp \left[ \frac{(1-\alpha) z F \eta}{RT} \right] \quad (2.19)$$

Further combination of Eq. (2.15) with Eq. (2.18) and Eq. (2.19) ultimately delivers a relationship between the overpotential  $\eta$  and the net current density  $j$ , known as the Butler-Volmer Equation<sup>[29]</sup>:

$$j = j_0 \left\{ \exp \left[ \frac{(1-\alpha) z F \eta}{RT} \right] - \exp \left[ -\frac{\alpha z F \eta}{RT} \right] \right\} \quad (2.20)$$

In the case of small overpotentials, equation (2.20) can be approximated to<sup>1</sup>:

$$j = j_0 \frac{zF}{RT} \eta \quad (2.21)$$

which shows that within a small range near the equilibrium potential, the current is linearly related to  $\eta$ . The charge-transfer resistance  $R_{ct}$ , an index of kinetic facility, is given by the ratio  $\eta/J$ :

$$R_{ct} = \frac{RT}{j_0 z F} \quad (2.22)$$

For large values of  $|\eta|$ , either the cathodic or the anodic partial current can be neglected and equation (2.20) becomes<sup>[30]</sup>:

$$j = j_0 \exp \left[ \frac{(1-\alpha) z F}{RT} \eta_{an} \right] \quad (2.23)$$

$$j = j_0 \exp \left[ \frac{-\alpha z F}{RT} \eta_{cat} \right] \quad (2.24)$$

or in terms of  $\eta$ :

$$\eta_{an} = \frac{2.3RT}{(1-\alpha)zF} \log(j_0) + \frac{2.3RT}{(1-\alpha)zF} \log(j) \quad (2.25)$$

and

---

<sup>1</sup>For small values of x, the exponential  $e^x$  can be approximated as  $1+x$ .

## 2 Theoretical Background

$$\eta_{cat} = \frac{2.3RT}{\alpha_z F} \log(j_0) - \frac{2.3RT}{\alpha_z F} \log(j) \quad (2.26)$$

which describe the Tafel lines for high anodic and cathodic overpotentials, respectively. The plot of  $\log(i)$  vs  $\eta$ , known as Tafel plot, is shown in Figure 2.2.

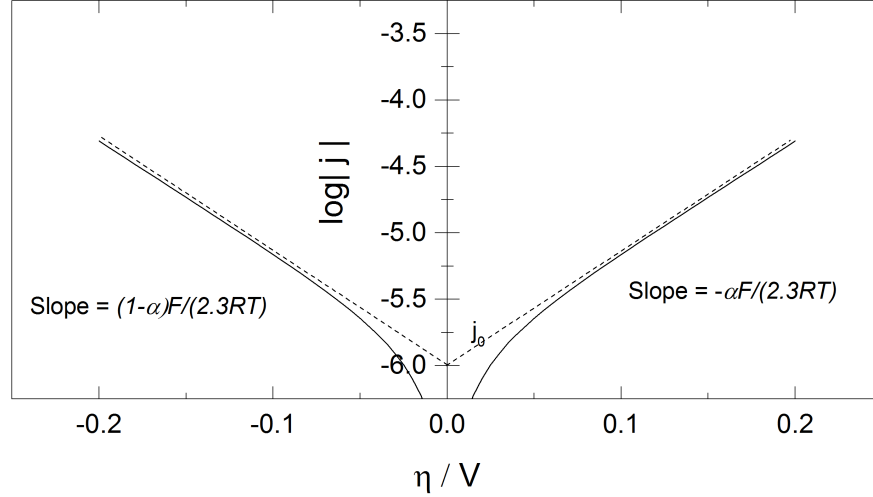


Figure 2.2: Simulated Tafel-plots for anodic and cathodic branches of the current-overpotential curve.  $\alpha = 0.5$ ,  $T = 298$  K, and  $j_0 = 10 \times 10^{-6} \text{ A cm}^{-2}$ . Redrawn according to Ref. [29]

### 2.1.2 The Electrochemical Double Layer

#### Metal - Solution Interphase

As an electrode of the metal  $M$  comes in contact with a solution containing the corresponding metal ions  $M^{z+}$ , metal ions are exchanged at the metal - electrolyte interphase. In this process, metal ions are released from the bulk electrode and in turn, ions from the solution are incorporated into the electrode<sup>[31]</sup>:



Depending on the equilibrium condition, one side of the equation is preferred causing an excess of positive or negative charge near the electrode. As a response to the excess charge at this interface, charges in the solution will be rearranged. The charge of the electrode will attract opposingly and repel samely charged ions, respectively. Several models have been postulated to describe how excess charges are distributed on each side of the interphase. The most significant will be shortly discussed in the rest of this section.



### Compact Double-Layer Model by Helmholtz

The model to describe the electrochemical double-layer by Helmholtz is the simplest. Here the double-layer is considered a rigid array, consisting of solvated ions at a given distance from the electrode (Figure 2.3). As there is no charge between electrode surface and the rigid layer, the electrical potential has to change in a linear fashion. The change of the electrical potential with the distance is given by the Poisson-equation<sup>[30,31]</sup>:

$$\frac{d^2\phi_x}{dx^2} = -\frac{\rho}{\epsilon_r\epsilon_0} = 0 \quad (2.28)$$

where  $\phi_x$  is the electric potential and  $\rho$  is the charge density at the rigid Helmholtz plane. With a distance  $a$  between the electrode and the ions at the interphase, which equals to the radius of the solvated ion species, the dependence of  $\phi$  from  $a$  can be described as:

$$\phi(x) = \phi_{el} - \frac{\phi_{el} - \zeta}{a}x \quad (2.29)$$

where  $\zeta$  represents the Zeta-potential, the potential at the rigid difference between the potential of the outer Helmholtz-layer and the bulk solution. This model represents a simple plate-type capacitor, which does not take statistically distributed ions into consideration. Experimental evidence also shows the dependence of the capacitance from the applied electrode potential, which is not accounted for in equation (2.29)<sup>[29]</sup>.

## 2 Theoretical Background

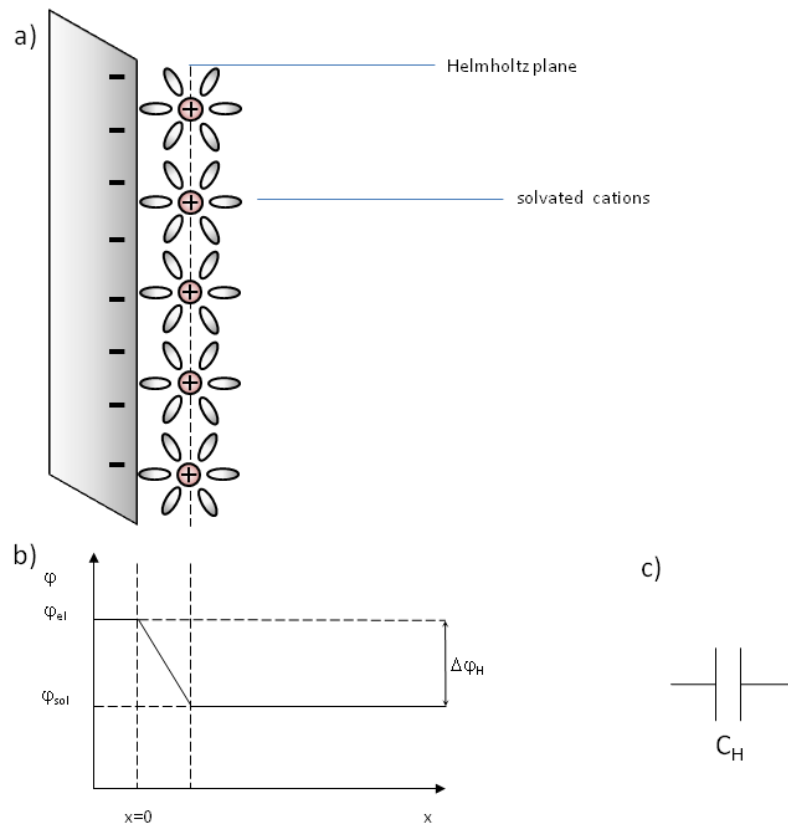


Figure 2.3: Electrochemical double-layer model by Helmholtz.

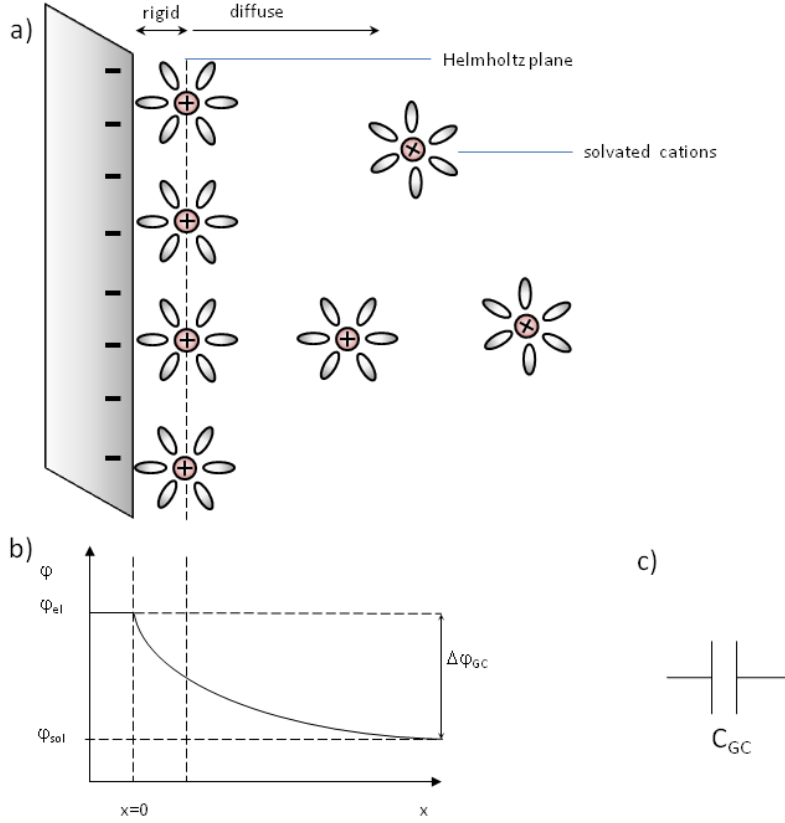


Figure 2.4: Electrochemical double-layer model by Gouy and Chapman.

### Double-Layer model by Gouy and Chapman

In contrast to the Helmholtz-model of the double-layer, Gouy and Chapman developed a model, in which ions are statistically distributed depending on the electrode potential (Figure 2.4)<sup>[30,31]</sup>. This distribution is a consequence of the superposition of electrostatic interaction and thermally induced motion, which in turn results in the formation of a rigid and a diffuse portion of the double layer. Within the rigid part, the electrode potential changes linearly and within the diffuse portion of the double-layer the potential changes exponentially with increasing distance to the electrode.

The diffuse portion (space charge) of the double-layer can be described in analogy to the ionic cloud theory by Debye and Hückel<sup>[30]</sup>:

$$\frac{d^2\phi(x)}{dx^2} = \frac{1}{\kappa} \rho(x) \quad (2.30)$$

with  $\kappa$  as the Debye-length  $\frac{1}{\kappa} = \sqrt{\frac{N_A e^2 \sum_i z_i^2 c_i}{\epsilon_r \epsilon_0 k T}}$  which represents the thickness of the diffuse

double-layer.

### Double-Layer model by Stern and Graham

The works of Stern and Graham led to a model, which unites and modifies both previous models and represents reality more quantitatively<sup>[30,31]</sup>.

In this model, the total capacitance  $C$  of the interface is given by the Helmholtz capacitance  $C_H$  and the Gouy-Chapman capacitance  $C_{GC}$  connected in series:

$$\frac{1}{C} = \frac{1}{C_H} + \frac{1}{C_{GC}} \quad (2.31)$$

The electrode surface is primarily covered by solvent molecules. Anions can also be only partly solvated and interact stronger with the electrode, while the primary solvent sheath of cations is stronger, thus preventing a closer approach. While specifically adsorbed anions are attracted by Van-der-Waals forces, solvated cations are attracted to the electrode by Coulombic interaction. As a consequence, two parts of the double-layer can be defined:

A rigid portion which consists of oriented solvent molecules and partially solvated, adsorbed anions, covering the electrode surface, building the inner and outer Helmholtz-layer, respectively. Next to this layer continues the diffuse layer, in which the spacing of metal ions to one another is governed by the ion concentration. The concepts and potential-distance profile embodied in the Stern-Graham model are illustrated in Figure 2.5.

### 2.1.3 Nucleation and Growth Models

The first theoretical model for electrochemical crystal growth in terms of atomistic models as described by Erdey-Gruz and Volmer in the 1930's considered the substrate as a perfect crystal surface<sup>[32,33]</sup>. As perfect surfaces do not have sites to promote growth, nucleation must be the first step in the process of electrodeposition. Subsequently, the imperfection of the substrate surface (Frank<sup>[34]</sup> and Burton<sup>[35]</sup>), thus the existence of a variety of growth sites was taken into account as well as experimental applications of in situ surface analytical methods, resulting in a variety of new models.

#### Formation and Growth of Adion Clusters

There are two fundamentally important processes in the formation and growth of adion clusters<sup>[30]</sup>:

1. The arrival and adsorption of atoms or ions at the surface

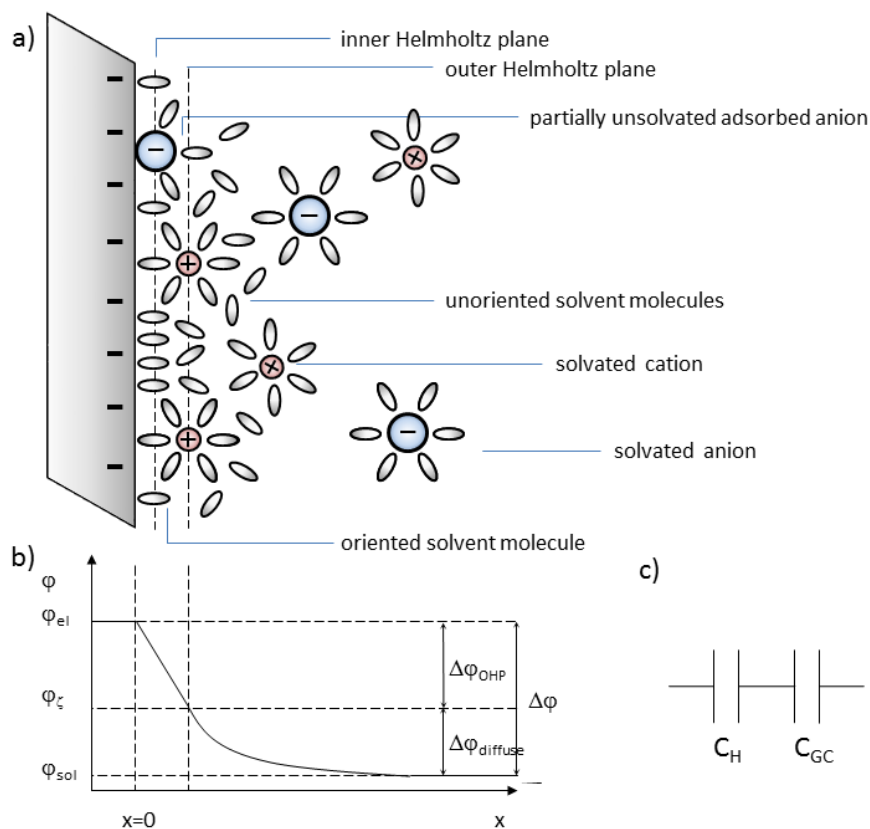


Figure 2.5: a) Stern-Graham model of the electrochemical double-layer. b) Potential-distance profile. c) Equivalent capacitor.

## 2 Theoretical Background

### 2. The motion of those adsorbed adatoms or adions on the surface

Each one of these processes can be further broken down. Preceding the adsorption of ions to the electrode, they must diffuse from the bulk electrolyte to the double layer. Following the adsorption, electron and ion transfer take place, in which case the adsorbed species partially or completely lose their solvation layer or ligands<sup>[13]</sup>. Next, adatoms diffuse on the electrode surface to form growth nuclei by formation of clusters, because the binding energy of single adions to a perfect crystal surface is small, thus unstable. The free energy of formation  $\Delta G(N)$  for a cluster of consisting of  $N$  ions can be expressed by<sup>[30]</sup>:

$$\Delta G(N) = -Nze|\eta| + \phi(N^{2/3}) \quad (2.32)$$

where the first term expresses the transfer of  $N$  ions from solution to the surface and increases linearly with  $N$  and the overpotential  $\eta$ . The second term expresses the increase of surface energy due to increasing cluster surface as a function of  $N$ <sup>[30]</sup>. The critical nucleus size  $N_c$ , at which spontaneous growth starts is given by<sup>[30]</sup>:

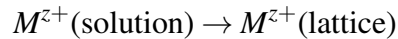
$$N_c = \frac{bs\varepsilon^2}{(ze\eta)^2} \quad (2.33)$$

where  $b^{-2}$  is a shape dependent, geometric factor,  $s$  is the area occupied by one atom on the cluster surface and  $\varepsilon$  is the surface energy.

The processes for electrocrystallization the dependence of the free energy of formation are shown in Figure 2.6.

#### 2.1.4 Atomistic Aspect of Metal Electrodeposition

In the electrodeposition of metals, a metal ion  $M^{z+}$  is transferred into the metal lattice from solution, which can be expressed as:



This reaction is followed by discharge of the ad-ion by  $z$  electrons and incorporation into a kink site (see Figure 2.7).

Surface inhomogenities cause the transition of  $M^{z+}(\text{solvated})$  to the final state  $M^{z+}(\text{kink})$  to occur via either of two possible mechanisms, namely step-edge site ion-transfer or terrace site ion-transfer mechanism.

---

<sup>2</sup> $b=P^2/4S$ , where  $P$  is the perimeter and  $S$  the surface area of the nucleus.

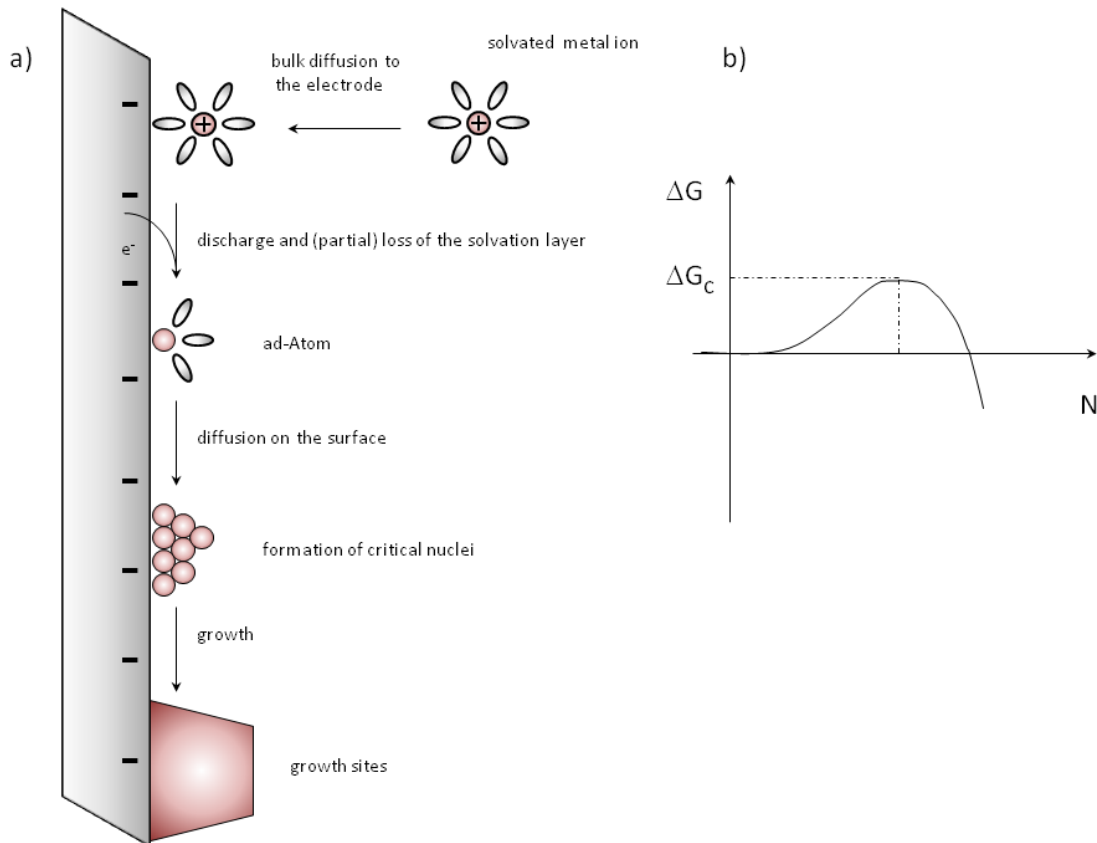


Figure 2.6: a) Electrocrystallization of solvated metal ions on the cathode. b) Free energy of formation for a 2D-cluster as a function of  $N$ <sup>[36]</sup>.

## 2 Theoretical Background

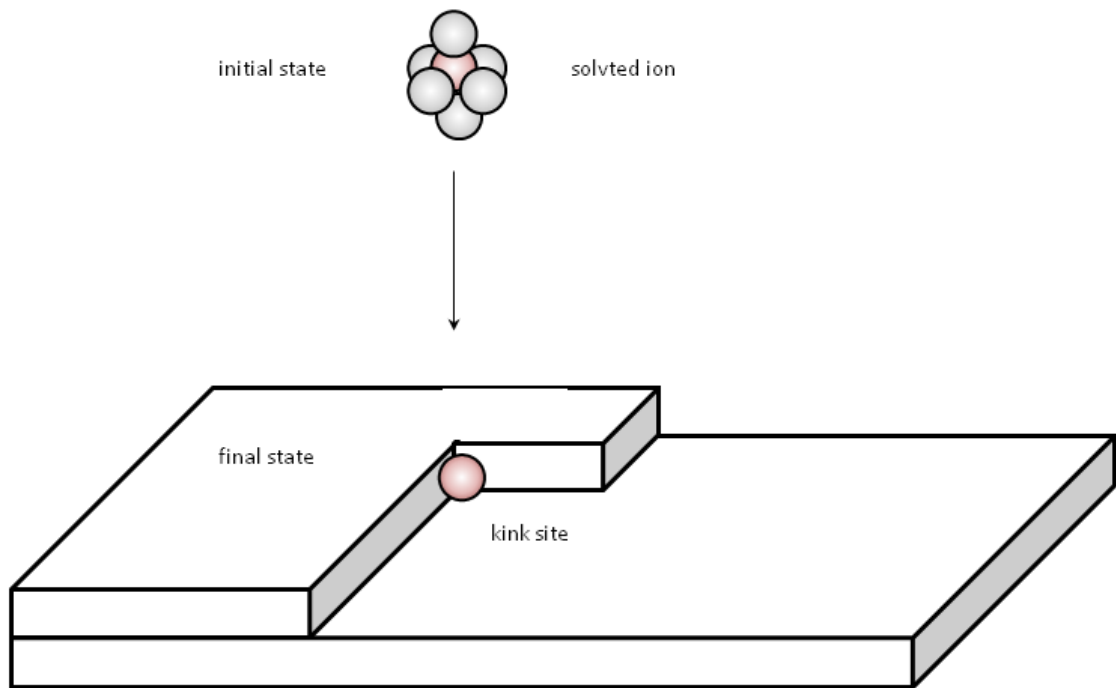


Figure 2.7: Initial and final states in metal deposition.

### Step-Edge Ion-Transfer

In this ion-transfer mechanism, an ion is transferred from solution to the kink site of a step edge (direct transfer mechanism) or to any other step edge site and subsequently diffuses to the kink site (step-edge diffusion mechanism). Both cases are illustrated in Figure 2.8. Both cases result in a partially solvated adatom in the crystal lattice of the metal.

### Terrace Ion-Transfer

A metal ion is transferred from solution to the flat face of a terrace in this mechanism. The metal ion is weakly bound to the crystal lattice, as it is in an adsorbed, adion state and has most of its solvent layer. To reach a state of lower energy, it diffuses on the surface to a kink site as the final position (Fig 2.8).

Depending on the type of nucleus, four types can be defined<sup>[13]</sup>:

**Zero-dimensional nuclei** The deposition of single ad-atoms to an active site.



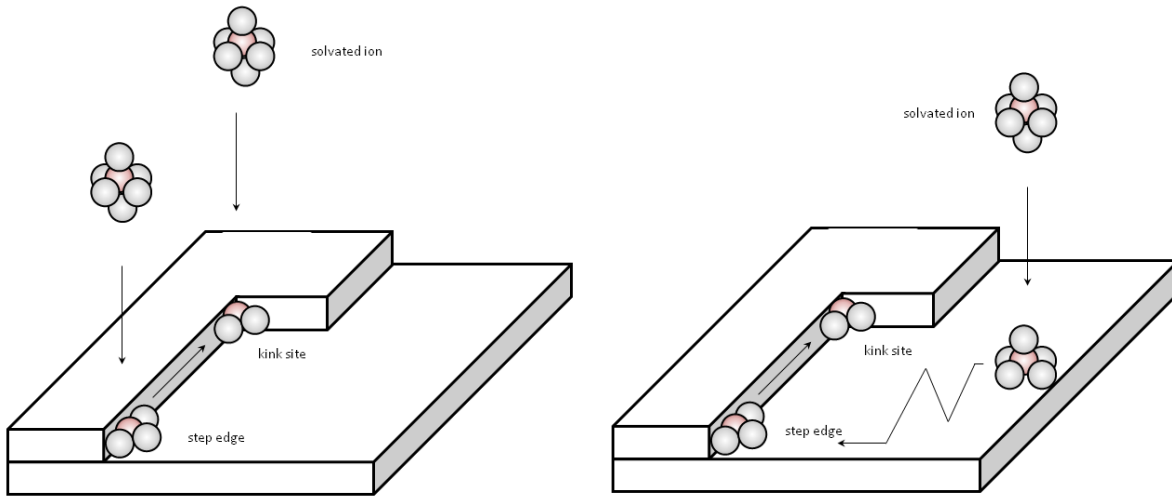


Figure 2.8: Illustration of the ion-transfer mechanisms. Left: Direct and diffusive step-edge ion-transfer mechanisms. Right: Terrace ion-transfer mechanism.

**One-dimensional nuclei** This type is described by a series of ad-atoms which congregate along the edge of a mono-atomic step.

**Two-dimensional nuclei** Planar agglomeration of ad-atoms influenced by the orientation of the underlying substrate (epitaxy).

**Three-dimensional nuclei** Spatial aggregation of ad-atoms, which is not influenced by the substrate lattice structure. In the case of similar lattice structures for metal and substrate, nucleation may exhibit epitaxial behavior. The existence of surface defects on the substrate such as edges, corners or steps can act as active centers, triggering nucleation and also being capable to influence its subsequent course.

The free energy of formation on zero-, one-, two- and three-dimensional crystal nuclei drastically increases with dimensionality.

### Growth mechanisms

Growth mechanisms are most importantly influenced by two parameters: The binding energy between deposited species (M-M), intermolecular interaction between the deposited species and the substrate (M-S) and the crystallographic misfit between M and S. These can be divided into two major categories<sup>[30]</sup>:

1. Bonding energy between deposited atoms (M-M) is higher than intermolecular forces between deposited species and substrate (M-S). This case leads to the formation of sin-

## 2 Theoretical Background

gle growth sites (crystallites) which grow in a three-dimensional motion, described by the model of Volmer and Weber (Figure 2.9 a)). In this case, the crystallographic misfit does not show any effect. The misfit  $mf$  is defined as:

$$mf = \frac{a_S - a_M}{a_M} \quad (2.34)$$

where  $a_S$  and  $a_M$  are the lattice spacings for the substrate and metal deposit, respectively.

2. If the opposite case is true and the binding forces between deposited species and substrate (M-S) are stronger than those among the species forming the layer (M-M), two subcases can be distinguished:
  - 2.1. If  $a_S \approx a_M$ , the misfit is close to zero and the mechanism of deposition will be layer by layer, also known as Frank-Van der Merve growth mechanism (Figure 2.9 b)).
  - 2.2. If  $a_S \neq a_M$ , a positive or negative misfit is present and growth proceeds in a Stranski-Krastanov mechanism, which includes two steps. First, a 2D overlayer on the substrate is formed and subsequently 3D crystallites grow on top of the predeposited overlayer, as shown in (Figure 2.9 c)).

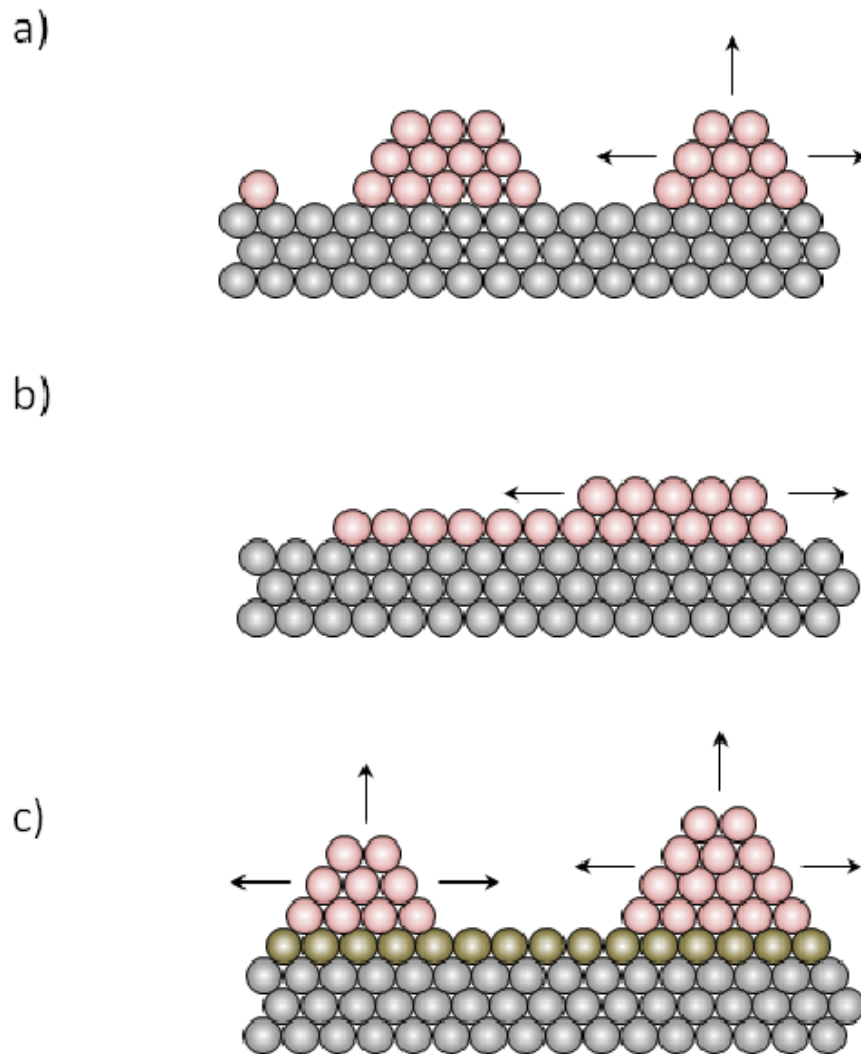


Figure 2.9: Illustration of different growth mechanisms: a) Volmer-Weber model. b) Frank-Van der Merve model. c) Stranski-Krastanov model. Red: deposit, grey: substrate, green: overlayer<sup>[30,31]</sup>.

### 2.1.5 Nucleation of Surface Nuclei

The uniform probability with time of conversion  $t$  of a site on the electrode into nuclei is given by the nucleation law, which represents a first-order kinetic model:

$$N = N_0(1 - e^{-At}) \quad (2.35)$$

where  $N_0$  is the maximum possible number of nuclei on the unit surface (total number of sites) and  $A$  is a nucleation rate constant. For the initial stages of nucleation (small  $t$ ), there are two limiting cases for equation 2.35:

- The nucleation rate constant is large. In this case the exponential term can be approximated to zero, which results in  $N \approx N_0$ , indicating that all electrode sites are converted to nuclei instantaneously (*instantaneous* nucleation).
- The nucleation rate constant is small. Here, equation (2.35) can be approximated to  $N \approx N_0At$  indicating the time dependence of the nucleation rate (*progressive* nucleation)<sup>3</sup>.

The diagnostic relationship and the possibility to experimentally distinguish these two limiting cases by use of potentiostatic current-time transients will be discussed in 2.1.5.

The rate of 2-dimensional nucleation  $J$  is given by<sup>[30]</sup>

$$J = k_1 \exp \left[ -\frac{bs\epsilon^2}{zekT\eta} \right] \quad (2.36)$$

where  $k_1$  is a rate constant. The other symbols have their usual meaning<sup>4</sup>.

### Layer Growth Mechanisms

#### *Diagnostic Relationships between Current and Time*

For two-dimensional nucleation, the theoretical relationships between time and current are given by the following equations:

$$\ln \frac{i}{t} = a - bt^2 \quad (2.37)$$

$$\ln \frac{i}{t^2} = c - dt^3 \quad (2.38)$$

<sup>3</sup>for a small exponent, the exponential term can be represented by linear approximation:  $-\exp^{-At} \approx -1 - At$

<sup>4</sup> $b$ ,  $s$  and  $\epsilon$  have been defined in (2.33).

for the case of instantaneous and progressive nucleation, respectively.  $a$ ,  $b$ ,  $c$  and  $d$  are constants.

#### *Diagnostic Relationships between Current, Maximum Current and Time*

A theory which deals with potentiostatic current transients for three-dimensional nucleation with diffusion-controlled growth was developed by Scharifker and Hills<sup>[37]</sup>. According to this theory, the diagnostic relationship for instantaneous and progressive nucleation is given by the following dimensionless (reduced) terms:

$$\left(\frac{j}{j_m}\right)^2 = \frac{1.9542}{t/t_m} \left\{ 1 - \exp \left[ -1.2564 \left( \frac{t}{t_m} \right) \right] \right\}^2 \quad (2.39)$$

for the case of instantaneous nucleation and

$$\left(\frac{j}{j_m}\right)^2 = \frac{1.2254}{t/t_m} \left\{ 1 - \exp \left[ -2.3367 \left( \frac{t}{t_m} \right)^2 \right] \right\}^2 \quad (2.40)$$

for the case of progressive nucleation. Figure 2.10 shows the theoretical current transients  $(i/i_m)^2$  vs  $(t/t_m)$  simulated for  $t/t_m = 0$  to 10 for instantaneous and progressive nucleation, respectively.

These non-dimensional relationships will be used in chapter 8 for analysis of experimental data.

## 2 Theoretical Background

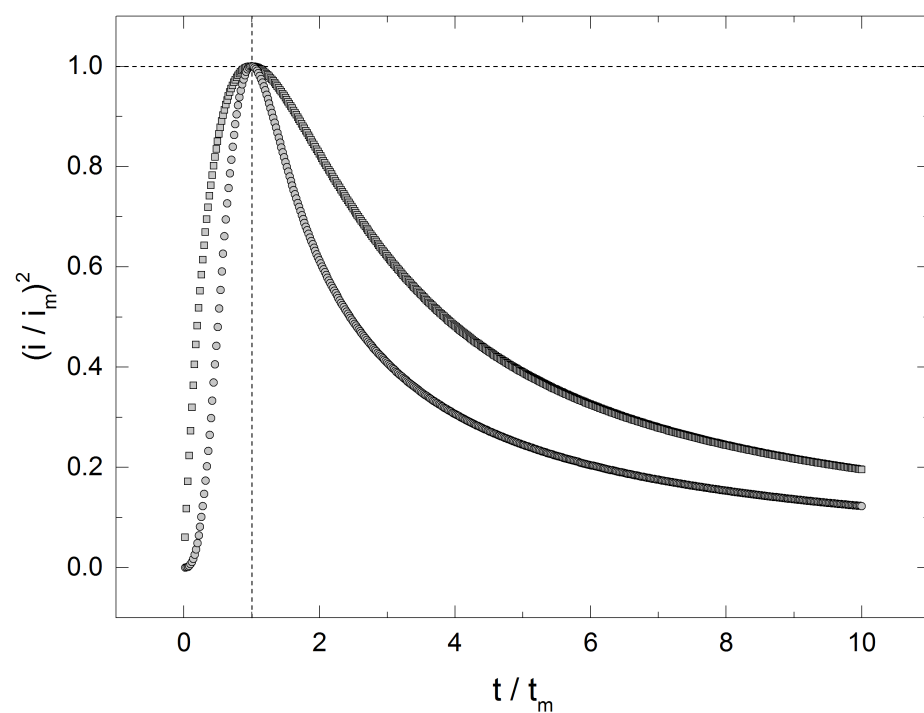


Figure 2.10: Theoretical, dimensionless current-time transients for instantaneous (squares) and progressive (circles) nucleation.

### 2.1.6 Electrolytes for Electrodeposition

#### Aqueous Solutions

The most important metals, which are electrodeposited commercially are Cu, Cr, Ni, Ag, Au, Zn, Cd and some Zn- and Cu-based alloys<sup>[38]</sup>. Because of the feasible deposition of these elements from aqueous solutions, the plating market is based on aqueous electrolytes. One exception is aluminum, which is deposited from non-aqueous organic solutions. For the deposition of more electronegative metals, other methods such as chemical vapor deposition or plasma deposition techniques are usually applied. The versatility of possible substrates as well as the fact that deposition is not restricted to pure metals, but also alloys or compounds (nitrides, oxides, carbides, silicides, etc.) can be deposited, makes these techniques very interesting. Major drawbacks involve high capital investment and relatively slow deposition rates which make it difficult to obtain thick coatings, thus making them commercially profitable only for high value niche markets<sup>[39]</sup>.

Aqueous solutions have numerous advantages, which have led them to be the mainstay of metal plating<sup>[40]</sup>:

- Low cost
- Non-flammability
- Electrolytes and metal salts are highly soluble
- High conductivities, thus low Ohmic losses and high throwing power
- Low viscosity, leading to high mass transfer rates.

Aqueous baths also exhibit striking limitations, to name a few<sup>[39]</sup>:

- Low potential windows
- Concurring gas evolution which can be extremely detrimental to the substrates (H<sub>2</sub>-embrittlement)
- Passivation of the electrode material can cause problems with cathodic and anodic processes
- Environmentally dangerous bath components (e.g. cyanide complexing agents, acids,...)
- Necessity of waste water treatment before return to the water course.

## 2 Theoretical Background

All these limitations prevent the use of aqueous solutions for the electrodeposition of technically important materials. Key goals include the replacement of environmentally toxic baths, deposition of semiconductors and innovative alloys and to develop new coating methods for reactive metals. The driving force for the research in non-aqueous electrochemistry has been the desire to deposit refractory metals, the likes of Al, Ti and W, known for their excellent corrosion resistance and abundance<sup>[39]</sup>.

### Non-aqueous Solutions

The interest in non-aqueous organic solvents, especially polar aprotic solvents, started in the 1950s in various fields of pure and applied chemistry. Since then, they have greatly contributed to numerous advances in chemical sciences and technologies<sup>[41]</sup>, such as the electroplating of reactive metals, development of high-performance batteries and electrochemical double layer capacitors, electrochromic applications and photoelectrochemical cells<sup>[40,45]</sup>.

Therefore, organic solvents have to show a number of favorable properties. For example, they must be physically and chemically stable over a wide temperature range, have low vapor pressures, high solubility of salts, wide potential windows, low viscosities and low toxicities and a low price.

Unfortunately, to obtain certain properties, others must be excluded. A low vapor pressure entails high viscosities and high dielectric permittivities<sup>5</sup> frequently result in high viscosities as well. For each application, a solvent (or oftentimes a combination thereof) has to be chosen that unites the most desired properties.

The use of non-polar organic solvents (predominantly aromatic hydrocarbons) has been applied with limited success. Low polarity also results in low solubility of metal salts and also extremely low conductivities. The exception is the very conductive and so far the only industrially important deposition of aluminum. Triethylaluminum is used as aluminum source in a toluene-based bath. In spite of the high pyrophoricity of  $\text{Al}(\text{Et})_3$  and flammability of toluene, the *SIGAL* (Siemens Galvanisch Aluminium) is one of the most important and currently the only electrochemical method for the deposition of aluminum<sup>[39]</sup>.

### High-Temperature Molten Salts and Ionic Fluids

The use of ionic liquids is an alternative to molecular solvents. Due to their high lattice energies, ionic materials usually melt at high temperatures. These high-temperature melts are

---

<sup>5</sup>The solubility of a salt in a solvent is determined by its dielectric permittivity  $\epsilon$ , dipole moment  $\mu$  and donor number  $DN$ <sup>[40]</sup>. As organic solvents obtain their polarity from electronegative elements such as N and O, they are by nature also good electron pair donors.



widely used in a number of industrial applications such as electro-winning of reactive metals (e.g. Li, Ca, Ti and Al) at temperatures ranging from 150 °C to 1000 °C, metal coating, energy conversion<sup>[42,43]</sup> and treatment of by-products<sup>[44]</sup>. They unify most advantages of aqueous electrolytes (high conductivities and solubility for metal salts, nitrides, oxides and carbides<sup>[42]</sup>) and overcome most of their limitations (wide potential windows, low vapor pressure). However, their operational conditions substantially limit the range of substrates that can be used for electrodeposition<sup>[39]</sup>. Another drawback is their highly corrosive character<sup>[43]</sup>. By reduction of the lattice energy by increasing the ionic size, a significant number of lower temperature molten salts have been developed in the 20th century. With the deposition of aluminum at low temperatures as a main objective, the first widely applied ionic liquids consisted of LiCl, KCl, AlCl<sub>3</sub> eutectics with melting points near 100 °C<sup>[39]</sup>. By substitution of the small cations by larger organic ions such as pyridinium or imidazolium, the symmetry and coulombic interactions are decreased by charge distribution, as a result crystallization is disfavored (Figure 2.11)<sup>[46,47]</sup>.

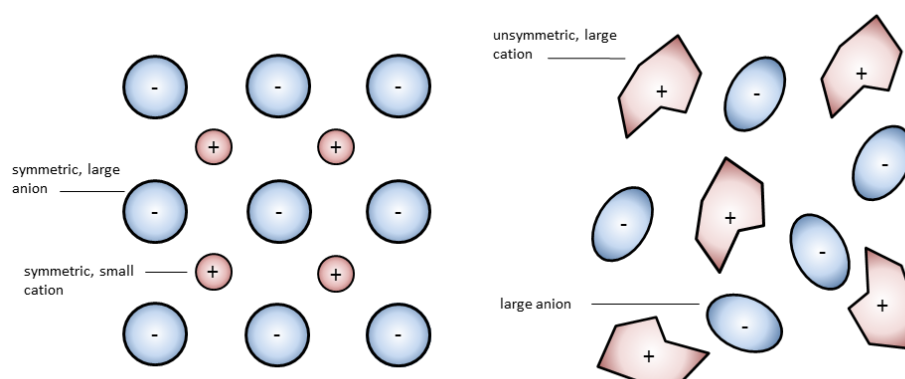


Figure 2.11: Schematic crystal lattices for conventional inorganic salts and ionic liquids.

Replacing the simple inorganic anions by larger, organic, often fluorinated anions with charge distribution over larger structures also contributes to a further reduction of the melting points to below room temperature, thus coining the term “room temperature ionic liquids”. Since the introduction of air- and water-stable anions, the interest in ionic liquids has increased dramatically.

The combination of different cations and anions leads to about  $10^{18}$  possible combinations, of which more than 1000 have been described in the literature and several hundred are commercially available<sup>[48]</sup>. A few of the chemical structures of commonly applied ionic liquids are shown in Figure 2.12.

## 2 Theoretical Background

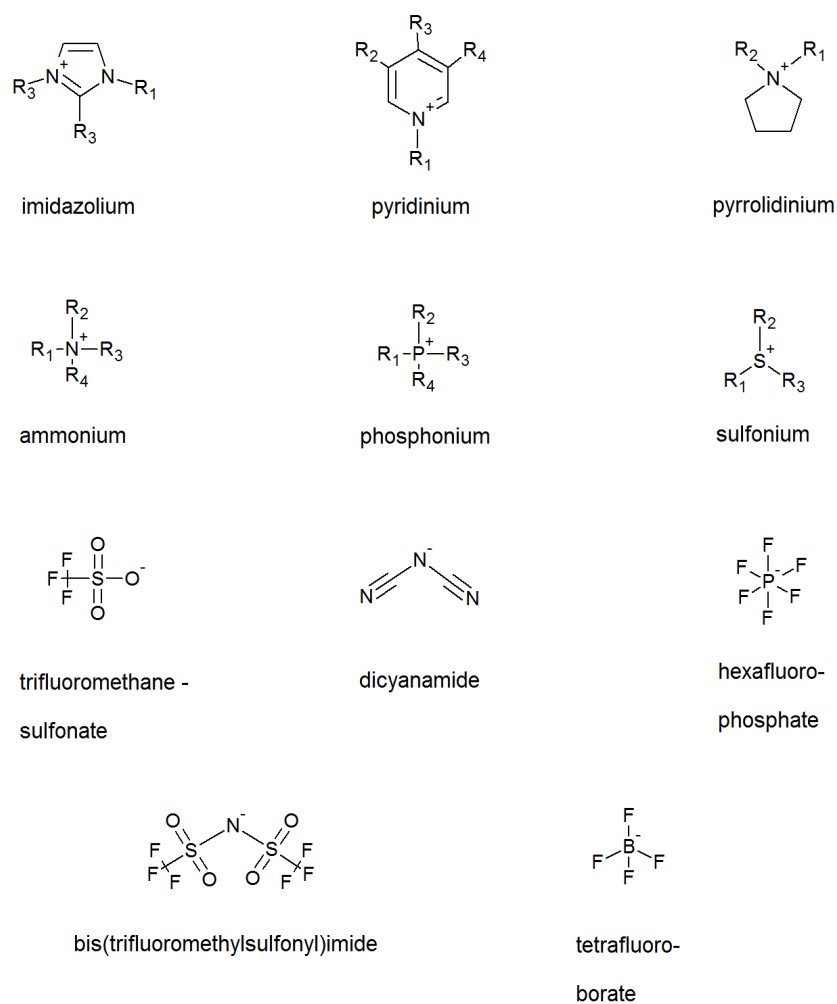


Figure 2.12: Chemical structures of commonly studied cations and anions used for ionic liquids.

Ionic liquids have found interest in a wide range of applications such as biosciences for the dissolution of cellulose, solvatization of proteins, biofuel cells and biomimetic applications<sup>[49]</sup>, electrolytes for metal and semiconductor deposition<sup>[39,50–52]</sup> deposition of nanomaterials<sup>[53]</sup>, synthesis and catalysis<sup>[54]</sup> and of course electrochemical devices such as electrochemical sensors<sup>[55]</sup>, organic ionic plastic crystals, actuators and conducting polymers<sup>[59]</sup>, photoelectrochemical solar cells<sup>[56]</sup> additives and electrolytes in lithium-ion batteries and capacitors<sup>[57,58]</sup>. For further introduction to the history and chemical as well as physical properties of ionic liquids, the reader is referred to extensive literature reviews<sup>[60–65]</sup> and books<sup>[66–68]</sup>.

## 2.2 Magnetism

### 2.2.1 Quantum Origin of Magnetism

#### Principal quantum number $n$

The principal quantum number  $n$  determines the energy of the electron level and although it does not determine the magnetic dipole moment directly, it influences the dipole moment due to the fact that it does determine which values for  $l$  and  $m_l$  are permitted<sup>[69,70]</sup>.  $n$  can obtain values of 1, 2, 3, 4,...

#### Orbital quantum number $l$

This orbital quantum number determines the magnitude of the electron's orbital angular momentum  $|L|$ .  $l$  is related to  $|L|$  of an individual electron by

$$|L| = \hbar \sqrt{l(l+1)} \quad (2.41)$$

$l = 0, 1, 2, \dots, n-1$  correspond to the labels  $s, p, d, \dots$  for the atomic orbitals.

#### Magnetic quantum number $m_l$

The magnetic quantum number  $m_l$  labels the (quantized) orientation of the orbital angular momentum with respect to a magnetic field. The values for  $m_l$  range from  $-l$  to  $+l$  in single integer steps.

#### Spin quantum number $m_s$

The spin quantum number describes the value for the electron spin which is  $1/2$ . Analogous to the magnitude of the orbital angular momentum  $|L|$ , the magnitude of the spin angular momentum of an individual electron  $|S|$  is given by

$$|S| = \hbar \sqrt{s(s+1)} = \frac{\sqrt{3}}{2} \hbar \quad (2.42)$$

#### Magnetic spin quantum number $m_s$

Just as  $m_l$ ,  $m_s$  is quantized with respect to a magnetic field.  $m_s$  can take values of  $-1/2$  and  $+1/2$ .

### 2.2.2 Many-Electron Systems

As stated above, the energy of electrons only depends on  $n$ . While this is correct for the hydrogen atom, in many-electron atoms the electrons interact with each other and the nucleus. As a result, the energy of an electron depends on  $n$  and  $l$ . Electrons with lower angular momentum are lower in energy, which leads to the known ordering of atomic orbitals 1s; 2s,2p; 3s,3p,3d; 4s,...

#### Spin-Orbit Coupling

The magnetic moment of an electron's spin interacts with the atomic magnetic moment due to the electron's orbital angular momentum (spin-orbit coupling). Its magnitude is proportional to  $Z^4$ , with  $Z$  as the atomic number. As a result, spin-orbit coupling is negligible for a hydrogen atom and becomes the more significant with increasing  $Z$ . Not only spin-orbit coupling exists but there is also spin-spin and orbit-orbit coupling (which becomes important for light atoms).

#### Pauli Principle and Hund's Rules

The Pauli principle states, that two electrons can't occupy the same set of quantum numbers. So, only two electrons can occupy an atomic orbital (which means  $n$ ,  $l$ ,  $m_l$  and  $s$  are equal) and they must have opposite spin orientations (different  $m_s$ )<sup>[69,70]</sup>.

Hund derived three rules by which the lowest energy configuration of electrons in a partially occupied shell can be identified<sup>[69,70]</sup>:

1. The electrons' total spin  $|S|$  has to be maximized. This means that each orbital will be occupied by one electron with the same spin orientation first and then will be paired with the remaining electrons of the opposite spin (Pauli's principle)
2. For a given spin arrangement the configuration with the lowest total atomic angular momentum  $L$  is the lowest in energy
3. The third rule differs between two cases:

Shell is less than half-full: The lowest total angular momentum quantum number  $J$  is the lowest in energy

Shell is more than half-full: The highest total angular momentum quantum number  $J$  is the lowest in energy.

### Total angular momentum $J$

The total angular momentum  $J$  can be calculated by combination of the total spin angular and the total orbital angular moments  $S$  and  $L$  in conjunction with Hund's third rule. This results in the following:

- Shell is less than half-full:  $J = L - S$
- Shell is more than half-full:  $J = L + S$

Due to interaction between the total orbital angular momentum and the total spin momentum, the observed effective momentum differs from the sum of  $J$  of all atoms. The effective magnetic moment can be calculated by:

$$\mu_{eff} = g_J J \mu_B \text{ with } g_J = 1 + \frac{J(J+1) + S(S+1) - L(L+1)}{2J(J+1)} \quad (2.43)$$

where  $\mu_B$  is the fundamental quantum value of the magnetic moment (the Bohr magneton) with a value of  $9.274009 \times 10^{-24} \text{ J T}^{-1}$ .  $g_J$  is the Landé g-factor.

In the solid bulk of the material there is an interaction of magnetic dipoles, the so called exchange interaction, of which characteristic and strength are given by the overlap of the electron orbits of adjacent atoms<sup>[69,70]</sup>.

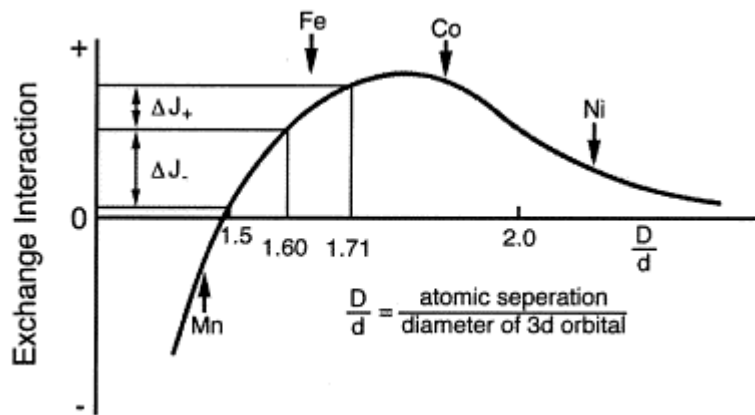


Figure 2.13: Strength of the exchange energy in as a function of the ratio of the interatomic distance  $D$  to the diameter  $d$  of the 3d shell.

The exchange interaction is a function of the relative atomic distance, the quotient of the inter-atomic distance and the diameter of the shell that contains the uncompensated electrons. It can cause an anti parallel coupling of the magnetic dipoles where they cancel each other out completely (antiferromagnetism) or partially (ferrimagnetism). The opposite case is a constructive coupling of the magnetic dipoles leading to intense, strong ferromagnetism<sup>[71]</sup>.

## 2 Theoretical Background

The so called Bethe-Slater curve (Figure 2.13) demonstrates this behaviour for some of the transition metals, namely Mn, Fe, Co and Ni. Negative interaction in Mn leads to antiferromagnetic behaviour while Fe, Co and Ni have the right ratio to exhibit parallel coupling, though it is possible to adjust the distance by alloying other metals, e.g. Al, Cu, etc.

Dipoles don't couple parallel over the whole body, they are confined in many lone domains, also known as Weiß domains separated by domain walls. The magnetization of adjacent domains are bound to certain directions in the crystal lattice (lattice anisotropy).

### 2.2.3 Magnetic Properties

#### Induction

The permeability  $\mu$  dictates how much magnetic induction  $B$  is generated in a given magnetic field strength  $H$ . The following relation applies for the vacuum field<sup>[72]</sup>:

$$B = \mu_0 H + J \quad (2.44)$$

The induction  $B_0$  is proportional to the applied magnetic field  $H$ .  $\mu_0$  is the permeability in vacuum with a value of  $4\pi \times 10^{-7} \text{ T m A}^{-1}$  and  $J$  as the magnetization. In equation 2.44  $J$  equals zero in the case of the vacuum field and  $J \neq 0$ , when a material is introduced.

Ferromagnets have high induction and because the magnetic dipoles can be aligned by an applied magnetic field, they also possess a high saturation field strength. Two kinds of materials can be distinguished. Soft magnets reach high saturation at relatively low field strength but their magnetization is easily reversible. Soft magnets have a low remanence  $B_r$  (for  $H=0$ ) as well as low coercive field strength  $H_c$ , the applied field to demagnetize the material ( $B=0$ ). Hard magnets show the opposite properties, namely high remanence and high coercive field strength.

#### Coercivity

As an intrinsic property,  $H_{cJ}$  describes the strength of the applied magnetic field needed to demagnetize the sample, in other words its resistance to demagnetization.  $H_{cJ}$  is a function of the magnetic saturation  $J_{\text{sat}}$

$$H_{cJ} = \frac{2k_1}{\mu_0 J_{\text{sat}}} \quad (2.45)$$

$k_1$  is a constant related to the preferred alignment of the magnetic dipole moments, the so called magnetocrystalline anisotropy and  $\mu_0$  is the permeability of vacuum<sup>[10]</sup>.

For differentiation between soft and hard (or permanent) magnets the coercivity is often used as a guideline by which to divide between these two types. Soft magnets have low and hard magnets have high values for  $H_{cJ}$ . Values below  $1000 \text{ Am}^{-1}$  are usually considered soft, values over  $10000 \text{ Am}^{-1}$  are considered hard<sup>[27]</sup>.

### Saturation Magnetization and Remanence

$J_{\text{sat}}$  is the extent to which the magnet can be magnetized and only depends on the magnitude of the atomic magnetic moments and the number of atoms per unit volume.

$$J_{\text{sat}} = \frac{N}{V} g_J J \mu_B \quad (2.46)$$

where  $N$  presents the number of atoms in a given volume  $V$ ,  $g_J$  the g-factor and  $J$  the total angular momentum, respectively.

The remanence  $B_r$  is the magnetic field produced by a given volume of material at zero field. After the applied magnetic field is removed from a previously magnetized (magnetic moments aligned) body, the magnet will revert to a residual magnetic state upon saturation after partial reversal of the magnetic moments into an unaligned state. This and the previously mentioned key values are shown in the hysteresis curve in Figure 2.14.

### Maximum Energy Product

The maximum energy product  $(BH)_{\text{max}}$  represents a magnet's ability to store energy or deliver work outside its volume. High  $(BH)_{\text{max}}$  values allow for low material volumes in a given application.  $(BH)_{\text{max}}$  can be depicted as the biggest rectangle fitting in a  $B(H)$  curve, as seen in Figure 2.14 The maximal energy product of an ideal magnet with the remanent polarization  $J_r$  is :

$$(BH)_{\text{max}} = \frac{1}{4\mu_0} J_r^2 \quad (2.47)$$

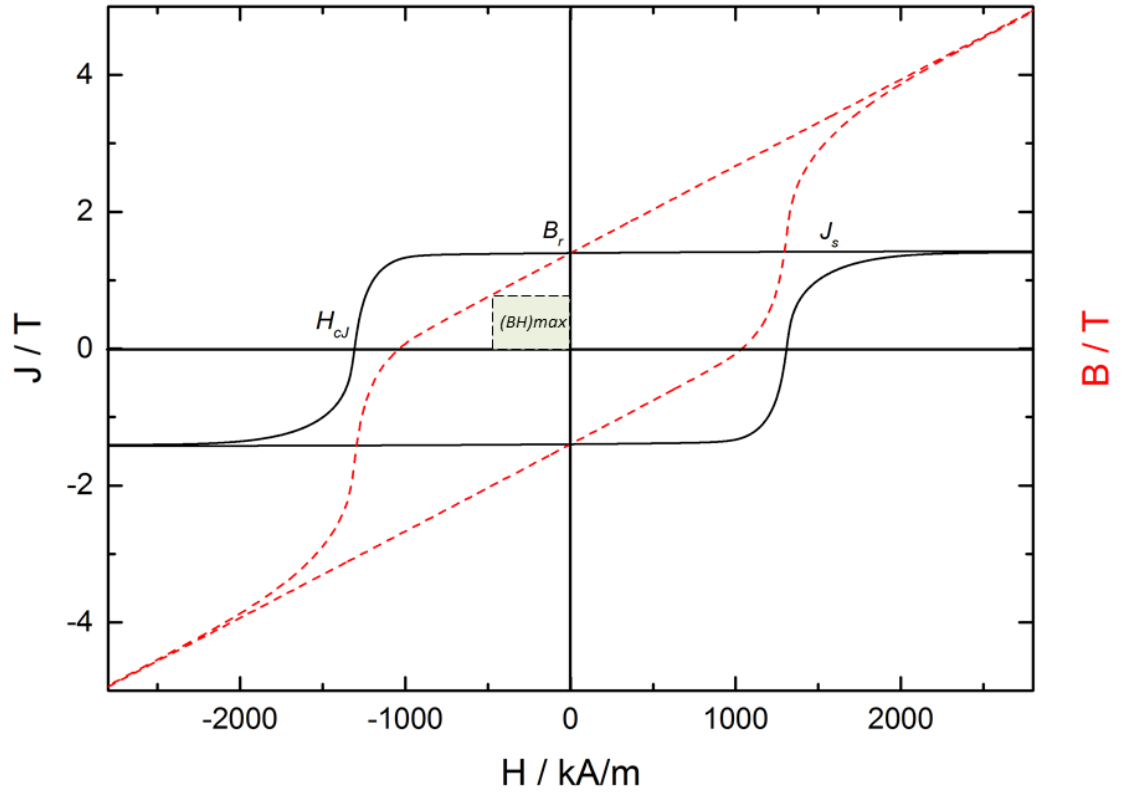


Figure 2.14: Generalized hysteresis curve. Black solid curve: magnetization  $J$ , red dashed curve: magnetic flux density  $B$  as a function of the magnetic field strength  $H$ , green:  $(BH)_{\max}$ .



### 2.2.4 Rare Earth-3d Metal Alloys

The 4f-electrons of rare earth elements are strongly shielded by the electrons of the outer shells ( $6s^2 6s^2$  and  $5d^1$ ) and can therefore maintain their magnetic moments. The magnetic moments of rare earth elements are high due to their incompletely filled 4f-shell, which can contain up to seven unpaired electrons with aligned spins. However, the temperature up to which these elements can withhold their ferromagnetic properties (so called Curie temperature) is well below room temperature<sup>[73]</sup>. Another significant advantage of rare-earth containing compounds is the high magnetic anisotropy, which means they are easy to magnetize in one particular direction at the expense of any other. By alloying rare earths with transition metals, such as the ferromagnetic Fe, Co or Ni with high ordering temperatures, the resulting Curie temperature can reach above room temperature<sup>[27]</sup>.

The combination of these unique properties (high magnetic moment and high magnetic anisotropy) result in high magnetic strength. Rare-earth-3d metal alloys combine the highly localized magnetism of the RE sublattice with the itinerant magnetism of the transition metal lattice.

A well-known example are SmCo-alloys. High performance permanent magnet materials such as  $\text{SmCo}_5$  and  $\text{Sm}_2\text{Co}_{17}$  exhibit excellent properties such as high temperature stability due to strong 3d-3d exchange interaction.

### 2.2.5 Nd-Fe-B-Type Magnetic Materials

Due to the high prices of Sm and especially Co in the 1980s and limited availability of these elements, researchers have tried to substitute Sm by more abundant rare earth elements such as Nd and Pr which also exhibit higher magnetic moments than Sm. Fe is also much more abundant compared to Co and it also possesses a 27 % larger magnetic moment. Binary RE-Fe compounds did not show satisfactory results as LREEs and Fe form few stable intermetallics with too low Curie temperature for practical application and too low uniaxial anisotropy to show sufficient coercivity<sup>[7]</sup>, but ternary compounds  $\text{RE}_2\text{Fe}_{14}\text{B}$ , especially  $\text{Nd}_2\text{Fe}_{14}\text{B}$  showed excellent properties<sup>[8]</sup>.

Magnets employed in high-performance applications are typically composed of rare-earth and transition-metal elements, each of these composing their own sublattice. While the rare-earth sublattice provides high magnetocrystalline anisotropy, high magnetostriction and high magnetic moments, the 3d sublattice causes high magnetic ordering temperature. To obtain optimal magnetic properties, the two sublattices must be strongly coupled. It is found, that light rare-earth and the 3d-spin moments couple parallel and 3d- and rare-earth-spin moments of

## 2 Theoretical Background

the heavier elements couple antiparallel<sup>[70]</sup>. Antiparallel coupling of the rare earths is caused by interaction of the 5d-rare-earth electrons and the 3d-transition metal electrons.

While all lanthanoids except of La form a stable tetragonal  $\text{RE}_2\text{Fe}_{14}\text{B}$ -phase, there are some major differences with regard to RE.

The saturation magnetization  $J_{\text{sat}}$  behaves in a similar fashion as other RE-TM compounds. Light RE-containing compounds show a higher magnetization than heavy RE-compounds. As previously described, the LRE sublattice couples ferromagnetically to the TM-sublattice resulting in a ferromagnetic material while the opposite is true for the HREs rendering these materials ferrimagnetic.

The Curie temperature  $T_c$  shows a maximum for Gd implying an enhancement of  $T_c$  with the exchange interaction between RE and Fe moments. The lower Curie temperature of REFe-binary compounds in comparison to  $\text{RE}_2\text{Fe}_{14}\text{B}$  may also result from an increase in itinerancy, changes in interatomic Fe-Fe distance or coordination number.

The magnetocrystalline anisotropy  $H_A$  is considered to arise from the single ion anisotropy. A summary of lattice parameters and magnetic properties of different  $\text{RE}_2\text{Fe}_{14}\text{B}$ -compounds is presented in Table 2.1.

Compound [K]	Lattice Parameter		$J_s$ [T]	$M$ [ $\mu_B/\text{F.U.}$ ]	$H_a$ [MA/m]	$T_c$ [°C]
	$a_0$ [nm]	$c_0$ [nm]				
$\text{Ce}_2\text{Fe}_{14}\text{B}$	0.877	1.211	1.16	22.7	3.7	424
$\text{Pr}_2\text{Fe}_{14}\text{B}$	0.882	1.225	1.43	29.3	10	564
$\text{Nd}_2\text{Fe}_{14}\text{B}$	0.882	1.224	1.57	32.1	12	585
$\text{Sm}_2\text{Fe}_{14}\text{B}$	0.880	1.215	1.33	26.7	basal	612
$\text{Gd}_2\text{Fe}_{14}\text{B}$	0.879	1.209	0.86	17.3	6.1	661
$\text{Tb}_2\text{Fe}_{14}\text{B}$	0.877	1.205	0.64	12.7	28	639
$\text{Dy}_2\text{Fe}_{14}\text{B}$	0.875	1.200	0.65	12.8	25	602
$\text{Ho}_2\text{Fe}_{14}\text{B}$	0.875	1.199	0.86	17.0	20	576
$\text{Er}_2\text{Fe}_{14}\text{B}$	0.874	1.196	0.93	18.1	basal	554
$\text{Tm}_2\text{Fe}_{14}\text{B}$	0.874	1.195	1.09	21.6	basal	541
$\text{Y}_2\text{Fe}_{14}\text{B}$	0.877	1.204	1.28	25.3	3.1	565

Table 2.1: Lattice parameters, atomic radii and magnetic properties of  $\text{RE}_2\text{Fe}_{14}\text{B}$ -compounds. Adopted and modified from [7].

## Magnetic Properties and Microstructure

There are three different phases in sintered Nd-Fe-B-magnets responsible for this material's magnetic properties. These are:

- $\Phi$ -phase - The  $\text{Nd}_2\text{Fe}_{14}\text{B}$ -phase is the hard magnetic, ferromagnetic phase of sintered Nd-Fe-B-magnets responsible for the exceptional properties. It crystallizes in a tetragonal lattice with anisotropy along the  $c$  axis due to the boron atoms which distort the cubic unit cell. As previously stated the light atoms in the RE sublattice couple parallel with the Fe sublattice. Figure 2.15 shows the unit cell of the hard magnetic  $\text{Nd}_2\text{Fe}_{14}\text{B}$ -phase<sup>[74]</sup>. While in real magnets the matrix grains are irregularly shaped, ideal magnets are composed of small grains of regular shape with their  $c$  axis aligned.

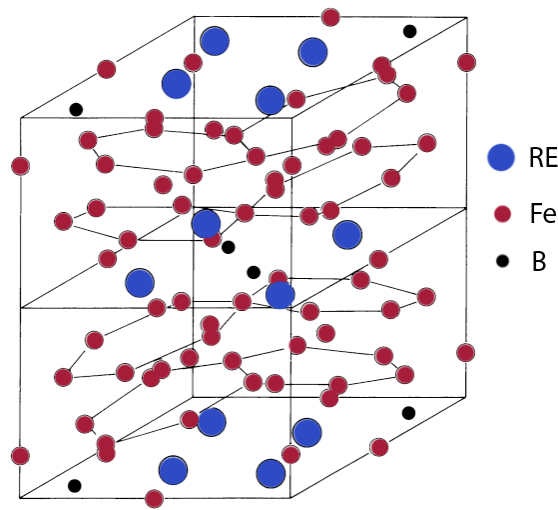


Figure 2.15: Crystall structure of the tetragonal  $\text{Nd}_2\text{Fe}_{14}\text{B}$  unit cell<sup>[8]</sup>.

- $\eta$ -phase - Isolation and decoupling of the grains with non magnetic, Nd-rich  $\text{Nd}_4\text{Fe}$  grain boundary phase ensures that reverse domains cannot spread as easily through the sample, which leads to enhanced coercive strength. This quite low melting phase enhances densification of the sintered magnets, thus increasing the magnetic and physical density. For the ideal magnet, the Nd-rich phase is evenly distributed providing highest possible isolation of the grains. High enthalpy of formation for NdO is the cause for the preferred incorporation of oxygen impurities in this phase and the corrosive behavior of Nd-Fe-B-magnets<sup>[75]</sup>.
- $\eta$ -phase - This boron-rich phase which mainly consists of  $\text{Nd}_{1+\epsilon}\text{Fe}_4\text{B}_4$  as well as the Nd-rich phase are located in the intergranular regions of the 2-14-1-matrix phase. A

## 2 Theoretical Background

schematic illustration of the microstructure of sintered Nd-Fe-B-magnets is shown in Figure 2.16. First Nd-Fe-B magnets containing a significant amount of excess (over stoichiometric) Nd to allow stable sintering processes were relatively sensitive to corrosion in the grain boundaries. In advanced magnets this extra Nd content is largely reduced leading to a higher magnetic moment (less non-magnetic  $\eta$ -phase), reduced sensitivity to corrosion and also reduced raw material costs.

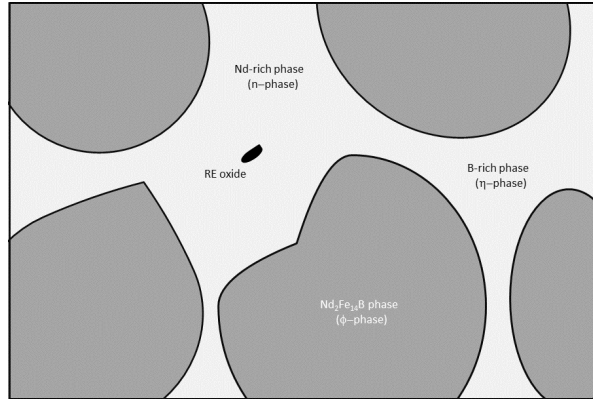


Figure 2.16: Schematic illustration of the Nd-Fe-B-sintered magnet microstructure<sup>[8]</sup>.

### 2.2.6 Production of sintered high performance Nd-Fe-B-magnets

#### Strategies to improve magnetic properties of Nd-Fe-B sintered magnets

There are a number of issues which have to be addressed to improve nanocrystalline as well as microcrystalline Nd-Fe-B permanent magnets. These include<sup>[15]</sup>:

- Higher maximum energy product. Basically, three factors affect the remanence  $B_r$  and because its proportionality to  $B_r^2$ , the maximum energy product  $(BH)_{\max}$ 
  1. The saturation magnetization: This is an intrinsic property of the magnetic phase and can only be affected by compositional changes.
  2. The proportion of magnetic phase: The remanence of a magnet is proportional to the volume fraction of magnetic phase and can only be improved by increasing the density of the magnet and decreasing the proportion of non-magnetic secondary phases or binder.
  3. The degree of crystal alignment for anisotropic magnets: The maximum remanence of an anisotropic magnet is proportional to the cosine of the angle of misalignment averaged over each grain. Therefore, maximum alignment would require the c-axis of each grain to be orientated in the direction of magnetization.
- Improved environmental stability and corrosion resistance at elevated operating temperatures.
- Reduction of grain size. The size of the hard-magnetic grains is desirably reduced to that of a single domain, so in presence of a magnetic field they can only be switched completely. An empirical relationship between grain size and coercive strength at room temperature  $H_{cJ}^{20}$  can be described by<sup>[77]</sup>:

$$H_{cJ}^{20} \propto (\text{grainsize})^{-0.44}$$

- Near-net-shape manufacture.
- Improved magnetization behavior.

### Fabrication of Nd-Fe-B-Sintered Magnets

The production route of RE-magnets starts with alloying<sup>[75]</sup>. The alloys for any rare earth permanent magnet type are commercially made by one of the following methods<sup>[16]</sup>:

- Melting of constituents in their metallic form, or
- Calcio-thermic reduction of the RE-oxides and transition metal constituents in vacuum induction furnaces and subsequent separation of the alloy powder from the melt.

The polycrystalline cast ingots are then ground into micron-sized particles after several mechanical crushing and milling procedures to achieve a defined texture, see Figure 2.17. At this point the easy axes and the magnetic moments are randomly distributed. The fine powders are compacted under an external magnetic field vertical to the pressing direction to pre-align the magnetic moments, if anisotropic magnets are desired. A following sintering procedure at about 1000 °C further densifies the material and facilitates final cutting or grinding steps to final shape. A final re-magnetizing step with an optional coating for corrosion protection completes the fabrication process.

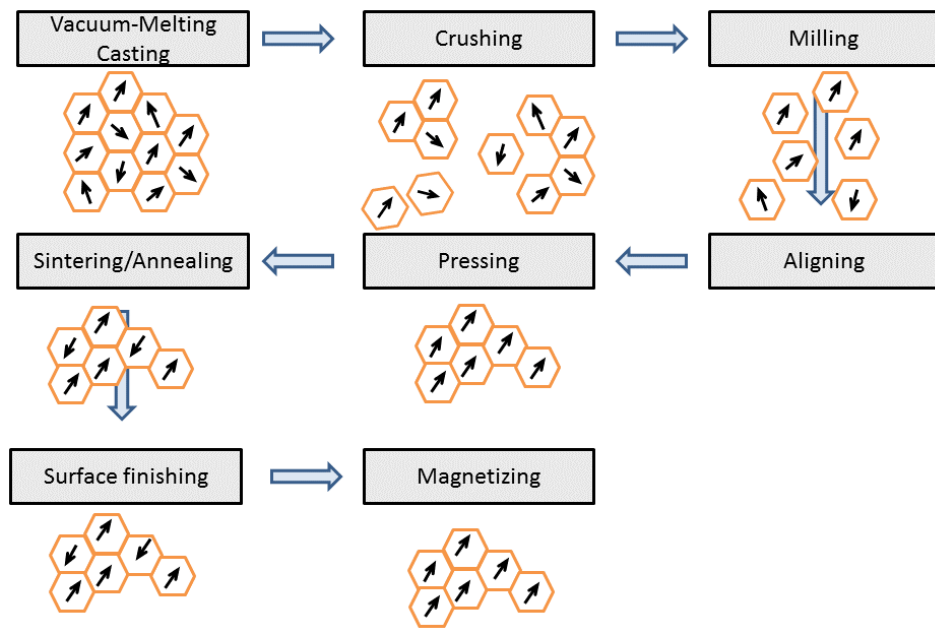


Figure 2.17: Schematic sequence of the Nd-Fe-B sintered magnet production steps<sup>[75]</sup>.

### 2.2.7 Grain Boundary Diffusion Process

As mentioned before, HREE-addition has shown to be essential for high temperature use of Nd-Fe-B-type magnets. The reason being that HRE increase the anisotropy of the 2-14-1-phase and therefore the coercivity leaving more safety against accidental demagnetization at elevated temperatures. One possibility to introduce HREE is the addition during the sintering process. A major drawback of this approach is the need of excessive amounts of expensive rare earth metal. By substituting larger amounts of the light rare-earth elements in the compound by heavy ones, raw material costs not only increase, but as discussed above, an antiparallel coupling of the HRE with the iron sublattice results in dramatic decrease of the remanence<sup>[17]</sup>. Although several propositions have been made to reduce HRE content, grain boundary diffusion excels among all of them. This process was first reported in a Japanese patent<sup>[78]</sup> and later presented to the scientific community by Park et al. in 2000<sup>[18]</sup>. It is still the method of choice to achieve high concentrations of HREEs in the grain boundary as well as cost reduction due to less need of expensive HREEs during the production process. Hereby the HREE is introduced into the material after the sintering process through annealing. The grain boundary diffusion process is schematically outlined in Figure 2.18.

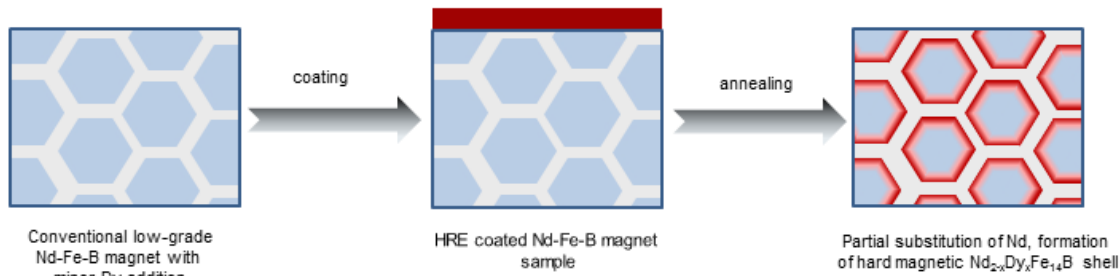


Figure 2.18: Schematic representation of the grain boundary diffusion process<sup>[18]</sup>

First, a coating containing the desired additive (in this case Dy or Tb) has to be applied to the magnet. Different methods have been successfully reported such as sputtering<sup>[19]</sup>, vapor deposition<sup>[20]</sup>, electrophoresis<sup>[12]</sup> and the use of powders, slurries or pastes. In the latter cases, different materials such as oxides<sup>[21,22]</sup>, sulfides<sup>[23]</sup> and fluorides<sup>[21,24]</sup> have been applied either as powders or suspensions in long-chain alcohols. Recently also the grain boundary diffusion treatment with low melting eutectic alloys has been investigated<sup>[25,26]</sup>.

Following the coating step, the magnet undergoes an annealing process, in which the magnet is exposed to elevated temperatures at about 800 °C to 1000 °C for several hours. This temperature is above the melting point of the Nd-rich phase (670 °C) but still low enough not to

## 2 Theoretical Background

promote grain growth or even melting of the matrix phase ( $T_{mp} = 1196\text{ }^{\circ}\text{C}^{[79]}$ ). During this step the HRE in the coating diffuses through the Nd-rich phase into the material, where it concentrates and partially substitutes Nd at the edges of the hard magnetic  $\text{Nd}_2\text{Fe}_{14}\text{B}$ -grains resulting in a hard magnetic  $\text{Nd}_{2-x}\text{HRE}_x\text{Fe}_{14}\text{B}$ -shell. The amount of substituted Nd increases with annealing time and results in an increase of  $H_{cJ}$  and a decrease in  $B_r$ , respectively. Since the HRE only substitutes Nd in a very small region along the grain boundaries, the reduction of  $B_r$  is much lower than for the case where Nd is substituted throughout the entire magnet body.

A subsequent, secondary heat treatment is applied in which the magnet is held at lower temperatures between  $300\text{ }^{\circ}\text{C}$  to  $500\text{ }^{\circ}\text{C}$  for several hours to release internal stress and reduce interfacial energy<sup>[80]</sup>.



# 3 Experimental Methods and Instrumentation

## 3.1 Electrochemical Techniques

### 3.1.1 Cyclic Voltammetry

Cyclic voltammetry is a very versatile technique and is thus called the electrochemist's spectroscopy<sup>[81]</sup>.

#### Fundamentals

A voltage applied to a WE against a reference electrode and is scanned linearly from an initial value,  $E_i$  to a predetermined limit  $E_1$ , where the scan direction is reversed (see Figure 3.1). In contrast to a linear sweep, where the scan ends at  $E_1$  the potential can be cycled from  $E_1$  back to another preselected value  $E_2$  while the current response is plotted as a function of the applied potential<sup>[82]</sup>. Linear sweep and cyclic voltammetry thus are potentiodynamic methods.

$$\vec{J}_i = -D_i \cdot \vec{\text{grad}} c_i + c_i \frac{D_i z_i F}{RT} \vec{E} + c_i \vec{v}_i^{\text{ext}} \quad (3.1)$$

Equation 3.1 which is called the Nernst-Planck-Equation<sup>[29]</sup>, describes the motion of chemical species in homogeneously dense media. The first term describes the diffusion of species caused by a concentration gradient. The second and third describe the migration caused by an applied field (in this case electric) and the convection caused when movement in the solution is forced, e.g. by stirring, respectively.

Migration and convection can be avoided by increasing the conductivity of the solution (e.g. use of conducting salts) and thermostatic control. Consequently, the measured currents arise from diffusion.

#### RE

Non-aqueous reference electrodes with the qualities of aqueous secondary electrodes should offer:

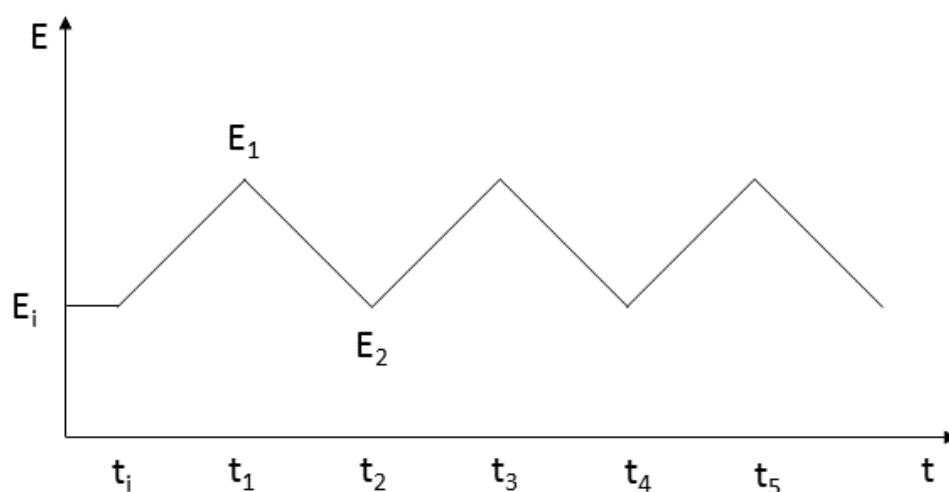


Figure 3.1: Potential profile with time in a CV-experiment.

- Stable, reproducible potentials with negligible temperature dependence
- Potentials not dependent on current (non-polarisable)
- Fast and reversible potential equilibrium of the redox-pair.

One non-aqueous reference electrode to conform to these conditions was suggested by Izutsu<sup>[83]</sup>. By complexation of  $\text{Ag}^+$ -ions by crown ethers in organic solvents (acetonitrile), stable complexes with high complexation constants are formed and the concentration of silver ions is fixed, similar to classical reference electrodes where highly insoluble  $\text{AgCl}$  or  $\text{Hg}_2\text{Cl}_2$  is responsible for the fixed concentration of  $\text{Ag}$ - and  $\text{Hg}$ -ions, respectively. The use of crown ethers also reduces the sensitivity of the electrode potential to water contents and to the used solvent itself.

Due to the fact that measurements at high temperatures were conducted in this study, reference electrodes consisting of organic solvents could not be applied. In the literature, other electrodes for the use in ionic liquids have been suggested. The redox reaction between silver and a monovalent silver species is a commonly used redox couple for reference electrodes in aqueous and non-aqueous media. The  $\text{Ag}/\text{Ag}^+$  electrode is composed of a  $\text{Ag}$  electrode immersed in an ionic liquid containing  $\text{Ag}^+$  at concentrations of 0.01 to 0.1 mol/L, introduced as silver trifluoromethanesulfonate ( $\text{Ag}[\text{OTf}]$ ) or silver bis(trifluoromethylsulfonyl)imide

(Ag[NTf<sub>2</sub>])<sup>[39,66]</sup>. This electrode has shown to share some of the merits of organic solvent-based, non-aqueous reference electrodes and some of their handicaps such as limited lifetime.

### Reference Substance

The comparison of different reference electrodes is achieved by the measurement of a reversible system. Due to its (nearly) solvent independent redox-potential and good solubility in most solvents, the ferrocene/ferrocenium-couple is a well established non-aqueous reference system<sup>[84]</sup>. The standard potential of a reversible system in a cyclic voltammogram (CV) equals to the half step potential (Figure 3.2(b)):  $E_{1/2} = (E_a^p + E_c^p)/2$  with  $E_a^p$  and  $E_c^p$  as the anodic and cathodic peak potentials, respectively<sup>[84]</sup>.

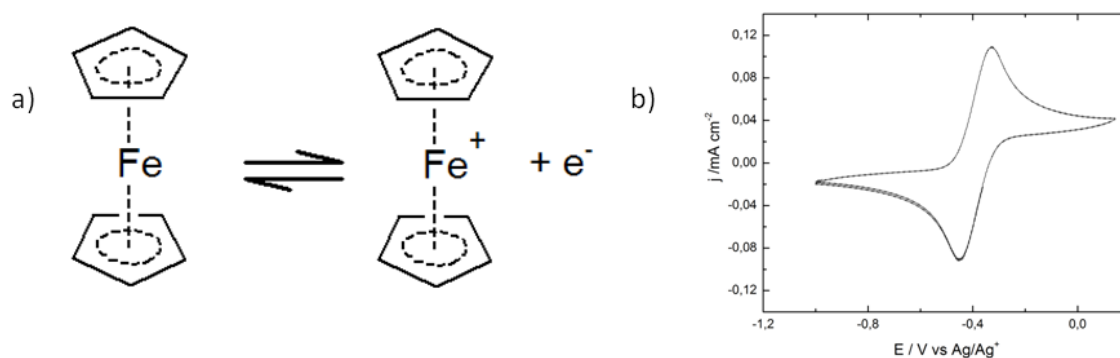


Figure 3.2: (a) Ferrocene-ferrocenium redox system. (b) Actual measurement of ferrocene against the Ag/Ag<sup>+</sup>-reference electrode applied in this study and described in<sup>[66]</sup>.

The reference electrode applied here consisted of a silver wire immersed in a 0.01 mol/kg Ag[NTf<sub>2</sub>] in 1-ethyl-1-methylimidazolium bis(trifluoromethylsulfonyl)imide ([EMIM][NTf<sub>2</sub>]). The electrolyte of the reference electrode was separated from the solution by a Vycor glass frit.

Long term stability of the Ag/Ag<sup>+</sup>-reference electrode applied in this work was periodically measured against ferrocene (*Merck*, purified by sublimation) and replaced once the redox potential shifted by more than 10 mV, which was the case after about 4 weeks, depending on actual experimental conditions (temperatures and electrolytes used). The potential of the Ag/Ag<sup>+</sup>-reference electrode against Fc/Fc<sup>+</sup> is 391 mV as shown in Figure 3.2. All the potentials are represented against this reference unless stated otherwise.

### 3.1.2 Chronoamperometry and Chronopotentiometry

Chrono methods are part of the so called non-stationary techniques based on the abrupt disturbance of a system in equilibrium while its response is recorded. It is necessary that the disturbance happens almost instantly, much faster than the response<sup>[85]</sup>.

#### Fundamentals

##### Chronoamperometry

With this technique the change of current is recorded after a potential is applied which forces diffusion for  $t > 0$ . At times  $t < 0$  the potential equals the equilibrium potential. After an initial potential  $E_i$  is applied, a fast rise in current is measured, which quickly declines. The high rise is caused by charge of the electrochemical double-layer, which acts as a capacitor. After a very short period the capacitive charge current  $i_{dl}$  drops and the measured current originates only from faradaic and adsorption processes ( $i_f$  and  $i_{ads}$ , respectively). Due to reduction/oxidation of species at the electrode surface, concentration changes occur and so occur changes in the measured current which become visible by a drop in current proportional to  $\frac{1}{\sqrt{t}}$ . Contributions to the total charge caused by adsorption ( $Q_{ads}$ ) and capacitance ( $Q_{dl}$ ) can be subtracted from total current by integration of the measured current  $i$  from  $t = 0$  to  $t = t_f$  and plotting of  $Q(t)$  as a function of  $\sqrt{t}$ <sup>[29]</sup>:

$$Q_{total} = Q_f + Q_{ads} + Q_{dl} = 2 \cdot n \cdot F \cdot A \cdot c_0 \cdot \sqrt{\frac{D \cdot t}{\pi}} + n \cdot F \cdot A \cdot \Gamma_0 + Q_{dl} \quad (3.2)$$

where  $\Gamma_0$  is the surface coverage of the electroactive area and the other symbols have their previously defined meaning. Eq. (3.2) corresponds to a linear plot, which can deliver the diffusion coefficient of the active species from the slope and contributions caused by the double-layer and by adsorption from the ordinate intercept, respectively.

Another possibility to describe the current-time relationship in chronoamperometric experiments is given by Cottrell<sup>[29,85]</sup>:

$$i = \frac{n \cdot F \cdot A \cdot c_i \cdot \sqrt{D_i}}{\sqrt{t} \pi} \quad (3.3)$$

it is visible, that the Cottrell-equation is the derivative of  $Q_f$  in Eq. (3.2) in respect to time.

### 3.1.3 The Fast Impedance Scanning - Quartz Crystal Microbalance

Since the introduction of the quartz microbalance as an analytical instrument by Sauerbrey<sup>[94]</sup>, its high sensibility to environmental changes has eased its advance to an important analytical instrument. Besides its high sensibility to mass changes on its surface the quartz microbalance is used as a temperature, pressure and acceleration sensor<sup>[86–88]</sup>. When coupled with electrochemical measurement systems, the electrochemical quartz microbalance becomes one of the most suitable methods for research of electrochemical processes.

#### Fundamentals

Quartz crystals are piezoelectric materials which can turn mechanical strain into electrical charges on the surface of the crystal. More so the inverse piezoelectrical effect converts electrical potential into mechanical deformation.

Thickness shear vibrations are excited by application of an electrical alternating potential on both evaporated (mostly gold) electrodes on both sides of the slice shaped quartz. This vibration expands as a transversal acoustic wave perpendicular to the surface of the crystal. If the right frequency is applied, the crystal can be excited to resonance, by this the acoustic wavelength equals the odd, half-integer multiple of the quartz thickness and a standing wave is created:

$$d = n/2\lambda, \quad n = 1, 2, 3, \dots \quad (3.4)$$

A basic approach to realize mechanical and electrical waves is given by the Mason-Model<sup>[89]</sup> for the one dimensional case, where no lateral expansion of a shear wave has to be taken into account. Near the resonance region, the Butterworth-van-Dyke-Model can be deduced for an undamped quartz (Figure 3.3)<sup>[90,91]</sup>.

The circuit consists of an oscillating circuit, the motional branch and of a parallel capacitance  $C_0$ . The components of the resonant circuit describe the piezoelectric properties of the quartz. The mass of the quartz equals the dynamic inductance  $L_s$ . The mechanical elasticity is described by the dynamic capacity  $C_s$  and the internal friction and damping by the resistance  $R_s$ . A plate capacitor is created by the evaporated gold electrodes on both sides of the disk shaped quartz in which the disk acts as dielectric. The only real term, the parallel capacitance  $C_0$  contains all induced capacitances (e.g. by all connections).

$L_s$ ,  $C_s$ ,  $R_s$  and  $C_0$  determine the resonance frequency of the quartz. Under consideration of Figure 3.3, the serial resonance frequency  $f_s$  and the parallel resonance frequency  $f_p$  can be

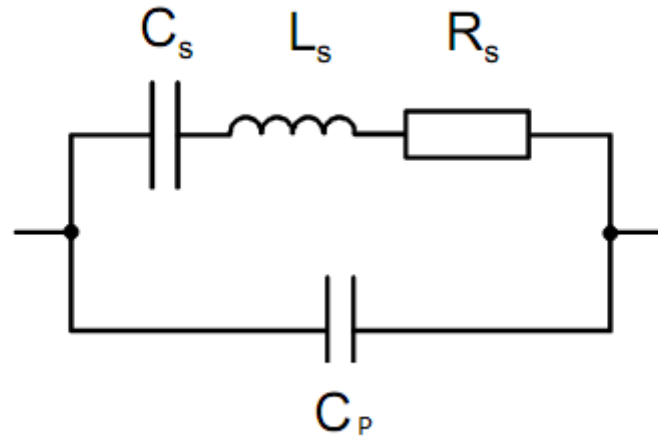


Figure 3.3: Equivalent circuit of a quartz according to the Butterworth-van-Dyke-Model.

determined as follows<sup>[92]</sup>:

$$f_s = \frac{1}{2\pi\sqrt{L_s C_s}} \quad f_p = \frac{1}{2\pi\sqrt{L_s \frac{C_s C_0}{C_s + C_0}}} \quad (3.5)$$

If one side of the resonator is in contact with a liquid, the impedance of the motional branch has to be completed as shown in Figure 3.4<sup>[93]</sup>:

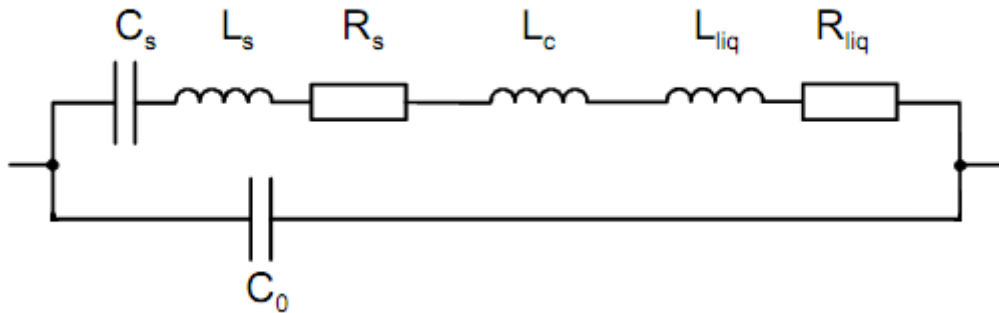


Figure 3.4: Adaption of the BVD-Model for a one-sided damped quartz.

The equivalent circuit is build by the same components but completed by elements which characterize the rigid layer on the quartz surface as well as the loading due to the liquid. These can be divided into an inductance  $L_c$  caused by a rigid layer, an inductance  $L_{liq}$  and a

resistor  $R_{liq}$  due to the contact with a liquid.

The frequency dependence of the mass loading of the quartz is described by the well-known Sauerbrey-equation<sup>[94]</sup>:

$$\Delta f = -\frac{2f_0^2}{nA\sqrt{\mu_Q\rho_Q}}\Delta m = -C_f\Delta m \quad (3.6)$$

$f_0$  is the frequency of the unloaded quartz,  $A$  the exposed area,  $\mu_Q$  the shear modulus,  $\rho_Q$  the density and  $n$  the order of the harmonic vibration of the quartz crystal.

By solving of the Sauerbrey-equation for the mass and area, a mass density is accessible from the frequency shift:

$$\frac{\Delta m}{A} = -\frac{\Delta f n \sqrt{\mu_Q\rho_Q}}{2f_0^2} = \rho_s \quad (3.7)$$

Equation (3.6) was developed for quartzes used in vacuum. Because the layer is interpreted as an expansion of the crystal thickness, following requirements have to be fulfilled<sup>[95]</sup>:

- The deposited mass has to be rigid
- The layer on the quartz surface has to be thin, rigid and even
- The frequency shift should be below 2% of the initial frequency.

The dependence of the frequency shift can be described by the following equation<sup>[96]</sup>:

$$\Delta f = -C_f\Delta m - C_{\eta\rho}(\eta\rho)^{1/2} + C_P\Delta P \quad (3.8)$$

$\eta$  and  $\rho$  stand for the viscosity and density of the solution,  $\Delta P$  the change in hydrostatic pressure.  $C_f$ ,  $C_{\eta\rho}$  and  $C_P$  are constants characteristic for the used material.

When the mass difference is caused by electrochemical experiments, Eq. 3.8 can be coupled with the second Faraday law to the following<sup>[97]</sup>:

$$\Delta f = -C_f\Delta m = -C_f\frac{M_x}{zF}\Delta Q \quad (3.9)$$

$M_x$  is the molar mass of the deposited/dissolved element,  $z$  the number of exchanged electrons,  $F$  the Faraday constant and the passed charge  $Q$ . This equation allows to gather information about the passed charge from the shift in frequency and vice versa.

Because the serial resonance frequency  $f_s$ , as shown above, is only determined by the properties of the crystal, the shift in  $f_s$  is exclusively used for the determination of a change in mass.

### 3 Experimental Methods and Instrumentation

The calibration factor  $C_f$  for a 6 MHz, 0.55 '' quartz crystal electrode (*INDOMET*, Gründau) at 25 °C was determined by electroplating of copper from a 0.1 mol l<sup>-1</sup> CuSO<sub>4</sub> · 5 H<sub>2</sub>O solution in diluted 1 mol l<sup>-1</sup> H<sub>2</sub>SO<sub>4</sub> [98]. As the presence of chloride can lead to error due to side reactions with copper, a Hg/HgSO<sub>4</sub>-reference electrode was used to avoid chloride contamination [99]. Prior to plating, the solution was flushed with N<sub>2</sub> for about 10 min to remove oxygen. The plating procedure was conducted at room temperature under galvanostatic conditions at -0.1 mA for 300 s and subsequently 0.1 mA for the same duration. A value of (246 ± 1) Hz μg<sup>-1</sup> could be determined for  $C_f$ .

A home built Teflon cell adopted from Ref. [100] was applied for EQCM measurements. For a safe operation inside the glovebox, the temperature was controlled by a custom built peltier-element-based thermostat capable to reach up to 150 °C with a precision of ±1 % of the temperature.

#### Fast Impedance Scanning - Quartz Crystal Microbalance

The vast majority of commercially available electrochemical quartz micro balance (EQCM) setups are either based on oscillator or network analyzer designs. While oscillator circuits are the most common for vacuum applications they are highly dependent on phase stability. High damping caused by liquids greatly reduces phase stability and interferes with the determination of the resonance frequencies  $f_s$  and  $f_p$ . During an experiment loading parameters can change continuously, so even the use of complex circuits which can be adjusted to the actual system can cease to work [90–92].

Setups based on network analyzer designs contain a high information density as they don't only scan over the resonance frequencies, but the whole impedance spectrum. The obtained data subsequently needs to be fitted to a BVD-circuit (see Figure 3.4) by non-linear curve fitting to extract information which (amongst other reasons) dramatically reduces data collection speed. Additionally, for the fit to converge, the starting parameters have to be very good to begin with [90–92].

The fast impedance scanning quartz micro balance (fis-QCM) developed in the workgroup "Electrochemistry and Electrolytes" at the University of Regensburg combines the advantages of both methods:

1. Well suited for heavily damped quartz crystals.
2. No need for manual compensation. Resonance frequencies are detected by a software algorithm.



3. Impedance measurements within wide frequency ranges from 1 MHz to 15 MHz.
4. High-speed linear curve fitting enables high data collection speeds <sup>1</sup>.
5. High frequency resolutions of  $< 0.2$  Hz.
6. Suitable for the use of cost-saving 0.55" crystals.

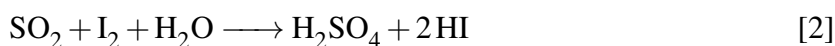
---

<sup>1</sup>An international patent was granted for this method of curve fitting: PCT/EP2008/065248

## 4 Analytical Methods

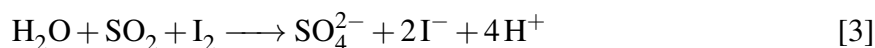
### 4.1 Determination of Water Contents

The KF is a method for quantitative and specific detection of water contents by titration developed by the German chemist Karl Fischer<sup>[101]</sup>. This method is based on the Bunsen-reaction, used for the determination of sulfur dioxide in water<sup>[102]</sup>:

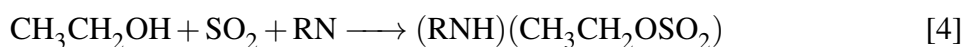


If there is an excess amount of  $\text{SO}_2$  and a base for scavenging acid, this reaction can be used to determine water. As this method was developed, toxic pyridine was used as the organic acid scavenger, as the pH of the solution has to be between 5 and 7 to proceed stoichiometrically and at its highest rate. Today's reagents are pyridine-free<sup>1</sup>.

In the absence of alcohols sulfur dioxide reacts with iodine in presence of water as follows<sup>[103]</sup>:



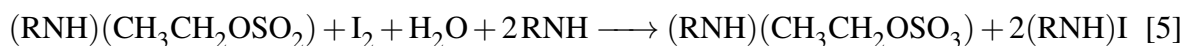
If ethanol is present in the solution, it reacts with sulfur dioxide to an acid ester, which is neutralized by a base RN:



In the titration step, in which iodine in ethanol is used in the titration solution, the ethyl sulfite-anion is oxidized to ethyl sulfate by the iodine in presence of water. Iodine is hereby reduced to colorless iodide<sup>[104]</sup>:

---

<sup>1</sup>Imidazole reacts similar to pyridine but it is odorless, more basic and less toxic. Imidazole is the most commonly used base in Karl-Fischer-Reagents nowadays. Methanol which was used initially has almost completely been replaced by less toxic alcohols such as ethanol as well<sup>[103]</sup>.



This reaction only takes place until all water is consumed. Modern titrators recognize the endpoint of the reaction by electrometrical detection instead of visual determination.

Karl-Fischer-Titration has become the reference method for water determination because of its qualities such as:

- High specificity and precision
- Wide detection window (from ppm to 100 %)
- Short measurement time.

Volumetric and coulometric techniques can be used for this method. In the volumetric method the titer contains the iodine needed for the reaction. High variation of the components is possible this way, so different substances (ketones, aldehydes, hydrophobic substances) can be analyzed. Water contents should be rather high for this method (100 ppm-100 %). The coulometric method coulometrically generates iodine directly in the iodide containing solution and is suited for very low moisture contents (1 ppm to 100 ppm). The apparatus for water determination used in this work is a *TitroLine KF Trace Module 3* coulometric titrator by *SI-Analytix GmbH*. The titrator was calibrated with a *Hydranal* water standard with 0.01% H<sub>2</sub>O by *Sigma Aldrich* before use.

## 4.2 Elemental Analysis

The determination of carbon, nitrogen, hydrogen and sulfur was conducted by combustion analysis <sup>2</sup>.

## 4.3 Thermogravimetric Analysis

In a thermogravimetric analysis (TGA) experiment the mass change  $\Delta m$  of a sample is recorded as a function of time  $t$  and temperature  $T$ . Here, the heating rate can be adjusted. Therefore, a basic instrumental setup for TGA are a high-resolution micro balance with a platinum pan loaded with the sample and a programmable furnace. The sample chamber inside the furnace can be purged with inert (Ar or N<sub>2</sub>) to prevent, or any other gas such as O<sub>2</sub> to illuminate specific reactions<sup>[106]</sup>. Thermogravimetric analysis was used to investigate the thermal stability of the synthesized metal salts. A TGA Q500 from TA Instruments, New Castle, USA, was used for TGA analysis. A constant heat rate of 10 °C/min was applied in a temperature range from room temperature up to 400 °C under nitrogen atmosphere. A sample of typically 2-5 mg was transferred to the platinum pan as fast as possible to avoid water uptake <sup>3</sup>.

## 4.4 Surface Analytical Methods

### 4.4.1 X-Ray Photoelectron Spectroscopy

X-ray photoelectron spectroscopy (XPS) is a powerful spectroscopic technique able to assess the elemental composition as well as chemical and electronic state of the analyzed sample. It is based on the photoelectric effect. Spectra are obtained through irradiation of the sample surface with x-rays. As the beam hits the surface, it penetrates about 10nm into the material and causes electrons from the inner atom shells to be emitted with a characteristic set of kinetic energies which are then measured<sup>[107]</sup>:

$$E_{\text{binding}} = E_{\text{photon}} - (E_{\text{kin}} + \phi) \quad (4.1)$$

$E_{\text{binding}}$  is the binding energy of an electron,  $E_{\text{photon}}$  is the energy of the photons and  $\phi$  is the workfunction of the spectrometer.

---

<sup>2</sup>At this point I thank the Siemens analytics department in Neuperlach-Sued, Munich for the sample analysis.

<sup>3</sup>My tanks to M. Futschik for performing the thermogravimetric analysis.

### 4.4.2 Electron Probe Micro-Analysis

In contrast to XPS, energy dispersive roentgen spectroscopy (EDX) and wavelength dispersive roentgen spectroscopy (WDX) are based on the x-ray emission after excitation by electrons<sup>[108]</sup>. Primary electrons usually have an energy range of 5 to 50keV, allowing them to penetrate and interact with the sample. Mainly three different processes occur:

- Elastic interaction: Electrons are scattered back. As a consequence the focused electron beam is broadened
- Bremsstrahlung: Incoming electrons are deflected and decelerated by the increasing coulomb force near the nucleus and irradiate x-rays with continuous energy
- Inelastic interaction: Sample-atoms are ionized pulling out electrons of the inner shells by the electron beam electrons. This vacancy is filled by an electron occupying a shell higher in energy. The discrepancy in energy is emitted as discrete x-ray radiation of characteristic energy. A competitive reaction is the emission of Auger-electrons, which is dominant for light elements with low binding energies. Both processes are represented in Figure 4.1

*EPMA* (Electron Probe Micro-Analysis) is a scanning electron microscope (SEM) which probes are usually equipped with several WDX detectors. This enables the detection of several elements at the same time. WDX offers a higher resolution in comparison to EDX, which allows to distinguish between elements with very similar spectral lines and offers an overall higher detection limit (about an order of magnitude higher than EDX).

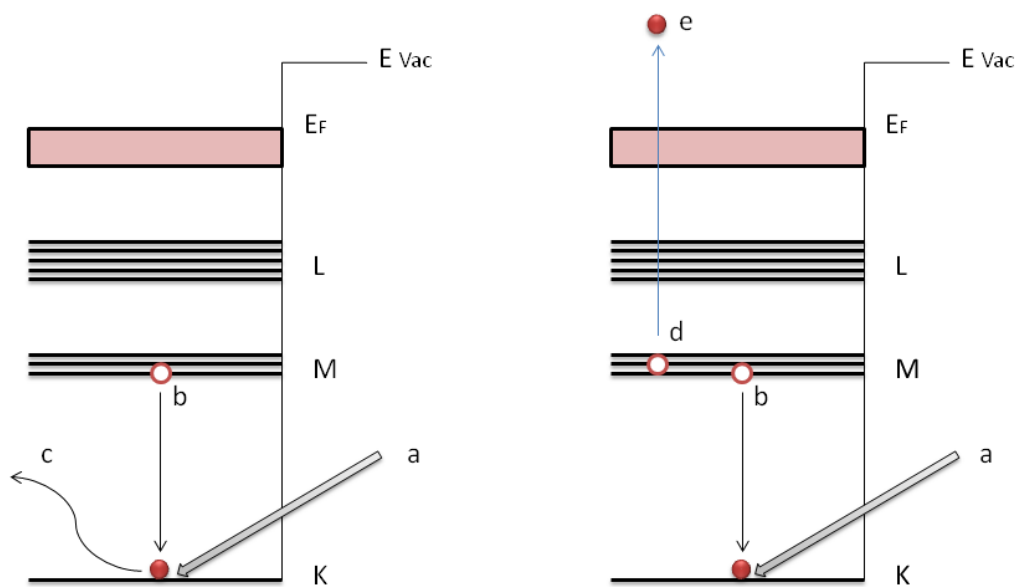


Figure 4.1: Schematic representation of x-ray fluorescence (left) and Auger electron emission (right): a) incident electron beam ejects a K-shell electron, b) relaxation by filling with an L<sub>1</sub>-shell electron, c) photon emission with energy  $E_K - E_{L_1}$ , d) energy difference is transmitted to another electron of the same or more shallow shell, e) emitted Auger electron<sup>[109]</sup>.

## 4.5 Magnetic Characterization

### 4.5.1 Hysteresis graph for Hard Magnetic Materials

The hysteresis graph is mainly used to record the second-quadrant hysteresis loop of bulk permanent magnets. This method of characterization allows to measure important material parameters such as remanence  $B_r$ , maximum energy product  $(BH)_{\max}$  and the coercivity  $H_{cJ}$ . For the measurement, the sample is placed between two pole caps (electromagnets of equal magnetic potential) and the upper pole can be lowered to close the magnetic circuit. If this condition is fulfilled, the sample is homogeneously magnetized and the field strength inside and outside of the sample are equal.

The used system utilizes a  $J$ -compensated surrounding coil <sup>4</sup> suitable for hard-magnetic materials. As seen in Figure 4.2 a) the coil consists of an inner winding enclosing the sample and an outer winding. The inner winding surrounds the sample and senses the magnetic flux penetrating the sample<sup>[110]</sup>:

$$\phi_s = B_s N_i A_s \quad (4.2)$$

where  $N_i$  is the number of windings of the inner coil and  $B_s$  the flux density and  $A_s$  the cross-sectional area of the magnet sample, respectively. As the coil is not completely filled by the specimen, the magnetic flux of the air between the winding and the sample,

$$\phi_{A_i} = \mu_0 H N_i (A_i - A_s) \quad (4.3)$$

is also detected, where  $A_i$  is the cross-sectional area of the inner coil. To remove this effect, the outer coil is used to measure only the air flux in the air next to the sample:

$$\phi_{A_o} = \mu_0 H N_o A_o \quad (4.4)$$

The area-turns of the coils are adjusted to be equal, leading to

$$N_i A_i = N_o A_o \quad (4.5)$$

with the total magnetic flux given by

$$\phi = \phi_s + \phi_i - \phi_o = (B - \mu_0 H) N_i A_s = J N_i A_s \quad (4.6)$$

---

<sup>4</sup>In the absence of a specimen, the output signal is zero, compensating the air flux, as shown in eq. (4.6).

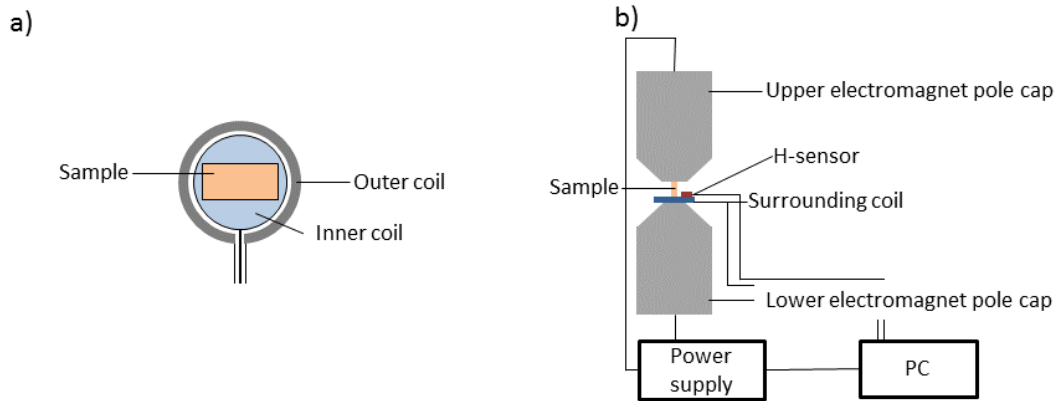


Figure 4.2: Schematic representation hysteresis graph setup: a) J-compensated surrounding coil b) Measuring setup.

The applied field strength  $H$  is measured by a third coil as shown in Figure 4.2.

A merit of this method is a high accuracy of the measured parameters due to the closed magnetic circuit. A major drawback is the limited measuring range due to the (soft magnetic) steel or iron-cobalt materials. Because of this, rare-earth permanent magnets have to be magnetized by a pulsed magnetic field prior to the measurement. This method was chosen for the case of inaccurate measurements of the remanence with the PFM and the measurements were conducted at the Siemens magnetic laboratories Neuperlach-Sued in Munich<sup>5</sup>. A *Magnet-Physik Dr. Steingroever IM-K010020A* pulse magnetizer coupled with a *Brockhaus HG 200* hysteresisgraph by *Brockhaus Messtechnik GmbH & Co. KG* were used to magnetize the samples and to record  $B(H)$  and  $J(H)$  hysteresis loops, respectively.

### 4.5.2 Pulse Field Magnetometer

Capacitive-discharge magnetizers are composed of two major components, namely the capacitor discharge magnetizer and the magnetizing fixture (coil)<sup>[110]</sup>. As the name implies, the capacitor discharger consists of a large capacitor bank, which stores electrical energy. As soon as enough energy is stored, a switch is closed and the capacitors are discharged in a fast pulse through the fixture, which in turn transforms as much electrical energy into a magnetic pulse of a few milliseconds (1-50 ms), thus magnetizing the sample. The efficiency for the conversion of electrostatic into magnetic energy is enhanced by the application of short pulses.

<sup>5</sup>At this point I thank Dr. Michael Krispin for providing access to the measurement equipment at the magnetism laboratories in the Siemens AG facilities in Neuperlach-Sued and his help with the measurements.



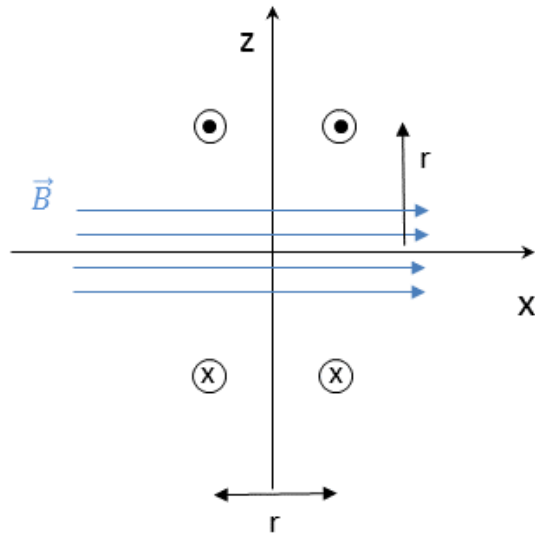


Figure 4.3: Scheme of the pickup coil setup in a PFM.

The method uses a system of so-called Helmholtz coils to measure the magnetization. This coaxial setup produces a high volume of (almost) homogeneous magnetic field (Figure 4.3)<sup>[110]</sup>

Due to the measurement in a magnetically open circuit, some corrections have to be made to get the correct hysteresis loop as a function of the internal field. One of them is the selection of the demagnetizing factor  $N$ , a number  $0 < N < 1$  depending on the symmetry of the sample.

Further, Eddy currents and magnetic-viscosity effects are another cause of error by the application of transient fields. In the first case, the dynamic field creates magnetic moments in conducting samples anti parallel to the external field. In the case of sintered permanent magnets, the specific resistivity is rather large, therefore errors are rather small. Errors caused by magnetic viscosity<sup>6</sup> scale with the duration of the pulse.

Hysteresis curves were assessed by using a capacitive discharge magnetizer (*CDMM magnetizer 28kJ 3kV*) in conjunction with a HyMPulse hysteresis meter from *Metis Instruments & Equipment NV*. Temperature was kept constant at  $29 \pm 0,5$  with a *NESLAB ThermoFlex 1400* recirculating chiller by *Thermo Scientific*.

<sup>6</sup>This property refers to a time dependent change in magnetization at constant applied field. In most cases the magnetization is related to time by a logarithmic function  $J(t) = J(0) + S \ln(t)$ , where  $J(0)$  is a constant and  $S$  is the magnetic viscosity coefficient<sup>[111]</sup>.

## 4.6 Materials and Purity

The water content of all purchased materials was determined before use. Ionic liquids were dried under vacuum at 100 °C for 15 to 20 h before use to reach water contents given in Table 4.1.

### 4.6.1 Solvents

Ionic Liquid	Manufacturer	Water [ppm]
1-Butyl-3-methylimidazolium trifluoromethanesulfonate	Sigma Aldrich	< 15 ppm
1-Butyl-2,3-dimethylimidazolium trifluoromethanesulfonate	Sigma Aldrich	< 15 ppm
1-Butyl-1-methylpyrrolidinium dicyanamide	Merck	< 30 ppm
1-Butyl-1-methylpyrrolidinium bis(trifluoromethylsulfonyl)imide	Merck	< 5 ppm
1-Butyl-1-methylpyrrolidinium trifluoromethanesulfonate	Sigma Aldrich	< 15 ppm
1-Ethyl-1-methylimidazolium tetrafluoroborate	Sigma Aldrich	< 15 ppm
Acetone	Prolabo	< 30 ppm

Table 4.1: Water content of the applied ionic liquids

### 4.6.2 Metal Salts

Ionic Liquid	Manufacturer	Water [ppm]
Silver-(I)-trifluoromethanesulfonate	Sigma Aldrich	< 40 ppm
Copper-(II)-trifluoromethanesulfonate	Sigma Aldrich	< 45 ppm
Dysprosium-(III)-trifluoromethanesulfonate	Sigma Aldrich	< 40 ppm
Terbium-(III)-trifluoromethanesulfonate	Sigma Aldrich	< 50 ppm
Neodymium-(III)-trifluoromethanesulfonate	Sigma Aldrich	< 50 ppm
Dysprosium-(III)-chloride, anhydrous	Sigma Aldrich	< 20 ppm

Table 4.2: Water content of applied commercially available metal salts

# 5 Metal Additions by Physical Vapor Deposition

The following chapters lie focus on the effect of metallic coatings prepared by physical vapor deposition (PVD) after subsequent grain boundary diffusion treatment of sintered Nd-Fe-B permanent magnets.

Reasoned in the concern about the future supply of heavy rare-earths, several attempts have been made to increase the coercivity without the addition of these elements. In the literature, aluminum has been added to HRE-free alloys of Nd-Fe-B before sintering to enhance  $H_{cJ}$  by increasing the isolation of the  $\text{Nd}_2\text{Fe}_{14}\text{B}$  matrix grains.

The addition of copper to HRE-free Nd-Fe-B alloys has shown an increase of  $H_{cJ}$  as well. Basically, the mechanism by which the coercivity is increased is the same as that of aluminum. Lower-melting intergranular phases enhance the wettability of the matrix grains which in turn improves their magnetic isolation.

In this study, the addition of Al and Co by grain boundary diffusion into Nd-Fe-B sintered magnets with minor Dy-content will be studied.

$\text{Tb}_2\text{Fe}_{14}\text{B}$  has a higher magnetocrystalline anisotropy than  $\text{Dy}_2\text{Fe}_{14}\text{B}$ . Superior results of GBD of terbium into Nd-Fe-B sintered magnets compared to dysprosium have been reported. Most of these studies have either just shown the improvement for a single addition of Tb in comparison to a reference sample, or a series of additions but no comment about the actual amount of used HRE was given. Coatings applied by PVD result in series of precise additions of this element to elucidate their effect on the magnetic properties of Nd-Fe-B- sintered magnets.

Finally, a comparison of the grain boundary diffusion treatment of Nd-Fe-B sintered magnets by dysprosium<sup>1</sup> and terbium is investigated. Therefore, the resulting demagnetization curves and the respective percentage increase with varying HRE-content are compared.

---

<sup>1</sup>The effects of metallic Dy-coatings applied by PVD on Nd-Fe-B sintered magnets were studied within the master thesis of Amanda Lorenz. At this point, the author expresses his gratitude for the data.

## 5.1 Addition of Aluminum

Aluminum is present in nearly all commercial Nd-Fe-B magnets as an impurity of boron. The substitution of Fe by Al has been shown to be beneficial for the coercivity as it increases the  $c/a$  ratio by entering the matrix phase. However, it causes a decrease of the Curie temperature by approximately 8 K / at. %<sup>[112]</sup>. The addition of Al leaves the magneto-crystalline anisotropy unaffected<sup>[113]</sup>, so the improvement in coercivity can be traced to a modification of the grain boundaries. Addition of Al causes a decrease in the contact angle between the grains and the liquid boundary phase though improving the wetting of the grains by the paramagnetic, intergranular phases resulting in a better distribution of Nd and a better isolation of the grains by magnetic decoupling<sup>[115]</sup>. Improvements in coercivity of up to 28 % have been reported for the addition of 2 at. % Al to HRE-free Nd-Fe-B alloys during the alloying process have been reported<sup>[112,116]</sup>.

Al has not only been added into the bulk material of Nd–Fe–B-sintered magnets to improve their magnetic properties but it has been used as a coating for corrosion protection, as well. Therefore, magnets have been coated with IVD-Aluminum (Ion Vapor Deposition) as this has several benefits compared to other metallic coatings (e.g. Zn, Ni) for corrosion prevention such as high temperature resistance, no cracking of the grain boundaries and no hydrogen embrittlement during the coating procedure<sup>[114]</sup>.

### 5.1.1 Deposition of Aluminum

Within this work Al was deposited by sputtering technique. Coatings of different thicknesses were applied to achieve different compositions, which are given in Table 5.1

Coating Thickness [nm]	Total Al-content [ $\Delta$ wt. %]
310	$7.5 \times 10^{-3}$
414	0.01
1447	0.035

Table 5.1: Correlation between Al-coating thickness and concentration in the Nd-Fe-B samples.

### 5.1.2 Effects of Al-addition

Prior to submission to the GBD-process, the samples were individually wrapped in Mo-foil and transferred into a quartz tube. The tube was evacuated ( $p < 1 \times 10^{-3}$  Pa) and reduced pressure was maintained until all following procedures were finished. All samples were annealed at 900 °C for 6 h with subsequent cooling to room temperature. A final aging procedure was conducted at 500 °C for 1 h. The demagnetization curves of the whole Al-series are shown in Figure 5.1. It is immediately visible that the coercivity declines with increasing Al-addition, while the opposite is true for the remanence. The shapes of the curves after GBD are similar to the reference, however  $H_{cJ}$  drops from 1120 kA m<sup>-1</sup> to 950 kA m<sup>-1</sup> and  $B_r$  increases slightly from 1.31 T to 1.35 T.

Fig.5.2(a) further illustrates the behavior described above. An increase of Al by  $7.5 \times 10^{-3}$  wt. % is accompanied by a dramatic drop in coercivity of about 20 %. A further increase of the Al-content only decreases  $H_{cJ}$  slightly.

However, an increase of the Al-content leads the contrary effect for  $B_r$ , as illustrated in Figure 5.2(b). Contrary to literature reports,  $B_r$  increases by 3.75 % for a total addition of 0.035 wt. % Al and shows a maximum at 0.035 wt. %. It must be pointed out, that literature reports investigated the addition of aluminum to HRE-free Nd-Fe-B alloys. Within the scope of this thesis, all treated samples contain an intrinsic amount of Dy of 0.5 wt. %. Further additions of this alloying element decrease the concentration of HRE in the base body and a reduction in  $H_{cJ}$  is measurable as a result. The slight decrease in remanence can be ascribed to a slight dilution of the matrix phase in the intergranular phases. Aluminum is able to enter both the matrix and grain boundary phase where it forms a paramagnetic Nd(FeAl) phase at the grain interfaces at the cost of the amount of matrix phase<sup>[112]</sup>. This offers an explanation for the slight increase in the remanent polarization, as shown in Figure 5.2(b).

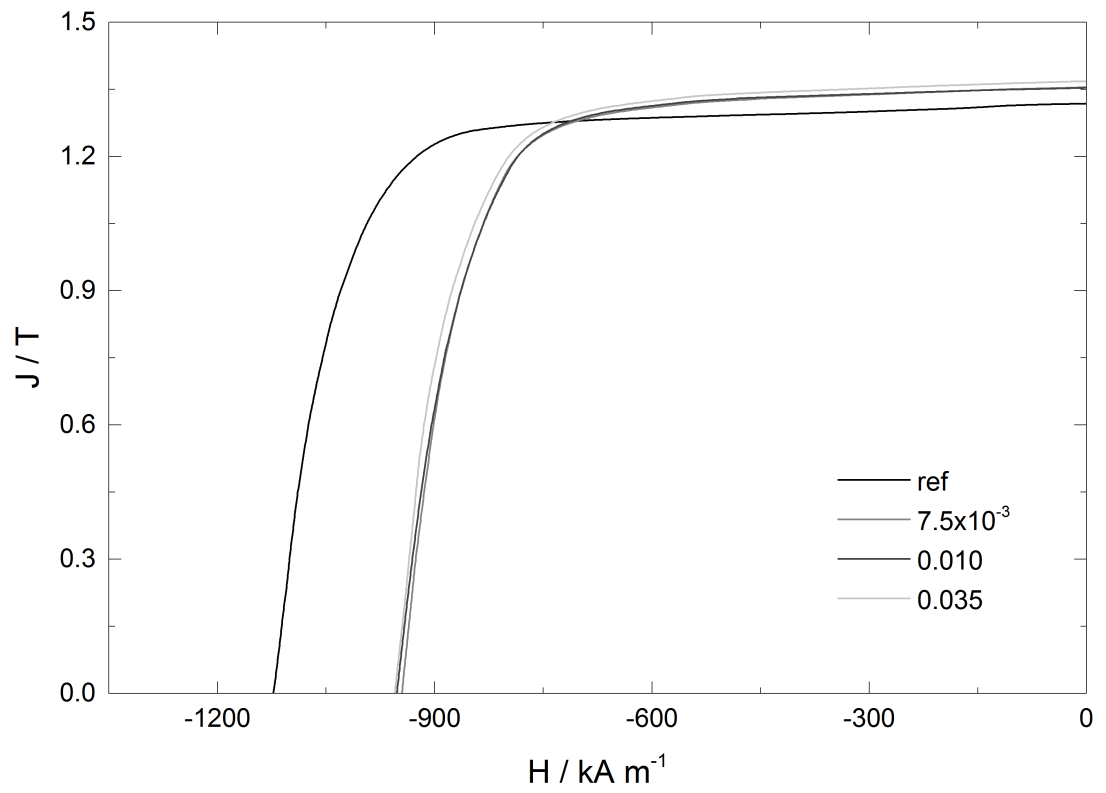


Figure 5.1: Demagnetization curves for GBD-treated samples with different additions of pure Al.

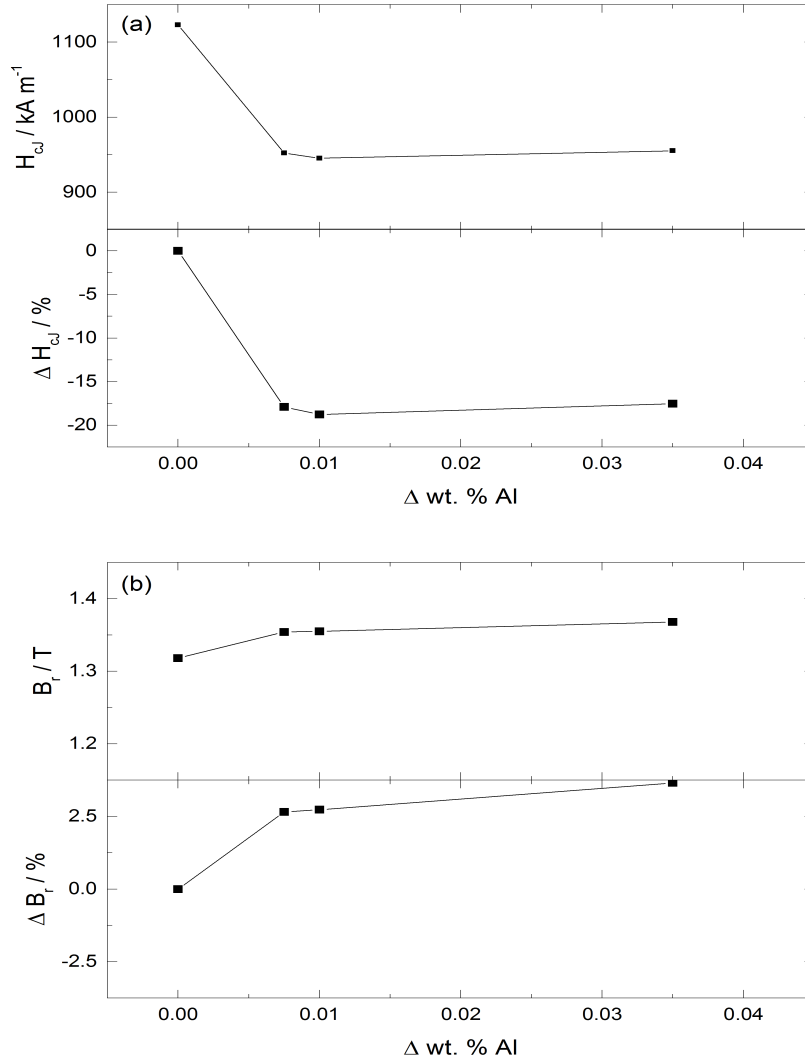


Figure 5.2: (a) Changes of the coercivity. (b) Changes of the remanence with increasing aluminum content.

## 5.2 Addition of Copper

The incorporation of Cu leads to inter-metallic compounds with lower melting points. They enhance the wetting ability of the liquid Nd-rich phase and enclose the hard magnetic grains of Nd-Fe-B magnets during sintering, leading to refined microstructures. Furthermore, an increase in coercivity due to impeded reverse domain growth, an increase of the energy density, an improved corrosion resistance and enhanced mechanical properties have been reported for the addition of copper to HRE-free alloys<sup>[117,118]</sup>.

## 5.3 Deposition of Copper

Different coating thicknesses were applied by sputtering to achieve different compositions, all of which are given in Table 5.2.

Coating Thickness [nm]	Cu-content [ $\Delta$ wt. %]
312	0.025
469	0.0375
625	0.05

Table 5.2: Correlation between Cu-coating thickness and concentration in the Nd-Fe-B samples.

### 5.3.1 Effects of Cu-addition

Prior to the grain boundary diffusion treatment, the samples were prepared as described in the previous section for Al-treated samples. Annealing took place at 900 °C for 6 h and an aging procedure at 500 °C was conducted for the duration of 1 h. Figure 5.3 shows the demagnetization curves after the incorporation of Cu by grain boundary diffusion. While the shapes of the curves for the Cu-diffused samples do not vary from the reference, the values of the remanence and coercivity decreased slightly after the GBDP.

In comparison to Al, the incorporation of Cu does not lead to a noticeable change in coercivity. A minor increase of about 1.5 % for an addition of 0.025 wt. % is visible, as presented in Figure 5.4(a). Further additions of Cu only lead to a slight decrease of the coercivity in comparison to the untreated reference of up to -2.5 % for the highest addition.

The effect of Cu-addition on the remanence is shown in Figure 5.4(b). While an increase of Al by 0.025 wt. % enhanced  $B_r$  by 5.1 %, the same amount of Cu results in a decrease of -8.8 % and recovers slightly to about -6 % for the largest addition.



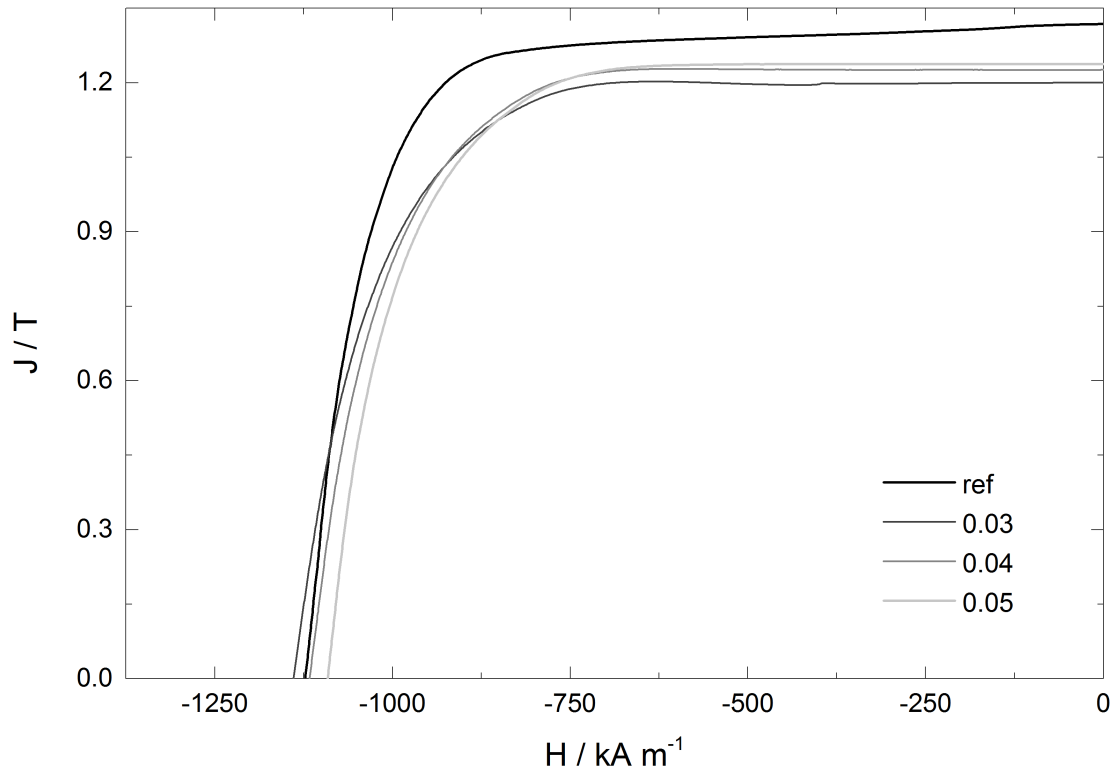


Figure 5.3: Demagnetization curves for GBD-treated samples with different additions of pure Cu.

As Cu does not enter the major  $\phi$ -phase, this results can be attributed to microstructural effects<sup>[119]</sup>. In this case, two opposing effects are apparent: On the one hand, the enhanced decoupling of the grains caused by the formation of  $\text{NdCu}_2$  slightly increases  $H_{cJ}$ , on the other hand the formation of additional non-isolating intergranular phases i.e.  $\text{NdFe}$  has the adverse effect on the coercivity. The amount of nonferromagnetic phases increases slightly for the addition of copper, which in turn leads to a decrease in remanence<sup>[119]</sup>.

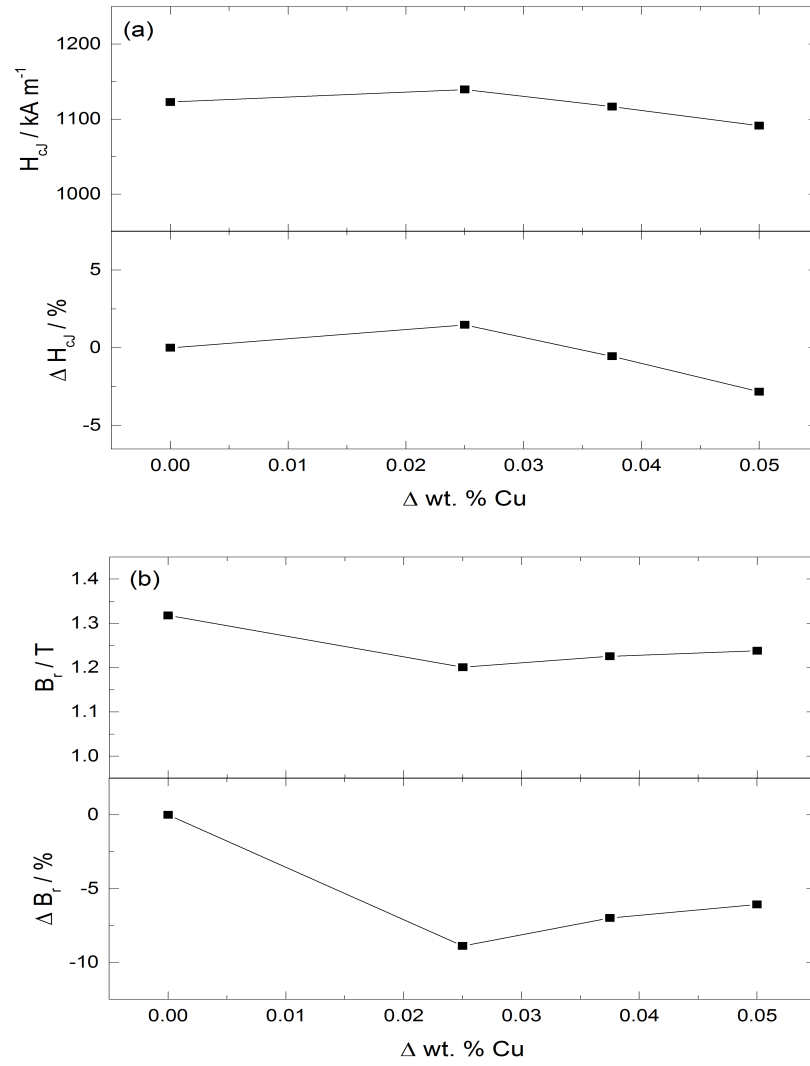


Figure 5.4: (a) Changes of the coercivity. (b) Changes of the remanence with increasing copper content.

## 5.4 Addition of Terbium

Due to the high magnetocrystalline anisotropy of  $\text{Tb}_2\text{Fe}_{14}\text{B}$  as reported by Sagawa et al.<sup>[7]</sup>, the addition of Tb by grain boundary diffusion into Nd–Fe–B sintered magnets has been widely studied. Although the substitution of Nd by Tb leads to higher coercivities than Dy due to a higher magnetocrystalline anisotropy constant  $H_A$  of the  $\text{Tb}_2\text{Fe}_{14}\text{B}$  phase (see Tab. 2.1), Dy has become more important for industrial application due to its lower price.

Tb has been applied to Nd–Fe–B sintered magnets in the form of oxides<sup>[21,125]</sup>, fluorides<sup>[121,122]</sup> and metallic coatings<sup>[123,124]</sup>. However, only very vague descriptions of the coating procedures were given by these authors. In this work, the effects of specified additions of heavy rare-earths on the magnetic properties is studied.

### 5.4.1 Deposition of Terbium

Terbium coatings were applied by physical vapor deposition as 1  $\mu\text{m}$ , 2  $\mu\text{m}$ , 5  $\mu\text{m}$  and 10  $\mu\text{m}$  thick layers on the pole sides ( $1 \times 1 \text{ cm}^2$  of the cuboid- shaped Nd–Fe–B-samples supplied by Vacuumschmelze Co. & K. G.). The additions in terms of  $\Delta \text{wt. \%}$  are given in Table 5.3. For the grain boundary diffusion treatment, the coated magnets were individually wrapped in Mo-foil and subdued to an annealing procedure at 900 °C for 5 h and a subsequent aging procedure at 500 °C for 1 h inside an evacuated quartz tube ( $p < 1 \times 10^{-3} \text{ Pa}$ ).

Coating Thickness [ $\mu\text{m}$ ]	Tb-content [ $\Delta \text{wt. \%}$ ]
1	0.07
2	0.15
5	0.37
10	0.73

Table 5.3: Correlation between Tb-coating thickness and concentration in the Nd–Fe–B samples.

### 5.4.2 Effects of Tb-Addition

#### Microstructural Analysis

Figure 5.5(a) shows a backscattered electron image and cross-section image of the near surface microstructure of a Nd–Fe–B sintered permanent magnet treated with 5  $\mu\text{m}$  Tb under the conditions described in section 5.4.1. It is found that near-surface  $\text{Nd}_2\text{Fe}_{14}\text{B}$ -matrix grains are smaller in size and become larger with increasing distance to the coated surface. The grains

in the vicinity of the surface show pronounced core-shell structures with Tb-rich shells about 0.5  $\mu\text{m}$  thick. The shells exhibit an enhanced BSE signal that appears brighter. This indicates a higher average atomic weight of the  $\text{Nd}_2\text{Tb}_{2-x}\text{Fe}_{14}\text{B}$ -shells while the inner grains show no noticeable substitution of Nd by Tb. A shell thickness of a few tens of  $\mu\text{m}$  can be estimated for the inner shells, consistent with literature reports<sup>[125]</sup>. At about 10  $\mu\text{m}$  from the Tb-sputtered surface, a rounding of the grains is visible as well as brightening and cracks of the grain boundaries which are still visible at depths of about 60  $\mu\text{m}$  to 70  $\mu\text{m}$ , as shown in the cross-sectional magnification in 5.5(b). Those are indications for the melting of the grain boundary phase near the surface which causes the rounding of the grains as well as the cracking of the grain boundary phase upon cooling but also explains the allocation of Tb within a distance close to the surface. Samardzija et al. report a decreasing Tb-concentration up to 200  $\mu\text{m}$  into the bulk of Nd–Fe–B permanent magnets<sup>[125]</sup>. In their report, the base body was coated with an alcoholic slurry containing  $\text{Tb}_4\text{O}_7$  followed by a grain boundary diffusion process at 850 °C for 10 h and aging at 500 °C for 1 h.

EPMA elemental intensity mapping (Figure 5.5(c)) of the area outlined in Figure 5.5(a) shows a correlation of the sharp, bright grain boundaries with an accumulation of Tb as well as a presence of this element in the oxidic Nd-Pr-intergranular phases whereas no terbium can be detected inside of the matrix grains at any depth. While HREs are found in the Nd-rich and grain boundary phases, there is no observation of HREs inside the  $\phi$ -phase. The distribution of heavy rare earths in grain boundary diffusion treated sintered magnets is a well studied subject. A sharp decrease in concentration within a few nanometers was found in the junction between  $(\text{NdTb})_2\text{Fe}_{14}\text{B}$ -grain boundary and  $\text{Nd}_2\text{Fe}_{14}\text{B}$ - matrix phase for terbium<sup>[125]</sup> as well as for dysprosium diffused sintered magnets<sup>[131]</sup>. The authors in Ref. [131] investigated the formation of HRE-rich shells with WDX and EDX along a line that crosses reaction phase, matrix grain and reaction phase. Elemental concentration profiles show a constant sum of the HRE and Nd atomic concentrations within the shell and the core which amounted to about 12, respectively. Simultaneously, while the ratio of HRE to Nd was close to 1:1 for near-surface grain shells and about 1:3 for the inner grain shells, no accumulation of the heavy rare earth elements inside the cores was found. This finding is of particular interest, as it indicates that the shell formation is unlikely to occur by a conventional diffusion process. A model for the formation of the surface region of  $(\text{Nd}_2\text{HRE}_{2-x})_2\text{Fe}_{14}\text{B}$  grains has been recently proposed by Sepehri-Amin et al. in which partial melting of the surface region of  $\text{Nd}_2\text{Fe}_{14}\text{B}$ -grains takes place. During the molten state, the grain boundaries enrich with heavy rare-earth element. After solidification and crystallization of the matrix grains upon cooling,  $(\text{NdHRE})_2\text{Fe}_{14}\text{B}$ -shells are formed<sup>[126]</sup>.

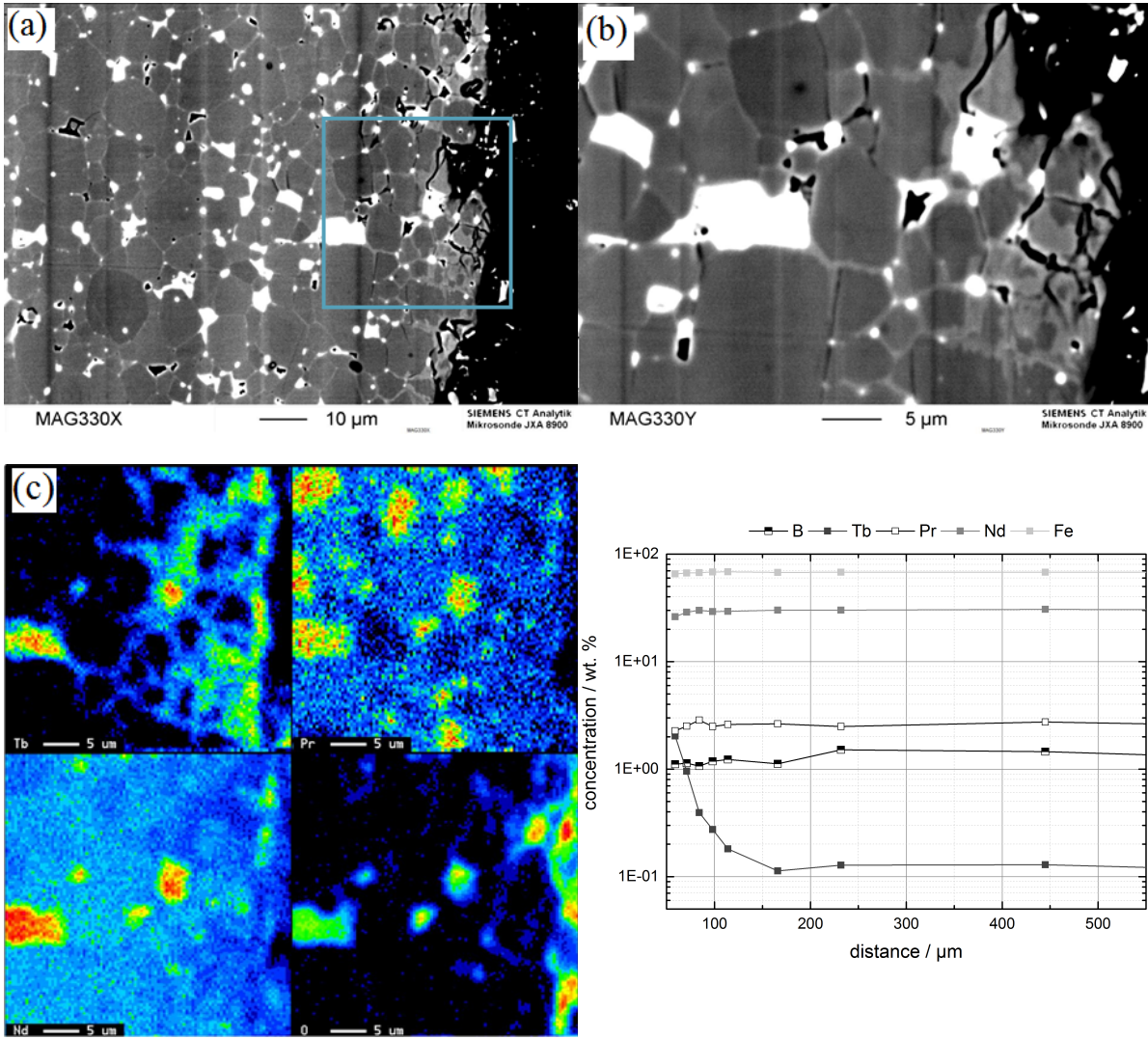


Figure 5.5: a) Backscatter electron image of the metallurgical cross-section of Tb-coated sample. b) Magnification of the outlined area. c) EPMA elemental intensity mapping of b). d) EPMA quantitative concentration depth profile for GBD-processed Nd–F–B-sintered magnet.

Differences in terms of crystal orientation and the orientation of magnetic domains between core and shell of the grains have been investigated by Löwe et al.<sup>[131]</sup>. Electron backscatter diffraction (EBSD) was applied to elucidate the crystal orientation of the grains and the results show that the intergranular misorientation angle was below the detection limit of  $1^\circ$  indicating epitaxial growth of the shells. In this same study, Kerr microscopy showed that there was no correspondence of BSE and Kerr contrast with the shell-core structures, meaning that the majority of the magnetic domains run uninterrupted through the shell-core interface but are also separated by the paramagnetic intergranular phases.

EPMA quantitative concentration depth profiling of the cross-section is presented in Fig-

ure 5.5(d). Simultaneously with a decrease of the concentration of the light rare earths Nd and Pr near the coated magnet surface, a higher Tb-concentration can be detected about up to 150  $\mu\text{m}$  inside the bulk of sample which declines rapidly with increasing diffusion depth. This concentration profile is characteristic for GBD-treated sintered magnets and has also been shown e.g. indirectly by measurement of the local coercivity in dependence from the surface of the magnets<sup>[128]</sup>. Brombacher et al. characterized Dy-diffusion processed Nd–Fe–B magnets and showed the same correlation between the concentration gradient of dysprosium and  $B_r$  as well as a distribution of  $H_{cJ}$  with the distance from the magnet surface. The dysprosium concentration inside the shells of Dy-diffusion processed samples in respect to the distance to the coated surface was measured by EDX and could be fitted with a simple effective medium diffusion model for a given temperature<sup>[127]</sup>:

$$c(x, t) = c_S - (c_S - c_B) \text{erf}(\beta) \quad (5.1)$$

where  $x$  represents the diffusion length,  $c_S$  is the surface concentration and  $c_B$  the bulk composition against at a point far from the interface, respectively. The parameter  $\beta$  is given by:

$$\beta = \frac{x}{\sqrt{4D_{eff}t}} \quad (5.2)$$

therein  $D_{eff}$  describes the effective diffusion coefficient and  $t$  the time. The error function  $\text{erf}(\beta)$ , is given by:

$$\text{erf}(\beta) = \frac{2}{\sqrt{\pi}} \int_0^\beta e^{-\tau^2} d\tau \quad (5.3)$$

In Ref. [127], the diffusion coefficient  $D_{eff}$  is reported to range between  $1.5 \times 10^{-14}$  to  $7 \times 10^{-13} \text{ m}^2 \text{ s}^{-1}$  for 5  $\mu\text{m}$  to 20  $\mu\text{m}$  thick metallic coatings applied by PVD and annealed at 900 °C for 6 h<sup>2</sup>. Cook et al. report a value of  $2.9 \times 10^{-16} \text{ m}^2 \text{ s}^{-1}$  for the diffusion coefficient  $D$  of dysprosium in  $\text{Nd}_2(\text{Fe}_{1-x}\text{Co}_x)_{14}\text{B}$  (no liquid Nd-rich phase) at 1050 °C<sup>[129]</sup>.

The Tb-profile of the EPMA concentration depth graph presented in Figure 5.5(d) was fitted to equation (5.1). From this fit, a diffusion coefficient could be determined to  $(4.3 \pm 0.6) \times 10^{-14} \text{ m}^2 \text{ s}^{-1}$ .

In accordance to the results reported in [127], Nakamura et al. also reported a noticeable concentration dependent decrease in surface coercivity with increasing distance from the surface. However, results from measurements of  $H_{cJ}$  with respect to the distance from the surface

<sup>2</sup>This study was conducted within the PerEMot project in cooperation with Vacuumschmelze GmbH & Co. KG, Technische Universität Darmstadt and IFW Dresden.

conclude that while the gradient in  $H_{cJ}$  increases with the amount of applied coating, but the diffusion depth is almost not affected by coating thickness. This behavior can be explained by the assumption that the diffusion process consists of mainly two steps<sup>[128]</sup>:

- Liquification of the Nd-rich grain boundary phase and diffusion to the surface. Once the melt reaches the surface, a reaction with the HRE-coating follows. This enables the diffusion of the HRE-dopants into the bulk through the grain boundary liquid phase.
- Volume diffusion into the  $\phi$ -phase which advances by partial exchange of light rare-earths (Nd, Pr) for the heavy rare earth element<sup>[121]</sup> is the rate-determining step in the grain boundary diffusion process, as diffusion along grain boundary diffusion is typically 4 to 6 orders of magnitude higher than bulk diffusion<sup>[130]</sup>. This substitution entails the refinement of the grain boundaries from rough to smooth ones and the formation of shell-core structures as shown in Figure 5.5 (a) and (b).

### Magnetic Properties

Figure 5.6(a) presents the demagnetization curves for treated and untreated Nd–Fe–B magnet samples. It reveals a considerable increase in coercivity by up to 48 % from 1100 to 1790 kA m<sup>-1</sup> for 10  $\mu$ m (shown in Figure 5.6(b)) thick coatings while showing remanence values at practically the same level as the reference sample (–20 mT which is about 1.5 %). Besides showing a good enhancement of magnetic properties compared to reference samples, the demagnetization curves of all additions maintained good squareness as the shapes of the demagnetization curves were not drastically altered by the grain boundary diffusion procedure of terbium coatings applied by PVD. A square shaped demagnetization curve is important to minimize irreversible demagnetization losses at operation conditions caused (for instance, by reverse fields<sup>[133]</sup>). Inappropriate heat treatment procedures or just unsuitable base body dimensions can explain this behavior by uneven distribution of the HREE inside the bulk material. In contrast to this, Nakamura et al.<sup>[128]</sup> reported a loss of squareness for GBD-processed Nd–Fe–B magnets coated with a suspension containing terbium fluoride Nd–Fe–B. The amounts of coating were specified (16, 41 and 96  $\mu$ g cm<sup>-2</sup>), however no further details about the composition of the suspension were given.

Change in coercivity with increasing terbium addition are given in Figure 5.6(b). A steep increase is seen for minor additions of 0.07 and 0.15 wt %. This is characteristic for the grain boundary diffusion treatment of sintered Nd-Fe-B magnets with HRE's. On the other side, the effect of terbium on  $H_{cJ}$  is less pronounced for high additions. Under the given conditions, a part of the coating does not reach sufficient depth to substitute Nd far inside the base body.

## 5 Metal Additions by Physical Vapor Deposition

Diffusion depth can be improved by longer annealing times. As a tradeoff, grain growth and higher energy consumption should be taken into account<sup>[134]</sup>.

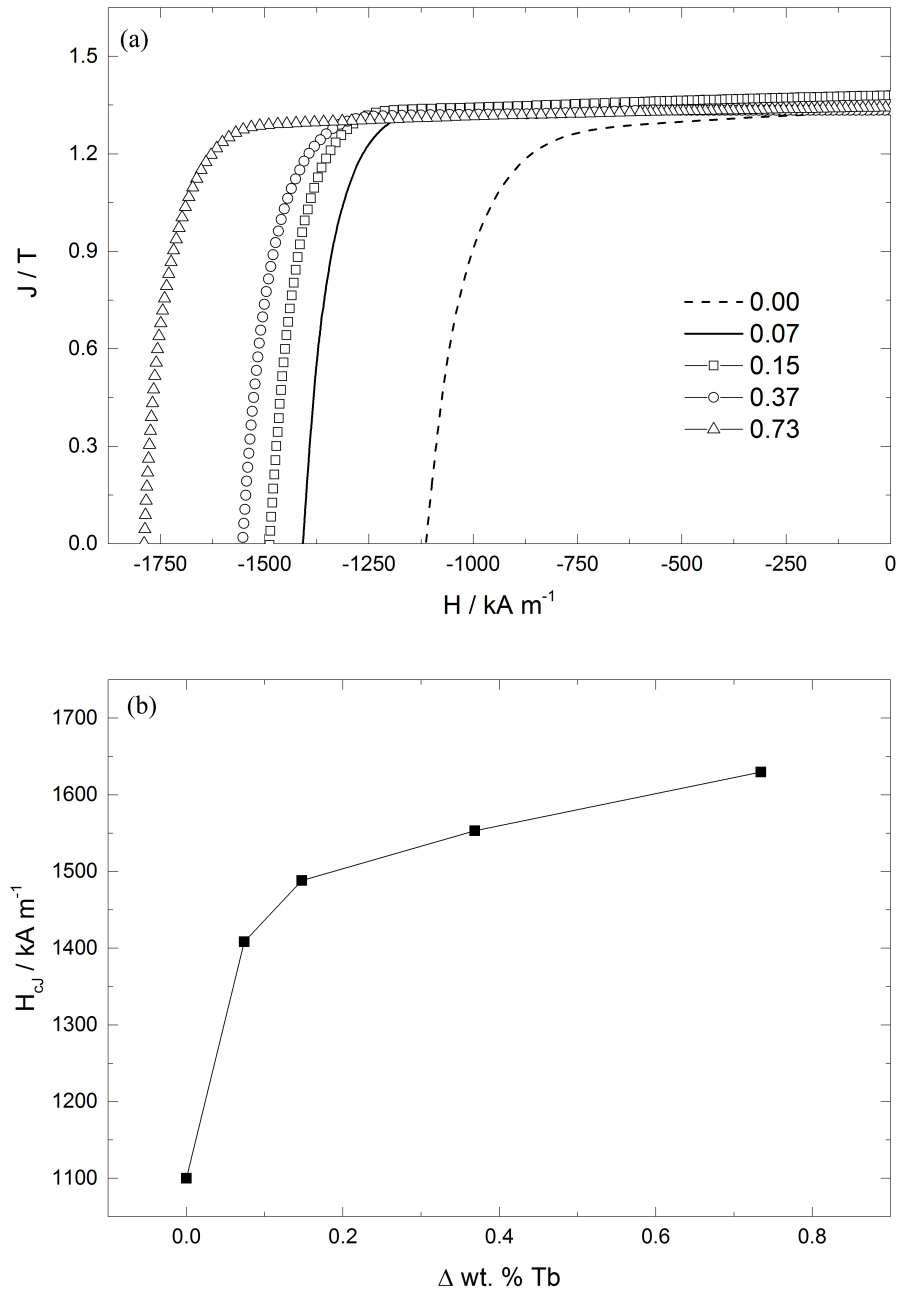


Figure 5.6: Change of magnetic properties with Tb-addition. (a) Demagnetization curves for GBD-treated samples with different Tb-content. (b) Change in  $H_{CJ}$  with Tb-addition.



To further illustrate the impact of uneven distribution of HRE on the properties of a GBD-processed magnet, a second series of terbium coated Nd–Fe–B-samples was prepared. Therefore, magnets were coated only on one of the pole sides with thicknesses between 1  $\mu\text{m}$  to 20  $\mu\text{m}$  and subdued to the same GBD-process as discussed above. The demagnetization curves of all samples are shown in Figure 5.7. It is obvious that single-sided coated magnets lose their squareness as compared to double-sided coated ones. When comparing curves with the same amount of Tb, an additional difference in the achieved coercivity can be noticed. Single-sided coated samples achieve an improvement about 4 % lower than their double-sided counterparts.

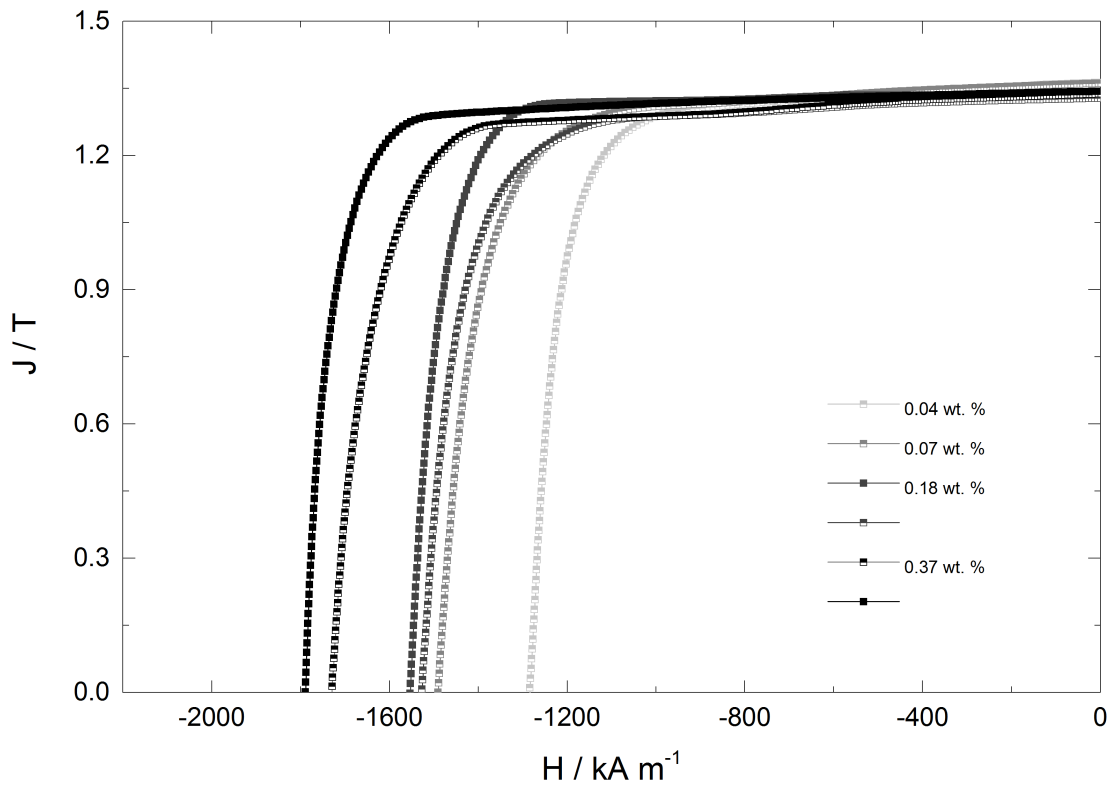


Figure 5.7: Demagnetization curves of single- and double-sided Tb-coated magnet samples. Full squares: double-sided, half-filled squares: single-sided coating.

### 5.4.3 Comparison of Dy and Tb Grain Boundary Treated Sintered Magnets

Metallic coatings of equal thickness were applied to sintered Nd-Fe-B magnets to produce samples with comparable mass ratios of Dy and Tb, respectively. A comparison of the results of Tb- and Dy-addition is shown by the demagnetization curves presented in Figure 5.8(a) and Figure 5.8(b), respectively. The superiority of Tb can be noticed instantly by comparison of the demagnetization curves. The demagnetization curves treated with Dy show a smaller degree in squareness compared with their Tb-diffused counterparts, in accordance to the results presented in Ref. [21]. The authors studied the effect of GBDP of Nd–Fe–B magnets coated with several millimeters of a mixture composed of ethanol or water mixed with TbF<sub>3</sub>, Dy<sub>2</sub>O<sub>3</sub> or DyF<sub>3</sub> in a 1:1 weight ratio. The superiority of terbium-diffused samples was shown, as is expected because the magnetic anisotropy field of Tb<sub>2</sub>Fe<sub>14</sub>B is higher than the one of Dy<sub>2</sub>Fe<sub>14</sub>B as reported by Hirosawa et al.<sup>[135]</sup> (also, see Table 2.1). Hirosawa also showed, that in the case of dysprosium, oxidic sources of the element delivered inferior results compared to fluorides. In contrast to Dy<sub>2</sub>O<sub>3</sub>, DyF<sub>3</sub> dissolves more easily in the Nd-rich phases by formation of NdOF with the neodymium oxide phases<sup>[22]</sup>, which as a consequence resulting in a higher effective concentration of free dysprosium.

The change in coercivity with Dy- and Tb-addition is further illustrated in Figure 5.8(c). The latter shows an increase in  $H_{cJ}$  of  $1790 \text{ kA m}^{-1}$ , which is about  $200 \text{ kA m}^{-1}$  (or about 14 %) higher than the Dy coated sample with  $1521 \text{ kA m}^{-1}$  for an addition around 0.73 wt. %.

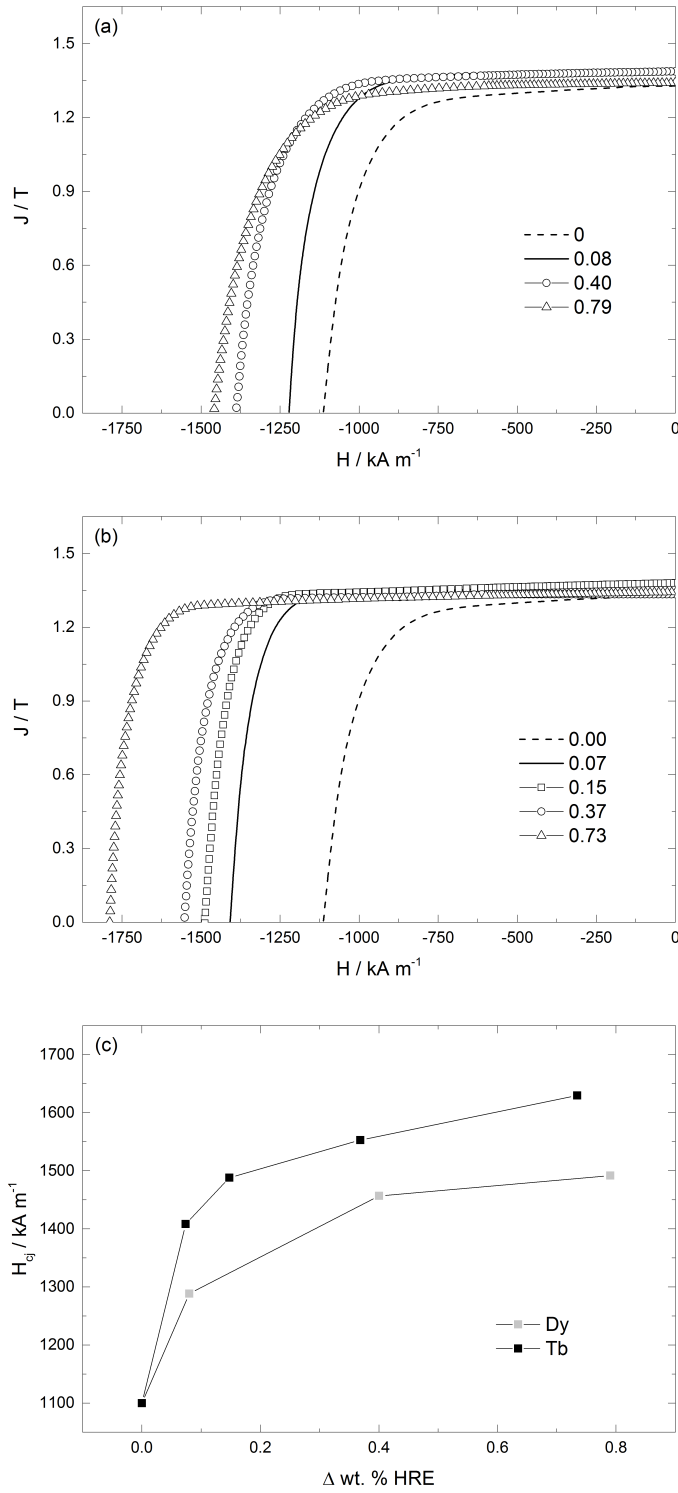


Figure 5.8: Comparative representation of the changes in the magnetic properties with Dy- and Tb-additions. (a) Demagnetization curves for GBD-treated samples with different Dy-content. (b) Demagnetization curves for GBD-treated samples with different Tb-content. (c) Change in  $H_{cj}$  with HRE-addition.

## 6 Grain Boundary Diffusion of Metal Alloys by Physical Vapor Deposition

The GBD-process has shown to have a great effect in the enhancement of the magnetic properties of Nd–Fe–B permanent magnets, however the very nature of this process also presents a drawback that can not be overlooked in respect to large scale industrial application. Based on the diffusion of a HRE from the surface into the bulk of the magnet, this process is not suited for samples of large thickness (respective distance perpendicular to coated surfaces) as a uniform distribution of the dopant inside the permanent magnet is needed to elicit optimal performance enhancement. Founded by the assumption that the use of melting-point depressants for the grain boundary phase increase the diffusivities of the elements, Oono et al. investigated the grain boundary diffusion of an eutectic alloy powder with the composition  $\text{Dy}_{73}\text{Ni}_{9.5}\text{Ni}_{17.5}$  suspended in paraffin<sup>[26]</sup>. This paste was applied on both pole sides of the  $7\text{ mm} \times 7\text{ mm} \times 5\text{ mm}$  sized squares with subsequent GBD-treatment at  $900^\circ\text{C}$  and  $500^\circ\text{C}$  for 3 h, respectively. Although no further specifications about the amount of diffused Dy are given, results show a substantial increase in coercivity of  $600\text{ kA m}^{-1}$ , reaching a level comparable with values reported for the treatment with metallic Tb-coatings in Ref. [121] as well as those reported within this work for an addition of 0.73 wt. % Tb. For this reason, two binary systems of low-melting eutectic alloys, namely Dy–Cu<sup>1</sup> and Dy–Al were investigated within the PerEMot project.

---

<sup>1</sup>The Dy–Cu-system was investigated in the scope of the master thesis of Amanda Lorenz and will not be further discussed here

## 6.1 Grain Boundary Diffusion of Aluminum-Dysprosium Alloys

Due to their application in the automotive and aerospace industry, the interest in aluminum-based, light-weight alloys is rising continuously. Recently, the effects of the incorporation of rare-earth elements into Mg–Al-alloys on their microstructure and mechanical properties have been studied. Several interesting effects such as the improvement of fluidity, hardness, high temperature tensile strength and ignition-proof performance have been shown<sup>[136]</sup>.

The binary system Dy–Al shows two eutectic equilibria, one on the Al-poor and one on the Al-rich region (henceforth named low-Dy and high-Dy alloys, respectively) both of which have a considerably lower melting point than pure Dy (1407 °C), as shown in Table 6.1.

Composition [wt. % Al]	Phase	Melting point [°C]
22	AlDy <sub>2</sub>	940
87.6	Al <sub>3</sub> Dy	636

Table 6.1: Compositions, phases and melting points of the applied eutectic alloys. Data taken from Ref. [137].

Coated Nd-Fe-B samples with the compositions described in Table 6.1 were produced by PVD. The used samples have an initial Al-content of 0.09 wt. %. The final content after deposition of the alloy in the samples is calculated by:

$$\omega_{Al} = \frac{m_{dep}^{Al} + \omega_{Sample}^{Al} \cdot m_{Sample}}{m_{dep}^{Al} + m_{dep}^{Dy} + m_{Sample}} \quad (6.1)$$

wherein  $m_{dep}^{Al}$  represents the deposited mass of Al,  $m_{dep}^{Dy}$  the deposited mass of Dy,  $\omega_{Sample}^{Al}$  initial mass fraction of Al in the sample and  $m_{Sample}$  the sample weight.

The mass fractions  $\omega_{Alloy}^{Al}$  and  $\omega_{Sample}^{Dy}$  in the alloy are fixed:

$$\frac{m_{Alloy}^{Al}}{m_{Alloy}^{Dy}} = \frac{\omega_{Alloy}^{Al}}{\omega_{Alloy}^{Dy}} \quad \text{from which follows:} \quad m_{Alloy}^{Dy} = \frac{m_{Alloy}^{Al} \cdot \omega_{Alloy}^{Dy}}{\omega_{Alloy}^{Al}} \quad (6.2)$$

Substitution of Eq. (6.2) into Eq. (6.1) and resolution of Eq. (6.1) into  $m_{dep}^{Al}$  gives:

$$m_{dep}^{Al} = \frac{(\omega_{Al} - \omega_{Sample}^{Al}) \cdot m_{Sample}}{1 - \omega_{Al} - \omega_{Al} \cdot \frac{\omega_{Alloy}^{Dy}}{\omega_{Alloy}^{Al}}} \quad (6.3)$$

With help of eq. (6.3) the needed mass of Dy and Al to obtain the desired total mass fraction of

aluminum in the coated magnet can be calculated. A concentration series for low-Dy and high-Dy alloys were produced, respectively. The needed mass in g was converted into a coating thickness  $d$  in  $\mu\text{m}$  according to the following relationship:

$$d = \frac{m_{dep}^{metal}}{2 \cdot \rho^{metal} \cdot A} \cdot 10^4 \quad (6.4)$$

where  $\rho^{metal}$  is the density of the sputtered metal in  $\text{g cm}^{-3}$ ,  $A$  the sample area in  $\text{cm}^2$  and the factor 2 accounts for the application of the coating on the pole-sides as alternating stacks Dy-Al-Dy-Al.

Restricted by the slow sputtering times for Al-coatings with the given set-up, only two types of coatings could be applied for the low-Dy series. The compositions of series are given in detail in Table 6.2.

		low-Dy			high-Dy		
		$\omega_{total}$	m [mg]	d [ $\mu\text{m}$ ]	$\omega_{total}$	m [mg]	d [ $\mu\text{m}$ ]
Comp. 1	Al	0.2	2.46	4.56	0.1	0.23	0.42
	Dy	0.52	0.38	0.22	0.69	4.34	2.54
Comp. 2	Al	0.4	6.95	12.88	0.11	0.46	0.84
	Dy	0.55	1.07	0.63	0.89	8.7	5.08
Comp. 3	Al				0.12	0.69	1.27
	Dy				1.08	13.08	7.64
Comp. 4	Al				0.13	0.90	1.7
	Dy				1.27	17.48	10.21

Table 6.2: Resulting mass fraction of Al and Dy in the magnet samples after coating with low- and high-Dy eutectic alloys.

### 6.1.1 Magnetic Properties of Grain Boundary Diffusion-Processed Sintered Magnets coated with Al–Dy-Alloys

#### Sintered Magnets Processed with Low-Dy-Alloys

Figure 6.1(a) shows the demagnetization curves of samples treated with the alloy-coatings as listed in Table 6.2. The squareness of the curves are well maintained, but in spite of a slight increase of the mass fraction of dysprosium in the magnet, the coercivity suffers a decrease of almost 20 %, as shown in the plot of  $H_{cJ}$  and  $B_r$  against the Al and Dy content in Figure 6.1(b). Pure Dy-coatings, as shown in the previous section in Figure 5.8, increases  $H_{cJ}$  by about  $180 \text{ kA m}^{-1}$  for an addition of 0.1 wt. %. This result is comparable to those presented in the previous chapter for the addition of pure Al. This could be explained by insufficient diffusion of dysprosium into the material as compared to the pure metal coating due to the application of alternating layers of Al and Dy.

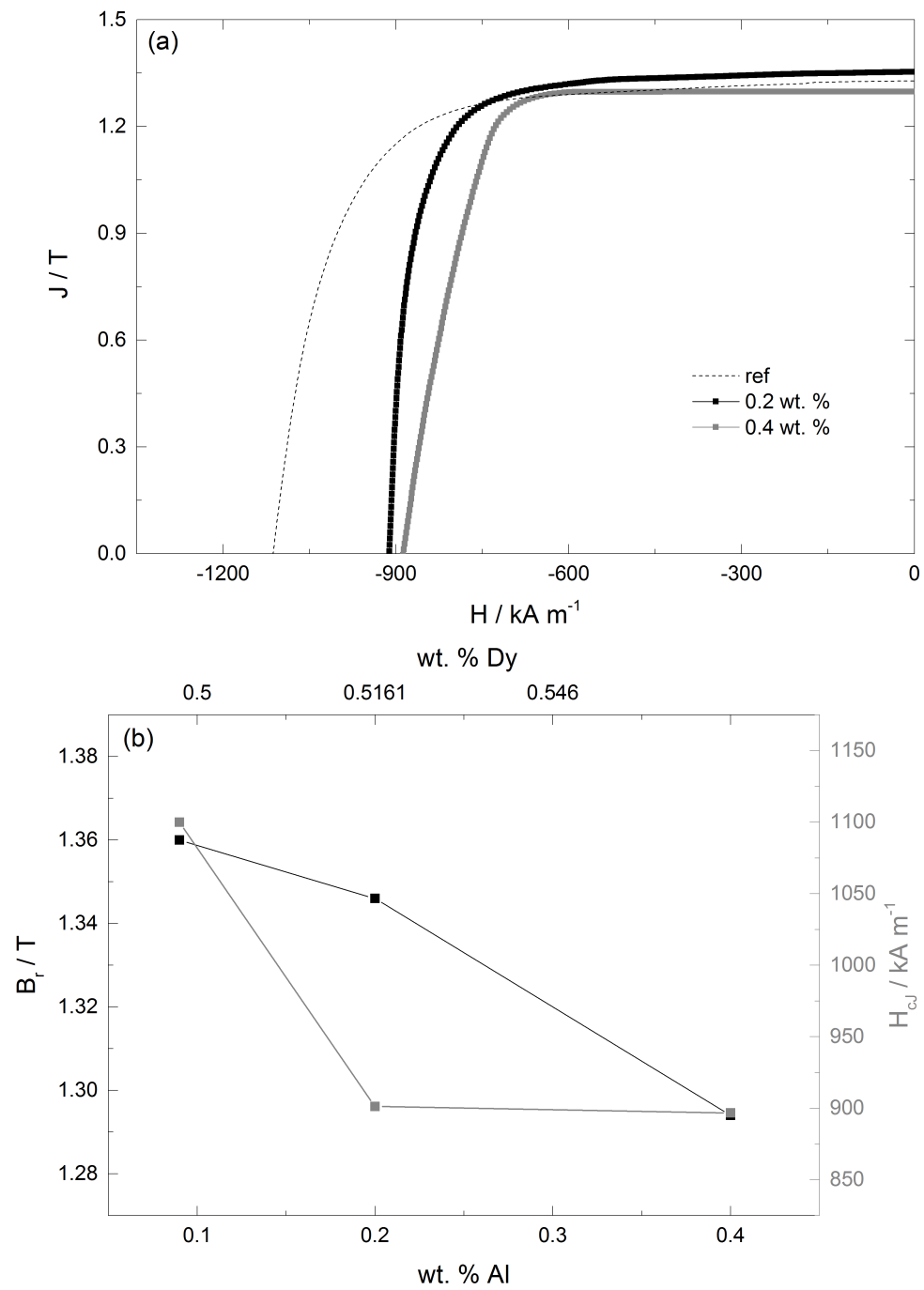


Figure 6.1: Change of magnetic properties after grain boundary diffusion treatment with low-Dy alloys. (a) Demagnetization curves for GBD-treated samples with low-Dy alloys. (b) Changes in  $H_{cJ}$  and  $B_r$  after GBD-treatment with low-Dy eutectic alloys.



### Sintered Magnets Processed with High-Dy-Alloys

The demagnetization curves of the treated Nd–Fe–B samples are shown in Figure 6.2(a), the extracted values for  $H_{cJ}$  and  $B_r$  with respect to Dy and Al incorporation are presented in Figure 6.2(b). For the remanence, it is observed that all values of  $B_r$  stay consistently lower than the reference sample (data points at 0.09 wt. % Al / 0.5 wt. % Dy) as well as the samples treated with pure Al, where a steady increase of  $B_r$  was confirmed. On the other hand,  $H_{cJ}$  decreases for the first sample in spite of an increase of the heavy rare-earth content. Compared to pure Dy, a mass fraction of ~0.7 % would lead to an increase of  $H_{cJ}$  by ~250 kA m<sup>-1</sup>. Figure 6.2(b) shows, that after an initial decrease,  $H_{cJ}$  increases due to an increasing dysprosium mass fraction and peaks at 0.89 wt.% Dy and 0.11 wt. % Al, respectively. At higher Al and Dy contents, the coercivity stays relatively constant while the remanence drops even further with each following addition.

Microstructural analysis was performed on the sample with 0.11 wt. % Al / 0.89 wt. % Dy as presented in Figure 6.3 for the near-surface analysis of the grain boundary diffused sample and a magnification of the outlined area of the BSE enhanced cross-sectional area illustrated in Figure 6.3(a). Compared to the BSE-images of Tb-treated sintered magnets, a difference in the microstructure is clearly visible. The sample treated with the Al–Dy-alloy shows a bright area near the surface, which can be appointed to a higher concentration of heavier elements, as in this case Dy. This can be affirmed by EDX maps of this area, presented in Figure 6.3(b). While a higher concentration of the coating material near the surface is characteristic for the GBDP, the heavy rare element seems to be confined at within the first 10 µm.

Figure 6.3(c) shows WDX concentration depth profiles of Al, Dy, Pr, Nd, Fe at depths up to 550 µm. This can be traced to the intrinsic content of Al and Dy. The profiles are consistent with the results of the BSE-images and EDX maps as they show that the concentrations of the added aluminum and dysprosium drop rather quickly within the first 100 µm. WDX concentration maps shown in Figure 6.3(d) additionally show that the added aluminum and dysprosium concentrate mostly in the intergranular phases.

Figure 6.4 shows the microstructural analysis of the same sample at distances of about 100 µm (Figure 6.4(a)-(c)) and 200 µm (Figure 6.4(d)-(f)) from the surface. At these depths, the microstructure seems unaffected by the GBD process. The main components, namely Nd and Fe are present, but Dy is not detected in the qualitative EDX maps (Figure 6.4(c) and Figure 6.4(f)).

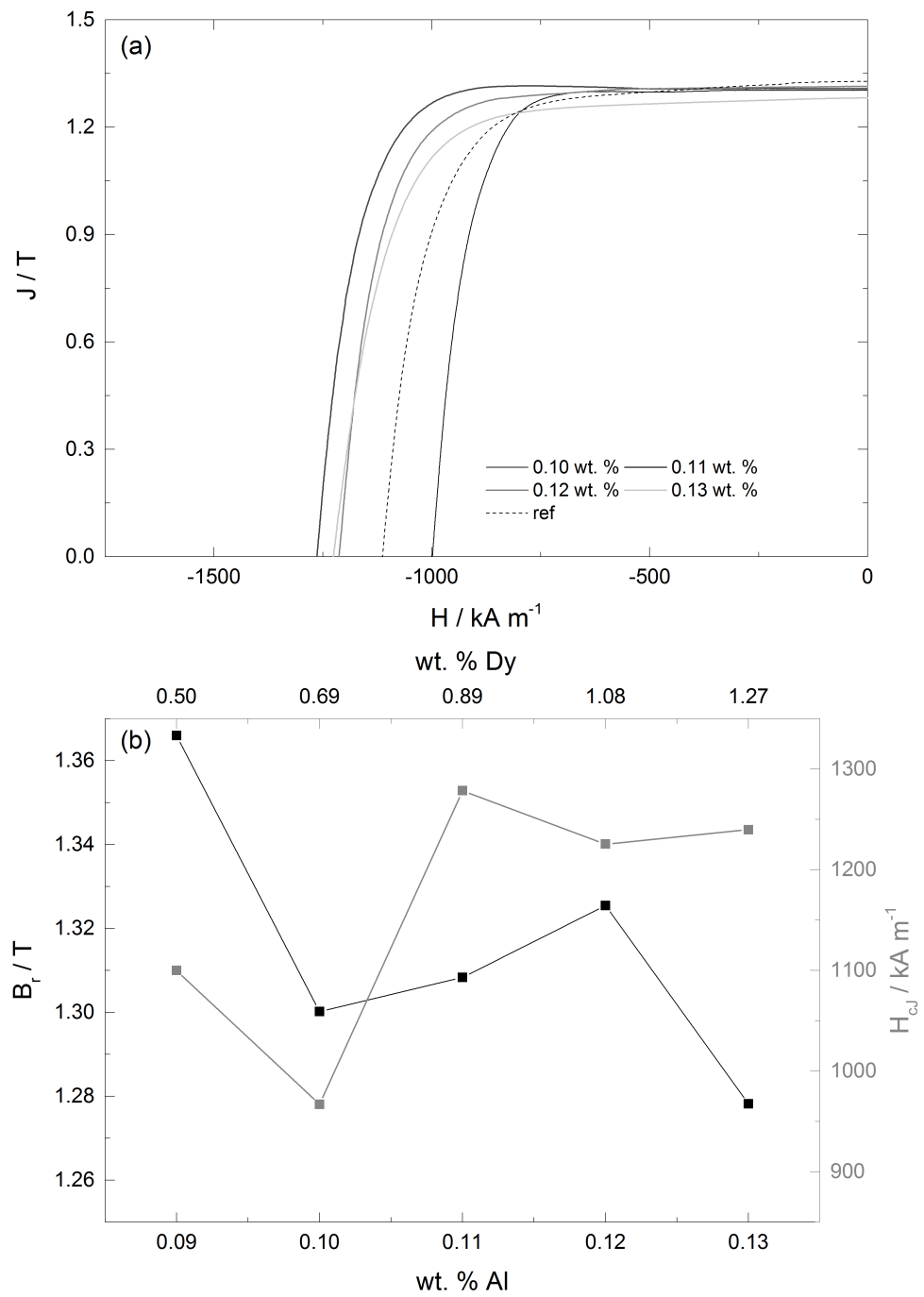


Figure 6.2: Change of magnetic properties after grain boundary diffusion treatment with high-Dy alloys. (a) Demagnetization curves for GBD-treated samples with high-Dy alloys. (b) Changes in  $H_{cJ}$  and  $B_r$  after GBD-treatment with high-Dy eutectic alloys.

## 6.1 Grain Boundary Diffusion of Aluminum-Dysprosium Alloys

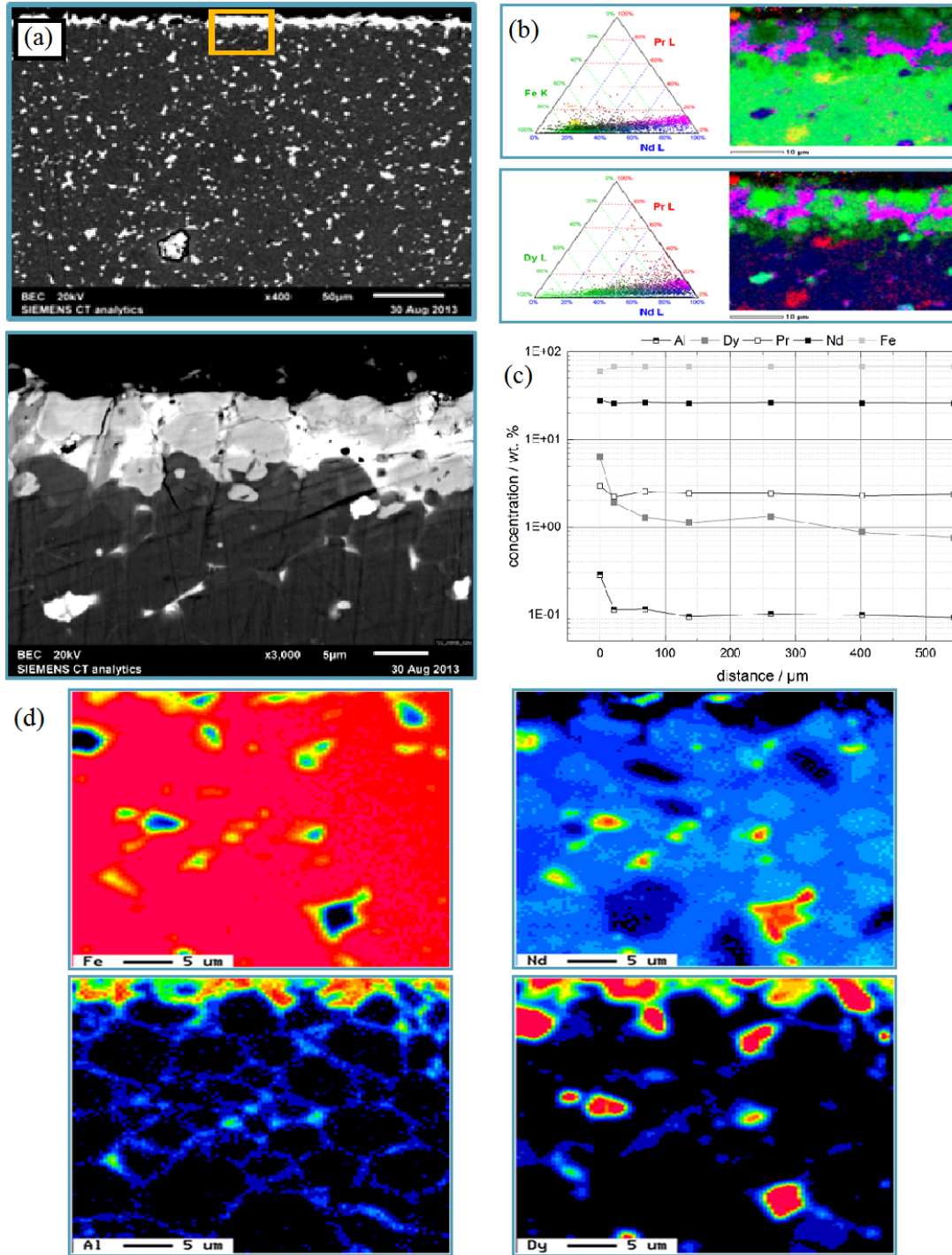


Figure 6.3: Near-surface cross-sectional images and elemental maps of Nd-Fe-B sintered magnet after GBD-treatment with an Al-Dy-alloy consisting of 22 wt. % Al and 78 wt. % Dy. (a) Cross-sectional SEM-BSE image. (b) Quantitative EDX maps. (c) WDX depth-profiles. (d) WDX intensity maps of the cross-sectional near-surface area highlighted in (a).

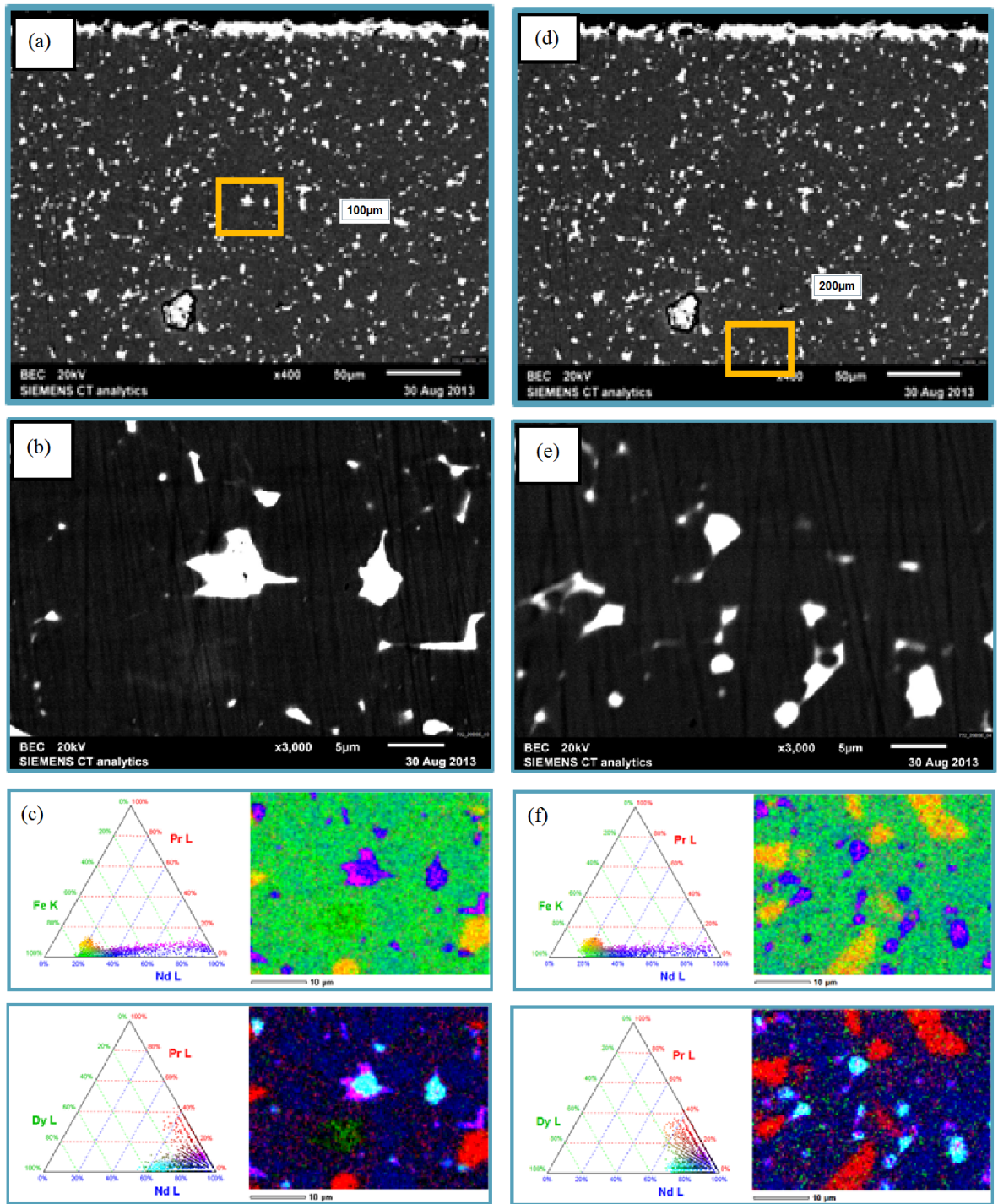


Figure 6.4: Microstructural characterization of Nd-Fe-B sintered magnet after GBD-treatment with Al-Dy-alloy. (a) Cross-sectional BSE-enhanced SEM micrograph. (b) Magnification of the area highlighted in (a). (c) Elemental map of (b) at a distance of 100µm from the coated surface. (d)-(f) show the same features for a distance of 200µm from the surface.

## 7 Material Synthesis

### 7.1 Synthesis of Silver-(I)-Bis(trifluoromethylsulfonyl)imide

Ag[NTf<sub>2</sub>] was prepared following the procedure reported by Vij et. al.<sup>[138]</sup>. It was prepared by reaction of 2.5 g (9.1 mmol) Ag<sub>2</sub>CO<sub>3</sub> (*Sigma Aldrich*) in an aqueous solution of 4.84 g (17.2 mmol) H[NTf<sub>2</sub>] (*Sigma Aldrich*) at room temperature for 2 h. After filtration and drying in vacuum ( pressure < 10<sup>-3</sup> mbar) at 150 °C for 48 h, 6.38 g (95.4 % yield) white powder was obtained.

Elemental analysis - calc: C, 6.19; N, 3.61; S, 16.53; found: C, 5.85; N, 3.42; S, 16.41. Water content ≤ 50 ppm

### 7.2 Synthesis of Copper-(II)-Bis(trifluoromethylsulfonyl)imide

Cu(I) bis(trifluoromethylsulfonyl)imide has been synthesized by electrochemical dissolution of a solid copper electrode in [BMPyr][NTf<sub>2</sub>]<sup>[160]</sup>.

In this case, copper-(II)-bis(trifluoromethylsulfonyl)imide (Cu[NTf<sub>2</sub>]<sub>2</sub>) has been prepared according to procedures reported in the literature<sup>[167]</sup> by using an aqueous solution of 4.2 g (19 mmol) CuCO<sub>3</sub> · Cu(OH)<sub>2</sub> (*Sigma Aldrich*) and 20.3 g (72.2 mmol) H[NTf<sub>2</sub>] (*Sigma Aldrich*). Filtration and drying at 150 °C for 48 h at reduced pressure (< 10<sup>-3</sup> mbar) provided 19.2 g (85.3 % yield) of a pale green powder.

Elemental analysis - calc: C, 7.7; N, 4.49; S, 20.56; found: C, 7.47; N, 4.51; S, 20.52. Water content ≤ 65 ppm.

### 7.3 Synthesis of Dysprosium-(III)-Bis(trifluoromethylsulfonyl)imide

This compound was prepared as described in Ref. [140] but  $\text{Dy}_2(\text{CO}_3)_3$  was used as starting material instead of  $\text{Dy}_2\text{O}_3$  as it resulted in a faster reaction time, in accordance to Ref. [141] as well as a higher yield (96.3 %) than the oxide (89 %). Therefore, 9.0 g (15.6 mmol)  $\text{Dy}_2(\text{CO}_3)_2 \cdot 4\text{H}_2\text{O}$  was gradually added to an aqueous solution of bis-(trifluoromethylsulfonyl)imide acid (25 g, 88.9 mmol) and stirred at 80 °C under reflux for 2 h until no carbonate was consumed. The remaining solid was filtered out and the solvent evaporated in a Schlenk setup under  $< 10^{-3}$  mbar at 200 °C for 41 h to obtain a white solid. Yield: 28.6 g (96.3 %). Elemental analysis - calc: C, 7.19; N, 4.19; S, 19.18; found: C, 7.6; N, 4.23; S, 19.2. Water content  $\leq 50$  ppm.

### 7.4 Synthesis of Terbium-(III)-Bis(trifluoromethylsulfonyl)imide

Terbium-(III)-bis(trifluoromethylsulfonyl)imide ( $\text{Tb}[\text{NTf}_2]_3$ ) was synthesized following the same procedure described for  $\text{Dy}[\text{NTf}_2]_3$  [140,141]. The salt was prepared by the reaction of 8.1 g (15.7 mmol)  $\text{Tb}_2(\text{CO}_3)_3$  with 25 g (88.9 mol)  $\text{H}[\text{NTf}_2]$  in water at 80 °C. After filtration and drying at 200 °C at reduced pressure ( $< 10^{-3}$  mbar). Yield: 28.4 g (96 % yield). Elemental analysis - calc: C, 6.68; N, 3.90; S, 17.83; found: C, 6.69; N, 3.91; S, 17.88. Water content  $\leq 50$  ppm.

### 7.5 Synthesis of Neodymium-(III)-Bis(trifluoromethylsulfonyl)imide

$\text{Nd}[\text{NTf}_2]_3$  was synthesized according to the procedure described in Ref. [142]. Instead of  $\text{Nd}_2\text{O}_3$ ,  $\text{Nd}_2(\text{CO}_3)_3 \cdot 4\text{H}_2\text{O}$  was used as precursor for the same reasons described before for the synthesis of  $\text{Dy}[\text{NTf}_2]_3$ . Therefore 25 g (88.9 mmol) bis(trifluoromethylsulfonyl)imidic acid reacted with a slight excess of  $\text{Nd}_2(\text{CO}_3)_3 \cdot 4\text{H}_2\text{O}$ , 8.4 g (15.6 mmol) in MilliQ quality  $\text{H}_2\text{O}$  at 80 °C. Unreacted carbonate was filtered off and water was removed by evaporation and subsequent drying at 200 °C for 48 h at reduced pressure ( $< 10^{-3}$  mbar). Yield: 26.3 g (90.3 %).

Elemental analysis - calc: C, 6.82; N, 3.98; S, 18.20; found: C, 6.75; N, 4.10; S, 18.17. Water content  $\leq 50$  ppm.

## 7.6 Synthesis of Cobalt-(II)-Bis(trifluoromethylsulfonyl)imide

$\text{CoCO}_3 \cdot \text{H}_2\text{O}$  (6.4 g, 46.8 mmol) was slowly added to a solution of 25 g ( 88.9 mmol) bis(trifluoromethylsulfonyl)imidic acid in deionized water. After stirring at room temperature for 2 h, the blue solution was filtered to remove unreacted carbonate followed by evaporation and vacuum drying (pressure  $< 10^{-3}$  mbar) at 200 °C for 48 h to obtain 5.3 g (87 % yield) pink crystals<sup>[143]</sup>.

Elemental analysis - calc: C, 7.76; N, 4.53; S, 20.71; found: C, 7.54; N, 4.55; S, 20.67. Water content  $\leq 50$  ppm.

## 7.7 Synthesis of Iron-(II)-Bis(trifluoromethylsulfonyl)imide

Metallic iron powder (2.61 g, 46.8 mmol) was suspended in deionized water under  $\text{N}_2$  atmosphere. Bis(trifluoromethylsulfonyl)imidic acid (25 g, 88.9 mmol) was added drop wise. The solution was stirred under reflux for 2 h at 80 °C<sup>[144]</sup>. Unreacted iron was removed by filtration and the solvent was evaporated. Drying at 200 °C for 48 h under reduced pressure ( $10^{-3}$  mbar) resulted in 21.5 g (yield 78.2 % ) of a white powder<sup>[144]</sup>.

Elemental analysis - calc: C, 7.80; N, 4.55; S, 20.81; found: C, 7.56; N, 4.56; S, 20.77. Water content  $\leq 55$  ppm.

## 8 Metal Electrodeposition

The main part of this work focuses on the replacement to the commonly used physical vapor deposition methods used in enhancing the coercivity of Nd-Fe-B sintered magnets.

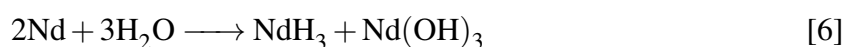
Based on the previous chapters and the failed attempts to plate dysprosium on bare Nd-Fe-B sintered magnets, the plating of a copper adhesion layer was investigated. As will be discussed in the following section, Nd-Fe-B are very prone to oxidation and the presence of moisture causes embrittlement of the alloy. Furthermore, chloride rapidly increases the corrosion of iron, which is present in very high amounts in this type of magnet. For these reasons, this work focuses on the application of chloride-free, air- and water-stable ionic liquids.

### 8.1 Electrodeposition of Copper

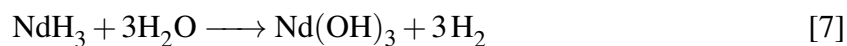
As shown in the previous section, the addition of Cu turned out to have the least negative effect on the coercivity after grain boundary diffusion treatment. Furthermore, it was shown that Dy could be electroplated on copper substrates as a dense layer but not on Nd-Fe-B magnet samples. For this reason, copper was chosen as an adhesion layer before any Dy-electroplating steps.

Electroplating of copper is essential for a multitude of purposes and has become a standard method of large scale use in the micro-electronics industry for production of circuit boards<sup>[145,146]</sup>, case hardening of steel<sup>[147]</sup> and as protective layers for the subsequent application of further coatings<sup>[148]</sup>.

Due to the positive redox potential, copper electrodeposition easily feasible from aqueous electrolytes. However, the substrates to be coated within this study are based on Nd–Fe–B-type alloys. Although the pure rare earth elements Nd, Pr and Dy present in the individual intergranular phases of sintered magnets are very prone to corrosion, the potential difference between the individual phases in the alloy further increase the corrosion rate. In the presence of water, corrosion is attributed to the selective oxidation of the intergranular phases along the grain boundaries<sup>[149]</sup> which decompose according to the following scheme<sup>[150]</sup>:







As shown in [6] and [7] the rare earth reacts to metal hydroxide and metal hydride. The latter is not stable under these conditions and decomposes to a stable hydroxide, releasing hydrogen which embrittles the remaining intergranular phase starting the cycle anew ([8]). Consequently, this selective dissolution of the Nd-rich intergranular phase facilitates the separation of  $\text{Nd}_2\text{Fe}_{14}\text{B}$  grains and granular B-rich phase ( $\text{Nd}_{1+\epsilon}\text{Fe}_4\text{B}_4$ ) from the magnet alloy (“white rust”)<sup>[151]</sup>.

For these reasons, the application of aqueous electrolytes had to be omitted. Cu- plating has been realized from simple deep eutectic solvents (DES) based on quaternary ammonium salts of the type  $\text{R}_1\text{R}_2\text{R}_3\text{R}_4\text{N}^+\text{X}^-$  and hydrogen bond donors (acids, amides, alcohols)<sup>[152–154]</sup>.

Since their introduction, many studies regarding the electrochemical behavior and electrodeposition of copper have been made in zinc and aluminum chloride-based ionic liquids<sup>[155–157]</sup>. The drawbacks of this type of ionic liquids has been discussed in section 2.1.6. Additionally, the presence of  $\text{Cl}^-$ -ions greatly accelerate the corrosion of Nd–Fe–B magnet materials<sup>[158]</sup>. Electroplating from water stable ionic liquids based on tetrafluoroborates  $[\text{BF}_4]^-$ <sup>[159]</sup>, bis(trifluoromethylsulfonyl)imides  $[\text{NTf}_2]^-$ <sup>[160–162]</sup>, trifluoromethanesulfonates  $[\text{OTf}]^-$ <sup>[153]</sup>, dicyanamides  $[\text{DCA}]^-$ <sup>[163]</sup> and salicylates<sup>[164]</sup> have been reported as well. In the studies cited, the use of  $\text{CuCl}$  as a copper source was the most common. While the solubility of this species in chloride-based ionic liquids or ILs with strongly coordinating anions such as dicyanamide, the solubility of  $\text{CuCl}$  or  $\text{CuCl}_2$  in the chloride-free ionic liquids based on weakly coordinating anions is rather low<sup>[160]</sup>. Copper species with the same anion as the IL applied were introduced by anodic dissolution of copper wires<sup>[159–161]</sup>.

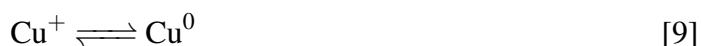
A major drawback of chlorometalate melts is their hydrophilic behavior as well as the undesired presence of  $\text{Cl}^-$  and the resulting evolution of chlorine gas during the electroplating process. Tetrafluoroborate and hexafluorophosphate containing ionic liquids suffer from hydrolysis, therefore the remaining (commercially available) candidates to realize the conditions described in 2.1.6 are trifluoromethylsulfonyl- and bis(trifluoromethylsulfonyl)imide - containing ILs. Although the water uptake by hydrophobic ionic liquids is by no means negligible, the handling of these ILs is by far more manageable than their chlorometalate counterparts. This work focuses on the electrochemistry of halide-free hydrophobic ionic liquids. For better

solubility, copper species with the same anions as the IL were used.

### 8.1.1 Electroplating of Copper from Triflate-based Electrolytes

#### Electrochemistry of Cu(II)-trifluoromethanesulfonate in 1-butyl-3-methylimidazolium trifluoromethanesulfonate

Copper-(II)-trifluoromethanesulfonate ( $\text{Cu}[\text{OTf}]_2$ ) was chosen for further investigation as it represents a halide-free, commercially available source of copper based on a hydrophobic, weakly coordinating anion. Figure 8.1(a) shows a cyclic voltammogram of  $0.1 \text{ mol kg}^{-1}$  solution of  $\text{Cu}[\text{OTf}]_2$  in 1-butyl-3-methylimidazolium trifluoromethanesulfonate ([BMIm][OTf]) recorded on a gold-sputtered quartz electrode. During a scan from the OCP to  $-2.5 \text{ V}$  vs REF to  $1.5 \text{ V}$  and back to OCP in Figure 8.1(a), two redox-pairs are present. The first pair  $a_1/c_1$  presents the following redox-reaction<sup>[160]</sup>:



and the second one, represented by the anodic and cathodic peaks  $a_2$  and  $c_2$ , respectively:



Figure 8.1(b) shows a chronoamperogram and of the system described above. The inset of Figure 8.1b shows the change in series resonance frequency  $f_s$ , which was simultaneously recorded.

By rearrangement of equation (3.9) and resolving into  $\frac{M_x}{z}$ , an equivalent mass change per mole of electrons (mpe) can be calculated<sup>[165]</sup>:

$$mpe = - \left( \frac{\Delta f}{\Delta Q} \right) \frac{F}{C_f} \quad (8.1)$$

where  $\Delta f/\Delta Q$  represents the slope in the plot of the change in frequency vs the passed charge. This plot is presented in Figure 8.1(c). The slope was calculated to be  $(0.0736 \pm 0.0001) \text{ MHz C}^{-1}$  by linear fitting of the data (red line), from which a mpe of  $28.9 \text{ g mol}^{-1}$  can be extracted. This is close to the theoretical mpe of  $31.8 \text{ g mol}^{-1}$  for copper. A comparison of the theoretical deposited and the experimentally deposited mass (shown in the inset in Figure 8.1(c)) shows a current efficiency of 91 %, which explains the low mpe value.

### 8.1 Electrodeposition of Copper

Copper was potentiostatically electroplated from a  $0.25 \text{ mol kg}^{-1}$  solution at  $100^\circ\text{C}$  for 900 s at  $-1 \text{ V}$  (passed charge:  $-0.62 \text{ C}$ ) to obtain Cu-coated Nd-Fe-B-samples. A current efficiency on this substrate was calculated by comparison of the theoretical deposited mass and the mass change of the sample after plating. The deposits were cleaned of any electrolyte residue with dry acetone and analyzed by SEM micrography and EDX analysis, which are shown in Figure 8.2(a) and Figure 8.2(b). This deposition conditions delivered a granular structure with deposits of about  $50 \mu\text{m}$ . The corresponding EDX pattern confirms the deposition of copper and minimal impurities of F.

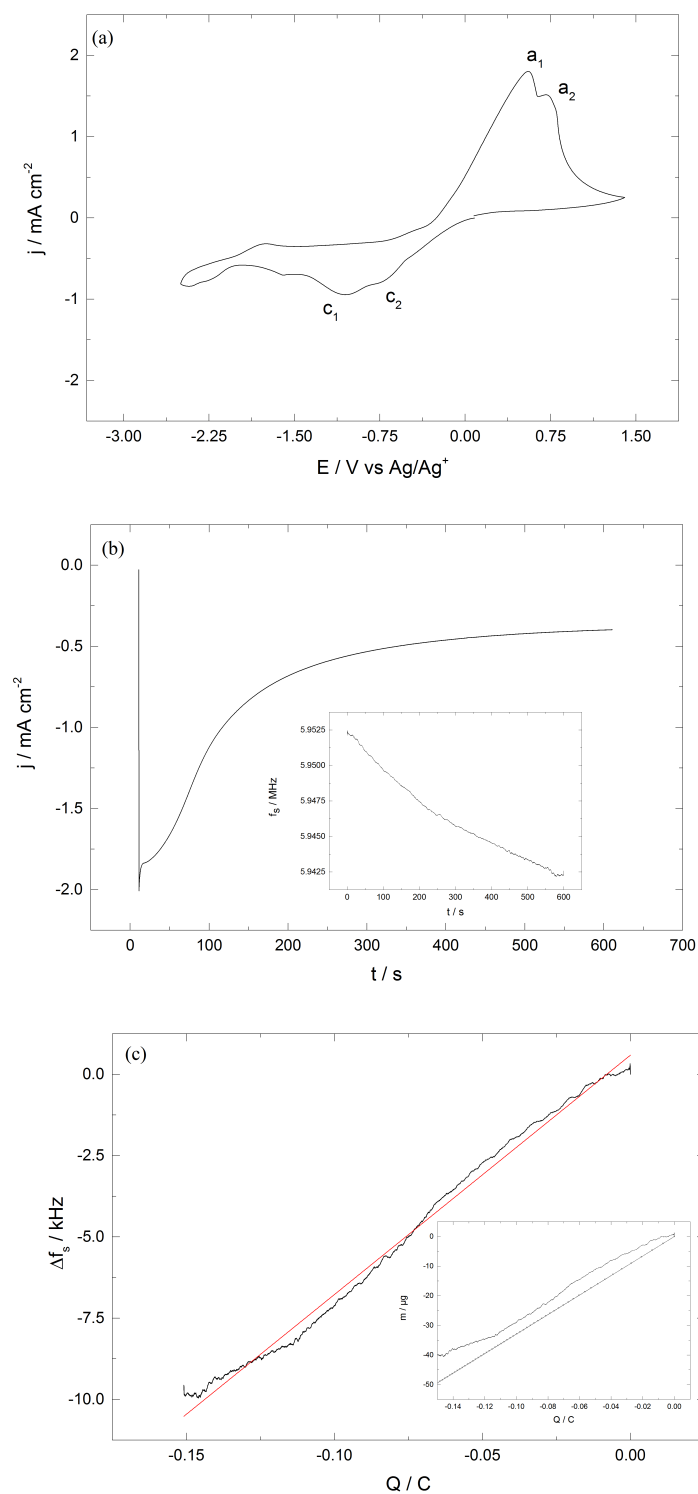


Figure 8.1: (a) Cyclic voltammogram and of  $0.1 \text{ mol kg}^{-1} \text{ Cu[OTf]}_2$  in  $[\text{BMIm}][\text{OTf}]$  on Au-quartz electrode  $25^\circ\text{C}$  recorded with  $5 \text{ mV s}^{-1}$ . (b) Chronoamperogram of  $0.1 \text{ mol kg}^{-1} \text{ Cu[OTf]}_2$  in  $[\text{BMIm}][\text{OTf}]$  on Au-quartz electrode  $25^\circ\text{C}$  recorded at  $-0.4 \text{ V}$  for 600 s. (c) Change of resonance frequency with passed charge from the CA in (b).

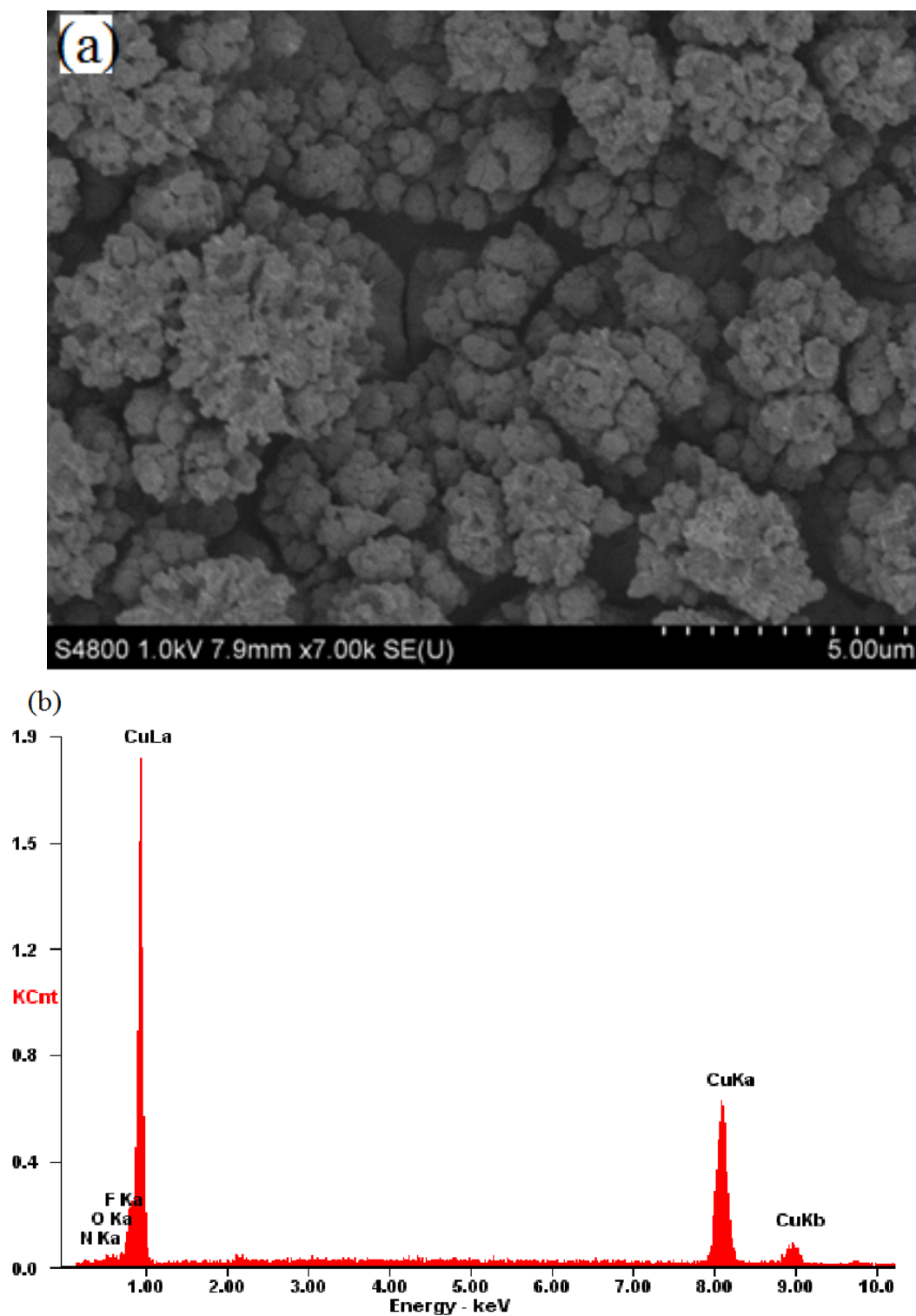


Figure 8.2: (a) SEM micrograph (b) EDX pattern of Cu deposited from  $0.25 \text{ mol kg}^{-1}$   $\text{Cu}[\text{OTf}]_2$  in  $[\text{BMIm}][\text{OTf}]$  on Nd-Fe-B substrate  $100^\circ\text{C}$ .

### Electrochemistry of Cu(II)-trifluoromethanesulfonate in 1-butyl-1-methylpyrrolidinium trifluoromethanesulfonate

A system based on the 1-butyl-1-methylpyrrolidinium cation was considered as well for its large cathodic stability and the commercial availability of 1-butyl-1-methylpyrrolidinium trifluoromethanesulfonate ([BMPyr][OTf]). Furthermore, the variation of the cation or anion have been ascribed to influence the morphology of the deposits as well<sup>[166]</sup>. A saturated solution of Cu[OTf]<sub>2</sub> in [BMPyr][OTf] has been reported by Zein El Abedin et al. for the deposition of nanocrystalline copper<sup>[160]</sup>. The electrochemical behavior of the Cu species was determined to be quasi-reversible and diffusion controlled at room temperature.

The electroplating process was investigated by the fis-QCM. The cyclic voltammogram shown in Figure 8.3(a) is as reported in Ref. [160]. The potential was scanned from OCP to  $-3$  V to  $1.5$  V back to OCP. Two reduction scans can be recorded during the cathodic scan, namely  $c_1$  and  $c_2$ .  $c_1$  can be ascribed to the bulk deposition of Cu<sup>0</sup>. While  $c_2$  is correlated to the underpotential deposition of copper, see Ref. [160]. However, chronoamperometry at the peak potential  $E_{c2}$  did not show a decrease in  $\Delta f_s$ , in disagreement with this assumption. A chronoamperogram of  $0.25 \text{ mol kg}^{-1}$  Cu[OTf]<sub>2</sub> in [BMPyr][OTf] recorded for 600 s at  $25^\circ\text{C}$  at  $-0.4$  V on a gold electrode is shown in Figure 8.3(b) and a complementary plot of the change in frequency with time is shown in the inset graph. The theoretical and the experimentally deposited mass are plotted in the inset of Figure 8.3(c). The theoretical mass calculated from the passed charge in the chronoamperometric experiment is very close to the experimental value (current efficiency 99.9 %). From the plot of the  $\Delta f_s$  against the passed charge (shown in Figure 8.3(c)) an mpe of  $31.7 \text{ g mol}^{-1}$  can be calculated.

A SEM micrograph of the deposits received after potentiostatic deposition ( $E = -1$  V,  $t = 900$  s,  $Q = -0.58$  C, current efficiency: 86 %) of a  $0.25 \text{ mol kg}^{-1}$  solution of Cu[OTf]<sub>2</sub> in [BMPyr][OTf] at  $100^\circ\text{C}$  is shown in Figure 8.4(a). A granular microstructure similar to the morphology of samples produced from [BMIm][OTf] can be observed for the cleaned sample. The influence of the cation on nucleation behavior of Al deposits deposited from mixtures of AlCl<sub>3</sub> in [EMIm][NTf<sub>2</sub>] and [BMPyr][NTf<sub>2</sub>] was reported by Moustafa et al. and ascribed to the different charge distribution in the [EMIm<sup>+</sup>] and [BMPyr<sup>+</sup>] and their influence on the double layer<sup>[166]</sup>. It can be assumed that the effect of the elevated temperature is more significant than the effect of the cation on the morphology of the deposits. EDX analysis shows deposition of copper and minor impurities of fluorine and sulfur as shown in Figure 8.4(b).

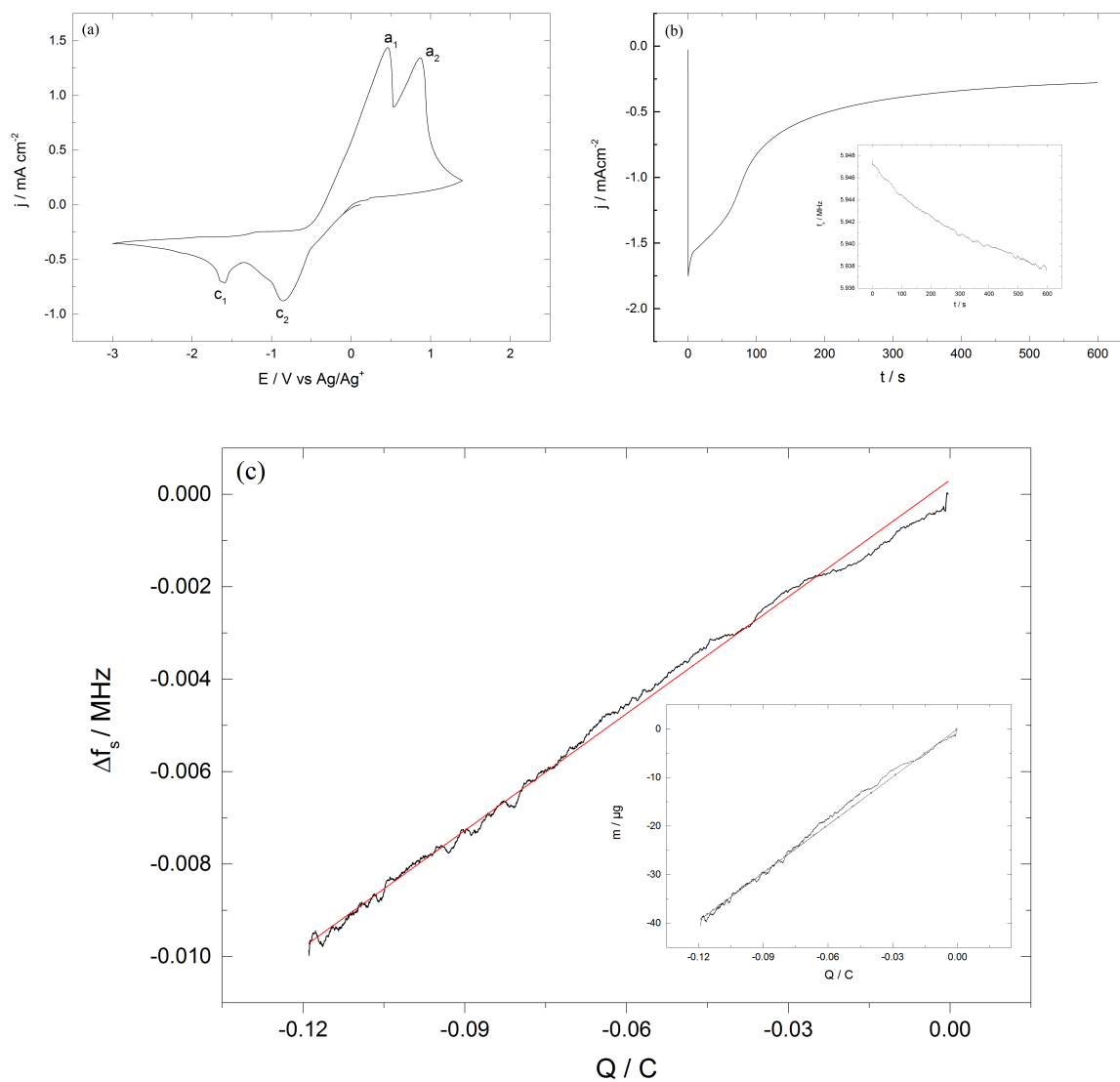


Figure 8.3: a) cyclic voltammogram and b) chronoamperogram of  $0.1 \text{ mol kg}^{-1} \text{ Cu[OTf]}_2$  in  $[\text{BMIM}][\text{OTf}]$  on Au-quartz electrode  $25^\circ\text{C}$ . c) change of resonance frequency with charge.

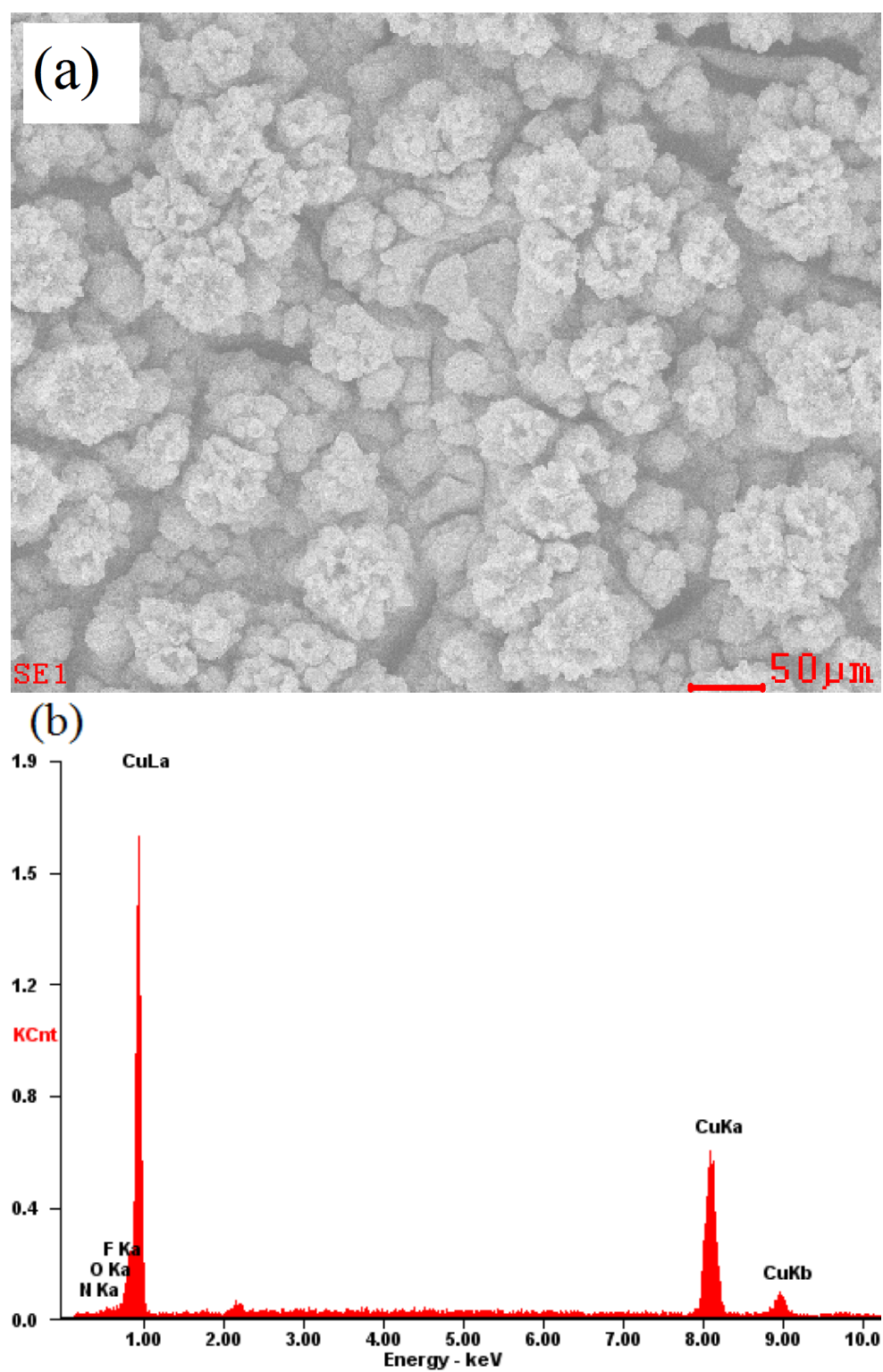


Figure 8.4: (a) SEM micrograph (b) EDX pattern of Cu deposited from  $0.25 \text{ mol kg}^{-1}$   $\text{Cu}[\text{OTf}]_2$  in  $[\text{BMPyr}][\text{OTf}]$  on Nd-Fe-B substrate  $100^\circ\text{C}$  under potentiostatic conditions ( $-1 \text{ V}$  vs REF). Passed charge  $-0.58 \text{ C}$ .



### 8.1.2 Electrodeposition from a bis(trifluoromethylsulfonyl)imide-based electrolyte

#### Electrochemistry of Cu(II)-bis(trifluoromethylsulfonyl)imide in 3-butyl-1-methylimidazolium bis(trifluoromethylsulfonyl)imide

Due to the favorable properties of the weakly coordinating, hydrophobic NTf<sub>2</sub><sup>-</sup> anion, an ionic liquid of with this anion was chosen as well. In this system, home made Cu[NTf<sub>2</sub>]<sub>2</sub> served as the Cu-source.

Figure 8.5(a) shows a cyclic voltammogram of 0.1 mol kg<sup>-1</sup> Cu[NTf<sub>2</sub>]<sub>2</sub> in [BMIm][NTf<sub>2</sub>] recorded at a scan speeds of 5 mV s<sup>-1</sup> at room temperature on a gold electrode. The potential was scanned from OCP in the cathodic direction to -2.5 V to 1.4 V back to OCP. As previously observed for the triflate-based systems, two redox-processes can be identified as the plating and stripping of copper (a<sub>1</sub>/c<sub>1</sub>) and oxidation/ reduction of monovalent Cu<sup>+</sup> to Cu<sup>2+</sup> (a<sub>2</sub>/c<sub>2</sub>), respectively. The results of a chronoamperometric experiment of this system conducted at -0.4 V at 25 °C for 570 s is presented in Figure 8.5(b). Simultaneously. the frequency  $f_s$  with respect to time was recorded with the fis-EQCM and is shown in the inset in Figure 8.5(b), where a drop in the frequency can be observed, corroborating the plating of Cu at the conditions applied.

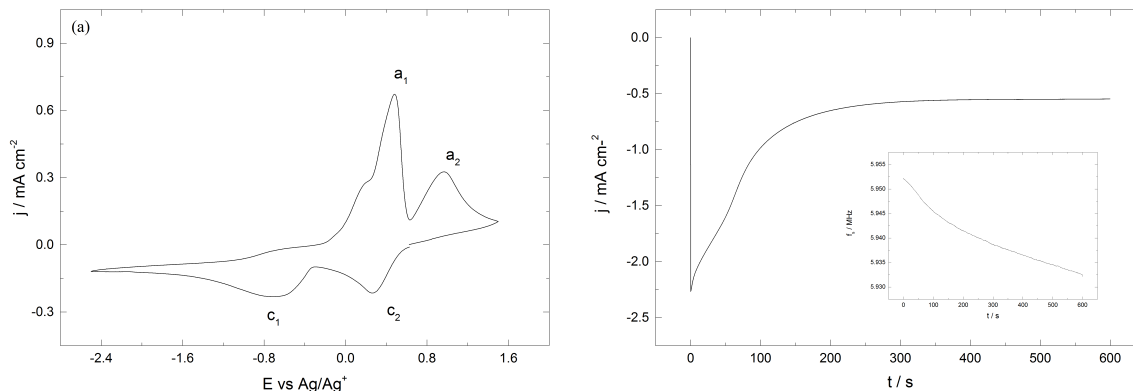


Figure 8.5: (a) cyclic voltammogram and (b) chronoamperogram of 0.1 mol kg<sup>-1</sup> Cu[NTf<sub>2</sub>]<sub>2</sub> in [BMIm][NTf<sub>2</sub>] on Au-quartz electrode 25 °C

Cu-plated Nd-Fe-B samples were produced by potentiostatic deposition at 100 °C for 900 s at -1 V, (charge passed: -0.6 C). This experiment resulted in a current efficiency of 87 %. Figure 8.6(a) shows a SEM micrograph a copper coated sample. The morphology observed for this sample is granular with deposits of about 40 μm diameter. The color of these coatings

## 8 *Metal Electrodeposition*

was slightly darker than the ones produced with triflate based electrolytes. EDX showed the presence of a thick copper layer with minor impurities of F and C from the ionic liquid.

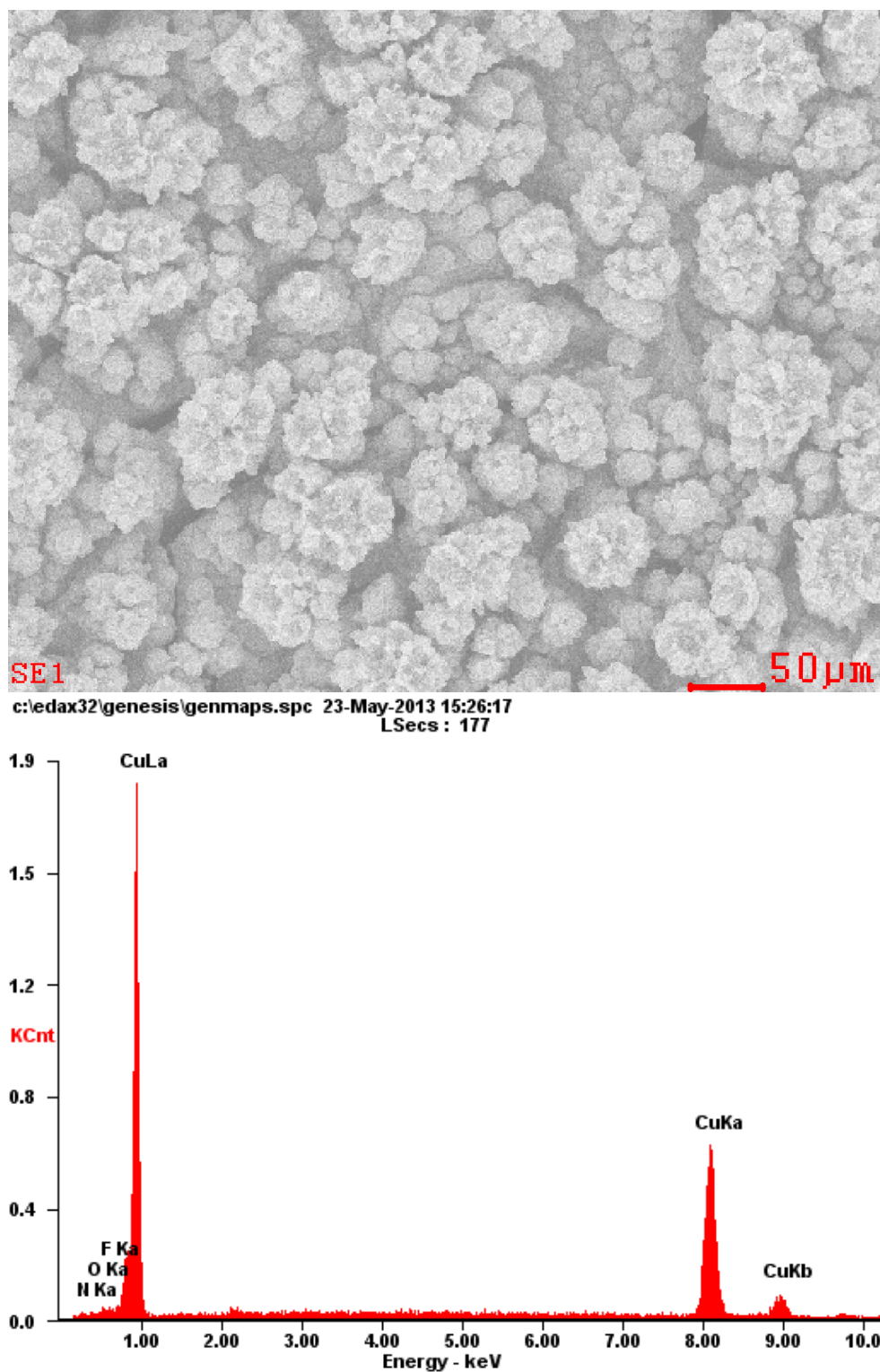


Figure 8.6: (a) SEM micrograph (b) EDX pattern of Cu deposited from  $0.25 \text{ mol kg}^{-1}$   $\text{Cu}[\text{OTf}]_2$  in  $[\text{BMPyr}][\text{OTf}]$  on Nd-Fe-B substrate  $100^\circ\text{C}$  under potentiostatic conditions ( $-0.1\text{V}$  vs  $\text{Ag}/\text{Ag}^+$ ). Passed charge  $-0.6 \text{ C}$ .

## 8.2 Electrodeposition of Dysprosium

The economical importance of dysprosium has come a long way from niche markets (magnetostrictive materials such as Terfenol, dopants for lasers, neutron catchers in fission reactors<sup>[168,169]</sup>) to an important and newly scarce resource as a component of temperature-stable high-performance permanent magnets. The rising importance of this element is mirrored by an increasing total world consumption, from 188 tonnes in 2010 to an estimated 331 to 864 t by 2015<sup>[170]</sup>. As a lanthanoid, dysprosium has a very negative standard potential of -2,3<sup>[104]</sup> and can't be deposited from aqueous media. Several studies on dysprosium deposition from organic media from  $\text{Dy}(\text{NO}_3)_3$  have been reported<sup>[171,172]</sup> and from  $\text{Dy}[\text{OTf}]_3$  in DMF by Lodermeier<sup>[14]</sup>.

Electroplating of reactive metals is quite common from high-temperature melts, the electrochemistry of dysprosium has been reported by several authors. Castrillejo et al. have investigated the deposition of Dy from  $\text{DyCl}_3$  in a  $\text{LiCl/KCl}$  eutectic melt at temperatures of 400 °C and above<sup>[173]</sup>. Saïla et al. have investigated  $\text{DyF}_3$  in a  $\text{LiF/CaF}_2$  melt in the temperature range of 840 °C to 930 °C<sup>[174]</sup>. With the intent in mind to promote sustainable nuclear fuel cycles, the efficient separation of actinoides and lanthanoids in spent nuclear fuel has been recently investigated in high-temperature  $\text{LiCl/KCl}$  melts as well<sup>[175–177]</sup>.

Recently, the electrochemistry of dysprosium in air- and water-stable, tailor-made phosphonium-based ionic liquid triethylpentylphosphonium bis(trifluoromethylsulfonyl)imide has been reported by Kurachi and Kazama<sup>[140,178]</sup>.

### 8.2.1 Electrodeposition from Solutions Based on Dysprosium-(III)-Halides

#### Electrochemistry of Dysprosium-(III)-Chloride in 1-Butyl-3-methylimidazolium Tetrafluoroborate

Pyonghun et al. reported the deposition of Dy metal from  $0.01 \text{ mol l}^{-1}$   $\text{DyCl}_3$  in 1-ethyl-1-methylimidazolium tetrafluoroborate ( $[\text{EMIM}][\text{BF}_4]$ )<sup>[179]</sup>. An intent to reproduce the results reported failed. Figure 8.7 shows a cyclic voltammogram of a  $10 \text{ mmol l}^{-1}$  solution of  $\text{DyCl}_3$  in  $[\text{EMIM}][\text{BF}_4]$ . The potential was scanned from the OCP to -3.2 V to 1.8 V and back to OCP. During the cathodic scan, starting at -2.5 V an increasing cathodic current is visible which can be ascribed to the reduction of  $\text{Dy}^{3+}$ . From the nucleation loop, an overvoltage of about 0.5 V can be estimated, consistent with the results reported by Pyonghun et al. The anodic peak can be partially be ascribed to the evolution of chlorine gas and the stripping of

the Dy. Attempts to plate Dy under potentiostatic and galvanostatic conditions failed. No deposition of Dy was observed upon SEM or EDX analysis even at temperatures as high as 150 °C. A variation of the ionic liquid for a more stable one, in this case [BMIM][BF<sub>4</sub>], did not show any improvement. Any further attempts to plate dysprosium from this system were not performed.

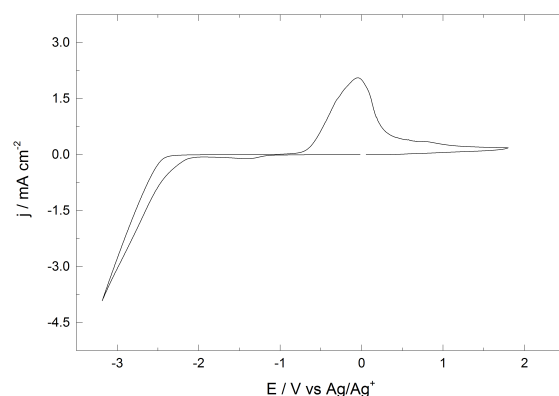


Figure 8.7: Cyclic voltammogram of 0.01 mol l<sup>-1</sup> DyCl<sub>3</sub> in EMIMBF<sub>4</sub> at 25 °C.

### Electrochemistry of Dysprosium-(III)-Chloride in 1-Butyl-1-methylpyrrolidinium Dicyanamide

Some of the benefits of ionic liquids based on the dicyanamide anion are low viscosity as well as high conductivities. DCA-based ionic liquids show very good solubilities to metal salts due to the good ligand properties caused by the Lewis basic character of the DCA-anion<sup>[180]</sup>. For this reasons a representative of this class, namely 1-butyl-1-methylpyrrolidinium dicyanamide ([BMPyr][DCA]) was chosen as a solvent. Figure 8.8(a) shows the cathodic branch of cyclic voltammograms of 0.1 mol kg<sup>-1</sup> at room temperature (straight line) and at 150 °C (dashed line). A rising cathodic current density is visible starting at -2.4 V and a cathodic peak is reached at -2.85 V at room temperature. The cathodic peak current increases and shifts to more positive potentials when high temperatures are applied. A chronoamperogram for a concentration of 0.5 mol kg<sup>-1</sup> is shown in Figure 8.8(b) recorded at -2.0 V at 150 °C for 5500 s. Although negative current densities were recorded, no deposits could be observed upon SEM and EDY analysis under these conditions. After all potentiostatic experiments, a strong smell of chlorine could be noticed when the deposition cell was opened. Attempts to obtain deposits under potentiostatic conditions at high temperatures up to 150 °C and high concentrations (> 0.5 mol kg<sup>-1</sup>) failed as well.

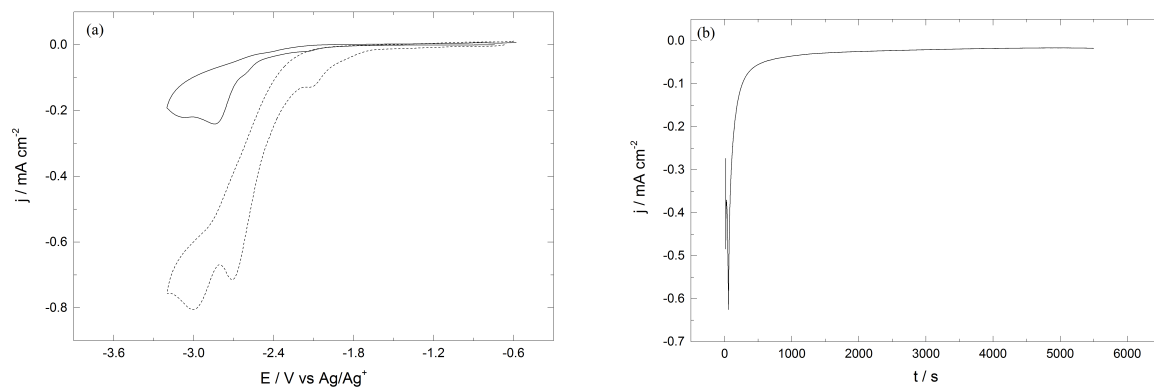


Figure 8.8: (a) Cyclic voltammograms of  $0.1 \text{ mol kg}^{-1}$   $\text{DyCl}_3$  in  $[\text{BMPyr}][\text{DCA}]$  at  $25^\circ\text{C}$  (straight line) and  $150^\circ\text{C}$  (dashed line) recorded with a scan speed of  $5 \text{ mV s}^{-1}$ . (b) Chronoamperogram of  $0.5 \text{ mol kg}^{-1}$   $\text{DyCl}_3$  in  $[\text{BMPyr}][\text{DCA}]$  at  $150^\circ\text{C}$ . WE: Au, CE: Dy.

### 8.2.2 Electrodeposition from Solutions Based on Dysprosium-(III)-trifluoromethanesulfonate

Metal trifluoromethanesulfonate salts have been widely studied as green catalysts due to their superior performance compared to conventional ones. Compounds of the type  $\text{Ln}[\text{OTf}]_3$  have shown to be highly selective (fewer by-products) and also allow the use of non-chlorinated reagents at mild reaction conditions while being less toxic than many transition metal based catalysts<sup>[68,181–184]</sup>. However, electroplating from OTf-based metal salts and ionic liquids is fairly uncommon. Only few attempts to study the electrochemistry of triflate metal salts have been reported, even less so in ionic liquids containing this anion.  $\text{Mg}[\text{OTf}]_2$ <sup>[185–188]</sup> has been studied as potential salt for magnesium ion batteries. Only a few lanthanoids, namely Yb, Gd and Y in their triflate forms have been studied in [OTf]- based ionic liquids by Glukhov et al.<sup>[189]</sup>. In this study, the possibility of their deposition from different ionic liquids 1-butyl-2,3-dimethylimidazolium trifluoromethanesulfonate ([BMMIm][OTf]), tributylmethylammonium trifluoromethanesulfonate ([Bu<sub>3</sub>MN][OTf]) and [BMPyr][OTf] at 100 °C was investigated. The successful plating of all those metals is claimed, as black deposits are formed on copper after deposition under potentiostatic and galvanostatic conditions. However, no further proof in the form of surface/composition analysis for the deposition of metallic layers was given by the authors. Lodermeier investigated the deposition of dysprosium from dysprosium-(III)-trifluoromethanesulfonate ( $\text{Dy}[\text{OTf}]_3$ ) in 1-ethyl-3-methylimidazolium trifluoromethanesulfonate ([EMIm][OTf]). Attempts to plate Dy from this electrolyte at room temperature failed, even after the addition of DMF to increase the conductivity / decrease viscosity<sup>[13]</sup>. Due to the commercial availability of dysprosium triflate, an attempt to plate dysprosium from different triflate-based systems was made in this work as well.

The more stable yet still low-viscous and highly conductive ionic liquid [BMIm][OTf] was applied. Figure 8.9 shows the cathodic branch of cyclic voltammograms of a 0.2 mol kg<sup>-1</sup> (0.23 mol l<sup>-1</sup>) solution of  $\text{Dy}[\text{OTf}]_3$  in [BMIm][OTf] recorded on a gold-sputtered quartz crystal electrode with a scan speed of 5 mV s<sup>-1</sup> at room temperature (black curve) and at 150 °C (gray curve). The potential was cycled from the OCP to -2.5 back to OCP. The onset of a cathodic current starts at about -0.9 V vs. REF, which can be assigned to the reduction of  $\text{Dy}^{3+}$ . Cathodic peak current density of this system increases at higher temperatures and the peak potential shifts to more positive values, which is caused by the enhanced mobility and a reduced overpotential.

The diffusion coefficient of  $\text{Dy}^{3+}$  was determined by semi-integral analysis of the voltammogram. This technique was first described by Oldham in the 70's<sup>[190–192]</sup>. Here, the semi-

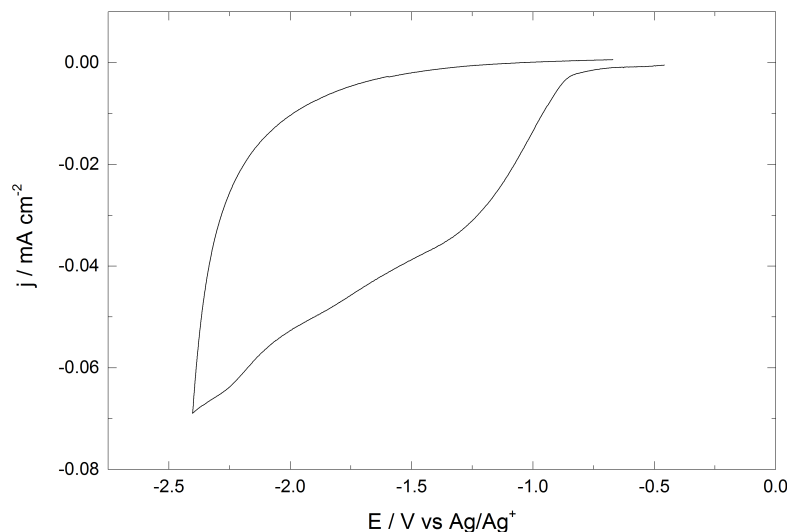


Figure 8.9: Cathodic branch of cyclic voltammograms of 0.23 mol l<sup>-1</sup> Dy[OTf]<sub>3</sub> in [BMIm][OTf] at 25 °C (black curve) 150 °C (gray curve).

integral of the current with time  $m(t)$  is given by the following equation<sup>[29,194]</sup>:

$$m(t) = \frac{d^{-1/2}}{dt^{-1/2}} i(t) \quad (8.2)$$

The result of this operation produces a quantity  $m(t)$  intermediate between the current  $i(t)$  and the charge  $Q(t)$ . Furthermore, the diffusion coefficient can be calculated from this neopolarogram as follows:

$$m^* = zFAc\sqrt{D} \quad (8.3)$$

where  $m^*$  is the value of  $m(t)$  at the end of the ramp in the polarogram. The following RL0<sup>1</sup> algorithm was used to calculate the values of  $m(t)$ <sup>[194]</sup>:

$$m(t) = \sqrt{\frac{\Delta t}{\pi}} \sum_{x=1}^{t/\Delta t} [i(x\Delta t) + i(x\Delta t - \Delta t)] \left[ \sqrt{\frac{t}{\Delta t} - x + 1} - \sqrt{\frac{t}{\Delta t} - x} \right] \quad (8.4)$$

From the recorded current-time transients, the current values  $i(0)$ ,  $i(\Delta t)$ ,  $i(2\Delta t)$ , ...,  $i(x\Delta t)$ ,  $i(t)$  can be read off at evenly spaced time intervals  $\Delta t$ . The CV for this system and the corresponding plot  $m(t)$  vs.  $E$  is shown in Figure 8.10b(a). According to (8.3) the diffusion coefficient was determined to be  $1.76 \times 10^{-9} \text{ cm}^2 \text{ s}^{-1}$ . Diffusion coefficients in the order of

<sup>1</sup>The RL0 algorithm is derived from the Riemann-Liouville definition of semi-integration and allows the numerical calculation of fractional integrals. It becomes exact as  $t/\Delta$  approaches infinity<sup>[194]</sup>.



$1 \times 10^{-12} \text{ cm}^2 \text{ s}^{-1}$  are reported for different electrode materials for the divalent  $\text{Mg}^{2+}$  in the system  $\text{Mg}[\text{OTf}]_2/[\text{BMIm}][\text{BF}_4]$  at room temperature<sup>[185]</sup> Unfortunately, no diffusion coefficients for Y, Gd or Yb are mentioned in Ref. [189] to draw comparisons.

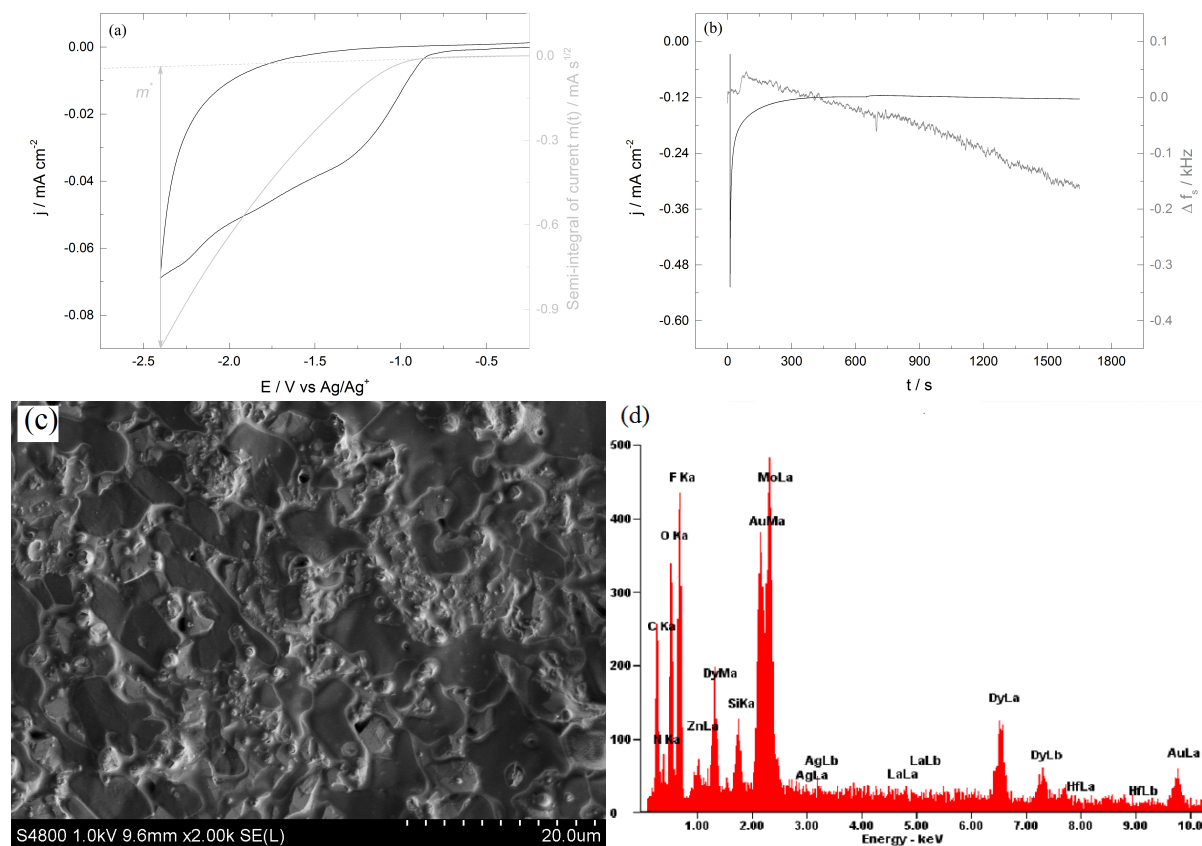


Figure 8.10: (a) Cathodic branch of the cyclic voltammogram of  $0.23 \text{ mol l}^{-1} \text{ Dy}[\text{OTf}]_3$  in  $[\text{BMIm}][\text{OTf}]$  (black curve) and convoluted curve (gray curve). AE: Au, CE: Dy. (b) Chronoamperogram of the same system recorded at  $150^\circ\text{C}$  at  $-2.0 \text{ V}$  (black curve) and change in resonance frequency during the CA experiment (grey curve). (c) SEM micrograph for coatings produced in galvanostatic mode from  $0.23 \text{ mol l}^{-1} \text{ Dy}[\text{OTf}]_3$  in  $[\text{BMIm}][\text{OTf}]$  at  $150^\circ\text{C}$ .  $j = 0.25 \text{ mA cm}^{-2}$ ,  $t = 30 \text{ min}$ . (d) Corresponding EDX pattern.

Electroplating was attempted from this system at  $150^\circ\text{C}$ . Although higher temperatures should further facilitate reduction kinetics, plating experiments showed no improvement<sup>2</sup>. Figure 8.10(b) shows a chronoamperogram of this solution at  $150^\circ\text{C}$ . The inset shows the shift in resonance frequency  $f_s$  recorded simultaneously during the CA-experiment. Cathodic current densities are recorded at  $-2.0 \text{ V}$  and a constant decrease of the resonant frequency is

<sup>2</sup>Despite the thermal stability of the used components far exceeds  $200^\circ\text{C}$ , the deposition solution changed its color to dark brown after the deposition experiments. The adhesion of the coatings suffered as well, which affected the coating thickness. This behavior can be explained by a reduction of the electrochemical window at higher temperatures

observable as well, indicating the plating of Dy metal.

Dy-coatings were obtained after deposition in galvanostatic mode with a current density of  $-0.25 \text{ A cm}^{-2}$  on an Au electrode for 2 h. A SEM micrograph is shown in Figure 8.10(c). As seen in the micrograph, it appears that the coating of is only partial. This assumption is confirmed by EDX analysis, as shown in Figure 8.10(d). Besides a signal for dysprosium, the coating shows F, S, N, C and O impurities and rather large signals of Au coming from the substrate. Variation of deposition parameters had no significant effect on the coating quality.

### 8.2.3 Electrodeposition from Solutions Based on Dysprosium-(III) Bis(trifluoromethylsulfonyl)imides

Ionic liquids based on the  $[\text{NTf}_2]^-$ -anion are highly conductive, low viscous, as well as thermally and electrochemically stable, it is for these reasons that these types of ionic liquids have found profound interest in research<sup>[193]</sup>. To increase the solubility of the dysprosium species in the bis(trifluoromethylsulfonyl)imide ionic liquids, an analogous dysprosium-(III)-bis(trifluoromethylsulfonyl)imide ( $\text{Dy}[\text{NTf}_2]_3$ ) salt was synthesized.

The electrochemistry of  $\text{Dy}[\text{NTf}_2]_3$  has been studied by Kurachi<sup>[140]</sup> and more recently by Kazama<sup>[178]</sup>. In those studies the ionic liquid applied was triethyl-pentylphosphonium bis(trifluoromethylsulfonyl)imide ( $[\text{P}_{2225}][\text{NTf}_2]$ ). For this study the commercially available 1-butyl-1-methylpyrrolidinium bis(trifluoromethylsulfonyl)imide ( $[\text{BMPyr}][\text{NTf}_2]$ ) was applied, as it shows a very wide electrochemical window as well as low viscosity.

#### Electrochemistry of Dysprosium-(III)-bis(trifluoromethylsulfonyl)imide in 1-Butyl-3-methylimidazolium bis(trifluoromethylsulfonyl)imide

As the  $[\text{BMIm}][\text{OTf}]$  ionic liquid showed first promising results,  $[\text{OTf}]^-$  was substituted for the  $[\text{NTf}_2]^-$ . Figure 8.11 shows a cyclic voltammogram of  $0.2 \text{ mol kg}^{-1} \text{ Dy}[\text{NTf}_2]_3$  in  $[\text{BMIm}][\text{NTf}_2]$ . An increasing cathodic current density is visible starting at  $-1.6 \text{ V}$  vs. REF. which can be assigned to the reduction of  $\text{Dy}^{3+}$ . As no other peaks are visible, it is assumed that no intermediate products are formed in accordance to Ref. [140]. The small anodic current density starting at about  $-0.2 \text{ V}$  vs. REF are assumed to originate from partial oxidation of decomposition products from the cathodic scan.

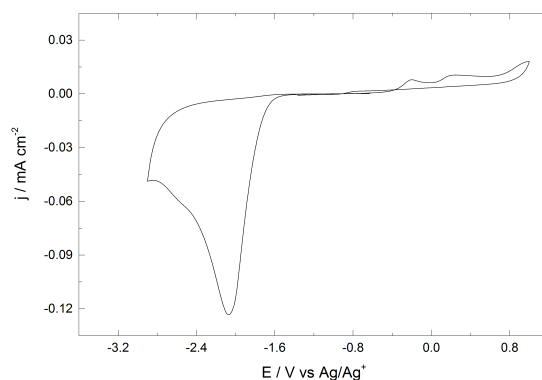


Figure 8.11: Cyclic voltammogram of  $0.2 \text{ mol kg}^{-1} \text{ Dy}[\text{NTf}_2]_3$  in  $[\text{BMIm}][\text{NTf}_2]$  at  $25^\circ\text{C}$  recorded on a gold electrode with  $v = 5 \text{ mV s}^{-1}$ . WE: Au, CE: Dy.

Potentiostatic as well as galvanostatic deposition on copper electrodes at  $150^\circ\text{C}$  resulted in

black, non-adhesive deposits which could not be submitted to composition analysis.

This result could be assigned to the cathodic breakdown of the [BMIm<sup>+</sup>] cation as shown by the rather large amounts of impurities in the deposits from Dy[OTf]<sub>3</sub> / [BMIm][OTf]. For this reason the more stable pyrrolidinium cation [BMPyr<sup>+</sup>] was applied.

### Electrochemistry of Dysprosium-(III)-bis(trifluoromethylsulfonyl)imide in 1-Butyl-1-methylpyrrolidinium bis(trifluoromethylsulfonyl)imide

In contrast to the triflate-based ionic liquid [BMPyr][OTf], the [NTf<sub>2</sub>]-based [BMPyr][NTf<sub>2</sub>] was able to dissolve large amounts of the triflamide dysprosium salt.

A series of cyclic voltammograms of 0.147 mol l<sup>-1</sup> was recorded at room temperature with scan speeds of 5 mV s<sup>-1</sup>, 10 mV s<sup>-1</sup>, 25 mV s<sup>-1</sup> and 50 mV s<sup>-1</sup> on gold sputtered quartz crystal electrodes. The corresponding CVs are shown in Figure 8.12(a). A rise of the peak current densities and a shift of the peak potentials is observable for increasing scan rates. A series of CVs recorded at temperatures of 25 °C, 50 °C, 100 °C and 150 °C at a scan rate of 25 mV s<sup>-1</sup> is shown in Figure 8.12(b). An increase of the mobility of Dy-ions as well as a reduction of nucleation overvoltages lead to higher current densities and a shift of  $E_{pc}$  to less negative values with higher temperatures.

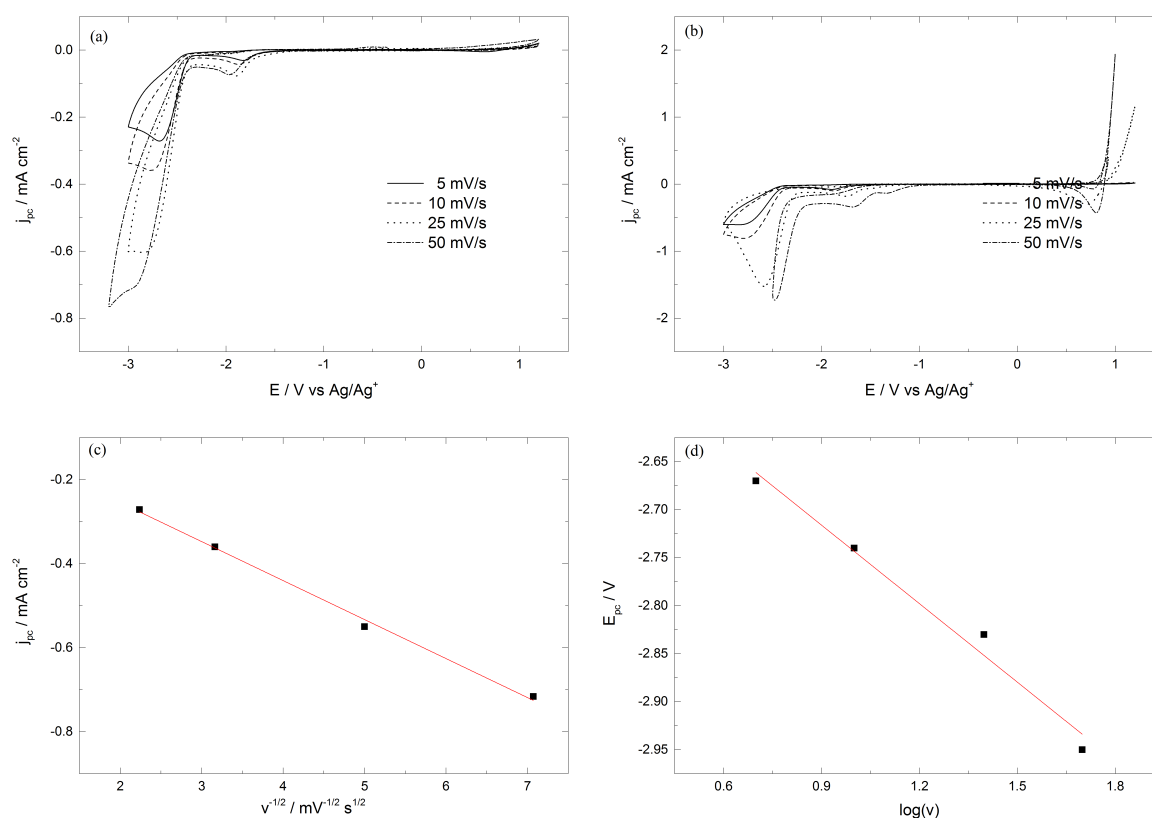


Figure 8.12: (a) Cyclic voltammograms of 0.147 mol l<sup>-1</sup> Dy[NTf<sub>2</sub>]<sub>3</sub> in [BMPyr][NTf<sub>2</sub>] recorded at room temperature on Au-WE,  $v = 5\ mV\ s^{-1}$ ,  $10\ mV\ s^{-1}$ ,  $25\ mV\ s^{-1}$  and  $50\ mV\ s^{-1}$ , CE:Dy. (b) Cyclic voltammograms at different temperatures at  $25\ mV\ s^{-1}$ . (c) Plot of the peak current densities against the square root of  $v$  at 25 °C. (d) Cathodic peak potential versus  $\log(v)$  at 25 °C.

The diffusion coefficient for this system was calculated by different methods.

$D$  can be obtained from the slope of the plot of the peak current density against the square root of the scan speed, as shown in Figure 8.12(c)<sup>[29]</sup>. As the peak potential is linearly dependent of the logarithm of the scan speed (Figure 8.12(d)) and of course there is no visible oxidation peak, this system can be considered irreversible by electrochemical definition. For an irreversible system, the cathodic peak potential  $E_{pc}$  and the cathodic half-wave potential  $E_{pc/2}$  are related according to the following relationship:

$$|E_{pc} - E_{pc/2}| = 1.857 \frac{RT}{\alpha n_{\alpha} F} \quad (8.5)$$

where  $\alpha$  is the charge transfer coefficient,  $n_{\alpha}$  is the number of exchanged electrons. The other constants have their usual meaning.

For an irreversible system, the relationship between the (cathodic) peak current density  $j_{pc}$  and the scan rate can be described by:

$$j_{pc} = 0.4958 n_{\alpha} F^{3/2} c \left( \frac{D v \alpha n_{\alpha}}{RT} \right)^{0.5} \quad (8.6)$$

The diffusion coefficient  $D$  can be determined from the slope of the plot of  $j_{pc}$  against  $\sqrt{v}$ .

By application of Eq. (8.5), a value for  $\alpha n_{\alpha}$  of 0.76 can be calculated. Inserting this value into Eq. (8.6) and solving for  $D$ , a value of  $(2.0 \pm 0.1) \times 10^{-8} \text{ cm}^2 \text{ s}^{-1}$  can be obtained.

Additionally, by calculation of the semi-integral of the CV,  $m(t)$  of this system is obtained, as shown in Figure 8.13(a). Inserting  $A = 1 \text{ cm}^2$ ,  $c = 0.147 \times 10^{-3} \text{ mol cm}^{-3}$ ,  $z = 3$ ,  $m^* = -0.00583 \text{ A s}^{1/2}$  into Eq. (8.3), delivers a value of  $D = 1.88 \times 10^{-8} \text{ cm}^2 \text{ s}^{-1}$ . The coefficients are close to the value of  $2.0 \times 10^{-7} \text{ cm}^2 \text{ s}^{-1}$  reported by Kurachi et al. for  $\text{Dy}[\text{NTf}_2]_3$  in  $[\text{P}_{2225}][\text{NTf}_2]$  at  $25^\circ\text{C}$  calculated by the semi-integral method<sup>[140]</sup>. Figure 8.13(b) shows a series of chronoamperograms recorded under different potentiostatic conditions at  $25^\circ\text{C}$ . The relationship between the squared dimensionless current density  $j/j_m$  and the dimensionless time  $t/t_m$  for the Dy(III) species in this system is shown in the inset in Figure 8.13(b), along with the theoretical curves derived from Eq. (2.39) and Eq. (2.40). From this plot, it is visible that the data quite well described by a progressive nucleation model.

Diffusion coefficients in different ionic liquids can be compared with the help of the well-known Stokes-Walden-rule stating that diffusion coefficients  $D$  and molar conductivities  $\Lambda$  in two different liquid electrolytes are inversely proportional to the liquid's viscosity<sup>[195,196]</sup>:

$$\frac{D^1}{D^2} \propto \frac{\Lambda^1}{\Lambda^2} \propto \frac{\eta^2}{\eta^1} \quad (8.7)$$

where the indexes 1 and 2 refer to two different temperatures or two different electrolytes

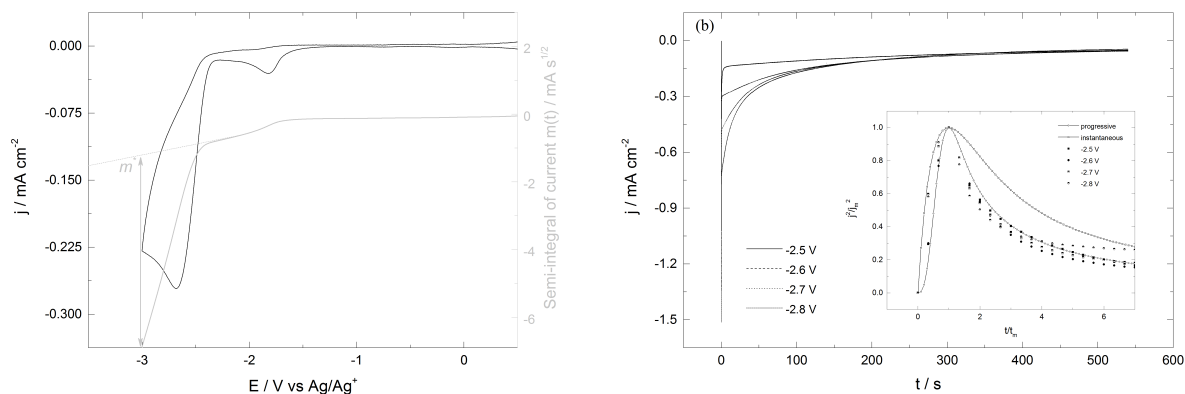


Figure 8.13: (a) Semi-integral analysis of 0.147 mol l<sup>-1</sup> Dy[NTf<sub>2</sub>]<sub>3</sub> in [BMPyr][NTf<sub>2</sub>] recorded at room temperature. WE: Au, CE: Dy. (b) Chronoamperograms of the same electrolyte recorded under different potentiostatic conditions at 25 °C.

altogether. This relationship described by Eq. (8.7) is also often written as:

$$D\eta = \text{const} \quad (8.8)$$

Table 8.1 summarizes the diffusion coefficients, their method of determination, as well as the viscosity of the applied ionic liquid and their calculated Walden products for all cited systems as well as the ones reported in this work.

Electrolyte		Diffusion coefficient	Method	Ref.	Viscosity	Walden product
Dy species	ionic liquid	cm <sup>2</sup> s <sup>-1</sup>			mPa s	mPa cm <sup>2</sup>
0.147 mol l <sup>-1</sup>	[BMPyr][NTf <sub>2</sub> ]	2.01 × 10 <sup>-8</sup>	CV		85 <sup>[196]</sup>	1.7 × 10 <sup>-6</sup>
Dy[NTf <sub>2</sub> ] <sub>3</sub>		1.88 × 10 <sup>-8</sup>	SI			
0.23 mol l <sup>-1</sup>	[BMIm][OTf]	1.76 × 10 <sup>-9</sup>	SI		109 <sup>[197]</sup>	1.92 × 10 <sup>-7</sup>
Dy[OTf] <sub>3</sub>		1.56 × 10 <sup>-8</sup> *)				
0.075 mol l <sup>-1</sup>	[P <sub>2225</sub> ][NTf <sub>2</sub> ]	2.0 × 10 <sup>-7</sup>	SI	[140]	88 <sup>[198]</sup>	1.76 × 10 <sup>-6</sup>
Dy[NTf <sub>2</sub> ] <sub>3</sub>						
0.1 mol l <sup>-1</sup>	[EMIm][BF <sub>4</sub> ]	4.87 × 10 <sup>-10</sup>	CV	[179]	219 <sup>[196]</sup>	1.06 × 10 <sup>-7</sup>
DyCl <sub>3</sub>		7.76 × 10 <sup>-9</sup> *)				

Table 8.1: Electrolyte compositions, diffusion coefficients, viscosities and Walden-products for different dysprosium electrolytes. \*) Diffusion coefficients predicted by the Walden-rule.

As shown in Table 8.1, the Walden products are predicted accurately for the systems based on

the NTf<sub>2</sub>-anion unlike the product for the tetrafluoroborate- electrolyte which is two orders of magnitude lower than predicted by Eq. (8.8), indicating a higher association of Dy<sup>3+</sup> by the BF<sub>4</sub><sup>-</sup> and Cl<sup>-</sup>-anions compared to the large, weakly coordinating NTf<sub>2</sub>- anion in phosphonium - and pyrrolidinium -based systems.

After the plating procedure, electrolyte residue was removed with dry acetone under Ar-atmosphere. A SEM micrograph of as-deposited Dy is shown in Figure 8.14(a). Complementary analysis by EDX and XPS are shown in Figure 8.14(b) and Figure 8.14(c), respectively. The morphology presented for the sample is slightly porous. Impurities of S, C, F and O are shown in the EDX spectrum of the sample. Additionally, the coating composition in respect to depth was investigated by XPS depth profiling by Ar-ion-sputtering. The results indicate that the impurities are only superficial as their atomic fractions nearly disappear with increasing etching time, as shown in Table 8.2. The shift of the Dy4d5 peak (shown in Figure 8.14(d) from 152.3 eV from metallic Dy to around 157 eV and a constant concentration of oxygen in the XPS depth profile indicate dysprosium oxide/hydroxide formation<sup>[199]</sup> which can be ascribed to short exposure to air during transfer into the XPS- chamber.

Atomic concentration %	Elemental peak						
	C1s	N1s	O1s	F1s	S2p	Dy4d5	Au4f
As deposited	14.6	2.2	59.3	9.9	4.1	6.8	2.1
After Ar-etching	0.0	1.0	59.0	2.9	0.1	8.4	11.0

Table 8.2: Composition analysis of electroplated coating shown in Figure 8.14a as deposited and after Ar-etching by XPS.



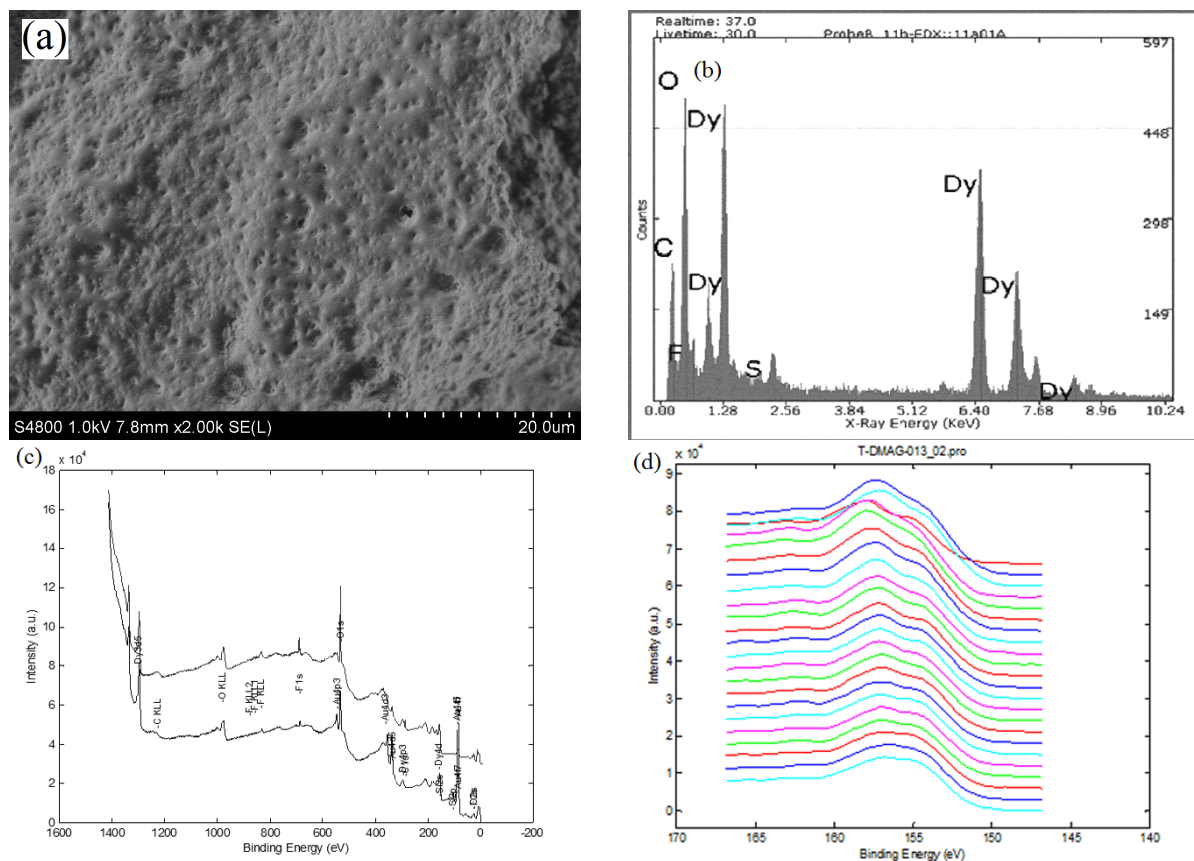


Figure 8.14: (a) SEM micrograph of as-plated dysprosium (b) EDX-pattern of the sample shown in (a). (c) XPS pattern before (top graph) and after (bottom graph) Ar-ion sputtering. (d) Shift of the Dy4d5 peak with increasing sputtering time (top to bottom) of a sample produced under galvanostatic conditions at  $-0.5 \text{ mA cm}^{-2}$  for 2 h at  $150^\circ\text{C}$  from  $0.147 \text{ mol l}^{-1}$   $\text{Dy}[\text{NTf}_2]_3$  in  $[\text{BMPyr}][\text{NTf}_2]$  on Au-sputtered quartz crystal electrode.

### Grain Boundary Diffusion of Nd-Fe-B Sintered Magnets

First attempts to plate Dy on bare Nd-Fe-B failed. After the deposition experiment, black deposits were found at the bottom the deposition cell. It became clear, that the deposits were not only deposited Dy but also parts of the magnet base body as they showed magnetic properties<sup>3</sup>. To still manage to coat the samples, an intermediate coating had to be applied. Based on the results of coatings deposited by PVD discussed in chapter 5 as well as previous results presented in this chapter, copper was chosen as the adhesion layer. Therefore, Nd-Fe-B samples were polished with 1200 and 2000 grit polishing paper and rinsed with dry acetone under Ar-atmosphere.

A bath of  $0.2 \text{ mol kg}^{-1} \text{ Cu[OTf]}_2$  in [BMIm][OTf] and a deposition time of 15 min at  $-1 \text{ V}$  at  $100^\circ\text{C}$  was used to deposit coatings of about 100 nm. The sample thickness was calculated by the passed current as well as the sample weight before and after deposition using a high precision microbalance with a resolution of  $10 \mu\text{g}$ , respectively.

Samples of varying Dy content were produced by galvanostatic deposition ( $-0.5 \text{ mA cm}^{-2}$ ) with a fixed temperature of  $150^\circ\text{C}$  for 1 h to 11 h. The Dy content was calculated by the following equation:

$$\omega_{\text{Dy}} = \frac{\omega_i s + m}{s + m} \quad (8.9)$$

where  $m$  represents the deposited mass of Dy and  $\omega_i$  and  $s$  are the initial dysprosium mass fraction in the magnet sample and the sample weight, respectively. The layer thickness after plating was calculated assuming an even distribution of the coating.

Each sample was cleaned from electrolyte residue with dry acetone and individually wrapped in molybdenum foil to decrease volatilization of the coating and transferred into a quartz tube. After evacuation of the tube ( $p < 1 \times 10^{-3} \text{ Pa}$ ) the samples were annealed at  $900^\circ\text{C}$  for 6 h and subsequently cooled to room temperature. The final aging procedure was done at  $400^\circ\text{C}$  for 2 h.

The demagnetization curves for all samples are demonstrated in Figure 8.15a. A good squareness of the curves is obtained for the samples with 0.55 and 0.62 wt. % while the samples with 0.72 and 0.91 wt. % show a knee in the intrinsic curve. As discussed in the previous chapter, an uneven distribution of local coercivity due to limited diffusion of the coating (thus decreasing concentration of  $\text{Nd}_{2-x}\text{Dy}_x\text{Fe}_{14}\text{B}$  shells) explains the loss of squareness with increasing coating thickness. Figure 8.15b further illustrates the percent increase of  $H_{cJ}$  with

<sup>3</sup>Dysprosium is ferromagnetic below its Curie Temperature ( $T_C = 88 \text{ K}$ ). Above  $T_C$ , this metal transfers to a helical anti-ferromagnetic ordering up to 180 K, which becomes paramagnetic for higher temperatures<sup>[200]</sup>.

Dy content for the electrochemically coated samples. The experimental conditions and the resulting properties of all magnet samples are summarized in Table 8.3.

Deposition Time [s]	Deposited Dy [mg]	Coating thickness [ $\mu\text{m}$ ]	Total Dy content [wt%]	Current Efficiency [%]	$\Delta H_{cJ}$ [%]
4500	1.01	0.29	0.55	79.9	10.3
12000	2.47	0.80	0.62	73.3	13.1
21600	4.55	1.48	0.72	75.1	16.4
39600	8.7	2.5	0.91	78.3	20.4

Table 8.3: Deposition times, mass of deposited Dy, coating thickness, current efficiencies and increase in  $H_{cJ}$  for different samples.

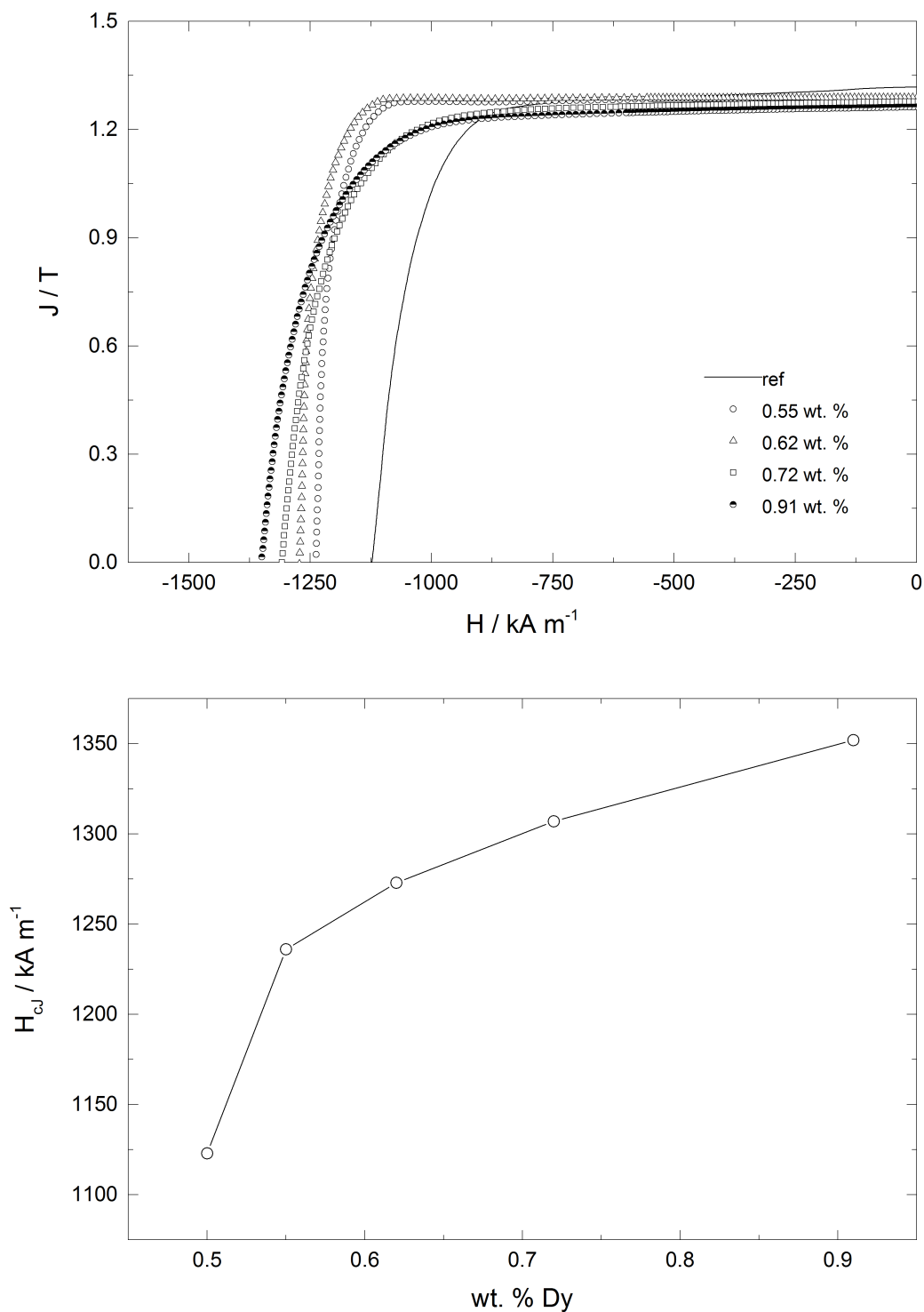


Figure 8.15: (a) Demagnetization curves obtained for a reference sample (straight line) and samples with 0.55 (open circles), 0.62 (open triangles), 0.72 (open squares) and 0.91 wt % (half shaded circles). Production of the samples is shown in Tab. 8.3. (b) Effects of Dy content on the coercivity of VD 722 magnets with a base Dy concentration of 0.5 wt. %. The additional Dy > 0.5 wt. % is added by GBD.

## 8.3 Electrodeposition of Terbium

Apart from being a component of the magnetostrictive alloy Terfenol-D<sup>4</sup> used in a number of electronic devices, terbium is used as a dopant in different solid state devices ( $\text{CaF}_2$ ,  $\text{CaWO}_4$ ,  $\text{SrMoO}_4$  as well as a stabilizer of high temperature fuel cells<sup>[168,169]</sup> The largest consumption of the world's terbium supply is represented by lighting technology, where it is used as a green phosphor<sup>[168,169]</sup>.

The electrochemistry of terbium has not been very well investigated. The electrochemical behavior of terbium in high temperature molten salts, namely the eutectic melt  $\text{LiCl-KCl}$  has been reported by Bermejo et al. and Kim et al.<sup>[203,204]</sup>. Qui et al. reported the synthesis of  $\text{TbFe}_2$  from terbium oxide  $\text{Tb}_4\text{O}_7$  and iron oxide  $\text{Fe}_2\text{O}_3$  in molten  $\text{CaCl}_2$ <sup>[205]</sup>. Sugitomo developed an electroplating bath for  $\text{Tb-Co-Fe}$  ternary alloys from polar aprotic solvents for magneto optical recording<sup>[206]</sup> and even the deposition of alloys from aqueous electrolytes has been claimed<sup>[207,208]</sup>, but to the author's knowledge, electroplating from air- and water-stable ionic liquids haven't been reported. From the previous chapter, the striking performance of GBD-processed  $\text{Nd-Fe-B}$  sintered magnets calls for an attempt to electroplate Tb. Keeping in mind the requirements that have to be met by the electrochemical process and based on the results of dysprosium deposition, the focus of this section lies on the electrochemistry of Tb-species in triflate- and triflamide based ionic liquids.

### 8.3.1 Electrodeposition from Solutions Containing Terbium-(III)-Trifluoromethanesulfonate

The attempted deposition from triflate based systems, namely  $0.01 \text{ mol kg}^{-1} \text{ Tb}[\text{OTf}]_3$  in  $[\text{BMPyr}][\text{OTf}]$  and  $[\text{BMIm}][\text{OTf}]$  was unsuccessful. Cyclic voltammograms recorded for both electrolytes at room temperature with a scan rate of  $5 \text{ mV s}^{-1}$  are shown in Figure 8.16(a) and Figure 8.16(b), respectively. The CVs show cathodic currents starting at about  $-1 \text{ V}$  and  $-1.5 \text{ V}$ , however no Tb could be plated from potentiostatic deposition at the respective peak potentials. Potentiostatic deposition at  $150^\circ\text{C}$  at ten-fold concentrations did not show any improvement either.

<sup>4</sup>When a magnetic field is applied, the boundaries between the domains shift and the domains rotate causing a change in the material's dimensions. This property is shown by ferromagnetic materials of which Terfenol-D ( $\text{Tb}_x\text{Dy}_{1-x}\text{Fe}_2$  ( $x \approx 0.3$ )) exhibits the strongest magnetostrictive behavior so far<sup>[201,202]</sup>.

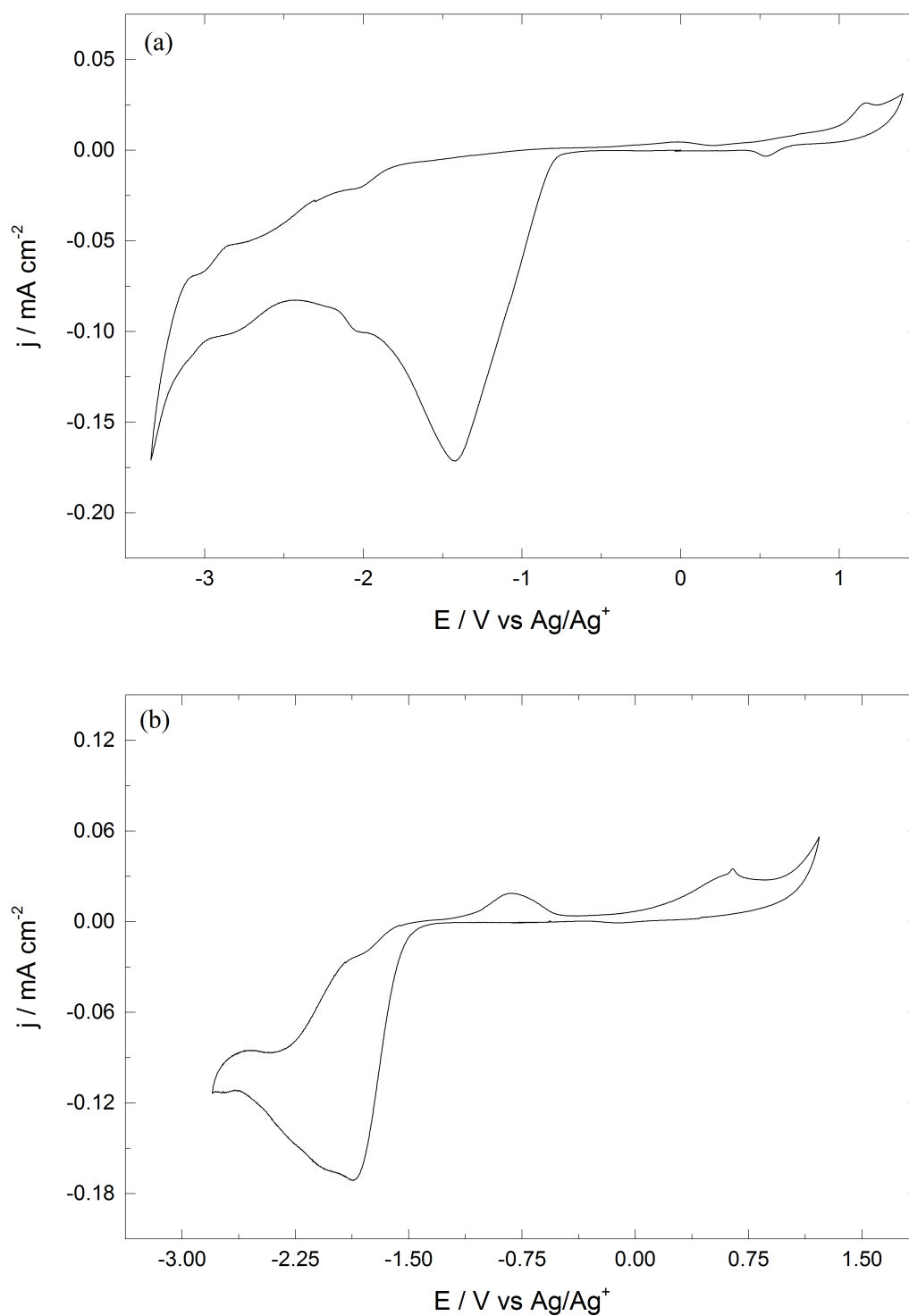


Figure 8.16: Cyclic voltammograms of (a)  $0.01 \text{ mol kg}^{-1} \text{ Tb}[\text{OTf}]_3$  in  $[\text{BMPyr}][\text{OTf}]$  (b)  $0.01 \text{ mol kg}^{-1} \text{ Tb}[\text{OTf}]_3$  in  $[\text{BMIm}][\text{OTf}]$  at  $25^\circ\text{C}$ .  $\nu = 5 \text{ mV s}^{-1}$ . WE: Au, CE: Tb

### 8.3.2 Electrodeposition from Solutions Containing Terbium-(III) Bis(trifluoromethylsulfonyl)imides

#### Electrochemical Deposition from $\text{Tb}[\text{NTf}_2]_3$ in 1-Butyl-1-methylpyrrolidinium Bis(trifluoromethylsulfonyl)imide

Previous study of  $[\text{BMIm}][\text{NTf}_2]$  for the electroplating of Dy showed that this IL was not suited. For this reason, this IL was not further tested.

Figure 8.17(a) shows a series of cyclic voltammograms for  $0.047 \text{ mol l}^{-1} \text{ Tb}[\text{NTf}_2]_3$  in  $[\text{BMPyr}][\text{NTf}_2]$  at  $25^\circ\text{C}$  at scan speeds of  $5$  to  $100 \text{ mV s}^{-1}$  recorded on a platinum WE. At room temperature, a cathodic current starts at about  $-0.9 \text{ V}$  vs. REF, and peaks at  $-3.3 \text{ V}$  vs. REF. A shift of the peak potentials is visible with increasing  $\nu$ , indicating that this system is irreversible. During the anodic scan, an oxidative peak is seen at about  $0.75 \text{ V}$ . The peak current density  $j_{pa}$  of this peak increases with  $\nu$ , whereas  $E_{pa}$  does not. A slight bump in the CV of the pure ionic liquid was seen as well. Therefore, this signal can be assigned to an impurity and not to stripping of plated Tb. Figure 8.17(b) shows CVs of this system at temperatures between  $25^\circ\text{C}$  to  $150^\circ\text{C}$  at a fixed scan speed of  $25 \text{ mV s}^{-1}$ . An increase of  $j_{pc}$  accompanied by a shift of  $E_{pc}$  to less negative values can be observed for increasing temperatures, which can be attributed to a facilitation of Tb deposition due to higher mobility of the  $\text{Tb}^{3+}$ -species and reduced overvoltages.

The relationship between the cathodic peak potential  $E_{pc}$  as well as the cathodic peak current density  $j_{pc}$  and the applied scan speed are presented in Figure 8.17(c) and Figure 8.17(d). As shown in the plot of  $j_{pc}$  against  $\sqrt{\nu}$ , the cathodic peak current is a linear function of the square root of the applied scan speed, indicating that the reduction of  $\text{Tb}^{3+}$  is diffusion controlled. The linear dependence of the cathodic peak potential on the logarithm of  $\nu$  (alongside an absence of the stripping peak) determines this system to be electrochemically irreversible.

From the plot shown in Figure 8.17(c), the diffusion coefficient for the  $\text{Tb}^{3+}$  species can be determined from the slope according to Eq. (8.6). By using all experimental values ( $\nu = 5 \text{ mV s}^{-1}$ ,  $c = 0.047 \text{ mol l}^{-1}$ ,  $A = 0.0707 \text{ cm}^2$ ,  $T = 25^\circ\text{C}$ ), a value of  $D$  can be determined to be  $(4.5 \pm 0.4) \times 10^{-8} \text{ cm}^2 \text{ s}^{-1}$ .

Electroplating of Tb was conducted using a  $0.25 \text{ mol kg}^{-1}$  solution of  $\text{Tb}[\text{NTf}_2]_3$  in  $[\text{BMPyr}][\text{NTf}_2]$  under galvanostatic conditions with a current density of  $-0.5 \text{ mA cm}^{-2}$  at a temperature of  $150^\circ\text{C}$  for 2 h on a Cu substrate inside an Ar-filled glovebox. After the plating procedure, the sample was cleaned of electrolyte residue with dry acetone. During the cleaning step, it was noticed that the adhesion of the dark grey deposits to the substrates was fairly poor. A change in deposition parameters was attempted as well.  $j$  was varied from  $0.25$

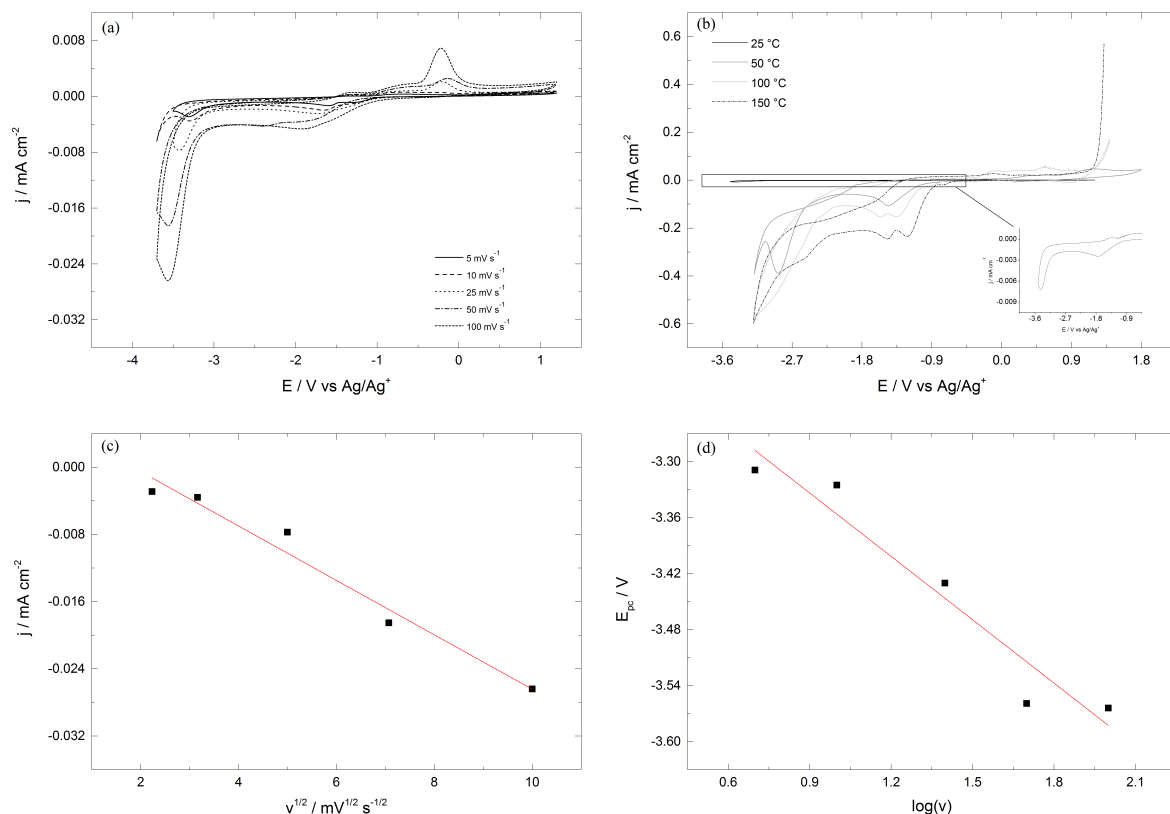


Figure 8.17: (a) Cyclic voltammograms of 0.047 mol l<sup>-1</sup> Tb[NTf<sub>2</sub>]<sub>3</sub> in [BMPyr][NTf<sub>2</sub>] recorded at room temperature on Pt-WE,  $\nu = 5 \text{ mV s}^{-1}$ ,  $10 \text{ mV s}^{-1}$ ,  $25 \text{ mV s}^{-1}$  and  $50 \text{ mV s}^{-1}$ . (b) Cyclic voltammograms at different temperatures at  $25 \text{ mV s}^{-1}$ . (c) Plot of the peak current densities against the square root of  $\nu$  at 25 °C. (d) Cathodic peak potential versus  $\log(\nu)$  at 25 °C.

to  $2 \text{ mA cm}^{-2}$ . Lower  $j$  led to the same results, higher  $j$  resulted in a fairly quick change in color of the solution to dark brown. A SEM micrograph of as-deposited Tb is shown in Figure 8.18(a). A magnification of this image, as presented in Figure 8.18(b), shows a rough and cracked surface of the coating.

The composition of this coating was analyzed by WDX (Figure 8.19). Some impurities of O, F, and S were detected, which can be traced to either entrapped ionic liquid or inclusion of its decomposition products. Oxygen impurities can be traced to exhibition of the sample to air during the transition into the WDX chamber. Due to the cracked morphology of the sample, a Cu signal can be detected, which is attributed to the substrate. The small amount of fluorine detected in the sample and rather large signal for sulfur are indicative for the incorporation of ionic liquid decomposition products over the entrapment of IL molecules. Additional WDX elemental maps were performed, as demonstrated in Figure 8.20. As seen in this image, the impurities F, S and O are well distributed over the majority of the surface. The signal



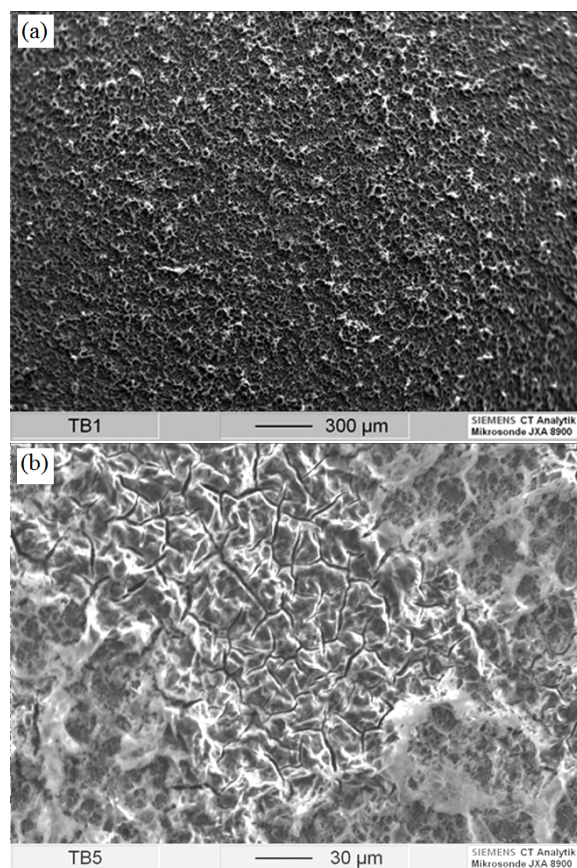


Figure 8.18: (a) SEM micrograph of as-deposited Tb from  $0.25 \text{ mol l}^{-1} \text{ Tb}[\text{NTf}_2]_3$  in  $[\text{BMPyr}][\text{NTf}_2]$  at  $150^\circ\text{C}$  (b) Magnification of (a). Deposition conditions:  $j = -0.5 \text{ mA cm}^{-2}$ ,  $t = 2 \text{ h}$ , WE: Cu, CE: Pt.

intensities of O and F are also well below S. From the magnification of the area highlighted in Figure 8.20(a), it can be seen that the surface is only partially covered, as the darker regions in the image shown strong signals of the underlying copper substrate. The intensity of sulfur is correlated to Tb. It can be considered, that the coating consists of  $\text{Tb}_2\text{S}_3$ .

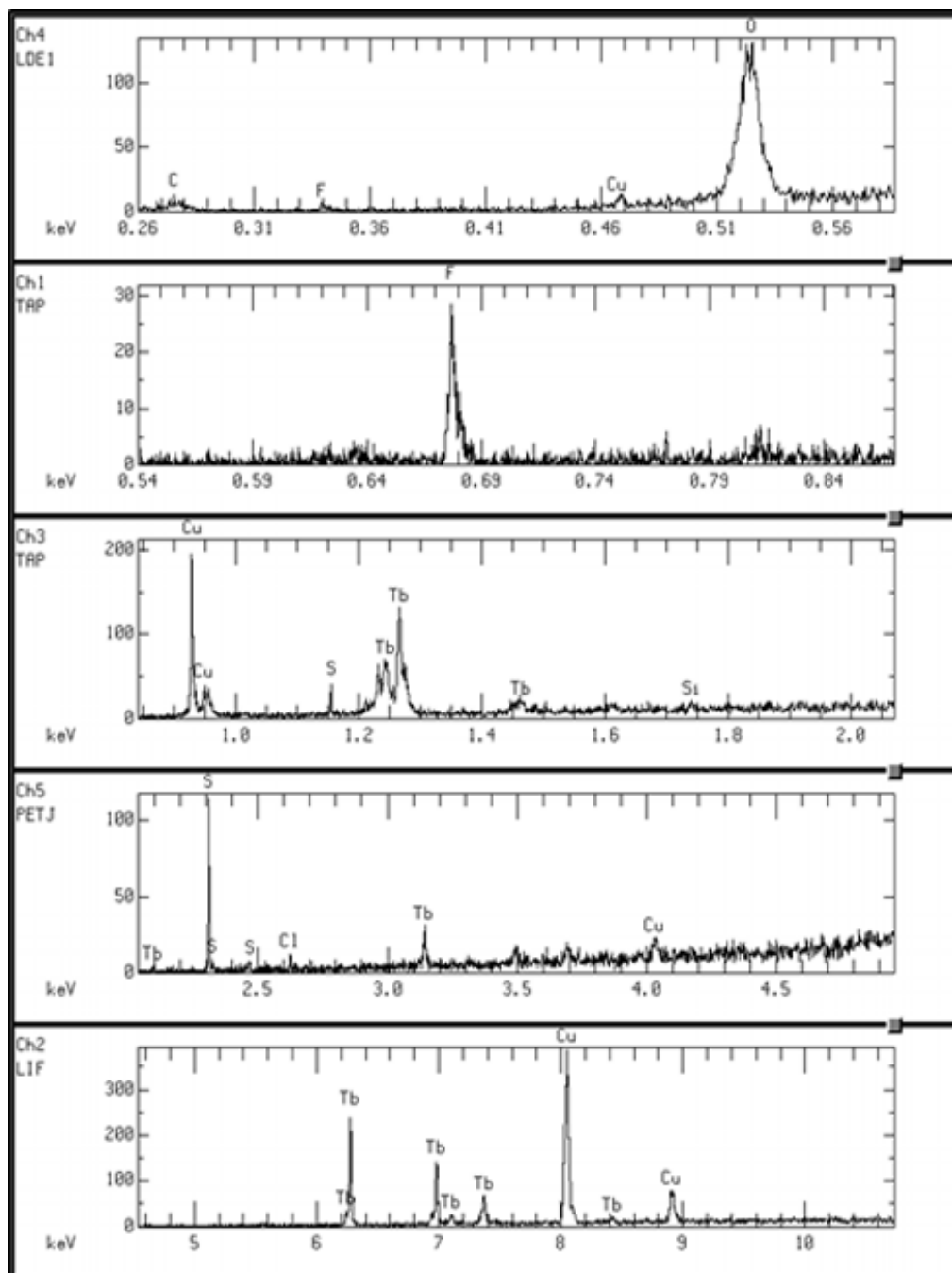


Figure 8.19: WDX analysis of electroplated Tb coating shown in Figure 8.18.

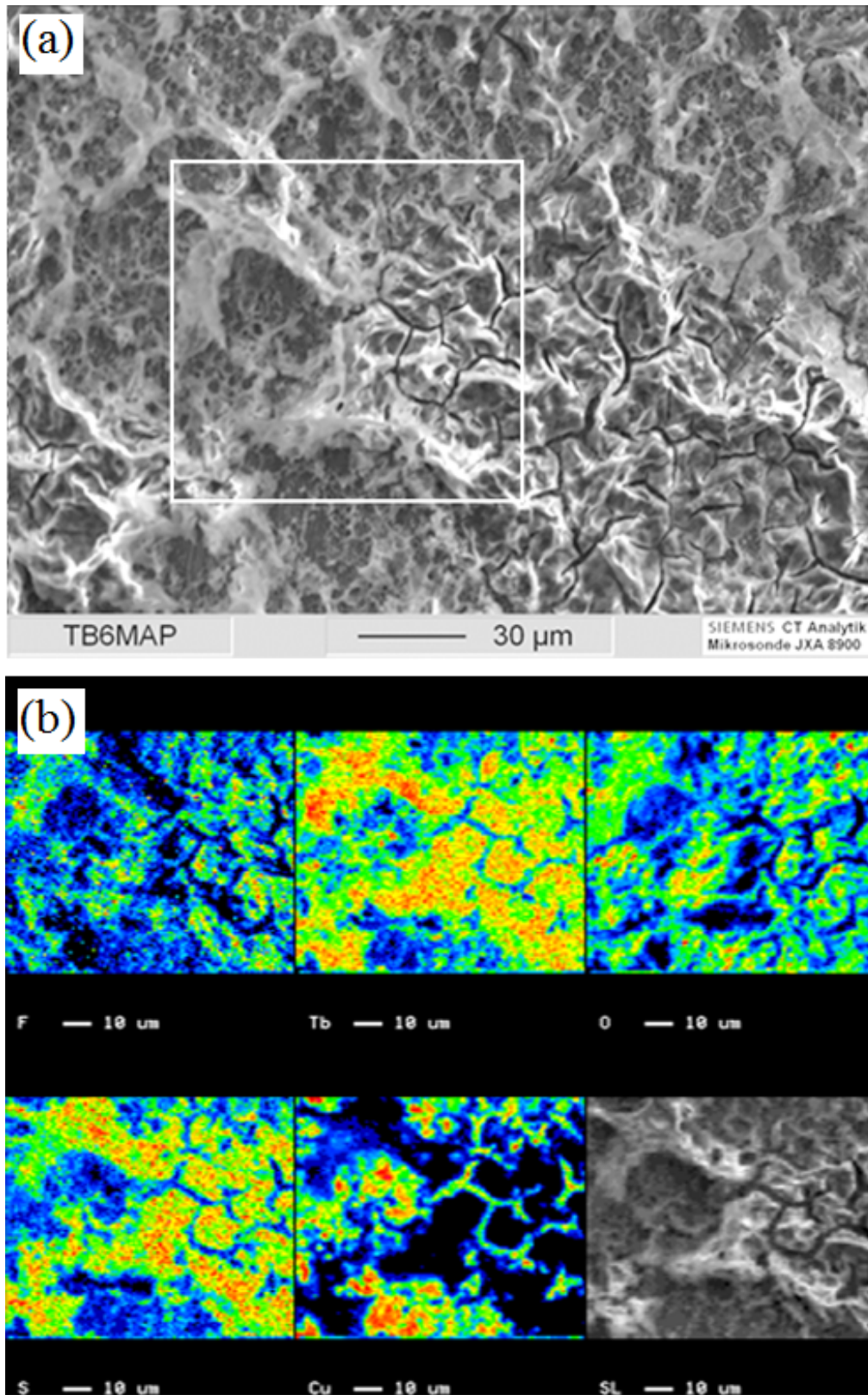


Figure 8.20: (a) SEM micrograph of the Tb-coated sample described above. (b) WDX elemental maps of the highlighted area.

### Grain Boundary Diffusion of Nd-Fe-B Sintered Magnets

Nd-Fe-B-samples were prepared by galvanostatic deposition with a current density of  $-0.5 \text{ mA cm}^{-2}$  with a fixed temperature of  $150^\circ\text{C}$  for 1 h to 3 h. Prior to this step, Nd-Fe-B-samples were coated with copper, as described in the previous section. Samples were cleaned from electrolyte residue with dry acetone and individually wrapped in molybdenum foil to decrease volatilization of the coating and transferred into a quartz tube. Poor adhesion of the coatings resulted in a partial loss of the coating prior to annealing. After the quartz tube was evacuated ( $p < 1 \times 10^{-3} \text{ Pa}$ ), the samples were annealed at  $900^\circ\text{C}$  for 6 h and subsequently cooled to room temperature. The final aging procedure was done at  $500^\circ\text{C}$  for 2 h.

Figure 8.21 shows the demagnetization curve of a grain boundary diffusion treated sample with electroplated terbium for the best performing sample. The increase in coercivity is small, which can be attributed to a small amount of diffused Tb. By comparison with the values obtained for the GBD-treatment with coatings prepared by PVD, an addition of Tb of about 0.02 wt. % can be estimated.

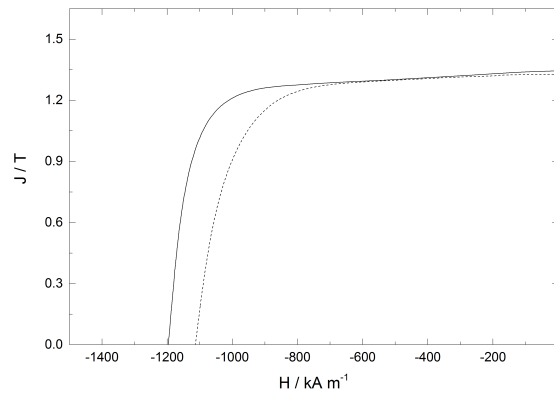


Figure 8.21: Demagnetization curve of grain boundary diffusion processed sample electroplated with Tb. Dotted line: untreated reference sample. Straight line: sample treated with electroplated Tb.

## 8.4 Electrodeposition of Neodymium

For the production of Nd-Fe-B sintered magnets a slight excess of Nd is needed to obtain their characteristic microstructure and magnetic properties. Close to stoichiometric amounts of Nd are used to produce a second group of Nd-Fe-B based magnetic materials- hot deformed anisotropic Nd-Fe-B magnets.

Hot-deformed anisotropic Nd-Fe-B magnets comprise of small  $\text{Nd}_2\text{Fe}_{14}\text{B}$  grains of about 300 nm in length and about 80 nm in thickness, which is one order of magnitude smaller than that of typical commercial sintered magnets with approximately  $8\text{ }\mu\text{m}$ <sup>[209]</sup>. However, recent studies on the microstructure of hot-deformed magnets have shown, that the lower-than-expected coercivity of these materials can be assigned to a substantial amount of iron in the intergranular Nd-rich phase which causes ferromagnetic coupling between grains<sup>[126,210]</sup>. Isolation of the grains by formation of a non-ferromagnetic intergranular layer could be a possibility to achieve higher values of  $H_{cJ}$ .

While further addition of neodymium to Nd-Fe-B-sintered magnets should not have any effect on the magnetic properties as they already possess Nd-rich, non-magnetic intergranular phases, GBD-treatment of hot-deformed Nd-Fe-B magnets with RE-TM eutectic alloys (where RE = light rare earth and TM = transition metal, mostly Cu) has been proposed and independently reported by several authors<sup>[211,212]</sup>.

The electrochemical behavior of Nd has been mostly studied in high temperature molten salts with the intent to deposit Nd alloys such as Nd-Ni<sup>[213,214]</sup>, Nd-Al<sup>[215]</sup> or for the separation of lanthanoids in spent nuclear fuel<sup>[216–218]</sup>.

Room temperature eutectic melts (acetamide-urea-NaB-KBr) have been reported for the deposition of RE-Co (RE= Dy, Nd, Eu) alloys<sup>[219]</sup> and electroplating of Nd from the ionic liquid  $[\text{P}_{2225}][\text{NTf}_2]$  has been reported by Kondo et al.<sup>[142]</sup>

### 8.4.1 Electrochemical Deposition from $\text{Nd}[\text{NTf}_2]_3$ in 1-Butyl-1-methylpyrrolidinium Bis(trifluoromethylsulfonyl)imide

In contrast to previously investigated  $[\text{OTf}^-]$ - rare earth metal compounds, the solubility of  $\text{Nd}[\text{OTf}]_3$  in different ionic liquids was extremely low, excluding this compound from further attempts to plate neodymium.

As reported in the previous sections, the triflamide compounds showed the most promising results. Based on this, an analogous compound,  $\text{Nd}[\text{NTf}_2]_3$ , was investigated for the electro-

plating of Nd.

Figure 8.22(a) shows a series of cyclic voltammograms of  $0.145 \text{ mol l}^{-1}$   $\text{Nd}[\text{NTf}_2]_3$  in  $[\text{BMPyr}][\text{NTf}_2]$  at  $25^\circ\text{C}$  recorded with different scan rates on a gold sputtered quartz crystal electrode. A reduction peak is visible starting at  $-2.5 \text{ V}$  vs. REF which is ascribed to the reduction of  $\text{Nd}^{3+}$ . The cyclic voltammograms of this system recorded at temperatures between  $25^\circ\text{C}$  to  $150^\circ\text{C}$  with a fixed scan speed of  $25 \text{ mV s}^{-1}$  are shown in Figure 8.22(b). While the cathodic peak potentials migrate to more positive potentials for increasing temperatures,  $E_{pc}$  shifts to more negative potentials for increasing values of the scan speed, as illustrated in Figure 8.22(d) and Figure 8.22(b), respectively. It is also noticeable, that the current density increases with increasing  $T$  and increasing  $V$ . The absence of a corresponding anodic peak as well as a linear relationship of  $E_{pc}$  to the logarithm of  $v$  (Figure 8.22(d)), indicate that the reduction of Nd is an electrochemical irreversible process. The cathodic peak current density increases with the square root of the scan speed in a linear manner, fitting to a diffusion controlled reaction as shown in the plot of  $j_{pc}$  against  $\sqrt{v}$  in Figure 8.22(c).

With Eq. (8.6), the diffusion coefficient of the  $\text{Nd}^{3+}$ -species in this system can be calculated. From the slope of the fit shown in Figure 8.22c, a diffusion coefficient of  $1.37 \times 10^{-9} \text{ cm}^2 \text{ s}^{-1}$  can be determined. Additionally, semi-integral analysis was performed to determine  $D$ . The convoluted curve of the CV recorded with a scan rate of  $5 \text{ mV s}^{-1}$  is shown in Figure 8.23

After insertion of the experimental values for  $A = 0.357 \text{ cm}^2$  and  $c = 0.145 \text{ mol l}^{-1}$ , into Eq. (8.3), a diffusion coefficient of  $3.92 \times 10^{-9} \text{ cm}^2 \text{ s}^{-1}$  can be calculated by the semi-integral method. From a plot of  $\ln(D)$  against  $1/T$  as presented by Kondo et al.<sup>[142]</sup>, a value for  $D$  of about  $7 \times 10^{-9} \text{ cm}^2 \text{ s}^{-1}$  at  $50^\circ\text{C}$  can be extracted, which is rather small in comparison to the values reported in this work.

Electroplating was attempted from a  $0.145 \text{ mol l}^{-1}$  solution of  $\text{Nd}[\text{NTf}_2]_3$  in  $[\text{BMPyr}][\text{NTf}_2]$  at  $150^\circ\text{C}$  on a copper substrate under galvanostatic conditions ( $j = -0.5 \text{ mA cm}^{-2}$ ). The microstructure of the obtained sample and the corresponding EDX pattern are shown in Figure 8.24(a) and Figure 8.24(b). A porous but well adhesive structure was obtained and rather large amounts of F, S and C are detected. The results show, that this system is suitable for the electroplating of Nd, but further investigation regarding the optimization of deposition parameters is needed.

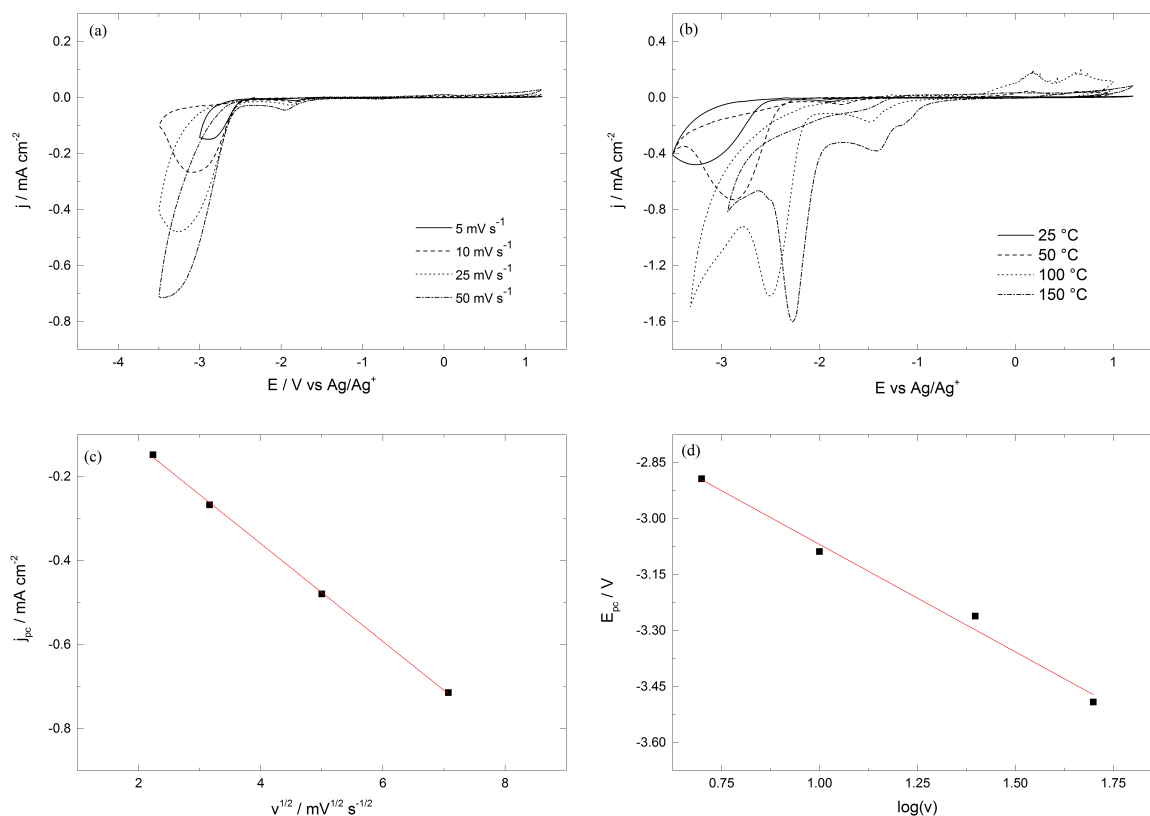


Figure 8.22: (a) Cyclic voltammograms of 0.145 mol l<sup>-1</sup> Nd[NTf<sub>2</sub>]<sub>3</sub> in [BMPyr][NTf<sub>2</sub>] recorded at room temperature on Au-WE,  $v = 5 \text{ mV s}^{-1}$ ,  $10 \text{ mV s}^{-1}$ ,  $25 \text{ mV s}^{-1}$  and  $50 \text{ mV s}^{-1}$ . (b) Cyclic voltammograms at different temperatures at  $25 \text{ mV s}^{-1}$ . (c) Plot of the peak current densities against the square root of  $v$  at 25 °C. (d) Cathodic peak potential versus  $\log(v)$  at 25 °C.

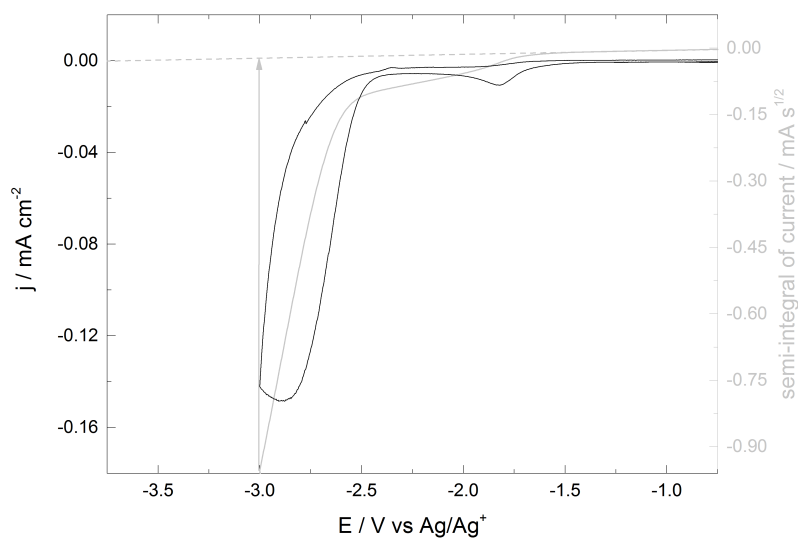


Figure 8.23: Black curve: cathodic branch of the cyclic voltammogram of 0.145 mol l<sup>-1</sup> Nd[NTf<sub>2</sub>]<sub>3</sub> in [BMPyr][NTf<sub>2</sub>], gray curve: convoluted curve.



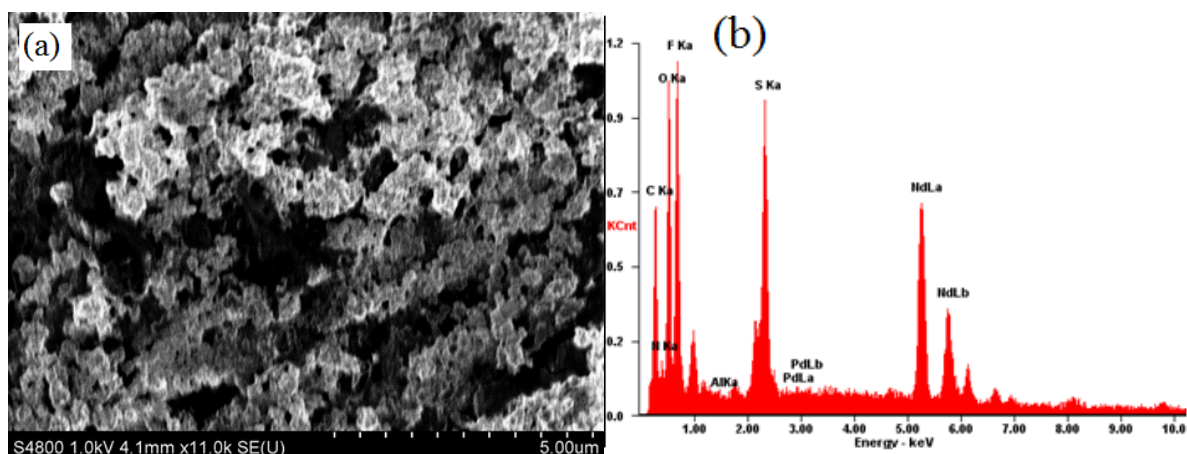


Figure 8.24: (a) SEM micrograph and (b) EDX pattern of electroplated neodymium. Conditions described in the text.

## 8.5 Electrodeposition of Transition-Metals and Rare-Earth-Transition-Metal Alloys

Rare-earth-transition-metal alloy exhibit interesting properties, such as giant magnetostriction in  $\text{Sm}_x\text{Fe}$ <sup>[221]</sup>, perpendicular magnetic anisotropy for magneto-optical recording media in  $\text{Gd}_x\text{Co}$ <sup>[222]</sup>, hydrogen storage functionality as for the case of  $\text{La}_x\text{Ni}$ <sup>[223,236]</sup>. Ternary alloys of the type  $\text{TM}_1\text{--TM}_2\text{--RE}$  have found application in magneto-optical recording<sup>[225,226]</sup> and they show promising properties for hydrogen storage<sup>[227]</sup>, as well.

Cobalt is one of the most important components for magnetic and corrosion-resistant alloys. Mainly due to the large magnetocrystalline anisotropy of  $\text{SmCo}_5$ ,  $\text{RECo}_5$  intermetallic compounds have received considerable interest<sup>[228]</sup>.

Ionic liquids are in a very promising position for industrial application for electroplating of Co as electroplating from aqueous solutions are generally difficult because of the narrow electrochemical window of aqueous electrolytes and the negative redox potential of Co of  $-0.28\text{ V}$  vs NHE<sup>[104]</sup>. Several studies have been published for the deposition of cobalt from ionic liquid based electrolytes, including chloroaluminates<sup>[229–231]</sup>,  $[\text{BF}_4^-]$  based ionic liquids<sup>[232]</sup> and triflamide-based ionic liquids<sup>[143,233,234]</sup>. However, in the presence of Cl, magnets quickly form red rust<sup>[150]</sup>. For this reason, the application of chloride compounds (ionic liquid and/or metal source) for the coating of Nd-Fe-B-sintered magnets is unfavorable.



## 8.6 Electrodeposition of Cobalt-Dysprosium Alloys

Deposition of Dy–Zn–Co from zinc chloride-1-ethyl-3-methylimidazolium chloride ionic liquids has been investigated by Hsu et al. A content of up to 24.5 % Dy was reported for potentiostatic deposition from a 50-50 mol %  $\text{ZnCl}_2$ –EMImCl melt containing 1.687 mol %  $\text{CoCl}_2$  and 1.114 mol %  $\text{DyCl}_3$  on a nickel electrode at 100 °C determined by EDX. However, hysteresis loops recorded for the deposited alloys showed a very small value for the coercivity suggesting that no reduction of the trivalent dysprosium to dysprosium metal but only incorporation of  $\text{Dy}_3^+$  occurred<sup>[237,238]</sup>. Samarium-cobalt alloys have been deposited from choline-chloride/ urea deep eutectic solvents with  $\text{Sm}(\text{NO}_3)_3$  and  $\text{CoCl}_2$  as the electroactive species<sup>[239]</sup>. Ispas et al. reported the electrodeposition of thin Sm-Co layers from the air- and water stable ionic liquid [BMPyr][NTf<sub>2</sub>] and taylor made  $\text{Co}[\text{NTf}_2]_2$  and  $\text{Sm}[\text{NTf}_2]_3$ <sup>[240]</sup>.

As previously mentioned for Tb and Nd compounds, experiments with  $\text{Co}[\text{OTf}]_2$  as the metal source showed a very small solubility of the triflate in various ionic liquids. Deposition and electrochemical characterization of cobalt from triflamide ionic liquids has been reported in the literature. Most frequently [BMPyr][NTf<sub>2</sub>] has been utilized either as a neat ionic liquid<sup>[241]</sup> or enriched with different additives such as acetone<sup>[241]</sup>, thiourea<sup>[143]</sup> or coumarin<sup>[143]</sup>. A very low crystallinity of the deposits as well as very poor adhesion to the substrate has been reported for the deposition of Co from neat [BMPyr][NTf<sub>2</sub>]<sup>[241]</sup>. Similar results have been reported for the deposition of iron<sup>[241]</sup> and nickel<sup>[235]</sup> in this ionic liquid.

As triflamide-based ionic liquids have shown promising results for the previous metals, in this study [BMIm][NTf<sub>2</sub>] was applied for the characterization and plating of cobalt and later on as electrolyte for the electroplating of Dy-Co alloys. Electroplating of Co from the system  $\text{Co}[\text{NTf}_2]_2$  / [BMIm][NTf<sub>2</sub>] has not been reported in the literature.

A series of cyclic voltammograms of  $0.1 \text{ mol l}^{-1}$   $\text{Co}[\text{OTf}]_2$  in [BMIm][NTf<sub>2</sub>] recorded at room temperature on a Pt WE at different scan speeds is presented in Figure 8.25(a). A cathodic peak at about –2 V is visible for plating of Co, while no corresponding anodic peak for the stripping of Co is visible. The current density increases and the peak potential shifts slightly to more negative values with  $v$ . Figure 8.25(b) shows CVs recorded at 25 °C and 100 °C at  $25 \text{ mV s}^{-1}$ , respectively. A large increase in current is visible as well as a shift of  $j_{pc}$  to a more positive potential. At 100 °C, the a peak in the anodic region, ascribed to the stripping of electroplated Co metal becomes visible at about –0.4 V. A linear relationship between the cathodic peak current densities and the scan speeds is visible for the series of CVs recorded at room temperature, as shown in Figure 8.25(c), indicating a diffusion control of the reduction mechanism. The cathodic peak potentials  $E_{pc}$  shift to more negative values with increasing

scan rate in a linear manner, as presented in the plot of  $E_{pc}$  vs  $\log(\nu)$  in Figure 8.25(d). Additionally, the anodic peak currents for the dissolution of Co are smaller than those of the deposition regardless of scan rate or temperature. This behavior has also been reported by Fukui et al. for the system  $\text{Co}[\text{NTf}_2]_2$  /  $[\text{BMPyr}][\text{NTf}_2]$ <sup>[143]</sup>. It is explained by the solubility of  $\text{Co}[\text{NTf}_2]_2$  in the ionic liquid and/or a change of the local viscosity in the vicinity of the electrode during the dissolution process. Oxidation of metallic Co forms  $\text{Co}[\text{NTf}_2]_2$  which quickly saturates the solution near the electrode because the diffusivity of ions is lower in this electrolyte compared to aqueous solutions. These observations suggest an electrochemically irreversible behavior of this system, so that Eq. (8.6) can be applied to calculate  $D$  from the slope of the plot in Figure 8.25(c). For  $\alpha = 0.09$  a value of  $(1.60 \pm 0.06) \times 10^{-8} \text{ cm}^2 \text{ s}^{-1}$  can be determined.

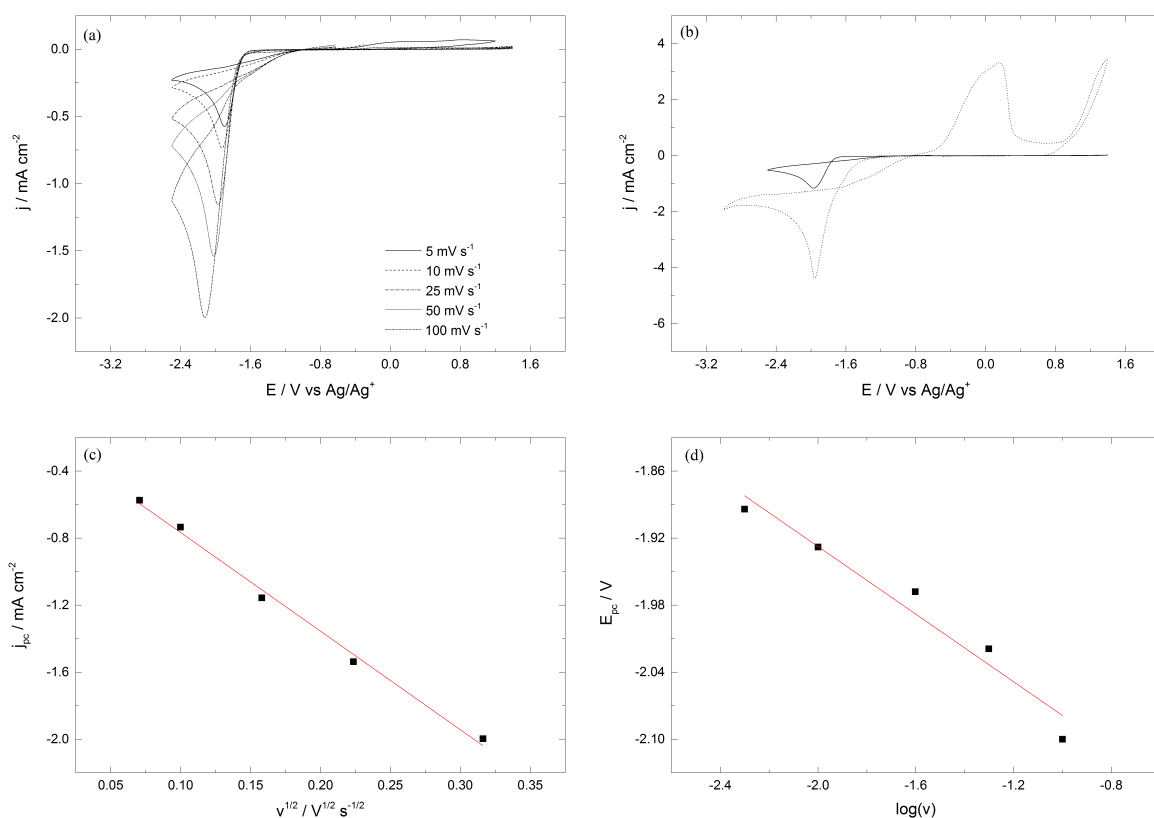


Figure 8.25: a) Cyclic voltammograms of  $0.141 \text{ mol l}^{-1} \text{ Co}[\text{NTf}_2]_2$  in  $[\text{BMIm}][\text{NTf}_2]$  recorded at room temperature on Pt-WE,  $\nu = 5 \text{ mV s}^{-1}$ ,  $10 \text{ mV s}^{-1}$ ,  $25 \text{ mV s}^{-1}$ ,  $50 \text{ mV s}^{-1}$  and  $100 \text{ mV s}^{-1}$ . b) Cyclic voltammograms at different temperatures at  $25 \text{ mV s}^{-1}$ . c) Plot of the peak current densities against the square root of  $\nu$  at  $25 \text{ }^\circ\text{C}$ . d) Cathodic peak potential versus  $\log(\nu)$  at  $25 \text{ }^\circ\text{C}$ .

Electrodeposition of cobalt was performed at different potentiostatic conditions at elevated temperature, as shown in a series of SEM micrographs in Figure 8.26. A change in the mi-

crostructure is visible with the change of potentials. For a change from  $-1.6\text{ V}$  to  $-1.8\text{ V}$  the appearance of the deposits becomes smoother and less granular. EDX analysis shows only small amounts of carbon and oxygen for both samples as well as a high concentration of cobalt. Further increase of the deposition potential to  $-2\text{ V}$  has a detrimental effect on the coating quality. What can be mistaken for a smooth coating from the SEM image is the sputtered Au substrate, as confirmed by the strong Au signal in the EDX spectrum. More negative potentials resulted in poor adhesion of the deposits to the substrate. During a cleaning procedure before EDX analysis to remove electrolyte components, parts of the coating could be rinsed off of the electrode.

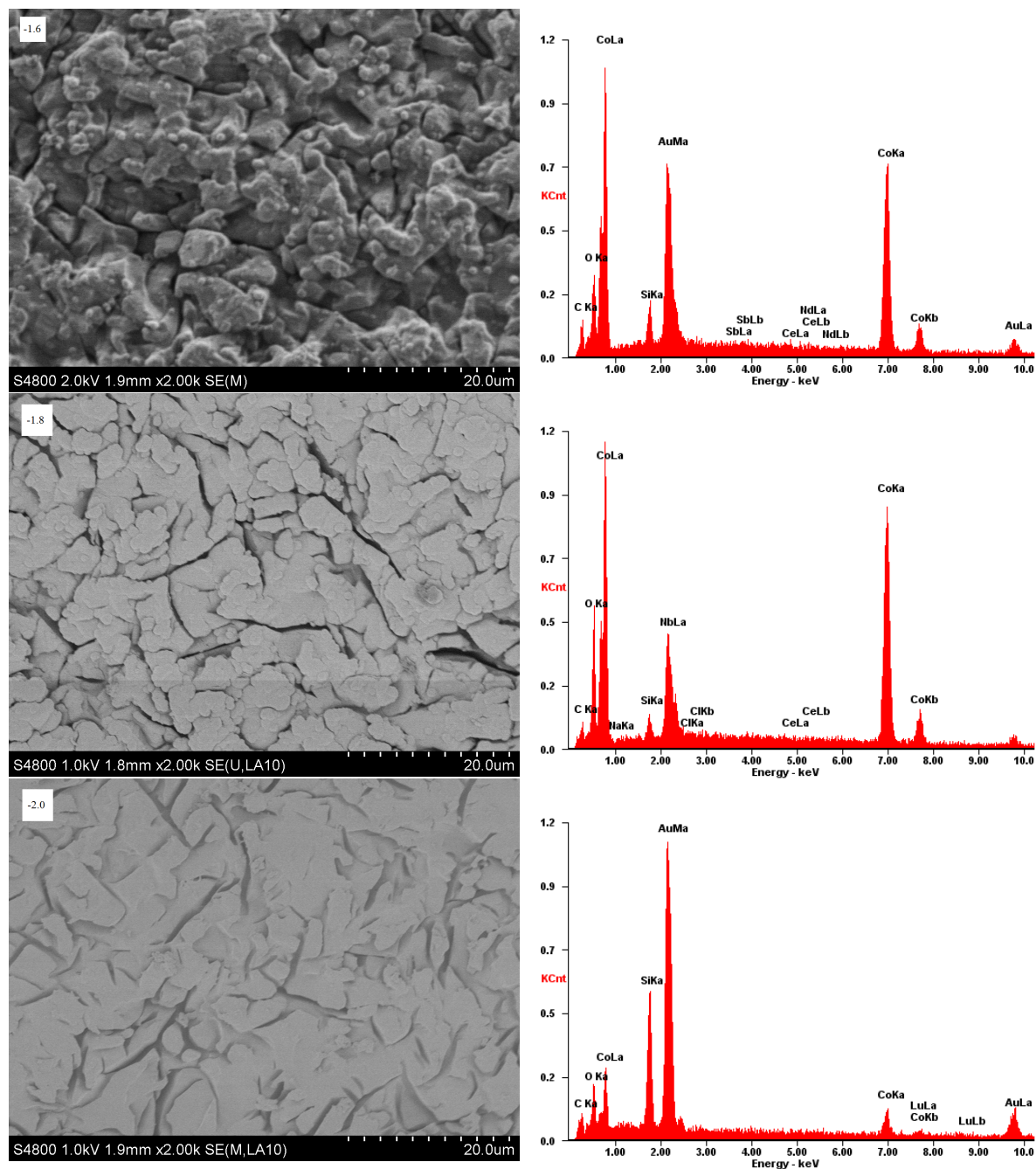


Figure 8.26: SEM micrographs and EDX patterns of electroplated cobalt under different potentiostatic conditions.  $E = -1.6$  V,  $-1.8$  V and  $-2.0$  V vs REF,  $T = 100$  °C, AE: Au, CE: Co.

## 8.6 Electrodeposition of Cobalt-Dysprosium Alloys

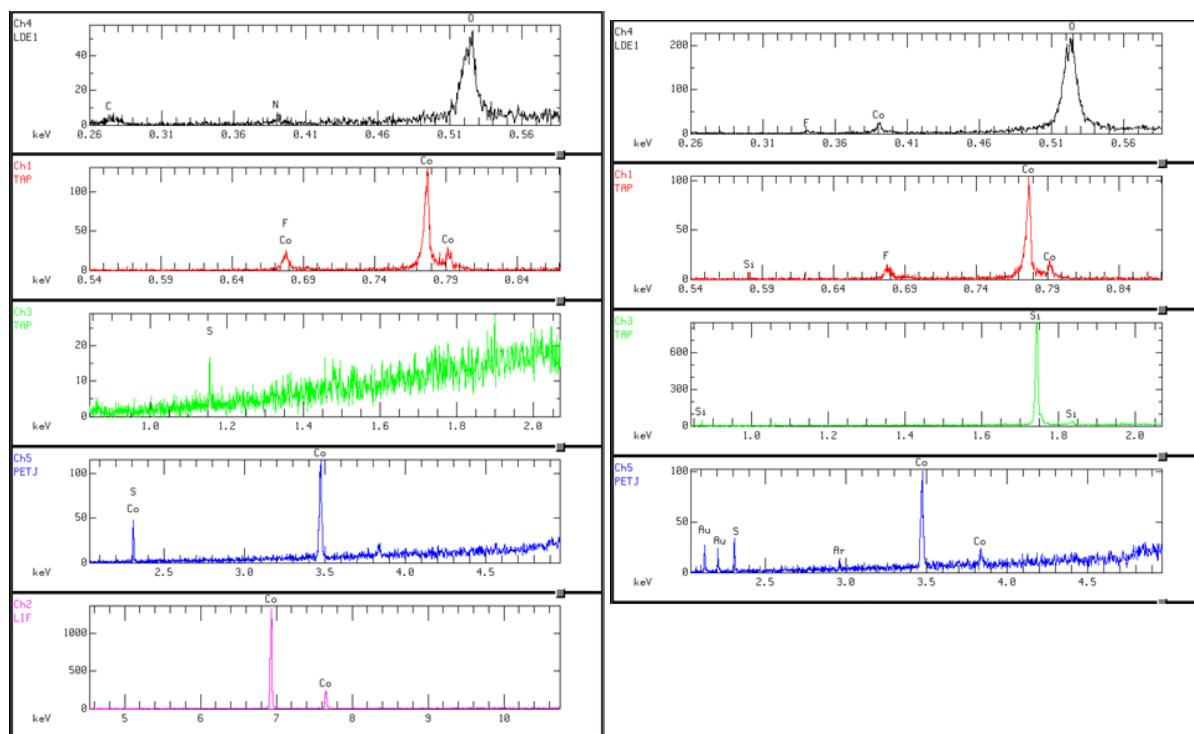


Figure 8.27: WDX pattern of electroplated cobalt at  $-1.6$  V at  $100^{\circ}\text{C}$  1 h on a gold substrate. Left: as-deposited. Right: after Ar-ion sputtering.

To further distinguish between superficial impurities and incorporation of extraneous elements into the coating, WDX analysis of a sample was performed as received and after argon ion etching. The spectra shown in Figure 8.27 show that N and O are just superficial impurities, whereas F and S can still be detected in the bulk material after sputtering which leads to the assumption that decomposition products containing higher amounts of these elements are incorporated into the coating during plating. The atomic composition of the coating before and after Ar-etching is given in Table 8.4.

Element	Atomic concentration %	
	As deposited	After Ar-ion etching
N	18.1	5.6
O	13.4	3.3
F	8.5	14.2
S	2.1	3.6
Co	57.9	73.3

Table 8.4: Composition analysis of electroplated cobalt coating as shown in Figure 8.26 as deposited and after Ar-etching.

Electrodeposition of Dy-Co alloys was investigated using an electrolyte consisting of different mixtures of  $\text{Dy}[\text{NTf}_2]_3$  and  $\text{Co}[\text{NTf}_2]_2$  in  $[\text{BMIm}][\text{NTf}_2]$ . The black curves in Figure 8.28(a) show cyclic voltammograms for mixtures of  $\text{Dy}[\text{NTf}_2]_3$  and  $\text{Co}[\text{NTf}_2]_2$  at molar ratios of 5:1 and 3:1 recorded at 100 °C, respectively. Differences to pure Co-containing electrolytes as previously shown in Figure 8.25(b) are clearly visible. During the anodic scan, two peaks can be seen in the CV of the mixed electrolyte, whereas no peak is visible for pure Dy and only one broad peak is visible for the pure Co-electrolyte. On the cathodic side, an increasing suppression of the current densities caused by cobalt deposition is visible for higher Dy-content. Similar behavior has been reported by Hsu et al. for the system  $\text{DyCl}_3\text{-CoCl}_2$  in  $\text{ZnCl}_2\text{-EMImCl}$ <sup>[237]</sup>. The change in resonance frequency was recorded with the fis-EQCM during the cyclic voltammogram of the mixture of a molar ratio of 5:1 as shown in Figure 8.28(b). During the scan in the cathodic direction, a decrease in  $\Delta f_s$  starts at about  $-0.6$  V simultaneously with an increasing cathodic current density in the CV and  $\Delta f_s$  follows the current density with a small delay. After reaching the cathodic potential limit of  $-2.4$  V,  $\Delta f_s$  continues to decrease until it reaches a plateau at about  $-1.3$  V and stalls up to about  $-0.6$  V. From the beginning dissolution of Co/Dy, an increase of  $\Delta f_s$  is expected at this point. Interestingly,  $\Delta f_s$  does not increase but even slightly decreases during the anodic scan. This is consistent with the assumption, that a change in viscosity near the electrode surface competes with the dissolution of the metallic coating affecting  $\Delta f_s$  as reported by Fukui et al.<sup>[143]</sup>. With positive current densities an increase in signal noise can be observed. This can be assigned to a roughening of the electrode surface.

Electrodeposition of Dy-Co-alloys was attempted at temperatures between 50 °C to 150 °C and potentials  $-1.4$  V to  $-1.8$  V but none succeeded for either of the mixtures.

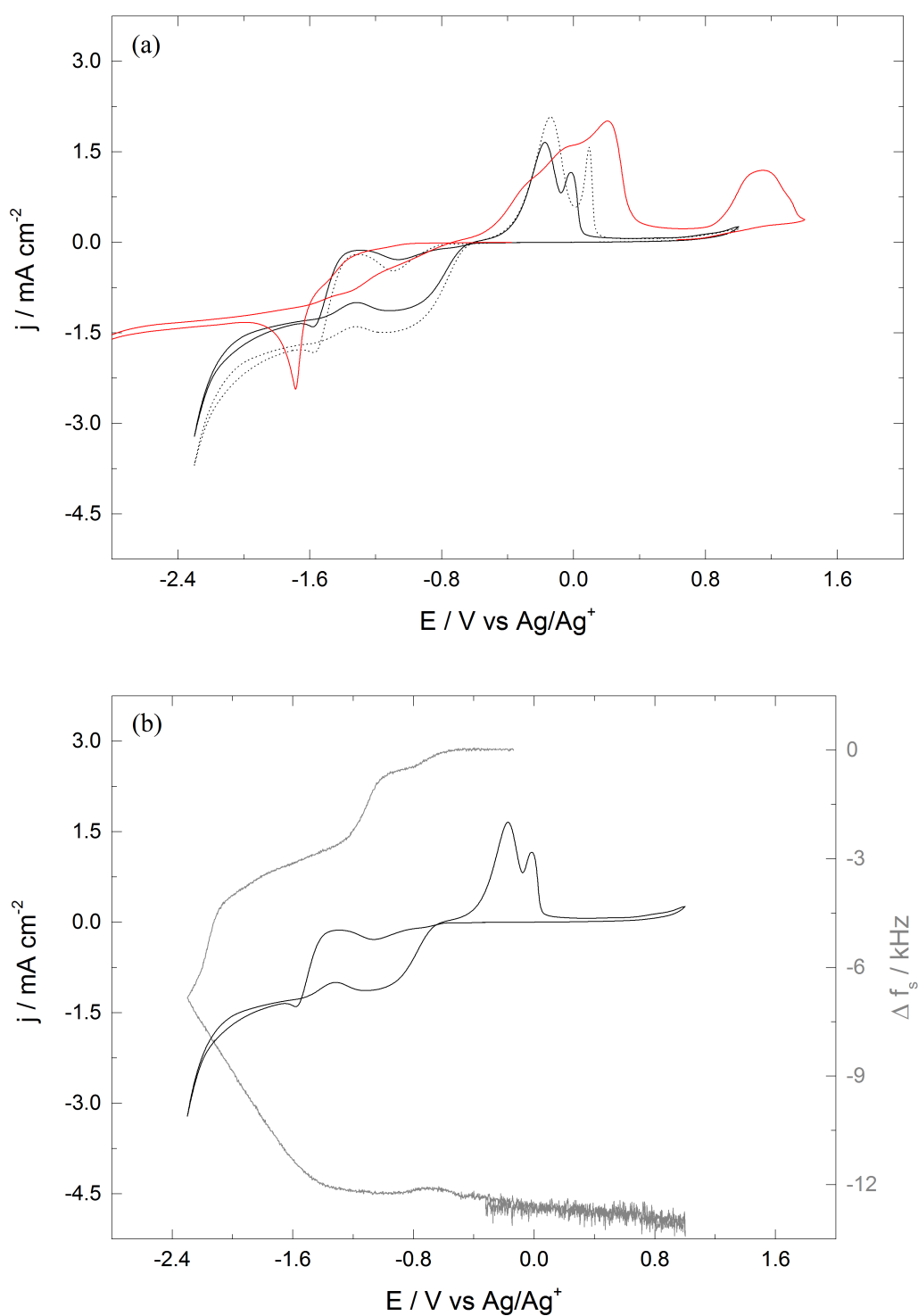


Figure 8.28: (a) Cyclic voltammograms of mixtures of  $\text{Dy}[\text{NTf}_2]_3$  and  $\text{Co}[\text{NTf}_2]_2$  in  $[\text{BMIm}][\text{NTf}_2]$ .  $\nu = 5 \text{ mV s}^{-1}$ ,  $T = 100^\circ\text{C}$ . Straight line:  $0.1 \text{ mol kg}^{-1} \text{ Dy}[\text{NTf}_2]_3$ ,  $0.02 \text{ mol kg}^{-1} \text{ Co}[\text{NTf}_2]_2$ . Dotted line:  $0.1 \text{ mol kg}^{-1} \text{ Dy}[\text{NTf}_2]_3$ ,  $0.033 \text{ mol kg}^{-1} \text{ Co}[\text{NTf}_2]_2$ . Red Line:  $0.1 \text{ mol l}^{-1} \text{ Co}[\text{NTf}_2]_2$ . (b) Cyclic voltammogram of  $0.1 \text{ mol kg}^{-1} \text{ Dy}[\text{NTf}_2]_3$ ,  $0.02 \text{ mol kg}^{-1} \text{ Co}[\text{NTf}_2]_2$  in  $[\text{BMIm}][\text{NTf}_2]$  (black curve), corresponding shift in resonant frequency (grey curve). AE: Au, CE: Pt.

## 8.7 Electrodeposition of Iron-Dysprosium Alloys

Fe–Dy-alloys have found academic as well as practical interest. Alloys with the formula  $\text{Fe}_{17}\text{RE}_2$  show high saturation magnetization  $J_{\text{sat}}$ , low Curie Temperatures ( $T_C$ ) and planar anisotropy<sup>[243]</sup>. A very interesting property of these materials is the ability to absorb a high amount of interstitials such as nitrogen or carbon with up to three atoms per formula unit which result in an change in volume as well as  $T_C$  and  $J_{\text{sat}}$ , because of an increase in the exchange interaction of the iron atoms<sup>[243]</sup>. For example, a Curie Temperature of 107 °C  $\text{Fe}_{17}\text{Dy}_2$  which increases to 362 °C for  $\text{DyFe}_2$ <sup>[244]</sup>. Binary Dy–Fe- alloys have been produced in high-temperature molten salts ( $\text{LiCl-KCl-DyCl}_3$  on Fe-electrodes)<sup>[246]</sup>, in acetamid-urea melts<sup>[247]</sup>, as well as ionic liquids like  $[\text{EMIm}]\text{Cl}$ <sup>[248]</sup>.

Iron can be electroplated from aqueous solutions, of which acidic sulfate- or chloride-based solutions are the most common<sup>[245]</sup>

The electrochemical behavior of the system  $\text{Fe}[\text{NTf}_2]_2$  in  $[\text{BMIM}][\text{TFSI}]$  was studied by cyclic voltammetry. Figure 8.29(a) presents a series of cyclic voltammograms of  $0.05 \text{ mol l}^{-1}$   $\text{Fe}[\text{NTf}_2]_2$  in  $[\text{BMIM}][\text{TFSI}]$  recorded at room temperature with different scan rates on a gold electrode. A cathodic peak ascribed to the plating of Fe is visible at about  $-2.1 \text{ V}$ . In contrast to the Co-system studied above, there is a noticeable anodic current density at about  $-0.4 \text{ V}$ , caused by stripping of previously plated Fe. An increase of the scan rate causes the peak potentials  $E_{\text{pc}}$  and  $E_{\text{pa}}$  to drift apart as well as an increase of the peak current densities  $j_{\text{pc}}$  and  $j_{\text{pa}}$ , respectively.

The effect of a higher temperature on the behavior of the plating/stripping process is shown in Figure 8.29(b). It is noticeable, that the peak current density increases for higher temperatures. Also, the peak potential difference between the cathodic and anodic peak potentials decrease with increasing temperature by a shift of  $E_{\text{pc}}$  of about 0.6 V. The effect of the temperature is not as pronounced for  $E_{\text{pa}}$ , as the potential shifts by just about 0.1 V.

The cathodic peak current densities are plotted against the square root of the scan rate in Figure 8.29(c). A linear response indicates that the reduction process is diffusion controlled. The linear behavior of the cathodic peak potential in respect to the logarithm of the scan rate, as shown in Figure 8.29(d) indicates that the process is electrochemically irreversible. From the slope in Figure 8.29(c) and a value of  $\alpha = 0.13$ , a diffusion coefficient of  $(6.68 \pm 0.02) \times 10^{-8} \text{ cm}^2 \text{ s}^{-1}$  can be calculated.

The effect of different deposition potentials on the morphology and composition on the electroplating of iron from  $0.05 \text{ mol l}^{-1}$   $\text{Fe}[\text{NTf}_2]_2$  in  $[\text{BMIm}][\text{NTf}_2]$  was investigated by SEM microscopy, EDX and WDX. Potentials from  $-1.6$  to  $-2.0 \text{ V}$  were applied for 1 h at 100 °C



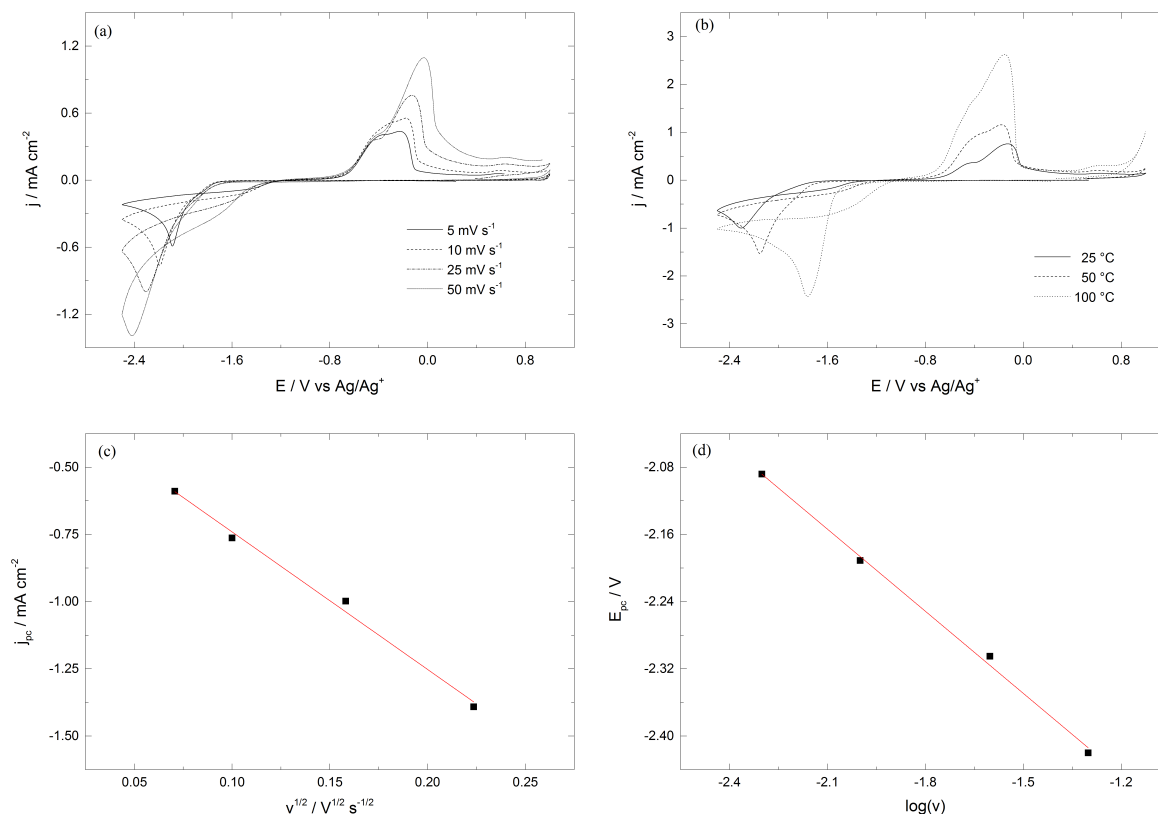


Figure 8.29: (a) Cyclic voltammograms of  $0.05 \text{ mol l}^{-1} \text{ Fe[NTf}_2\text{]}_2$  in  $[\text{BMIm}][\text{NTf}_2]$  recorded at room temperature on Au-WE,  $\nu = 5 \text{ mV s}^{-1}$ ,  $10 \text{ mV s}^{-1}$ ,  $25 \text{ mV s}^{-1}$  and  $50 \text{ mV s}^{-1}$ . (b) Cyclic voltammograms at different temperatures at  $25 \text{ mV s}^{-1}$ . (c) Plot of the peak current densities against the square root of  $\nu$  at  $25 \text{ }^\circ\text{C}$ . (d) Cathodic peak potential versus  $\log(\nu)$  at  $25 \text{ }^\circ\text{C}$ .

to obtain iron-plated Au-sputtered quartz substrates. The effect of  $E$  is demonstrated in Figure 8.30. At  $-1.6 \text{ V}$ , SEM micrograph shows small deposits, which partially cover the substrate. Au-signals that are present in the corresponding EDX pattern corroborate this observation. The sample is rather pure, as no impurities from the electrolyte can be detected.

A more negative potential ( $-1.8 \text{ V}$ ) produces a thick, cracked layer of iron. The corresponding EDX pattern shows no significant impurities. The presence of oxygen and carbon can be attributed to the exposure of the sample to air.

In the SEM micrograph presented for deposits produced at  $-2.0 \text{ V}$ , the underlying substrate is visible, just as for the deposition of Co at this potential. EDX analysis shows that there are no significant impurities present, but that the surface is not covered by iron as shown by the large signals of gold and silicon.

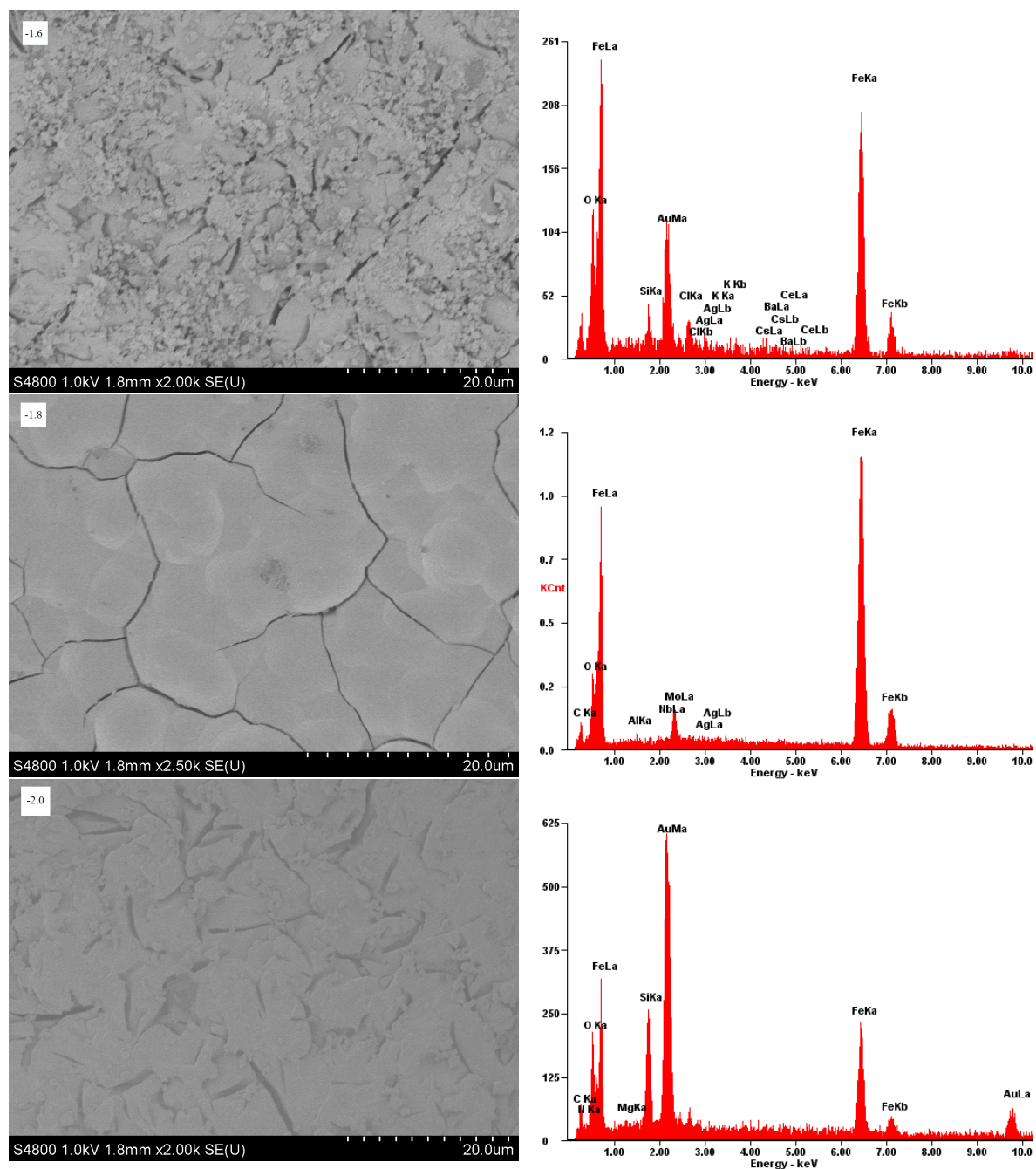


Figure 8.30: SEM micrographs and EDX patterns of electroplated iron under different potentiostatic conditions from  $0.05 \text{ mol l}^{-1}$  solution of  $\text{Fe}[\text{NTf}_2]_2$  in  $[\text{BMIm}][\text{NTf}_2]$ .  $E = -1.6 \text{ V}$ ,  $-1.8 \text{ V}$  and  $-2.0 \text{ V}$  vs REF,  $T = 100^\circ\text{C}$ , AE: Au, CE: Fe.

Complementary WDX analysis was performed for a sample with potentiostatic conditions at  $-1.8$  V as it showed to be mechanically stable and pure iron from EDX analysis. WDX patterns recorded for an as-deposited sample are shown on the left spectrum in Figure 8.31. The spectrum recorded after Ar-sputtering is shown on the right. It is visible, that the (superficial) signals for fluorine and sulfur are reduced after the sputtering procedure and the signal from nitrogen even disappears completely. The iron as well as oxygen signals remain present after sputtering, indicating partial oxidation of the layer throughout the entire sample. The amount of impurities given in at. % are summarized in Table 8.5.

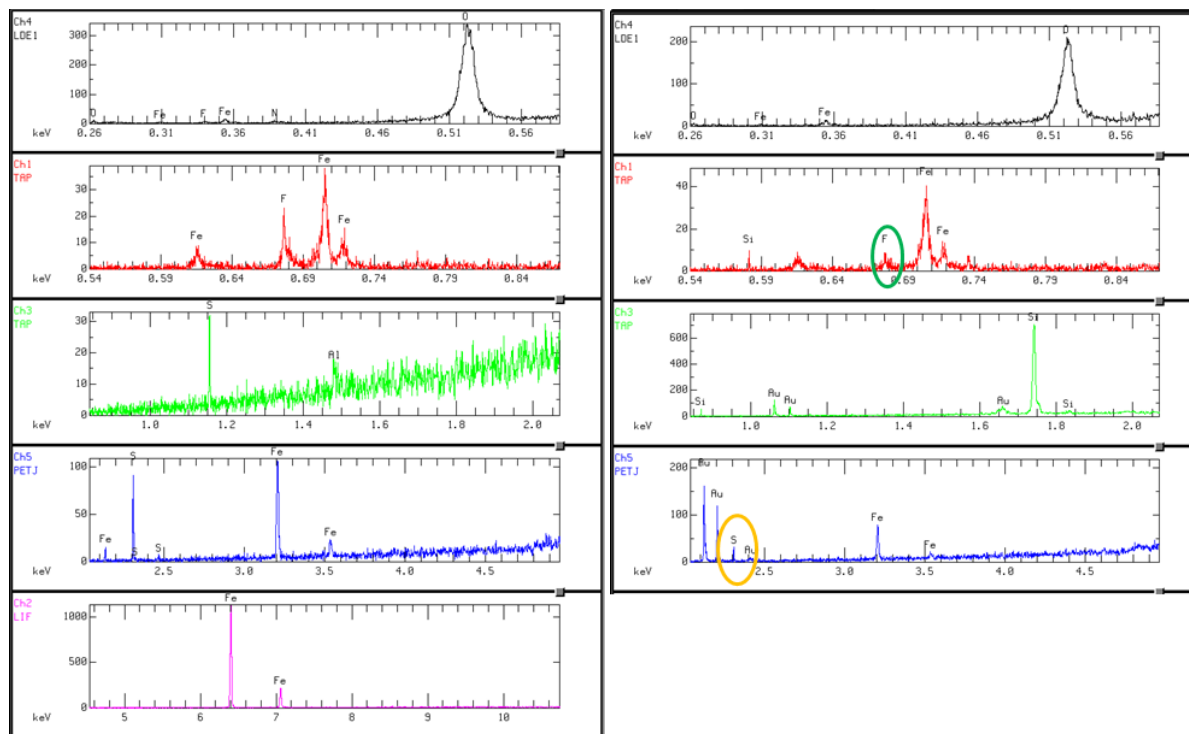


Figure 8.31: WDX pattern of electroplated iron from  $0.05 \text{ mol l}^{-1} \text{ Fe[NTf}_2\text{]}_2$  in  $[\text{BMIM}][\text{NTf}_2]$ .  $E = -1.8$  V,  $T = 100$  °C. WE: Au, CE: Fe. Left: as-deposited. Right: after Ar-ion sputtering.

Mixtures of different molar ratios of  $\text{Dy[NTf}_2\text{]}_3$  and  $\text{Fe[NTf}_2\text{]}_2$  in  $[\text{BMIm}][\text{NTf}_2]$  were investigated to attempt the electrodeposition of Dy-Fe alloys. Figure 8.32(a) shows the cyclic voltammograms of 5:1 ( $0.1 \text{ mol l}^{-1} : 0.02 \text{ mol l}^{-1}$ ) and 3:1 ( $0.1 \text{ mol l}^{-1} : 0.033 \text{ mol l}^{-1}$ ) ratios of Dy to Fe at  $100$  °C. The red curve shows the CV for an electrolyte containing only iron. It is instantly noticeable, that the shapes of the voltammograms shown for the mixtures containing Dy deviate from one without dysprosium. Furthermore, for the 5:1 and 3:1 mixtures, a cathodic peak at about  $-2.4$  V is visible, whereas for the iron solution, the peak corresponding to the reduction of iron is seen at  $-1.8$  V. The cathodic peak disappears almost completely. Small anodic current densities are seen, which are shifted to more positive values in compari-

Element	Atomic concentration %	
	As deposited	After Ar-ion etching
N	7.0	-
O	17.4	17.7
F	11.2	9.6
S	5.9	3.3
Fe	58.3	69.4

Table 8.5: Composition analysis of electroplated iron coating as shown in Figure 8.30 as deposited and after Ar-etching.

son to the peak corresponding to the stripping of pure Fe from  $-0.4$  V to  $0$  V. An explanation can be given by co-deposited Dy, which shows irreversible behavior in this system (also, see previous chapter). Electroplated Dy could not be dissolved in this ionic liquid. This means, that either a substantial amount of the charge passed during the cathodic scan in the CV is attributed to the reduction of  $\text{Dy}^{3+}$ , which can not be dissolved during the anodic scan or that co-deposited Dy inhibits the stripping of iron.

Recording of the CV of a 5:1 mixture of Dy:Fe was accompanied by the recording of the resonant frequency by the fis-EQCM. The plot of the change in resonant frequency  $\Delta f_s$  during the CV is shown in Figure 8.32(b). The scan was started from OCP to  $-2.8$  V.  $\Delta f_s$  starts to decrease at about  $-1$  V along with an increasing cathodic current density, where the frequency stays relatively constant until about  $-2$  V where it starts to drop again and the current density starts to increase as well. During the scan back to  $1.5$  V,  $\Delta f_s$  does not drop any further until it starts rising at about  $0$  V where also anodic current densities are visible.

Attempts to deposit Dy-Fe-alloys were not successful. Variations of the temperature between  $50$  to  $150^\circ\text{C}$  and of the potential between  $-1.5$  to  $-2.0^\circ\text{C}$  delivered very poorly adhesive black deposits which were not suitable for SEM or EDX analysis.

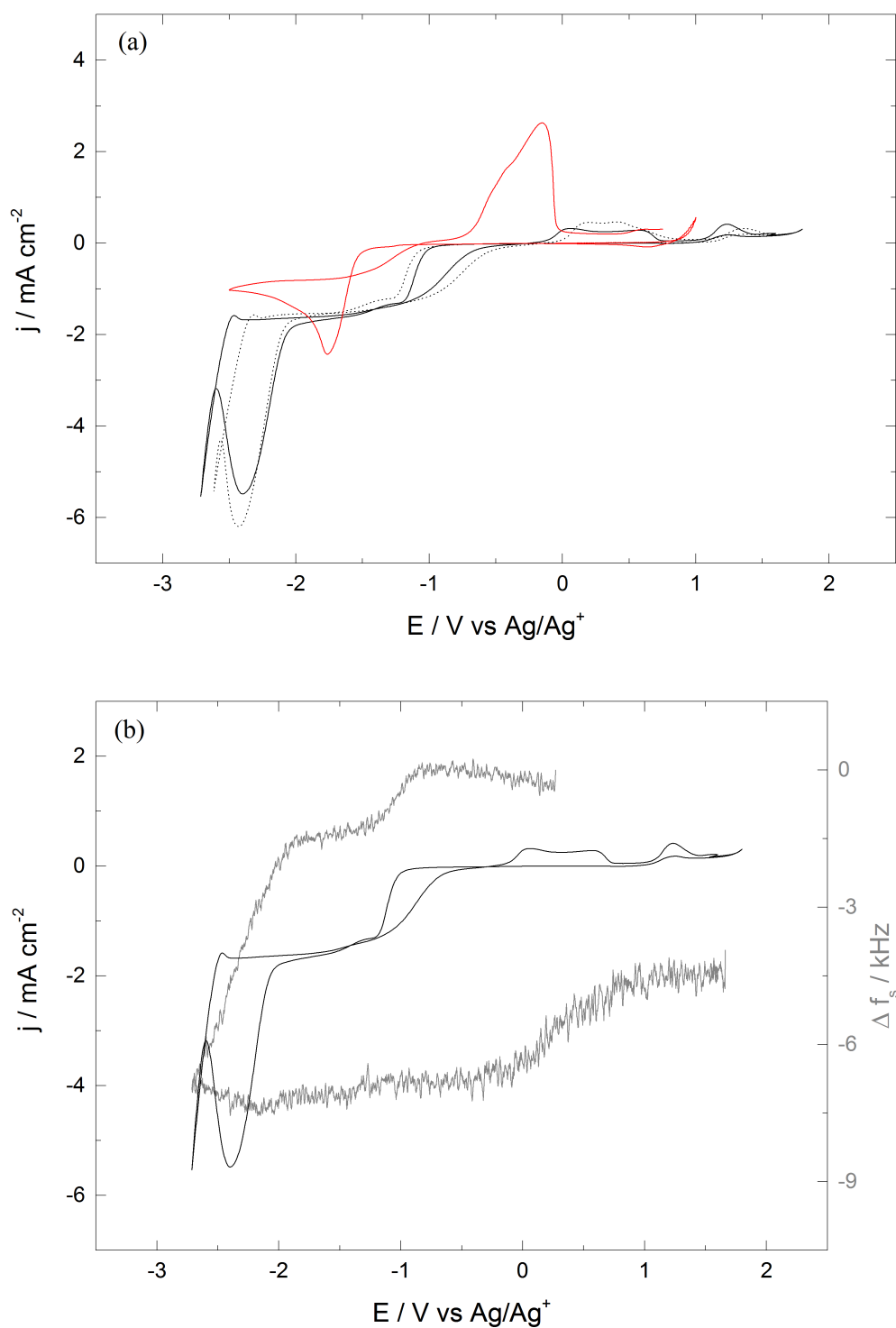


Figure 8.32: (a) Cyclic voltammograms of mixtures of  $\text{Dy}[\text{NTf}_2]_3$  and  $\text{Fe}[\text{NTf}_2]_2$  in  $[\text{BMIm}][\text{NTf}_2]$ .  $\nu = 5 \text{ mV s}^{-1}$ ,  $T = 100^\circ \text{C}$ . Straight line: 0.1 mol kg<sup>-1</sup>  $\text{Dy}[\text{NTf}_2]_3$ , 0.02 mol kg<sup>-1</sup>  $\text{Fe}[\text{NTf}_2]_2$ . Dotted line: 0.1 mol kg<sup>-1</sup>  $\text{Dy}[\text{NTf}_2]_3$ , 0.033 mol kg<sup>-1</sup>  $\text{Fe}[\text{NTf}_2]_2$ . Red Line: 0.1 mol l<sup>-1</sup>  $\text{Fe}[\text{NTf}_2]_2$ . (b) Cyclic voltammogram of 0.1 mol kg<sup>-1</sup>  $\text{Dy}[\text{NTf}_2]_3$ , 0.02 mol kg<sup>-1</sup>  $\text{Fe}[\text{NTf}_2]_2$  in  $[\text{BMIm}][\text{NTf}_2]$  (black curve), corresponding shift in resonant frequency (gray curve). AE: Au, CE: Pt.

# 9 Summary and Conclusions

## 9.1 Aim and Results of this Thesis

The presented thesis aims at the improvement the magnetic properties of Nd-Fe-B-sintered magnets by grain boundary diffusion. This approach was reported in Chapters 5 and 6 using grain boundary diffusion treatment of Nd–Fe–B-sintered magnets coated with different metals produced by physical vapor deposition.

Literature reports positive effects on the addition of aluminum and copper to HRE-free Nd-Fe-B sintered magnets. This work studied the effect of grain boundary diffusion of HRE-free coatings on the magnetic properties of Nd-Fe-B sintered magnets with a low initial HRE content. It could be shown that the grain boundary diffusion treatment with non-rare-earths, namely Cu and Al did not lead to positive changes the coercivity  $H_{cJ}$ , the most important application-oriented key value. The addition of Al led to a substantial decrease in coercivity of almost 20 %, even for the lowest addition. In comparison to Al, Cu decreased the coercivity by about 7.5 %.

Grain boundary diffusion treatment of magnetic samples with the heavy rare earths dysprosium and terbium led to an increase of  $H_{cJ}$  of up to 34 % and 48 %, respectively. The response of the coercivity with increasing addition is characteristic for grain boundary diffusion-processed sintered magnets where small additions of up to 0.07 wt % result in a strong increase of the coercivity of about 16 % and 28 % for dysprosium and terbium, respectively. Analysis of cross-sectional SEM micrographs show a rounding and cracking of near-surface grains caused by melting of intergranular phases and their fast solidification upon cooling. Wavelength dispersive x-ray spectroscopy depth-profiling and EPMA elemental mapping was used to determine the distribution of the dopants inside the material. Depth-profiling revealed a decreasing concentration of the heavy rare earth detectable up to about 100  $\mu\text{m}$  perpendicular to the coated surface. From the fit of the WDX depth-profile to a simple effective medium diffusion model a diffusion coefficient for Tb was calculated. EPMA elemental mapping revealed a concentration of heavy rare earth along the grain boundaries while no HRE is present inside the  $\text{Nd}_2\text{Fe}_{14}\text{B}$  matrix grains, distinctive for grain boundary diffusion treated magnets. In order to increase diffusion depth, a series of coatings with low-melting eutectic binary alloys consisting of Al and Dy were applied. Grain boundary diffusion of a series of alloys with a

fixed weight fraction of 22 % aluminum and 78 % dysprosium (“low-Dy alloy”) resulted in a negative effect on the coercivity in spite of a total increase in heavy rare earth content for each sample of the series. A second series with a fixed weight ratio of 87.6 % aluminum and 12.4 % dysprosium (“high-Dy alloy”) was investigated as well. Grain boundary diffusion treatment of samples coated with this alloy showed an increase of the coercivity up to additions of 0.11 wt. % Al. Cross sectional SEM microscopy of high-Dy alloy treated samples revealed the microstructure characteristic of GBD-processed sintered magnets. WDX depth-profiling conclude that the application of this alloy did not have an effect on the diffusion of Dy. EPMA analysis was conducted to reveal the concentration of Al and Dy of GBD-processed samples and showed that Al was concentrated in the intergranular phases.

The second and main part of this thesis, presented in Chapter 7 focused on the electrochemistry of rare earth and transition metal elements and their electroplating as the first step of the grain boundary diffusion process.

Air- and water-stable room temperature ionic liquids were for the plating baths, as their properties makes them more favorable for the treatment of Nd-Fe-B-sintered magnets than ionic liquids based on chlorometalate-based ILs and high temperature molten salts. Plating on bare Nd-Fe-B proved to be fairly difficult, and based on the results obtained for GBD-treatment with HRE-free coatings, copper was selected as an adhesion layer. Electroplating of Cu on Nd-Fe-B-samples was successfully conducted from different ionic liquids and various copper sources, among which copper-(II)-bis(trifluoromethylsulfonyl)imide was synthesized and characterized.

Electroplating of dysprosium was attempted from different ionic liquids and various dysprosium salts as the metal source, including tailor-made dysprosium-(III)-bis(trifluoromethylsulfonyl)imide. Electroplating from triflate-based electrolytes did not show satisfactory results, as seen by SEM-microscopy and EDX analysis, and the attempts to plate Dy from tetrafluoroborate-based ILs, as reported in the literature, as well as from a dicyanamide-based IL failed. However, electroplating from triflamide-based systems, specially from a pyrrolidinium-based ionic liquid with the corresponding Dy salt allowed the deposition of dense Dy-coatings of up to 2.5  $\mu\text{m}$  thickness with current efficiencies of around 78 %. EDX and WDX analysis showed only superficial impurities of the coatings. This system was thoroughly characterized by cyclic voltammetry and chronoamperometry and the diffusion coefficient of this system was determined. A subsequent grain boundary diffusion process with electrochemically coated Nd-Fe-B-samples enhanced the coercivity by up to 20.4 %.

Given by the results for the GBD-treatment of magnet samples with terbium by PVD, electroplating of this element from an ionic liquid-based electrolyte was attempted as well. Based

on the results of dysprosium deposition, [OTf]- and [NTf<sub>2</sub>]- based ionic liquids presented the focus of the study. Despite the promising features of the corresponding CVs and CAs, potentiostatic as well as galvanostatic deposition from triflate-based ionic liquids failed. A NTf<sub>2</sub>-based system on the other hand showed that a the deposition of Tb is feasible from Tb[NTf<sub>2</sub>]<sub>3</sub> in 1-butyl-1-methylpyrrolidinium bis(trifluoromethylsulfonyl)imide. This system was thoroughly characterized. SEM-microscopy showed a fibrous, cracked morphology for the coating for the received for the applied deposition conditions. WDX analysis and elemental mapping showed a high concentration of sulfur and terbium in the coating indicating the formation of Tb<sub>2</sub>S<sub>3</sub>. Nd-Fe-B-magnets coated with the thin, brittle coating were subdued to a GBD-process and demonstrated an increase of the coercivity of about 9.1 %, comparable an addition of about 0.02 wt % Tb.

Studies on the grain boundary diffusion treatment of hot-deformed Nd-Fe-B magnets with alloys containing neodymium and copper have reported an increase in the coercivity, due to a better isolation of the matrix grains by the formation of non-magnetic intergranular phases. Similar treatment as Nd-Fe-B sintered magnet is conceivable for hot-deformed magnets, therefore the deposition of Nd was studied in different ionic liquids. Triflate-based electrolytes were excluded, as the solubility of the Nd-salt was very low, even at elevated temperatures. just as shown for Dy and Tb, [Tf<sub>2</sub>]-based electrolytes showed the best results. Porous but well adhesive deposits were obtained for galvanostatic deposition. Composition analysis by EDX shows significant impurities of F, S and C. Nonetheless, this system might show considerable improvement in coating quality upon further optimization.

Finally, the deposition of transition metals and RE-TM-alloys (RE = Dy; TM = Co, Fe) from ionic liquid-based electrolytes were investigated. Well adhesive, dense coatings of cobalt and iron could be deposited under potentiostatic conditions at  $-1.6$  V and  $-1.8$  V, respectively. WDX analysis of a sample plated with Co showed superficial impurities of N and O, whereas F is found after removal of the top layers by Ar-sputtering. In the case of iron, F and O are found throughout the entire sample thickness, N and S are mostly superficial.

The deposition of Dy–Co alloys from 5:1 and 3:1 molar mixtures of Dy[NTf<sub>2</sub>]<sub>3</sub> and Co[NTf<sub>2</sub>]<sub>2</sub> was investigated by cyclic voltammetry. An effect of an increasing molar ration of Dy on the shapes of the voltammograms could be observed. The change of resonant frequency with the potential could be observed that confirmed the deposition of Dy/Co as expected from the cathodic currents of the CV. During the anodic scan, there is no apparent increase of the frequency, indicating that the electroplated coating is not stripped from the electrode despite anodic current densities in the CV. This observation was ascribed to an increase of the viscosity near the electrode upon dissolution of Dy and Co and saturation of the IL with Dy and Co



salts. A damping effect on the crystal electrode as well as a roughening of the surface caused by stripping of the coating. Deposition of alloys under different potentiostatic conditions and temperatures were not successful.

Electrolytes containing 5:1 and 3:1 molar ratios of  $\text{Dy}[\text{NTf}_2]_3$  and  $\text{Fe}[\text{NTf}_2]_2$  were studied at elevated temperatures. It is visible, that the cathodic peak currents shift to more negative potentials with increasing Dy concentration. In contrast to the system Dy-Co, the stripping peak observed for the pure iron-system is almost completely suppressed in the presence of Dy. An explanation for this particular behavior was given by the irreversible plating of co-deposited Dy. The change in resonant frequency was recorded for the cyclic voltammogram of 5:1 Dy:Fe. A decrease of  $\Delta f_s$  was observed with cathodic current densities, indicating a deposition process. As the potential scan was reversed, the frequency remained fairly constant and slightly increased as anodic current densities increased but did not return to zero. Passed cathodic charge was higher than the anodic charge, corroborating the incomplete stripping of Dy/Fe during the previous cathodic scan. Different potentiostatic conditions and temperatures were applied to deposit alloys from these mixtures. The deposits obtained were black and not adherent to the substrate.

## 9.2 Innovations presented in this Work

First of all, a new method was presented to coat Nd-Fe-B-sintered magnets with copper by an electroplating process from an air- and water-stable ionic liquid. Electroplating of Nd-Fe-B-sintered magnets with corrosion-protecting coatings of Zn, Al, and Ni from chlorometalate melts have been reported. However to the author's knowledge no plating of Cu on this type of material has been attempted for subsequent plating / GBD-treatment.

To investigate the most suitable electrolytes for plating of rare earths, routes for TM- and RE-salt synthesis described in the literature were modified by using carbonate-precursors. It was found that the substitution of dysprosium oxide by dysprosium carbonate led to an increase of the yield from 89 to 96.3 % as well as a reduction of reaction time for the synthesis of  $\text{Dy}[\text{NTf}_2]_3$ . The substitution of metal oxides by their respective carbonates showed similar results for the synthesis of  $\text{Tb}[\text{NTf}_2]_3$ ,  $\text{Nd}[\text{NTf}_2]_3$ ,  $\text{Co}[\text{NTf}_2]_2$ ,  $\text{Cu}[\text{NTf}_2]_3$  and  $\text{Ag}[\text{NTf}_2]$  for which in the most cases yields well over 90 % were obtained. Table 9.1 gives an overview of the salts synthesized according the new procedure and their respective yields.

Metal salt	Yield [ % ]
$\text{Ag}[\text{NTf}_2]$	95.4
$\text{Co}[\text{NTf}_2]_2$	87
$\text{Cu}[\text{NTf}_2]_2$	85.3
$\text{Fe}[\text{NTf}_2]_2$	78.2
$\text{Dy}[\text{NTf}_2]_3$	96.3
$\text{Nd}[\text{NTf}_2]_3$	90.3
$\text{Tb}[\text{NTf}_2]_3$	96

Table 9.1: Listing of the synthesized salts used in this work

Within this work, a procedure for the electroplating of dense, well adhesive Dy-coatings is presented. Furthermore, this procedure can be successfully applied as the first step in the grain boundary diffusion treatment of Nd-Fe-B-sintered magnets to improve the magnetic properties of this material. These results were presented at several conferences (see section 9.3).

Following the plating of Dy, attempts were made to plate metallic Tb from air- and water-stable RTILs. Despite the fact that the obtained coatings contained major amounts of sulfur, to this point the electroplating of pure Tb from ionic liquids has not been reported in the literature.

The grain boundary diffusion treatment of hot-deformed with Nd-Cu-alloys presents a feasible way to increase their coercivity. The electrochemistry of neodymium in different electrolytes was studied. Albeit the plating procedure to obtain metallic Nd coatings requires further optimization, this rare earth element was deposited from a triflamide-based electrolyte, of which there are no reports in the literature.

Attempts were made to deposit Dy-Co as well as Dy-Fe alloys from an imidazolium-based ionic liquid. Although the deposition of the alloys failed, the transition metals could be deposited from the so far unreported systems  $\text{Co}[\text{NTf}_2]_2$  /  $[\text{BMIm}][\text{NTf}_2]$  and  $\text{Fe}[\text{NTf}_2]_2$  /  $[\text{BMIm}][\text{NTf}_2]$ , respectively.

In conclusion, a summary of the determined diffusion coefficients, their method of determination and the investigated system of all rare-earth systems studied in this work as well as others reported in the literature are given in Table 9.2 for comparison.

$\text{Ln}^{3+}$ - species	$D \cdot 10^8 \text{ cm}^2 \text{ s}^{-1}$	Method	Ionic liquid	Reference
$0.145 \text{ mol l}^{-1} \text{ Nd}[\text{NTf}_2]_3$	1.37	CV	$[\text{BMPyr}][\text{NTf}_2]$	this work
	3.92	SI		this work
$0.25 \text{ mol l}^{-1} \text{ Nd}[\text{NTf}_2]_3$	0.7 (at $50^\circ\text{C}$ )	CP	$[\text{P}_{2225}][\text{NTf}_2]$	[142]
$0.1 \text{ mol l}^{-1} \text{ Sm}[\text{NTf}_2]_3$	3.1	CA	$[\text{BMPyr}][\text{NTf}_2]$	[220]
	2.7	CP		[220]
$0.1 \text{ mol l}^{-1} \text{ Eu}[\text{NTf}_2]_3$	3.1	CA	$[\text{BMPyr}][\text{NTf}_2]$	[220]
	2.8	CP		[220]
$0.147 \text{ mol l}^{-1} \text{ Dy}[\text{NTf}_2]_3$	2.01	CV	$[\text{BMPyr}][\text{NTf}_2]$	this work
	1.88	SI		this work
$0.075 \text{ mol l}^{-1} \text{ Dy}[\text{NTf}_2]_3$	2.0	SI	$[\text{P}_{2225}][\text{NTf}_2]$	[140]
$0.047 \text{ mol l}^{-1} \text{ Tb}[\text{NTf}_2]_3$	$4.5 \pm 0.4$	CV	$[\text{BMPyr}][\text{NTf}_2]$	this work
$0.1 \text{ mol l}^{-1} \text{ Yb}[\text{NTf}_2]_3$	3.6	CA	$[\text{BMPyr}][\text{NTf}_2]$	[220]
	3.4	CP		[220]
$0.141 \text{ mol l}^{-1} \text{ Co}[\text{NTf}_2]_2$	$1.60 \pm 0.06$	CV	$[\text{BMIm}][\text{NTf}_2]$	this work
$0.1 \text{ mol l}^{-1} \text{ Co}[\text{NTf}_2]_2$	10 (at $27.8^\circ\text{C}$ )	CA	$[\text{BMPyr}][\text{NTf}_2]$	[241]
$0.05 \text{ mol l}^{-1} \text{ Fe}[\text{NTf}_2]_2$	$6.68 \pm 0.02$	CV	$[\text{BMIm}][\text{NTf}_2]$	this work
$0.1 \text{ mol l}^{-1} \text{ Fe}[\text{NTf}_2]_2$	9.7	CA	$[\text{BMPyr}][\text{NTf}_2]$	[242]

Table 9.2: Summary of diffusion coefficients of trivalent  $\text{Ln}^{3+}$ -species in  $[\text{BMPyr}][\text{NTf}_2]$  determined in this work and reported in the literature. CV: Cyclic voltammetry. CP: Chronopotentiometry. CA: Chronoamperometry. SI: Semi-integral method.

## 9.3 Scientific Contributions

### 9.3.1 Poster Presentations

G. Suppan, M. Ruehrig, H. J. Gores: *Stronger high performance Nd-Fe-B- magnets by electroplating dysprosium from ionic liquids and subsequent grain boundary diffusion*, **7 th Green Solvents Conference**, Dresden 2014

G. Suppan, C. Brombacher, M. Katter, M. Rührig: *Grain Boundary Diffusion in Nd-Fe-B Permanent Magnets using an Electrochemical HRE Deposition Process*, **23rd Rare Earth and Future Permanent Magnets and their Applications**, Annapolis, USA 2014

### 9.3.2 Oral Contributions

G. Suppan, M. Ruehrig, H. J. Gores - Electroplating of dysprosium from ionic liquids as the first step of the grain boundary diffusion process for stronger Nd-Fe-B- magnets, **Electrochemistry 2014**, Mainz, 2014

G. Suppan - Grain Boundary Diffusion of dysprosium in Nd-Fe-B- sintered magnets, **Siemens IEC Seminar lecture series**, Erlangen, 2013

### 9.3.3 Publications

G. Suppan, M. Ruehrig, H. J. Gores, "Grain Boundary Diffusion in Nd-Fe-B Magnets Using an Electrochemical Dysprosium Deposition Process", (2015) *IEEE Transactions on Magnetics*, in preparation

G. Suppan, H. J. Gores, M. Ruehrig, A. Kanitz, "Production of high performance NdFeB magnets by grain boundary diffusion of electroplated Dysprosium", (2015) *Journal of the Electrochemical Society*, submitted

G. Suppan, A. Lorentz, M. Ruehrig, H. J. Gores, "Grain Boundary Diffusion of Dysprosium and Terbium - A Comparative Study", (2015) *IEEE Transactions on Magnetics*, in preparation

G. Suppan, M. Ruehrig, C. Brombacher, M. Katter, "Grain Boundary Diffusion in Nd-Fe-B Permanent Magnets using an Electrochemical HRE Deposition Process", (2014) *Proceedings*

of the 23<sup>rd</sup> Rare Earth and Future Permanent Magnets and their Applications, 342-344

Franz E. Wudy, Dominik J. Moosbauer, Michael Multerer, Georg Schmeer, Hans-Georg Schweiger, Christoph Stock, Peter F. Hauner, Gottfried A. Suppan, Heiner J. Gores, "Fast Micro-Kelvin Resolution Thermometer Based in NTC Thermistors", *J. Chem. Eng. Data*, **56** (12), 4823-4828 (2011)

#### 9.3.4 Patents

G. Suppan, M. Ruehrig, "Electroplating of metallic Terbium for the production of high performance rare-earth permanent magnets", 2014, (Patent number pending)

G. Suppan, M. Ruehrig, "Electrodeposition of metallic Neodymium for the production of high performance rare-earth permanent magnets", 2014, (Patent number pending)

M. Ruehrig, G. Schmid, G. Suppan, A. Kanitz, W. Kantlehner, G. Maas, "Ionic liquids as electrolytes for the electrochemical deposition of reactive metals with very negative redox potentials", 2013, (Patent number pending)



# List of Figures

1.1	Usage of rare-earth elements . . . . .	1
1.2	Price trends for selected rare earths . . . . .	2
2.1	Change in free energy $\Delta G^\#$ with the potential $\Delta E$ . . . . .	7
2.2	Simulated Tafel-plots for anodic and cathodic branches of the current-overpotential curve $a = 0.5$ , $T = 298$ K, and $j_0 = 10 \times 10^{-6} \text{ A cm}^{-2}$ . . . . .	10
2.3	Electrochemical double-layer model by Helmholtz. . . . .	12
2.4	Electrochemical double-layer model by Gouy and Chapman. . . . .	13
2.5	Electrochemical double-layer model by Stern-Graham . . . . .	15
2.6	Steps in the electrocrystallization process . . . . .	17
2.7	Initial and final states in metal deposition. . . . .	18
2.8	Illustration of the ion-transfer mechanisms . . . . .	19
2.9	Illustration of different growth mechanisms . . . . .	21
2.10	Current-time transients for instantaneous and progressive nucleation . . . . .	24
2.11	Schematic crystal lattices for conventional inorganic salts and ionic liquids. . . . .	27
2.12	Chemical structures of commonly studied cations and anions used for ionic liquids. . . . .	28
2.13	Strength of the exchange energy in as a function of the ratio of the inter-atomic distance $D$ to the diameter $d$ of the 3d shell. . . . .	31
2.14	Generalized hysteresis curve . . . . .	34
2.15	Crystall structure of the tetragonal $\text{Nd}_2\text{Fe}_{14}\text{B}$ unit cell <sup>[8]</sup> . . . . .	37
2.16	Schematic illustration of the Nd-Fe-B-sintered magnet microstructure . . . . .	38
2.17	Schematic sequence of the Nd-Fe-B sintered magnet production steps <sup>[75]</sup> . . . . .	40
2.18	Schematic representation of the grain boundary diffusion process <sup>[18]</sup> . . . . .	41
3.1	Potential profile with time in a CV-experiment. . . . .	44
3.2	(a) Ferrocene-ferrocenium redox system. (b) Standard potential of the $\text{Ag}/\text{Ag}^+$ -reference electrode against ferrocene. . . . .	45
3.3	Equivalent circuit of a quartz according to the Butterworth-van-Dyke-Model. . . . .	48
3.4	Adaption of the BVD-Model for a one-sided damped quartz. . . . .	48

4.1	Schematic representation of x-ray fluorescence and Auger electron emission.	56
4.2	Schematic representation hysteresis graph setup. . . . .	58
4.3	Scheme of the pickup coil setup in a PFM. . . . .	59
5.1	Demagnetization curves for GBD-treated samples with pure Al. . . . .	64
5.2	(a) Changes of the coercivity. (b) Changes of the remanence with increasing aluminum content. . . . .	65
5.3	Demagnetization curves for GBD-treated samples with pure Cu. . . . .	67
5.4	(a) Changes of the coercivity. (b) Changes of the remanence with increasing copper content. . . . .	68
5.5	Backscattered electron image and cross-section of Tb-coated sample . . . . .	71
5.6	Change of magnetic properties with Tb-addition. . . . .	74
5.7	Difference between single- and double-sided coated magnet samples. . . . .	75
5.8	Comparative representation of the changes in the magnetic properties with Dy- and Tb-additions. . . . .	77
6.1	Change of magnetic properties after grain boundary diffusion treatment with low-Dy alloys. . . . .	82
6.2	Change of magnetic properties after grain boundary diffusion treatment with high-Dy alloys. . . . .	84
6.3	Near-surface microstructural analysis of high-Dy alloy GBD-treated magnet .	85
6.4	Microstructural characterization of high-Dy alloy GBD-treated magnet . . . .	86
8.1	(a) Cyclic voltammogram and of $0.1 \text{ mol kg}^{-1} \text{ Cu[OTf]}_2$ in [BMIm][OTf] on Au-quartz electrode $25^\circ\text{C}$ recorded with $5 \text{ mV s}^{-1}$ . (b) Chronoamperogram of $0.1 \text{ mol kg}^{-1} \text{ Cu[OTf]}_2$ in [BMIm][OTf] on Au-quartz electrode $25^\circ\text{C}$ recorded at $-0.4 \text{ V}$ for 600 s. (c) Change of resonance frequency with passed charge from the CA in (b). . . . .	94
8.2	SEM micrograph and EDX pattern of Cu deposited from $0.25 \text{ mol kg}^{-1} \text{ Cu[OTf]}_2$ in [BMIm][OTf]. . . . .	95
8.3	Cyclic voltammogram (top) and chronoamperogram (bottom) of $0.1 \text{ mol l}^{-1} \text{ Cu[OTf]}_2$ in BMIM OTf at $25^\circ\text{C}$ . . . . .	97
8.4	SEM micrograph and EDX pattern of Cu deposited from $0.25 \text{ mol kg}^{-1} \text{ Cu[OTf]}_2$ in [BMPyr][OTf]. . . . .	98
8.5	Cyclic voltammogram (a) and chronoamperogram (b) of $0.1 \text{ mol l}^{-1} \text{ Cu[NTf}_2\text{]}_2$ in [BMIm][NTf <sub>2</sub> ] at $25^\circ\text{C}$ . . . . .	99



8.6	SEM micrograph and EDX pattern of Cu deposited from 0.25 mol kg <sup>-1</sup> Cu[OTf] <sub>2</sub> in [BMPyr][OTf]. . . . .	101
8.7	Cyclic voltammogram of 0.01 mol l <sup>-1</sup> DyCl <sub>3</sub> in EMIMBF <sub>4</sub> at 25 °C. . . . .	103
8.8	(a) Cyclic voltammograms of 0.1 mol kg <sup>-1</sup> DyCl <sub>3</sub> in [BMPyr][DCA] at 25 °C (straight line) and 150 °C (dashed line) recorded with a scan speed of 5 mV s <sup>-1</sup> . (b) Chronoamperogram of 0.5 mol kg <sup>-1</sup> DyCl <sub>3</sub> in [BMPyr][DCA] at 150 °C. WE: Au, CE: Dy. . . . .	104
8.9	Cyclic voltammograms of 0.23 mol l <sup>-1</sup> Dy[OTf] <sub>3</sub> in [BMIm][OTf] at 25 °C and at 150 °C. . . . .	106
8.10	(a) Cathodic branch of the cyclic voltammogram of 0.23 mol l <sup>-1</sup> Dy[OTf] <sub>3</sub> in [BMIm][OTf] recorded at room temperature with a scan rate of 10 mV s <sup>-1</sup> (black curve) and convoluted curve (gray curve). AE: Au, CE: Dy. (b) Chronoamperogram of the same system recorded at 150 °C at -2.0 V (black curve) and change in resonance frequency during the CA experiment (grey curve). (c) SEM micrograph for coatings produced in galvanostatic mode. (d) Corresponding EDX pattern. . . . .	107
8.11	Cyclic voltammogram of 0.2 mol kg <sup>-1</sup> Dy[NTf <sub>2</sub> ] <sub>3</sub> in [BMIm][NTf <sub>2</sub> ] at 25 °C recorded on a gold electrode with $\nu = 5 \text{ mV s}^{-1}$ . . . . .	109
8.12	(a) Cyclic voltammograms of 0.147 mol l <sup>-1</sup> Dy[NTf <sub>2</sub> ] <sub>3</sub> in [BMPyr][NTf <sub>2</sub> ] recorded at room temperature on Au-WE, $\nu = 5 \text{ mV s}^{-1}$ , 10 mV s <sup>-1</sup> , 25 mV s <sup>-1</sup> and 50 mV s <sup>-1</sup> , CE: Dy. (b) Cyclic voltammograms at different temperatures at 25 mV s <sup>-1</sup> . (c) Plot of the peak current densities against the square root of $\nu$ at 25 °C. (d) Cathodic peak potential versus log( $\nu$ ) at 25 °C. . . . .	111
8.13	(a) Semi-integral analysis of 0.147 mol l <sup>-1</sup> Dy[NTf <sub>2</sub> ] <sub>3</sub> in [BMPyr][NTf <sub>2</sub> ] recorded at room temperature. WE: Au, CE: Dy. (b) Chronoamperograms of the same electrolyte recorded under different potentiostatic conditions at 25 °C. . . . .	113
8.14	SEM micrograph, EDX and XPS patterns of electroplated Dy . . . . .	115
8.15	(a) Demagnetization curves obtained for a reference sample (straight line) and samples with 0.55 (open circles), 0.62 (open triangles), 0.72 (open squares) and 0.91 wt. % (half shaded circles). Production of the samples is shown in Tab. 8.3. (b) Effects of Dy content on the coercivity of VD 722 magnets with a base Dy concentration of 0.5 wt. %. The additional Dy > 0.5 wt. % is added by GBD. . . . .	118
8.16	Cyclic voltammograms of (a) 0.01 mol kg <sup>-1</sup> Tb[OTf] <sub>3</sub> in [BMPyr][OTf] and (b) 0.01 mol kg <sup>-1</sup> Tb[OTf] <sub>3</sub> in [BMIm][OTf] at 25 °C. $\nu = 5 \text{ mV s}^{-1}$ . . . . .	120

8.17	(a) Cyclic voltammograms of $0.047 \text{ mol l}^{-1} \text{ Tb[NTf}_2\text{]}_3$ in [BMPyr][NTf <sub>2</sub> ] recorded at room temperature on Pt-WE, $\nu = 5 \text{ mV s}^{-1}$ , $10 \text{ mV s}^{-1}$ , $25 \text{ mV s}^{-1}$ and $50 \text{ mV s}^{-1}$ . (b) Cyclic voltammograms at different temperatures at $25 \text{ mV s}^{-1}$ . (c) Plot of the peak current densities against the square root of $\nu$ at $25^\circ\text{C}$ . (d) Cathodic peak potential versus $\log(\nu)$ at $25^\circ\text{C}$ . . . . .	122
8.18	(a) SEM micrograph of as-deposited Tb from $0.1 \text{ mol l}^{-1} \text{ Tb[NTf}_2\text{]}_3$ in [BMPyr][NTf <sub>2</sub> ] at $150^\circ\text{C}$ (b) Magnification of (a). . . . .	123
8.19	WDX analysis of electroplated Tb coating shown in Figure 8.18. . . . .	124
8.20	(a) SEM micrograph of the Tb-coated sample described above. (b) WDX elemental maps of the highlighted area. . . . .	125
8.21	Demagnetization curve of grain boundary diffusion processed sample electroplated with Tb. . . . .	126
8.22	(a) Cyclic voltammograms of $0.145 \text{ mol l}^{-1} \text{ Nd[NTf}_2\text{]}_3$ in [BMPyr][NTf <sub>2</sub> ] recorded at room temperature on Au-WE, $\nu = 5 \text{ mV s}^{-1}$ , $10 \text{ mV s}^{-1}$ , $25 \text{ mV s}^{-1}$ and $50 \text{ mV s}^{-1}$ . (b) Cyclic voltammograms at different temperatures at $25 \text{ mV s}^{-1}$ . (c) Plot of the peak current densities against the square root of $\nu$ at $25^\circ\text{C}$ . (d) Cathodic peak potential versus $\log(\nu)$ at $25^\circ\text{C}$ . . . . .	129
8.23	Cathodic branch of the cyclic voltammogram of $0.145 \text{ mol l}^{-1} \text{ Nd[NTf}_2\text{]}_3$ in [BMPyr][NTf <sub>2</sub> ]. . . . .	129
8.24	SEM micrograph and EDX pattern of electroplated neodymium. . . . .	130
8.25	Electrochemical characterization of $0.141 \text{ mol l}^{-1} \text{ Co[NTf}_2\text{]}_2$ in [BMIm][NTf <sub>2</sub> ]. . . . .	132
8.26	SEM micrographs and EDX patterns of electroplated cobalt under different potentiostatic conditions. . . . .	134
8.27	WDX pattern of electroplated cobalt at $-1.6 \text{ V}$ at $100^\circ\text{C}$ for 1 h. on Au . . .	135
8.28	(a) Cyclic voltammograms of mixtures of $\text{Dy[NTf}_2\text{]}_3$ and $\text{Co[NTf}_2\text{]}_2$ in [BMIm][NTf <sub>2</sub> ] at $100^\circ\text{C}$ . (b) CV and corresponding shift in resonant frequency	137
8.29	Electrochemical characterization of $0.05 \text{ mol l}^{-1} \text{ Fe[NTf}_2\text{]}_2$ in [BMIm][NTf <sub>2</sub> ].	139
8.30	SEM micrographs and EDX patterns of electroplated iron under different potentiostatic conditions. . . . .	140
8.31	WDX pattern of electroplated iron at $-1.8 \text{ V}$ at $100^\circ\text{C}$ . . . . .	141
8.32	(a) Cyclic voltammograms of mixtures of $\text{Dy[NTf}_2\text{]}_3$ and $\text{Fe[NTf}_2\text{]}_2$ in [BMIm][NTf <sub>2</sub> ] at $100^\circ\text{C}$ . (b) CV and corresponding shift in resonant frequency	143

# List of Tables

2.1	Lattice parameters, atomic radii and magnetic properties of $\text{RE}_2\text{Fe}_{14}\text{B}$ -compounds.	36
4.1	Water content of the applied ionic liquids . . . . .	60
4.2	Water content of applied commercially available metal salts . . . . .	60
5.1	Correlation between Al-coating thickness and concentration in the Nd-Fe-B samples. . . . .	63
5.2	Correlation between Cu-coating thickness and concentration in the Nd-Fe-B samples. . . . .	66
5.3	Correlation between Tb-coating thickness and concentration in the Nd-Fe-B samples. . . . .	69
6.1	Compositions, phases and melting points of the applied eutectic alloys. Data taken from Ref. [137] . . . . .	79
6.2	Resulting mass fraction of Al and Dy in the magnet samples after coating with low- and high-Dy eutectic alloys. . . . .	80
8.1	Electrolyte compositions, diffusion coefficients, viscosities and Walden-products for different dysprosium electrolytes. . . . .	113
8.2	Composition analysis of electroplated coating shown in Figure 8.14a as deposited and after Ar-etching by XPS. . . . .	114
8.3	Deposition times, mass of deposited Dy, coating thickness, current efficiencies and increase in $H_{cJ}$ for different samples . . . . .	117
8.4	Composition analysis of electroplated cobalt coating as shown in Figure 8.26 as deposited and after Ar-etching. . . . .	136
8.5	Composition analysis of electroplated iron coating as shown in Figure 8.30 as deposited and after Ar-etching. . . . .	142
9.1	Listing of the synthesized salts used in this work . . . . .	148
9.2	Summary of diffusion coefficients of trivalent $\text{Ln}^{3+}$ -species in $[\text{NTf}_2^-]$ based ionic liquids determined in this work and reported in the literature. . . . .	149



# Bibliography

- [1] J. G. W. West, "DC, Induction, Reluctance and PM Motors for Electric Vehicles", *Power Eng. J.*, **8** (2), 77-88 (1994)
- [2] R. Fischer: Elektrische Maschinen, 16. Auflage, Carl Hanser Verlag München, München 2013
- [3] E. Hau: Windkraftanlagen - Grundlagen, Technik, Einsatz, Wirtschaftlichkeit, 5. Auflage, Springer-Verlag, Berlin Heidelberg, 2014
- [4] M. Humphries, "'Rare Earth Elements: The Global Supply Chain", CRS report for Congress, Congressional Research Service R41347 (2013)
- [5] A. V. Naumov, "'Review of the World Market of Rare-Earth Metals", *Russ. J. Non-Fer. Met.*, **49** (1), 18-27 (2008)
- [6] ISE Institut für seltene Erden und Metalle, "Aktuelle und historische Marktpreise der gängigsten Seltenen Erden", accessed 26 February 2015  
<http://institut-seltene-erden.org/aktuelle-und-historische-marktpreise-der-gangigsten-seltenen-erden/>
- [7] M. Sagawa, S. Fujimura, H. Yamamoto, Y. Matsuura, "Permanent Magnet Materials based on the Rare Earth - Iron - Boron Tetragonal Compounds", *IEEE TRANS. Magn.*, **20**, 1584-1589 (1984)
- [8] M. Sagawa, S. Hirosawa, H. Yamamoto, S. Fujimura, Y. Matsuura, "Nd-Fe-B Permanent Magnet Materials" *Japanese Journal of Applied Physics*, **26**, 785-800, (1987)
- [9] T. Nishiuchi, N. Nozawa, T. Ohkubo, K. Ohno, H. Sepheri-Amin, J. Yamasaki, S. Yamano, T. Tanaka, M. Okano, K. Sumiyama, "Recent Efforts Toward Rare-Metal-Free Permanent Magnets in Japan" REPM-10-Proceedings of the 21st Workshop on Rare Earth Permanent Magnets and their Applications, Bled, Slovenia (2010)
- [10] D.C. Jiles, "Recent Advances and Future Directions in Magnetic Materials", *Acta Mat.*, **51**, 5907-5939 (2003)
- [11] M. Sagawa, "Development and Prospect of the Nd-Fe-B Sintered Magnets" REPM-10-Proceedings of the 21st Workshop on Rare Earth Permanent Magnets and their Applications, Bled, Slovenia (2010)

- [12] M. Soderznik, K. Z. Rozman, S. Kobe, P. McGuiness, "The grain-boundary diffusion process in Nd-Fe-B sintered magnets based on the electrophoretic deposition of DyF<sub>3</sub>", *Intermet.*, **23**, 158-162 (2012)
- [13] J. Lodermeier, "Elektrochemische Abscheidung von Metallen und Legierungen aus nichtwässrigen Systemen und Aktivierung von passivierten Metalloberflächen zur Abscheidung nanoporöser Schichten aus wässrigen Lösungen", Doctoral Thesis, Regensburg, 2006
- [14] J. Lodermeier, M. Multerer, M. Zistler, S. Jordan, H. J. Gores, W. Kipferl, E. Diaconu, M. Sperl, G. Bayreuther, "Electroplating of Dysprosium, Electrochemical Investigations and Study of Magnetic Properties", *J. Electrochem. Soc.*, **153** (4), C242-C248 (2006)
- [15] D. Brown, B. M. Ma, Z. Chen, "Developments in the processing and properties of NdFeB-type permanent magnets", *J. Mag. Mag. Mat.*, **248**, 432-440 (2002)
- [16] K. J. Strnat, "Modern Permanent Magnets for Applications in Electro-Technology", *Proceedings of the IEEE*, **78** (6), 1-35 (1990)
- [17] T. Hidaka, C. Ishizaka, M. Hosako, "The Effect of Dy Source Size on the Magnetic Properties and Microstructure of Nd-Fe-B Sintered Magnets in the H-HAL (Homogenous-high Anisotropy Field Layer) Process", REPM-10-Proceedings of the 21st Workshop on Rare Earth Permanent Magnets and their Applications, Bled, Slovenia (2010)
- [18] K.T. Park, K. Hiraga, M. Sagawa, Proceedings of the Sixth International Workshop on Rare-Earth Magnets and Their Applications, JIM, Sendai, 2000,
- [19] K. Machida, S. Suzuki, T. Kawasaki, D. S. Li, T. Kitamon, K. Nakamura, Y. Shimizu, "High-coercive Nd-Fe-B sintered magnets diffused with Dy or Tb metal and their applications", *INTERMAG Asia 2005. Digests of the IEEE International Magnetism Conference, 2005*, 947-948
- [20] H. Sepehri-Amin, T. Ohkubo, K. Hono "Grain boundary structure and chemistry of Dy-diffusion processed Nd-Fe-B sintered magnets", *J. Appl. Phys.*, **107**, 09A745 (2010)
- [21] K. Hirota, H. Nakamura, T. Minowa, M. Honshima, "Coercivity Enhancement by the Grain Boundary Diffusion Process to Nd-Fe-B Sintered Magnets", *IEEE Trans. Magn.*, **42**, 2909-2911 (2006)
- [22] H. Nakamura, K. Hirota, M. Shimao, T. Minowa, M. Honshima, "Magnetic Properties of Extremely Small Nd-Fe-B Sintered Magnets", *IEEE Trans. Magn.*, **41**, 3844-3846 (2005)
- [23] A. M. Gabay, M. Marinescu, W. F. Li, J. F. Liu, G. C. Hadjipanayis, "Dysprosium-saving improvement of coercivity in Nd-Fe-B sintered magnets by Dy<sub>2</sub>S<sub>3</sub> additions", *J. Appl. Phys.*, **109**, 083916 (2011)

- [24] H. Suzuki, Y. Satsu, M. Komuro, "Magnetic properties of a Nd-Fe-B sintered magnet with Dy segregation", *J. Appl. Phys.*, **105**, 07A734 (2009)
- [25] H. Sepehri-Amin, T. Ohkubo, T. Nishiuchi, S. Hirosawa, K. Hono, "Coercivity enhancement of hydrogenation-disproportionation-desorption-recombination processed Nd-Fe-B powders by the diffusion of Nd-Cu eutectic alloys", *Scr. Mat.*, **63**, 1124-1127 (2010)
- [26] N. Oono, M. Sagawa, R. Kasada, H. Matsui, A. Kimura, "Production of this high-performance sintered neodymium magnets by grain boundary diffusion treatment with dysprosium-nickel-aluminum alloy", *J. Mag. Mag. Mat.*, **323**, 297-300 (2011)
- [27] L. Q. Yu, R. S. Liu, K. T. Dong, Y. P. Zhang, "Key Techniques for Ultrahigh Performance Sintered Nd-Fe-B Magnets Preparation", 1-36 (2012)
- [28] B. E. Davies, R. S. Mottram, I. R. Harris, "Recent Developments in the Sintering of NdFeB", *Mat. Chem. Phys.*, **67**, 272-281 (2001)
- [29] A. J. Bard, L. R. Faulkner: *Electrochemical Methods : Fundamentals and Applications*, John Wiley & Sons, Inc, 2001
- [30] M. Paunovic, M. Schlesinger: *Fundamentals of Electrochemical Deposition*, John Wiley & Sons, Inc, Hoboken, New Jersey 2006
- [31] N. Kanani: *Electroplating - Basic Principles, Processes and Practice*, Elsevier Ltd, Oxford 2004
- [32] T. Erdey-Gruz and M. Volmer, "Zur Theory der Wasserstoffüberspannung", *Z. Phys. Chem.* **A150**, 201 (1930)
- [33] T. Erdey-Gruz and M. Volmer, "Zur Frage der elektrolytischen Metallüberspannung", *Z. Phys. Chem.* **A157**, 165 (1931)
- [34] F. C. Frank, "The Influence of Dislocations on Crystal Growth", *Discuss. Faraday Soc.*, **5**, 48-54 (1949)
- [35] W. K. Burton, N. Cabrera F. C. Frank, "The Growth of Crystals and the Equilibrium Structure of their Surfaces", *Philos. Trans. R. Soc. London A*, **243**, 299-358 (1951).
- [36] J. Karthaus, "Galvanische Abscheidung von Metallen aus nichtwässrigen Elektrolyten für die Mikrosystemtechnik", Doctoral Thesis, Karlsruhe, 2000
- [37] B. Scharifker, G. Hills, "Theoretical and experimental studies of multiple nucleation", *Electrochim. Acta* **28**, 879-889 (1983)
- [38] M. Schlesinger and M. Paunovic: *Modern Electroplating*, 5th edn, John Wiley & Sons, Inc., New York 2010

- [39] F. Endres, A. P. Abbot, D. R. MacFarlane: *Electrodeposition from Ionic Liquids*, WILEY-VCH Verlag GmbH & Co KGaA, Weinheim 2008
- [40] J. Barthel, H. J. Gores, "Solution Chemistry: A Cutting Edge in Modern Electrochemical Technology" in G. Mamantov, A. I. Popov (eds.): *Chemistry of Nonaqueous Solutions. Current Progress*, VCH, New York 1994
- [41] K. Izutsu: *Electrochemistry in Nonaqueous Solutions*, 2nd Edition, WILEY-VCH Verlag GmbH & Co. KGaA, Weinheim 2009
- [42] M. Gaune-Escard, G. M. Haarberg: *Molten Salts Chemistry and Technology*, John Wiley & Sons, Ltd., West Sussex 2014
- [43] F. Lantelme, H. Groult: *Molten Salts Chemistry- From Lab to Applications*, Elsevier Inc. 2013
- [44] J. Zhang, "Electrochemistry of Actinides and Fission Products in Molten Salts-Data Review", *J. Nucl. Mater.*, **447**, 271-284 (2014)
- [45] J. Barthel, H. J. Gores, G. Schmeer, R. Wachter, "Non-Aqueous Electrolyte Solutions in Chemistry and Modern Technology" in *Topics of Current Chemistry*, Vol 111, Springer, Berlin Heidelberg 1983
- [46] R. Hagiwara, Y. Ito, "Room Temperature Ionic Liquids of Alkylimidazolium Cations and Fluoroanions", *J. Fluorine Chem.*, **105**, 221-227 (2000)
- [47] H. Xue, R. Verma, J. M. Shreeve, "Review of Ionic Liquids with Fluorine-Containing Anions", *J. Fluorine Chem.*, **127**, 159-176 (2006)
- [48] O. Zech, "Ionic Liquids in Microemulsions - a Concept to Extend the Conventional Thermal Stability Range of Microemulsions", *Doctoral Thesis*, Regensburg, 2010
- [49] M. Armand, F. Endres, D. R. MacFarlane, H. Ohno, B. Scrosati, "Ionic-Liquid Materials for the Electrochemical Challenges of the Future", *Nature Materials*, **8**, 621-629 (2009)
- [50] S. Zein El Abedin, F. Endres, "Electrodeposition of Metals and Semiconductors in Air- and Water-Stable Ionic Liquids", *Chem. Phys. Chem.*, **7**, 58-61 (2006)
- [51] F. Endres, "Ionic Liquids: Solvents for the Electrodeposition of Metals and Semiconductors", *Chem. Phys. Chem.*, **3**, 144-154 (2002)
- [52] A. P. Abbott, K. J. McKenzie, "Application of ionic liquids for the electrodeposition of metals", *Phys. Chem. Chem. Phys.*, **8**, 4265-4279 (2006)
- [53] S. Zein El Abedin, M. Pölleth, S. A. Meiss, J. Janek, F. Endres, "Ionic Liquids as Green Electrolytes for the Electrodeposition of Nanomaterials", *Green Chem.*, **9**, 549-553 (2007)



- [54] T. Welton, "Room-Temperature Ionic Liquids. Solvents for Synthesis and Catalysis", *Chem. Rev.*, **99**, 2071-2083 (1999)
- [55] D. Wei, A. Ivaska, "Applications of ionic liquids in electrochemical sensors", *Analytica Chimica Acta*, **607**, 126-135 (2008)
- [56] D. R. MacFarlane, M. Forsyth, P. C. Howlett, J. M. Pringle, J. Sun, G. Annat, W. Neil, E. I. Izgorodina, "Ionic Liquids in Electrochemical Devices and Processes: Managing interfacial Electrochemistry" *Acc. Chem. Res.*, **40**, 1165-1173 (2007)
- [57] M. Galinski, A. Lewandowski, I. Stepniak, "Ionic Liquids as Electrolytes", *Electrochimica Acta*, **51**, 5567-5580 (2006)
- [58] A. Lewandowski, A. Swiderska-Mocek, "Ionic Liquids as Electrolytes for Li-Ion Batteries - An Overview of Electrochemical Studies", *J. Power Sources*, **194**, 601-609 (2009)
- [59] Sigma Aldrich, ChemFiles - Ionic Liquids, accessed 26 February 2015  
  
[http://www.sigmaaldrich.com/content/dam/sigma-aldrich/docs/Aldrich/Brochure/al\\_chemfile\\_v5\\_n6.pdf](http://www.sigmaaldrich.com/content/dam/sigma-aldrich/docs/Aldrich/Brochure/al_chemfile_v5_n6.pdf)
- [60] T. Tsuda, C. L. Hussey. "Electrochemistry of Room-Temperature Ionic Liquids and Melts" in: "Modern Aspects of Electrochemistry No. 45" Springer Science+Business Media, LLC 2009
- [61] M. C. Buzzeo, R. G. Evans, R. Compton, "Non-Haloaluminate Room-Temperature Ionic Liquids in Electrochemistry- A Review", *Chem. Phys. Chem.*, **5**, 1106-1120 (2004)
- [62] F. Endres, S. Zein El Abedin, "Air and water stable ionic liquids in physical chemistry", *Phys. Chem. Chem. Phys.*, **8**, 2101-2116 (2006)
- [63] S. Zhang, N. Sun, X. He, X. Lu, X. Zhang, "Physical Properties of Ionic Liquids: Database and Evaluation", *J. Phys. Chem. Ref. Data*, **35**, 1475-1517 (2006)
- [64] P. Hapiot, C. Lagrost, "Electrochemical Reactivity in Room-Temperature Ionic Liquids", *Chem. Rev.*, **108**, 2238-2264 (2008)
- [65] T. Tsuda, C. Hussey, "Electrochemical Application of Room-Temperature Ionic Liquids", *Electrochem. Soc. Interface*, Spring 2007
- [66] H. Ohno: *Electrochemical Aspects of Ionic Liquids*, John Wiley & Sons, Inc., Hoboken, New Jersey, 2005
- [67] A. Kokorin : *Ionic Liquids: Theory, Properties, New Approaches*, InTech, Rijeka, Croatia, 2011
- [68] P. Wasserscheid, T. Welton: *Ionic Liquids in Synthesis*, Wiley-VCH Verlag GmbH & Co. KGaA, Weinheim, 2002

- [69] C. G. Stefanita: Magnetism - Basics and Applications, Springer-Verlag, Berlin, Heidelberg, 2012
- [70] K. H. J. Buschow, F. R. de Boer: Physics of Magnetism and Magnetic Materials, Kluwer Academic Publishers, New York, 2004
- [71] A. Sommerfeld, H. Bethe: Elektronentheorie der Metalle, Springer-Verlag Berlin, 1967
- [72] D. Halliday, R. Resnick, J. Walker: Fundamentals of Physics, John Wiley & Sons, Inc, 2001
- [73] S. Chikazumi: Physics of Ferromagnetism, 2<sup>nd</sup> Edition, Oxford University Press, 1997
- [74] J. F. Herbst, J. J. Croat, W. B. Yelon, "Structural and magnetic properties of Nd<sub>2</sub>Fe<sub>14</sub>B", *J. Appl. Phys.* **57**, 4086-4090 (1985)
- [75] M. Katter, K. Uestuener, "Industrial Sintered Nd-Fe-B Permanent Magnets and their Applications", Permanent Magnets: Current Materials and Future Exploitation, One-Day Seminar, University of Liferpool 2006
- [76] L. Schultz, A. M. El-Aziz, G. Barkleit, K. Mummert, "Corrosion Behaviour of Nd-Fe-B Permanent Magnetic Alloys", *Mat. Sci. Eng.* **A267**, 307-313 (1999)
- [77] J. P. Jakubovics: Magnetism and Magnetic Materials, The University Press, Cambridge 1994
- [78] J.D. Kaino, K. Fujii, H. Shimizu, JP Patent Application 62274799 (TAIYO YUDEN CO LTD. 1987)
- [79] J. Tang, L. Zhang, C. Wei, Y. Wen, L. Yang, Y. Mei, "Calculating the proportion of Nd-rich phase in NdFeB alloy via Matlab software", *J. Chongqing Univ. Eng. Ed.*, **12**, 7-10 (2013)
- [80] Y. Shinba, T. J. Konno, K. Ishikawa, K. Hiraga, M. Sagawa, "Transmission electron microscopy study on Nd-rich phase and grain boundary structure of Nd-Fe-B sintered magnets", *J. Appl. Phys.*, **97**, 053504 (2005)
- [81] J. Heinze, "Cyclovoltammetrie - die „Spektroskopie" des Elektrochemikers", *Ange wandte Chemie*, **11**, 823-839, (1984)
- [82] G. A. Mabbott, "An introduction to cyclic voltammetry", *J. Chem. Ed.*, **60**, 697-702 (1983)
- [83] K. Izutsu, M. Ito, E. Sarai, "Silver-silver cryptate (2,2) ion electrode as a reference electrode in nonaqueous solvents", *Analytical Sciences*, **1**, 341-344 (1985)
- [84] P. H. Rieger: Electrochemistry-Second edition, Chapman & Hall, New York, 2001

- [85] C. H. Hamann, A. Hamnett, W. Vielstich: *Electrochemistry*, 2nd Edition, Wiley-VCH Verlag GmbH & Co. KGaA, Weinheim 2007
- [86] G. Kulwanoski, J. Schnellinger, Kistler Instrument Corp., “The Principles of Piezoelectric Accelerometers”, accessed 26 February 2015  
<http://www.sensormag.com/sensors/acceleration-vibration/the-principles-piezoelectric-accelerometers-1022>
- [87] J. Nosek, J. Zelenka, “Quartz Strip Resonators as a Temperature Sensor”, *Ultrasonics*, **39**, 465-468, (2001)
- [88] F. L. Walls, J. J. Gagnepain, “Environmental Sensitivities of Quartz Oscillators”, *IEEE Transactions on Ultrasonics, Ferroelectrics and Frequency Control*, **39**, 241-249, (1992)
- [89] W. P. Mason: “Physical Acoustics: Principles and Methods Vol. II”, Academic Press, New York, 1965
- [90] F. Wudy, M. Multerer, C. Stock, G. Schmeer, H.J. Gores, “Rapid impedance scanning QCM for electrochemical applications based on miniaturized hardware and high-performance curve fitting”, *Electrochim. Acta*, **53**, 6568-6574, (2008)
- [91] F. Wudy, C. Stock, H. J. Gores: Basics: Measurement techniques: Electrochemical Quartz Crystal Microbalance in *Encyclopedia of Electrochemical Power Sources*, Editor: L. Garche, Elsevier, 2009 Elsevier, 2009
- [92] F. Wudy, “Beiträge zur Entwicklung neuer physikalisch-chemischer Messinstrumente. Eine Quarzmikrowaage nach der neuen Methode der schnellen Impedanzauswertung kombiniert mit einem hochpräzisen Potentiostat/Galvanostat und einem Präzisionsthermometer. Grundlagen, vernetzte Messtechnik und Anwendungen in Elektrochemie und Thermodynamik”, Doctoral Thesis, Regensburg, 2009
- [93] R. Lucklum, F. Eichelbaum, “Interface Circuits for QCM Sensors”, *Springer Ser. Chem. Sens. Biosens.*, **5**, 3-47, (2007)
- [94] G. Sauerbrey, “Verwendung von Schwingquarzen zur Wägung dünner Schichten und zur Mikrowägung”, *Z. Phys.*, **155**, 206-222, (1959)
- [95] W. Visscher, J.F.E. Gootzen, A. P. Cox, J. A. R. Van Veen, “Electrochemical Quartz Crystal Microbalance Measurements of CO Adsorption and Oxidation on Pt in Various Electrolytes”, *Electrochim. Acta*, **43**, 533, (1998)
- [96] R. Lucklum, P. Hauptmann, “The Quartz Crystal Microbalance: Mass Sensitivity, Viscoelasticity and Acoustic Amplification”, *Sensors and Actuators B*, **70**, 30-36, (2000)
- [97] M. R. Deakin, O. Melroy, “Underpotential Metal Deposition on Gold Monitored in Situ with a Quartz Micro Balance”, *J. Electroanal. Chem.*, **239**, 321, (1988)

- [98] S. Kologo, M. Eyraud, L. Bonou, F. Vacandio, and Y. Massiani, "Voltametry and EQCM Study of Copper Oxidation in Acidic Solution in Presence of Chloride Ions", *Electrochim. Acta*, **52** (9), 3105-3113 (2007)
- [99] D. M. Soares, S. Wasle, K. G. Weil, K. Doblhofer, "Copper ion reduction catalyzed by chloride ions", *J. Electroanal. Chem.*, **532**, 353-358 (2002)
- [100] D. Moosbauer, "Elektrochemische Charakterisierung von Elektrolyten und Elektroden für Lithium-Ionen-Batterien - Entwicklung einer neuen Messmethode für elektrochemische Untersuchungen an Elektroden mit der EQCM", Doctoral Thesis, Regensburg, 2010
- [101] K. Fischer, "Neues Verfahren zur maßanalytischen Bestimmung des Wassergehaltes von Flüssigkeiten und festen Körpern", *Angewandte Chemie*, **48**, 394-396, (1935)
- [102] P. Brüttel, R. Schlink: Monographie Wasserbestimmung durch Karl-Fischer-Titration. Metrohm AG, Herisau, Schweiz, 2006
- [103] E. Scholz: Karl-Fischer-Titration. Springer-Verlag Berlin, Heidelberg, 1984
- [104] N. Wiberg: Lehrbuch der Anorganischen Chemie, (Holleman-Wiberg), 102. Auflage, Walter de Gruyter Verlag, Berlin, 2007
- [105] M. Hesse, H. Meier, B. Zeeh: "Spektroskopische Methoden in der organischen Chemie", 6. Editio, Thieme Verlag, Stuttgart (2002).
- [106] A. W. Coats, J. P. Redfern, "Thermogravimetric Analysis. A Review", *Analyst*, **88**, 906-924, (1963)
- [107] S. Hüfner: Photoelectron spectroscopy: principles and applications, Springer, Berlin Heidelberg 1995
- [108] A. Buman, D. Pecard, L. Pecard, "EDX vs WDX: Head to Head", accessed 26 February 2015  
[http://www.bruker.com/fileadmin/user\\_upload/8-PDF-Docs/X-rayDiffraction\\_ElementalAnalysis/XRF/Webinars/Bruker\\_AXS\\_EDX\\_vs\\_WDX\\_Webinar\\_Slides.pdf](http://www.bruker.com/fileadmin/user_upload/8-PDF-Docs/X-rayDiffraction_ElementalAnalysis/XRF/Webinars/Bruker_AXS_EDX_vs_WDX_Webinar_Slides.pdf)
- [109] D. Briggs, M. P. Sheah: Practical surface analysis, Vol.1: Auger and X-ray Photoelectron Spectroscopy. 2. Edition, Otto Salle Verlag Frankfurt (1990)
- [110] H. Czchos, T. Saito, L. Smith: Springer Handbook of Materials Measurement Methods, Springer-Verlag Berlin Heidelberg (2006)
- [111] N. D. The, N. H. Hai, H. D. Anh, V. V. GHiep, L. V. Vu, C. X. Huu, N. Chau, "Magnetic Properties and Magnetic Viscosity of  $\text{Pr}_4\text{Fe}_{76}\text{Co}_{10}\text{B}_6\text{Nb}_3\text{Cu}_1$  Nanocomposite Magnet", *J. Korean Phys. Soc.*, **52** (5), 1414-1418 (2008)

- [112] R. S. Mottram, A. J. Williams, I. R. Harris, “Blending additions of aluminum and cobalt to Nd<sub>16</sub>Fe<sub>76</sub>B<sub>8</sub> milled powder to produce sintered magnets”, *J. Magn. Magn. Mater.*, **222**, 305-313 (2000)
- [113] W. Rodewald: Proceedings of the Ninth International Workshop on Rare-Earth Magnets and their Applications, Bad Soden, 1987
- [114] : Vacuumschmelze GmbH & Co. KG, Product Information, accessed 26 February 2015  
<http://www.vacuumschmelze.com/en/products/permanent-magnets-assemblies/coating/ivd-aluminium-aluminium-yellow-chromate.html>
- [115] K. G. Knoch, B. Grieb, E.T. Henig, H. Kronmüller, G. Petzow, “Upgraded Nd-Fe-B-AD (AD=Al,Ga) magnets: wettability and microstructure”, *IEEE Trans. Magn.*, **26**, 1951-1953, (1990)
- [116] B. Grieb, E. T. Henig, G. Martinek, H. H. Stadelmaier, G. Petzow, “Phase relations and magnetic properties of new phases in the Fe-Nd-Al and Fe-Nd-C systems and their influence on magnet”, *IEEE Trans. Magn.*, **26**, 1367-1369 (1990)
- [117] M. Velicescu, W. Fernengel, W. Rodewald, P. Schrey, B. Wall, “High-Energy Sintered Nd-Fe-B magnets with Co and Cu additions”, *J. Magn. Magn. Mater.*, **214**, 61-68 (2000)
- [118] J. Jiang, Z. Zeng, J. Wu, M. Tokunaga, “Influence of Alloying Elements on Mechanical Properties and Microstructures of Sintered Nd-Fe-Co-B magnet”, *J. Magn. Magn. Mater.*, **214**, 61-68 (2000)
- [119] S. Szymura, H. Bala, H. Stoklosa, V. V. Sergeev, “Microstructure, Magnetic Properties, and Corrosion Behaviour of the Copper-Doped Nd-Fe-B Sintered Magnets”, *Phys. Status Solidi A*, **137** (1), 179-188 (1993)
- [120] Z. Samardzija, P. McGuinness, M. Soderznik, S. Kobe, M. Sagawa, “Microstructural and Compositional Characterization of Terbium-Doped Nd–Fe–B Sintered Magnets”, *Mat. Char.*, **67**, 27-33 (2012)
- [121] N. Watanabe, H. Umemoto, M. Ishimaru, M. Itakura, M. Nishida, K. Machida, “Microstructure Analysis of Nd–Fe–B Sintered Magnets Improved by Tb-Metal Vapour Sorption”, *J. Microsc.*, **236**, 104-108 (2009)
- [122] M. Komuro, Y. Satsu, H. Suzuk, “Increase of Coercivity and Composition Distribution in Fluoride-Diffused NdFeB Sintered Magnets Treated by Fluoride Solutions”, *IEEE Trans. Mag.*, **46**, 3831-3833 (2010)
- [123] M. Yue, W. Liu, D. Zhang, Z. Jian, A. Cao, J. Zhang, “Tb Nanoparticles Doped Nd–Fe–B Sintered Permanent Magnet with Enhanced Coercivity”, *Appl. Phys. Lett.*, **94**, 092501 (2009)

- [124] N. Watanabe, M. Itakura, N. Kuwano, D. Li, S. Suzuki, K. Machida, “Microstructure Analysis of Sintered Nd–Fe–B Magnets Improved by Tb-vapor Sorption”, *Mat. Trans.*, **48**(5), 915-918 (2007)
- [125] Z. Samardzija, P. McGuinness, M. Soderznik, S. Kobe, M. Sagawa, “Microstructural and Compositional Characterization of Terbium-Doped Nd–Fe–B Sintered Magnets”, *Mat. Char.*, **67** 27-33 (2012)
- [126] H. Sepheri-Amin, T. Ohkubo, K. Hono, “The Mechanism of Coercivity Enhancement by the Grain Boundary Diffusion Process of Nd–Fe–B-Sintered Magnets”, *Acta Mat.*, **61**, 1982-1990 (2013)
- [127] C. Brombacher, K. Loewe, O. Gutfleisch, M. Ruehrig, M. Katter, “Characterization of Dydiffusion processed High Performance Nd–Fe–B Permanent Magnets”, *Proceedings of the 22<sup>nd</sup> Rare Earth and Future Permanent Magnets Workshop*, Nagasaki, Japan (2012) P2-034
- [128] H. Nakamura, K. Hirota, T. Ohashi, T. Minowa, “Coercivity Distributions in Nd-Fe-B Sintered Magnets Produced by the Grain Boundary Diffusion Process”, *J. Phys. D; Appl. Phys.*, **44**, 1-5 (2011)
- [129] B. Cook, J. Harringa, F. Laabs, K. Dennis, A. Russell, R. McCallum, “Diffusion of Fe, Co Nd and Dy in  $R_2(Fe_{1-x}Co_x)_{14}B$  where R=Nd or Dy”, *J. Mag. Mag. Mat.*, **233**, L136-141 (2001)
- [130] H. Mehrer: *Diffusion in Solids- Fundamentals, Methods, Materials, Diffusion-Controlled Processes*, Springer Verlag: Berlin Heidelberg. 2007
- [131] K. Loewe, C. Brombacher, M. Katter, O. Gutfleisch, “Temperature-Dependent Dy Diffusion Process in Nd–Fe–B Permanent Magnets”, *Acta Mater.*, **83**, 248-255 (2015)
- [132] S. Szymura, H. Bala, G. Pawlowska, Y. M. Rabinovich, V. V. Sergeev, D. V. Pokrovskii, “Modification of the Magnetic Properties and Corrosion Resistance of Nd–Fe–B Permanent Magnets with Addition of Cobalt”, *J. Macrosc.*, **236**, 104-108 (2009)
- [133] R. Fischer: *Elektrische Maschinen*, 16<sup>th</sup> Edition, Carl Hanser Verlag, Munich 2013
- [134] X. L. Liu, J. P. He, Q. f. Dong, S. Z. Zhou, “A Study of Grain Growth Kinetics in Sintered NdFeB Magnets”, *J. Rare Earths*, **19** (3), 209-213 (2001)
- [135] S. Hirosawa, Y. Matsuura, H. Yamamoto, S. Fujimora, M. Sagawa, H. Yamauchi, “Magnetization and Magnetic Anisotropy of  $R_2Fe_{14}B$  Measured on Single Crystals”, *J. Appl. Phys.*, **59**(3), 873-879 (1986)
- [136] S. De Negri, A. Saccone, G. Cacciamani, R. Ferro, “The Al–R–Mg (R=Gd,Dy,Ho) Systems. Part 1: Experimental Investigation”, *Intermet.*, **11**, 1125-1134 (2003)

- [137] L. Jin, Y. B. Kang, P. Chartrand, C. D. Fuerst, "Thermodynamic Evaluation and Optimization of Al–Gd, Al–Tb, Al–Dy, Al–Ho and Al–Er Systems Using a Modified Quasichemical Model for the Liquid", *CALPHAD*, **34**, 456-466 (2010)
- [138] A. Vij, Y. Y. Zheng, R. L. Kirchmeier, J. M. Shreeve, "Electrophilic Addition and Substitution Reactions of Bis(trifluoromethylsulfonyl)amide and Its N-Chloro Derivative", *Inorg. Chem.* **33** 3281-3288 (1994)
- [139] S. Zein El Abedin, A.Y. Saad, H.K. Farag, N. Borisenko, Q.X. Liu, F. Endres, "Electrodeposition of Selenium, Indium and Copper in an Air- and Water-stable Ionic Liquid at Variable Temperatures", *Electrochim. Acta*, **52**, 2746-2754 (2007)
- [140] A. Kurachi, M. Matsumiya, K. Tsunashima, S. Kodama, "Electrochemical Behavior and Electrodeposition of Dysprosium in Ionic Liquids based on Phosphonium Cations", *J. Appl. Electrochem.*, **42**, 961-968 (2012)
- [141] D. B. Baudry, A. Dormond, F. Duris, J. M. Bernard, J. R. Desmurs, "Lanthanide Bis(trifluoromethanesulfonyl)amides, Synthesis, Characterization and Catalytic Activity", *J. Fluor. Chem.*, **121**, 233-238 (2003)
- [142] H. Kondo, M. Matsumiya, K. Tsunashima, S. Kodama, "Attempts to the Electrodeposition of Nd from Ionic Liquids at Elevated Temperatures", *Electrochim. Acta*, **66**, 313-319 (2012)
- [143] R. Fukui, Y. Katayama, T. Miura, "The Effect of Organic Additives in Electrodeposition of Co from an Amide-Type Ionic Liquid", *Electrochim. Acta*, **56**, 1190-1196 (2011)
- [144] M. Yamagata, N. Tachikawa, Y. Katayama, T. Miura, "Electrochemical Behavior of Several Iron Complexes in Hydrophobic Room-Temperature Ionic Liquids", *Electrochim. Acta*, **52**(9), 3317-3322 (2007)
- [145] P.C. Andricacos, C. Uzoh, J.O. Dukovic, J. Horkans and H. Deligianni, "Damascene Copper Electroplating for Chip Interconnections" *IBM Journal of Research and Development*, **42** (5), 567-574 (1998)
- [146] P. C. Andricacos, "Electroplated Copper Wiring on IC Chips", *Interface*, **7**, 22-25 (1998)
- [147] B. C. Inwood, A. E. Garwood, "Electroplated Coatings for Wear Resistance", *Tribol. Int.*, **11** (2), 113-119 (1978)
- [148] C. A. Huang, C. K. Lin, Y. H. Yeh, "The Corrosion and Wear Resistances of Magnesium Alloy (LZ91) Electroplated with Copper and Followed by 1  $\mu$ m-Thick Chromium Deposits", *Thin Solid Films*, **519** (15), 4774-4780 (2011)
- [149] K. Tokuhara, S. Hirosawa, "Corrosion Resistance of Nd–Fe–B Sintered Magnets", *J. Appl. Phys.*, **69** (8), 5521-5523 (1991)

- [150] M. Katter, L. Zapf, R. Blank, W. Fernegel, W. Rodewald, "Corrosion Mechanism of Re-Fe-Co-Cu-Ga-Al-B Magnets" 8<sup>th</sup> Joint MMM-Intermag Conference, San Antonio, Texas, USA, January 7-11, 2001
- [151] H. Bala, G. Pawlowska, S. Szymura, "Corrosion Characteristics of Nd-Fe-B Sintered Magnets Containing Various Alloying Elements", *J. Mag. Mag. Mat.*, **87**, L255-L259 (1990)
- [152] P. Sebastián, E. Vallés, E. Gómez, "Copper Electrodeposition in a Deep Eutectic Solvent. First Stages Analysis Considering Cu(I) Stabilization in Chloride Media", *Electrochim. Acta*, **123**, 285-295 (2014)
- [153] S. Ghosh, S. Roy, "Electrochemical Copper Deposition from an Ethaline-CuCl<sub>2</sub> · 2 H<sub>2</sub>O DES", *Surf. Coat. Tech.*, **238**, 165-173 (2014)
- [154] A. Mandroyan, M. Mourad-Mahmoud, M. L. Doche, J. Y. Hihn, "Effects of Ultrasound and Temperature on Copper Electro Reduction in Deep Eutectic Solvents (DES)", *Ultrason. Sonochem.*, Article in Press
- [155] Y. W. Lin, C. C. Tai, I. W. Sun, "Electrochemical Preparation of Porous Copper Surfaces in Zinc Chloride-1-Ethyl-3-Methyls Imidazolium Chloride Ionic Liquid", *J. Electrochem. Soc.*, **154** (6), D316-D321 (2007)
- [156] R. T. Carlin, H. C. De Long, J. Fuller, P. C. Trulove, "Microelectrode Evaluation of Transition Metal-Aluminum Alloy Electrodepositions in Chloroaluminate Ionic Liquids", *J. Electrochem. Soc.*, **145** (5), 1598-1607 (1998)
- [157] B. J. Tierney, W. R. Pitner, J. A. Mitchell, C. L. Hussey, G. R. Stafford, "Electrodeposition of Copper and Copper-Aluminum Alloys from a Room-Temperature Chloroaluminate Molten Salt", *J. Electrochem. Soc.*, **145**, 3110-3116 (1998)
- [158] G. W. Warren, G. Gao, Q. Li, "Corrosion of NdFeB Permanent Magnet Materials", *J. App. Phys.*, **70**, 6609-6611 (1991)
- [159] P. Y. Chen, I. W. Sun, "Electrochemical Study of Copper in a Basic 1-Ethyl-3-Methylimidazolium Tetrafluoroborate Room Temperature Molten Salt", *Electrochim. Acta*, **45**, 441-450 (1999)
- [160] S. Zein El Abedin, A.Y. Saad, H.K. Farag, N. Borisenko, Q.X. Liu, F. Endres, "Electrodeposition of Selenium, Indium and Copper in an Air- and Water-stable Ionic Liquid at Variable Temperatures", *Electrochim. Acta*, **52**, 2746-2754 (2007)
- [161] P. Y. Chen, M. J. Deng, D. X. Zhuang, "Electrochemical Codeposition of Copper and Manganese from Room-Temperature N-Butyl-N-Methylpyrrolidinium Bis(trifluoromethylsulfonyl)imide Ionic Liquid", *Electrochim. Acta*, **54**, 6935-6940 (2009)



- [162] T. Katase, K. Murase, T. Hirato, Y. Awakura, "Redox and Transport Behaviors of Cu(I) Ions in TMHA–NTf<sub>2</sub> Ionic Liquid Solution", *J. Appl. Electrochem.*, **37**, 339-344 (2007)
- [163] S. Zein El Abedin, A. Prowald, F. Endres, "Fabrication of Highly Ordered Macroporous Copper Films Using Template-Assisted Electrodeposition in an Ionic Liquid", *Electrochem. Com.*, **18**, 70-73 (2012)
- [164] P. Y. Chen, Y. T. Chang, "Voltammetric Study and Electrodeposition of Copper in 1-Butyl-3-Methylimidazolium Salicylate Ionic Liquid", *Electrochim. Acta*, **70**, 339-346 (2012)
- [165] D. Buttry, M. D. Ward, "Measurement of interfacial processes at electrode surfaces with the electrochemical quartz crystal microbalance", *Chem. Rev.*, **92** (6), 1355-1379 (1992)
- [166] E. M. Moustafa, S. Zein El Abedin, A. Shkurankov, E. Zschippang, A. Y. Saad, A. Bund, F. Endres, "Electrodeposition of Al in 1-Butyl-1-methylpyrrolidinium Bis(trifluoromethylsulfonyl)imide and 1-Ethyl-3-methylimidazolium Bis(trifluoromethylsulfonyl)imide Ionic Liquids: In Situ STM and EQCM Studies", *J. Phys. Chem. B*, **111**, 4693-4704 (2007)
- [167] P. Forte, A. Sachse, M. Maes, A. Galarneau, D. De Vos, "Selective Continuous Flow Extractive Denitrogenation of Oil containing S- and N-Heteroaromatics using Metal-Containing Ionic Liquids Supported on Monolithic Silica with Hierarchical Porosity", *RSC Adv.*, **4**, 1045-1054 (2014)
- [168] C. R. Hammond "The Elements" in: in CRC Handbook of Chemistry and Physics, Internet Version 2005, David R. Lide, ed., <http://www.hbcpnetbase.com>, CRC Press, Boca Raton, FL, 2005
- [169] C. K. Gupta, N. Krishnamurthy: Extractive Metallurgy of Rare Earths, CRC Press, 2005
- [170] M. Hart: "Evaluating United States and World Consumption of Neodymium, Dysprosium, Terbium, and Praseodymium in Final Products", Colorado School of Mines, Master Thesis 2011
- [171] P.P. Kumbhar, C.D. Lokhande, "Electrodeposition of Dysprosium from a Nonaqueous Bath", *Metal Finishing*, **92**, 70 (1994)
- [172] P.P. Kumbhar, C.D. Lokhande, "Electrodeposition of dysprosium from non-aqueous bath", *Indian Journal of Chemical Technology*, **1**, 194 (1994)
- [173] Y. Castrillejo, M.R. Bermejo, A.I. Barrado, R. Pardo, E. Barrado, A.M. Martinez, "Electrochemical behaviour of dysprosium in the eutectic LiCl-KCl at W and Al electrodes", *Electrochimica Acta*, **50**, 2047-2057 (2005)

- [174] A. Saita, M. Gibilaro, L. Massot, P. Chamelot, P. Taxil, A.M. Affoune, "Electrochemical behaviour of dysprosium(III) in LiF-CaF<sub>2</sub> on Mo, Ni and Cu electrodes", *J. Electroanal. Chem.*, **642**, 150-156 (2010)
- [175] L. L. Su, K. Liu, Y. L. Liu, L. Wang, L. Y. Yuan, L. Wang, Z. J. Li, X. L. Zhao, Z. F. Chai, W. Q. Shi, "Electrochemical Behaviors of Dy(III) and its Co-Reduction with Al(III) in Molten LiCl-KCl Salts", *Electrochim. Acta*, **147**, 87-95 (2014)
- [176] M. Zhang, Y. Yang, W. Han, M. Li, Y. Sun, Y. Yan, "Separation of SmCl<sub>3</sub>-DyCl<sub>3</sub> System by Electrolysis in KCl-LiCl-MgCl<sub>2</sub> Molten Salts", *Energy Procedia*, **39**, 375-381 (2013)
- [177] Y. S. Yang, M. L. Zhang, W. Han, P. Y. Sun, B. Liu, H. L. Jiang, T. Jiang, S. M. Peng, M. Li, K. Ye, Y. D. Yan, "Selective Electrodeposition of Dysprosium in LiCl-KCl-GdCl<sub>3</sub>-DyCl<sub>3</sub> Melts at Magnesium Electrodes: Application to Separation of Nuclear Wastes", *Electrochim. Acta*, **118**, 150-156 (2014)
- [178] R. Kazama, M. Matsumiya, N. Tsuda, K. Tsunashima, "Electrochemical Analysis of Diffusion Behavior and Nucleation Mechanism for Dy(II) and Dy(III) in Phosphonium-Based Ionic Liquid", *Electrochim. Acta*, **113**, 269-279 (2013)
- [179] K. Pyonghun, X. Hongwei, M. Jing, Z. Yuchun, "Electrodeposition Behavior of Dysprosium in EMIMBF<sub>4</sub> Ionic Liquid", *Rare Metal Mat. Eng.*, **41** (5), 881-884 (2012)
- [180] M. J. Deng, P. Y. Chen, T. I. Leong, I. W. Sun, J. K. Chang, W. T. Tsai, "Dicyanamide Anion based Ionic Liquids for Electrodeposition of Metals", *Electrochem. Comm.*, **10**, 213-216 (2008)
- [181] S. Kobayashi, I. Hachiya, "Lanthanide Triflates as Water-Tolerant Lewis Acids. Activation of Commercial Formaldehyde Solution and Use in the Aldol Reaction of Silyl Enol Ethers with Aldehydes in Aqueous Media", *J. Org. Chem.*, **59** (13), 3590-3596 (1994)
- [182] S. Kobayashi, H. Ishitani, "Lanthanide(III)-Catalyzed Enantioselective Diels-Alder Reactions. Stereoselective Synthesis of Both Enantiomers by Using a Single Chiral Source and a Choice of Achiral Ligand", *J. Am. Chem. Soc.*, **116** (9), 4083-4084 (1994)
- [183] J. M. Harrowfield, D. L. Kepert, J. M. Patrick, A. H. White, "Structure and Stereochemistry in 'F-Block' Complexes of high Coordination Number. VIII. The [M(unidentate)<sub>9</sub>] System. Crystal structures of [M(OH<sub>2</sub>)<sub>9</sub>] [CF<sub>3</sub>SO<sub>3</sub>]<sub>3</sub>, M = La, Gd, Lu, Y", *Aust. J. Chem.*, **36** (6), 483-492 (1983)
- [184] S. Kobayashi, K. Manabe, "Green Lewis Acid Catalysis in Organic Synthesis", *Pure Appl. Chem.*, **72** (7), 1373-1380 (2000)
- [185] Y. N. NuLi, J. Yang, P. Wang, "Electrodeposition of Magnesium Film from BMIMBF<sub>4</sub> Ionic Liquid", *Appl. Surf. Sci.*, **252**, 8086-8090 (2006)

- [186] P. Wang, Y. N. NuLi, J. Yang, Z. Feng, "Mixed Ionic Liquids as Electrolyte for Reversible Deposition and Dissolution of Magnesium", *Surf. Coat. Tech.*, **201**, 3783-3787 (2006)
- [187] N. Amir, Y. Vestfrid, O. Chusid, Y. Gofer, D. Aurbach, "Progress in Nonaqueous Magnesium Electrochemistry", *J. Power Sources*, **174**, 1234-1240 (2007)
- [188] B. Dilasari, K. Kwon, C. K. Lee, H. Kim, "Electrodeposition of Some Selective Metals Belonging to Light, Refractory and Noble Metals from Ionic Liquid Electrolytes", *J. Kor. Electrochem. Soc.*, **15** (3), 135-148 (2012)
- [189] L. M. Glukhov, A. A. Greish, L. M. Kustov, "Electrodeposition of Rare Earth Metals Y, Gd, Yb in Ionic Liquids", *Rus. J. Phys. Chem. A*, **84** (1), 111-115 (2010)
- [190] K. B. Oldham, "Signal-Independent Electroanalytical Method", *Anal. Chem.*, **44** (1), 196-198 (1972)
- [191] K. B. Oldham, J. Spanier, "The Replacement of Fick's Laws by a Formulation Involving Semidifferentiation", *J. Electroanal. Chem. Interfacial Electrochem.*, **26**, 331-341 (1970)
- [192] K. B. Oldham, "New Approach to the Solution of Electrochemical Problems Involving Diffusion", *Anal. Chem.*, **41**, 1904-1905 (1969)
- [193] J. Park, Y. Jung, P. Kusumah, J. Lee, K. Kwon, C. K. Lee, "Application of Ionic Liquids in Hydrometallurgy", *Int. J. Mol. Sci.*, **15**, 15321-15342 (2014)
- [194] M. Grenness, K. B. Oldham, "Semiintegral Electroanalysis: Theory and Verification", *Anal. Chem.*, **44** (7), 1121-1129 (1972)
- [195] H. J. Gores, J. Barthel, S. Zugmann, D. Moosbauer, M. Amereller, R. Hartl, and A. Maurer in: *Handbook of Battery Materials* 2nd Edition, p.525-626, Wiley-VCH Verlag GmbH & Co. KGaA, Weinheim, 2011
- [196] C. Schreiner, S. Zugmann, R. Hartl, H. J. Gores, "Fractional Walden Rule for Ionic Liquids: Examples from Recent Measurements and a Critique of the So-Called Ideal KCl Line for the Walden Plot", *J. Chem. Eng. Data*, **55**, 1784-1788 (2010)
- [197] A. Acidi, M. Hasib-ur-Rahman, F. Larachi, A. Abbaci, "Ionic Liquids [EMIM][BF<sub>4</sub>], [EMIM][OTf] and [BMIM][OTf] as Corrosion Inhibitors for CO<sub>2</sub> Capture Applications", *Korean J. Chem. Eng.*, **31** (6), 1043-1048 (2014)
- [198] K. Tsunashima, M. Sugiya, "Physical and Electrochemical Properties of Low-Viscosity Phosphonium Ionic Liquids as Potential Electrolytes", *Electrochem. Comm.*, **9** (9), 2353-2358 (2007)
- [199] T. M. Pan, C. H. Lu, "Effect of Postdeposition Annealing on the Structural and Electrical Properties of thin Dy<sub>2</sub>TiO<sub>5</sub> Dielectrics", *Thin Solid Films*, **519**, 8149-8153 (2011)

- [200] K. D. Jayasuriya, S. J. Campbell, A. M. Stewart, “Magnetic Transitions in Dysprosium: A Specific-Heat Study”, *Phys. Rev. B*, **31** (9), 6032-6046 (1985)
- [201] Active Material Laboratory UCLA, “ Magnetostriction and Magnetostrictive Materials”, accessed 5 March 2015  
<https://web.archive.org/web/20060202050523/http://aml.seas.ucla.edu/research/areas/magnetostrictive/mag-composites/Magnetostriction\%20and\%20Magnetostrictive\%20Materials.htm>
- [202] C. Rodríguez, M. Rodriguez, I. Orue, J. L. Vilas, J. M. Barandiarán, M. L. F. Gubieda, L. M. Leon, “New Elastomer-Terfenol-D Magnetostrictive Composites”, *Sensors and Actuators A*, **149** 251-254 (2009)
- [203] M. R. Bermejo, J. Gómez, A. M. Martínez, E. Barrado, Y. Castrillejo, “Electrochemistry of Terbium in the Eutectic LiCl-KCl”, *Electrochim. Acta*, **53**, 5106-5112 (2008)
- [204] B. Y. Kim, D. H. Lee, J. Y. Lee, J. I. Yun, “Electrochemical and Spectroscopic Investigations of Tb(III) in Molten LiCl-KCl”, *Electrochem. Comm.*, **12**, 1005-1008 (2010)
- [205] G. Qui, D. Wang, M. Ma, X. Jin, G. Z. Chen, “Electrolytic Synthesis of TbFe<sub>2</sub> from Tb<sub>4</sub>O<sub>7</sub> and Fe<sub>2</sub>O<sub>3</sub> Powders in Molten CaCl<sub>2</sub>”, *J. Electroanal. Chem.*, **589**, 139-147 (2006)
- [206] K. Sugimoto, Jpn. Pat. 02232392 (1990).
- [207] J. Gong, E. J. Podlaha, “Electrodeposition of Fe-Tb Alloys from an Aqueous Electrolyte”, *Electrochem. Solid-State Lett.*, **3** (9), 422-425 (2000)
- [208] R. Mishra, “ELECTRODEPOSITION OF RARE EARTH-TRANSITION METAL ALLOY THIN FILMS AND NANOSTRUCTURES”, Doctoral thesis, Louisiana, 2007
- [209] T. Akiya, J. Liu, H. Sepehri-Amin, T-Ohkubo, A. Hattori, K. Hono, “Low Temperature Diffusion Process using Rare Earth-Cu Eutectic Alloys for Hot-Deformed, Nd-Fe-B Bulk Magnets”, “*J. Appl. Phys.*”, **114**, 17A766-1, 17A66-3 (2014)
- [210] J. Liu, H. Sepehri-Amin, T. Ohkubo, K. Hattori, T. Schrefl, K. Hono, “Effect of Nd content on the microstructure and coercivity of hot-deformed Nd-Fe-B permanent magnets”, *Acta Mat.*, **61** (14), 5387-5399 (2013)
- [211] H. Sepehri-Amin, T. Ohkubo, T. Nishiuchi, S. Hirose, and K. Hono, “1124-1127”, *Scr. Mater.*, **63**, 1124 (2010).
- [212] C. Mishima, K. Noguchi, M. Yamazaki, H. Mitarai, and Y. Honkuta, in Proceedings of 21th Workshop on Rare Earth Magnets and Their Applications, Bled, Slovenia (2010), p. 253.

- [213] K. Yasuda, S. Kobayashi, T. Nohira, R. Hagiwara, "Electrochemical Formation of Nd-Ni Alloys in Molten NaCl–KCl–NdCl<sub>3</sub>
- [214] C. Nourry, L. Massot, P. Chamelot, P. Taxil, "Formation of Ni-Nd Alloys by Nd(III) Electrochemical Reduction in Molten Fluoride", *J. New Mat. Electrochem. Systems*, **10**, 117-122 (2007)
- [215] M. Gibilaro, L. Massot, P. Chamelot, P. Taxil, "Study of Neodymium Extraction in Molten Fluorides by Electrochemical Co-Reduction with Aluminium", *J. Nuc. Mat.*, **382**, 39-45 (2008)
- [216] P. Taxil, L. Massot, C. Nourry, M. Gibilaro, P. Chamelot, L. Cassayre, "Lanthanides Extraction Processes in Molten Fluoride Media. Application to Nuclear Spent Fuel Re-processing", *J. Fluorine Chem.*, **130** (1), 94-101 (2009)
- [217] P. Taxil, P. Chamelot, L. Massot and C. Hamel, "Electrodeposition of Alloys or Compounds in Molten Salts and Applications", *J. Min. Met.*, **39** (1-2)B, 177-200 (2003)
- [218] P. Chamelot, L. Massot, C. Hamel, C. Nourry, P. Taxil, "Feasibility of the Electrochemical Way in Molten Fluorides for Separating Thorium and Lanthanides and Extracting Lanthanides from the Solvent", *J. Nuclear Mat.* **360**, 64-74 (2007)
- [219] B. Q. Fan, H. Lai, J. X. Li, Z. G. Huang, "Electrodeposited RE-TM (RE=Dy, Nd, Eu: TM=Co= Alloy Films and Their Magnetic Properties", *Chin. Rare Earths*, **32** (3), 8-13 (2011) (Chinese)
- [220] M. Yamagata, Y. Katayama, T. Miura, "Electrochemical Behavior of Samarium, Europium, and Ytterbium in Hydrophobic Room-Temperature Molten Salt Systems", *J. Electrochem. Soc.*, **153** (1), E5-E9 (2006)
- [221] J.M.D. Coey, H. Sun, "Improved Magnetic Properties by Treatment of Iron-Based Rare Earth Intermetallic Compounds in Ammonia", *J. Magn. Magn. Mater.*, **87**, L251-L254 (1990)
- [222] O.S. Anilturk, A.R. Koymen, "ELEMENT specific magnetization of GdCo composite system using Spin polarized Auger electron spectroscopy (SPAES)", *J. Magn. Magn. Mater.*, **272-276**, 531-533 (1990)
- [223] M. Z. An, J. L. Wang, D. Z. Sun, "Electrodeposition of La-Ni alloy films in a Nonaqueous System", *J. Appl. Electrochem.*, **31**, 891-896 (2001)
- [224] J. Li, H. Lai, B. Fan, B. Zhuang, L. Guan, Z. Huang, "Electrodeposition of RE-TM (RE=La, Sm, Gd; TM=Fe, Co, Ni) Films and Magnetics Properties in Urea Melt, *J. Alloy. Compd.*, **477**, 547-551 (2009)
- [225] M. H. Kryder, "Advances in Magneto-Optic Recording Technology", *J. Mag. Mag. Mat.*, **83**, 1-5 (1990)

- [226] P. Hansen, "Magneto-Optical Recording Materials and Technologies", *J. Mag. Mag. Mat.*, **83**, 6-12 (1990)
- [227] M. Nuding, P. Lamparter, S. Steeb, "X-Ray Diffraction with Amorphous and Hydrogenated Nickel-Dysprosium Alloys", *J. Non-Cryst. Solids*, **205-207**, 583-586 (1996)
- [228] S. G. Sankar, V. U. S. Rao, E. Segal, W. E. Wallace, W. G. D. Frederick, H. J. Garrett, "Magnetocrystalline Anisotropy of  $\text{SmCo}_5$  and its Interpretation on a Crystal-Field Model", *Phys. Rev. B*, **11**, 435-439 (1975)
- [229] C. L. Hussey, T. M. Laher, "Electrochemical and Spectroscopic Studies of Cobalt(II) in Molten Aluminum Chloride-N-n-Butylpyridinium Chloride", *Inorg. Chem.*, **20**, 4201-4206 (1981)
- [230] R. T. Carlin, P. C. Trulove, H. C. De Long, "Electrodeposition of Cobalt-Aluminum Alloys from Room Temperature Chloroaluminate Molten Salt", *J. Electrochem. Soc.*, **143**, 2747-2758 (1996)
- [231] W. Freyland, C. A. Zell, S. Zein El Abedin, F. Endres, "Nanoscale Electrodeposition of Metals and Semiconductors from Ionic Liquids", *Electrochim. Acta*, **48**, 3053-3061 (2003)
- [232] C. Su, M. An, P. Yang, H. Gu, X. Guo, "Electrochemical Behavior of Cobalt from 1-Butyl-3-methylimidazolium Tetrafluoroborate Ionic Liquid", *Appl. Surface Sci.*, **256**, 4888-4893 (2010)
- [233] S. Schaltin, P. Nockermann, B. Thijs, K. Binnemans, J. Fransaer, "Influence of the Anion on the Electrodeposition of Cobalt from Imidazolium Ionic Liquids", *Electrochem. Solid-State Lett.*, **10** (10), D104-D107 (2007)
- [234] P. Nockemann, M. Pellens, K. Van Hecke, L. Van Meervelt, J. Wouters, B. Thijs, E. Vanecht, T. N. Parac-Vogt, H. Mehdi, S. Schaltin, J. Fransaer, S. Zahn, B. Kirchner, K. Binnemans, "Cobalt(II) Complexes of Nitrile-Functionalized Ionic Liquids", *Chem. Eur. J.*, **16**, 1849-1858 (2010)
- [235] Y. L. Zhu, Y. Katayama, T. Miura, "Effects of Acetonitrile on Electrodeposition of Ni from a Hydrophobic Ionic Liquid", *Electrochim. Acta*, **55**, 9019-9023 (2010)
- [236] J. Li, H. Lai, B. Fan, B. Zhuang, L. Guan, Z. Huang, "Electrodeposition of RE-TM (RE = La, Sm, Gd; TM = Fe, Co, Ni) Films and Magnetic Properties in Urea Melt", *J. Alloy. Compd.*, **477**, 547-551 (2009)
- [237] H. Y. Hsu, C. C. Yang, "Conductivity and Electrochemistry of Cobalt(II) and Dysprosium Chloride in Zinc Chloride-1-Ethyl-3-Methylimidazolium Chloride Room Temperature Molten Salt", *Electrochemical Society Proceedings*, **19**, 690-699 (2002)

- [238] H. Y. Hsu, C. C. Yang, "Conductivity, Electrodeposition and Magnetic Property of Cobalt(II) and Dysprosium Chloride in Zinc Chloride-1-Ethyl-3-Methylimidazolium Chloride Room Temperature Molten Salt", *Z. Naturforsch.*, **58b**, 139-146 (2003)
- [239] E. Gómez, P. Cojocaru, L. Magagnin, E. Valles, "Electrodeposition of Co, Sm and SmCo from a Deep Eutectic Solvent", *J. Electroanal. Chem.*, **658**, 18-24 (2011)
- [240] A. Ispas, M. Buschbeck, S. Pitula, A. Mudring, M. Uhlemann, A. Bund, F. Endres, "Electrodeposition of Co, Sm and Co-Sm Thin Layers", *ECS Transactions*, **16** (45) 119-127 (2009)
- [241] R. Fukui, Y. Katayama, T. Miura, "Electrodeposition of Cobalt from a Hydrophobic Room Temperature Molten Salt System", *Electrochemistry*, **73**, 567-570 (2005)
- [242] M. Yamagata, N. Tachikawa, Y. Katayama, T. Miura, "Electrochemical Behavior of Iron(II) Species in a Hydrophobic Room-temperature Molten Salt", *Electrochemistry*, **73**, 564-566 (2005)
- [243] A. R. B. de Castro, G. B. Fraguas, P. T. Fonseca, R. N. Suave, S. Gama, A. A. Coelho, I. A. Santos, "Circular Magnetic Dichroism of Fe<sub>17</sub>Dy<sub>2</sub>", *J. Electron Spectros.*, **101-103**, 725-728 (1999)
- [244] A. S. Van Der Goot, K. H. J. Buschow, "The Dysprosium-Iron System: Structural and Magnetic Properties of Dysprosium-Iron Compounds", *J. Less Common Met.*, **21**, 151-157 (1970)
- [245] Á. Llavona, L. Pérez, M. C. Sánchez, V. de Manuel, "Enhancement of Anomalous Codeposition in the Synthesis of Fe-Ni Alloys in Nanopores", *Electrochim. Acta*, **106**, 392-397 (2013)
- [246] H. Konishi, T. Nohira, Y. Ito, "Formation of Dy-Fe Alloy Films by Molten Salt Electrochemical Process", *Electrochim. Acta*, **47**, 3533-3539 (2002)
- [247] P. Liu, Y. P. Du, Q. Q. Yang, G. R. Li, Y. X. Tong, "Electrochemical Behavior of Fe(II) in Acetamide-Urea-NaBr-KBr Melt and Magnetic Properties of Inductively Codeposited Nd-Fe Film", *Electrochim. Acta*, **52**, 710-714 (2006)
- [248] Z. Hong-ru, Y. Yun-dan, W. Guo-ying, G. Hong-liang, "FePt Thin Films Electrodeposited from Non-Aqueous Liquids", *Int.J. Electrochem. Sci.*, **7**, 5544-5556 (2012)





# Symbols

Symbol	Annotation	Units
$c$	concentration	$\text{mol l}^{-1}$
$E$	energy	J
$H$	magnetic field strength	$\text{A m}^{-1}$
$\hbar$	reduced Planck's constant	$1.054571628 \times 10^{-34} \text{ J s}$
$k_B$	Boltzmann constant	$1.3806504 \times 10^{-23} \text{ J K}^{-1}$
$m$	mass	kg
$\mu$	magnetic moment	$\text{A m}^2$
$\omega$	mass fraction	
$T$	thermodynamic temperature	K
$V$	volume	$\text{m}^3$
$E$	potential	V
$t$	time	s
$i$	current	A
$Z$	impedance	$\Omega$
$e$	elementary charge	$1.6021764871 \times 10^{-19} \text{ A s}$
$\varepsilon$	dielectric permittivity	$\text{A s V}^{-1} \text{ m}^{-1}$
$C$	capacitance	$\text{C mol}^{-1}$
$R$	ohmic resistance	$\Omega$
$Q$	electric charge	C
$\kappa$	conductivity	$\Omega^{-1}$
$L$	inductance	H
$f$	resonance frequency	Hz
$\Delta f$	frequency shift	Hz
$\rho_s$	mass density	$\mu\text{g cm}^2$
$\Delta m$	mass change	$\mu\text{g}$
$\mu_Q$	quartz shear modulus	$2.947 \times 10^{11} \text{ g cm}^{-1} \text{ s}^{-2}$
$\rho_Q$	quartz density	$2.648 \text{ g cm}^{-3}$
$\eta$	dynamic viscosity	$\text{kg m}^{-1} \text{ s}^{-1}$
$\Delta P$	change in hydrostatic pressure	$\text{kg s}^{-2}$
$C_f$	calibration constant for mass change	$\text{Hz } \mu\text{g}^{-1}$
$M$	molar mass	$\text{g mol}^{-1}$
$F$	Faraday constant	$96485 \text{ C mol}^{-1}$
$z$	exchanged electrons	1
$\Delta G$	Gibbs energy	J

# Appendix

Ag[NTf <sub>2</sub> ]	silver bis(trifluoromethylsulfonyl)imide
Ag[OTf]	silver trifluoromethanesulfonate
Cu[NTf <sub>2</sub> ] <sub>2</sub>	copper-(II)-bis(trifluoromethylsulfonyl)imide
Cu[OTf] <sub>2</sub>	copper-(II)-trifluoromethanesulfonate
Dy[NTf <sub>2</sub> ] <sub>3</sub>	dysprosium-(III)-bis(trifluoromethylsulfonyl)imide
Dy[OTf] <sub>3</sub>	dysprosium-(III)-trifluoromethanesulfonate
Tb[NTf <sub>2</sub> ] <sub>3</sub>	terbium-(III)-bis(trifluoromethylsulfonyl)imide
[BMIm][OTf]	1-butyl-3-methylimidazolium trifluoromethanesulfonate
[BMMIm][OTf]	1-butyl-2,3-dimethylimidazolium trifluoromethanesulfonate
[BMPyr][DCA]	1-butyl-1-methylpyrrolidinium dicyanamide
[BMPyr][NTf <sub>2</sub> ]	1-butyl-1-methylpyrrolidinium bis(trifluoromethylsulfonyl)imide
[BMPyr][OTf]	1-butyl-1-methylpyrrolidinium trifluoromethanesulfonate
[EMIM][BF <sub>4</sub> ]	1-ethyl-1-methylimidazolium tetrafluoroborate
[EMIM][NTf <sub>2</sub> ]	1-ethyl-1-methylimidazolium bis(trifluoromethylsulfonyl)imide
[EMIm][OTf]	1-ethyl-3-methylimidazolium trifluoromethanesulfonate
[P <sub>2225</sub> ][NTf]	triethyl-pentylphosphonium bis(trifluoromethylsulfonyl)imide
CE	counter electrode
CV	cyclic voltammogram
EDX	energy dispersive roentgen spectroscopy
EQCM	electrochemical quartz micro balance
EV	electric vehicle
fis-QCM	fast impedance scanning quartz micro balance
HEV	hybrid electric vehicle
KF	Karl-Fischer
mpe	equivalent mass change per mole of electrons
RE	reference electrode
TGA	thermogravimetric analysis
WDX	wavelength dispersive roentgen spectroscopy

WE	working electrode
XPS	X-ray photoelectron spectroscopy

# Curriculum Vitae

## Personal Details

---

Date of Birth	31 st of January 1985
Place of Birth	Quito, Ecuador
Nationality	Austrian, Ecuadorian
Contact	+49 151 / 211 36 149 gott.suppan@hotmail.de

## Education

---

03/2011 - present	Doctoral Thesis in Chemistry University of Regensburg - In cooperation with Siemens AG Research and Technology Center - CT T MAT MSR-DE, Erlangen Supervision by Prof. Dr. Heiner J. Gores
10/2008 - 01/2011	Study of Chemistry (Master of Science) University of Regensburg, Germany - In cooperation with Continental AG Institute for Theoretical and Physical Chemistry Thesis subject: Electrochemical corrosion studies
10/2005 - 10/2008	Study of Chemistry (Bachelor of Science) University of Regensburg, Germany
1996 - 2005	German Abitur Goethe Gymnasium, Regensburg, Germany

# Declaration

I hereby declare that I am the sole author of this thesis and the work reported herein.  
Information derived from the published and unpublished work of others has been acknowledged in the text and references are given in the list of sources.

Regensburg, the 12<sup>th</sup> of Mai 2015

.....

Gottfried Suppan

